UNIVERSITÀ DEGLI STUDI DI TORINO

DOTTORATO IN FISICA E ASTROFISICA

Design and development of the Calorimeter for the FOOT experiment

Author:
Lorenzo SCAVARDA

Supervisor:
Prof. Stefano ARGIRÒ
Dr. Piergiorgio CERELLO

"It's something unpredictable,
but in the end is right,
I hope you had the time of your life"

B.J.Armstrong

Per Mamma e Papà

Contents

Introduction

Charged Particle Therapy (CPT) is a form of radiotherapy which uses charged ions, mainly protons and ^{12}C, to treat tumours. CPT has several advantages compared to conventional radiotherapy such as an higher precision in the localization of the dose, a better preservation of healthy tissues and the higher biological effectiveness of charged hadrons over X-rays. For these reasons, in the last few years the number of centers that deliver this kind of treatments and the number of treated patients are increasing. At the moment, 109 particle therapy facilities operate all over the world and 37 other structures are under construction. From 1994 to 2020 about $\sim$ 40000 people have been treated with carbon ion beams and $\sim$ 250000 people with proton beams [1]. However, a non-negligible fraction of the beam particles ($\sim$ 4%) undergoes nuclear processes and can cause beam or target (i.e. tissue) fragmentation. In the case of heavy ion therapy ($Z \geq 2$) the nuclear interactions can also lead to the fragmentation of the projectile. Secondary particles are emitted mostly in the same direction and with similar kinetic energy per nucleon of the projectiles, but, having a lower mass compared to the primary, they have a longer range. Thus, the fragments cause an energy deposition outside the tumour volume that can be particularly dangerous for the healthy tissues or organs at risk in the vicinity.

A similar effect is present also in proton-therapy where nuclear interaction lead to target fragmentation. In this case the fragments, generated from atoms at rest, have a range of order of few μm with a non-neglibile dose deposition along the beam entrance channel. All these processes are taken into account in current *Treatment Planning System* (TPS), the tools used by radiation oncologists and medical physicists for planning the appropriate treatment for a cancer patient. However, as pointed out by different studies [2] [3], the accuracy of the dose deposition calculation caused by the nuclear fragmentation must be improved. In particular, the state of the art points out a lack of experimental data of nuclear differential cross sections ($d^2\sigma/d\Omega \cdot dE$) relevant for particle therapy applications. These data are required to improve TPSs both in proton and in heavy ion therapy and to benchmark *Monte Carlo* (MC) simulation tools.

The fragmentation processes are also relevant for radio-protection in space, in view of long duration manned missions, such as new lunar landings and journeys to Mars [4]. In this kind of missions, the astronauts are exposed to *Solar Particle Events* (SPE) and *Galactic Cosmic Rays* (GCR), the main sources of energetic particles in space. SPE are mainly composed of protons, with an energy spectrum that peaks just before the GeV region and could inflict a lethal dose to the astronauts. GCR consist of high energy protons and highly energetic charged particles, i.e. nuclei, originated from supernovae within the Milky Way Galaxy with an energy spectrum that ranges from MeVs to TeVs. The radiation field reaching the astronauts is modified by the interaction with the walls of the spacecraft and its shielding materials. As for particle therapy, there is a lack of differential cross section measurements about the nuclear inelastic interactions of the particles involved in space radiations. Thus, in order to minimize the dose received by astronauts, the design of the spacecraft shielding requires a detailed knowledge of fragmentation processes.

FragmentatiOn Of Target (FOOT) is a nuclear physics experiment, currently under construction, that will measure differential cross sections of fragments produced in nuclear interactions relevant for both CPT and radioprotection for space missions. In particular FOOT aims at measuring processes for ^{12}C and ^{16}O beams up to 800 MeV/u kinetic energy impinging on targets composed of ^{12}C and C_2H_4. In order to study the fragmentation of the target material relevant for proton-therapy, FOOT adopts an inverse kinematic approach and a subtraction of cross section method, measuring the differential cross sections ($d\sigma/dE$) of ^{12}C and ^{16}O beams at 200 MeV/u on targets of ^{12}C and C_2H_4.

FOOT has been designed in order to identify fragments with two different setups depending on their emission angle distribution. For light fragments ($Z \leq 3$) with emission angle up to 90° an apparatus derived from the nuclear emulsion technology developed and adopted in the OPERA experiment [5] is used. The main component of the emulsion setup is a compact detector composed of different layers of nuclear emulsions and absorbing materials. The second setup is an apparatus composed of different sub-detectors optimized to detect heavy ($Z \geq 3$) fragments with a narrower angular distribution ($\Theta \leq 10°$). In this case, the electronic spectrometer is composed of a beam monitoring system, three tracking detectors working in a magnetic field provided by two permanent magnets, a time of flight measurement system, an energy loss detector and a calorimeter.

My Ph.D. project focuses on the design, construction and operation tests of the calorimeter of the FOOT experiment. The aim of the calorimeter is to provide a linear response and a resolution below 2% on the kinetic energy measurement. In the thesis all the tests performed to make the design choices which achieved these performances will be discussed in details. Several test beams have been performed at *Centro Nazionale Adroterapia Oncologica* (CNAO) in Pavia (Italy) in order to select the photo-detector, choose the crystal wrapping, design the front-end readout board, the *data acquisition system* (DAQ), the mechanics, the temperature control system, etc. Recently, a calorimeter module (9 crystals) has been successfully operated in the first FOOT data taking with all the sub-detectors at the *Gesellschaft fur Schwerionenforschung* (GSI) accelerator facility (Germany). The energy of the fragments created in the interaction of 200-400 MeV/u ^{16}O beams and ^{12}C or C_2H_4 targets has been measured and used to reconstruct the fragments mass. In Chapter 1 an overview of the physics and the biological aspects underlying the interactions of hadrons with matter will be presented. In addition, a focus on the role of the nuclear inelastic interactions in particle therapy and in space radioprotection will be discussed. Chapter 2 is dedicated to describe the FOOT experiment, its aims, its measurements strategy, the experimental setups and the associated software. The principle of operations of the calorimeter detectors will be presented in Chapter 3, together with a detailed description of the FOOT calorimeter. In Chapter 4 the results of all the test beams performed to make all the design choices will be discussed. Chapter 5 will be dedicated to study of crystal response and to the crystal calibration. In Chapter 6 the preliminary results of the calorimeter stand-alone analysis are presented and, finally, in Chapter 8 the calorimeter in the FOOT software framework is discussed.

Chapter 1

Physics motivations

1.1 Introduction

The goal of CPT is to treat tumours using hadrons [1], exploiting their physics properties in the interaction with matter and the biological response of the irradiated tissues. Differently from conventional radiotherapy, which employs photon beams, the particles adopted are mainly protons and ^{12}C ions, although other ions such as ^{4}He and ^{16}O are under study [4]. The main advantages of this approach are given by the higher precision in the dose localization and the better preservation of healthy tissues providing an increase of the biological effectiveness of treatments.

Studying the effects of charged ions radiation is relevant also for other applications, like radioprotection in space. Indeed, galactic cosmic rays are mainly composed by protons (86%), ^{4}He (12%) and C (1%): the same particles involved in the CPT even if with a slightly different energy range. Moreover, in both fields the nuclear inelastic interaction plays an important role and cannot be neglected. In CPT it can modify the results of the treatments if not properly considered, while in space radiation protection the fragmentation of cosmic rays on the spacecraft material contributes to the damaging dose absorbed by the astronauts that can lead to carcinogenesis and tissues degeneration.

In this chapter the fundamentals of charged particles interaction with matter are presented in Sec. 1.2, followed by an overview of the biological aspects involved in CPT in Sec. 1.3. The state of the art of the particle therapy and the space radioprotection open issues will be presented in Sec. 1.4.

1.2 Interaction of charged particles with matter

When a charged particle passes through matter different phenomena occur. Focusing on the particles involved in CPT, the main interactions of an incident hadron are:

- Electromagnetic Energy Loss (inelastic scattering)
- Multiple Coulomb Scattering (elastic scattering)
- Nuclear Reactions

1.2.1 Electromagnetic Energy Loss

The effect of the Coulomb force is an excitation or ionization of the orbital electrons of the target material atoms, with an energy transfer from and the consequent energy

[1] Hadrons are non-elementary particles composed by two or more quarks held together by the strong force.

loss of the incident particle. In addition, the projectile initial direction is tilted as described by the multiple Coulomb scattering theory. The energy loss of a charged particle traversing a given absorber material is described by the *stopping power*, defined as the particle energy variation (dE) per unit path length (dx):

$$S = -\frac{dE}{dx} \tag{1.1}$$

and therefore measured in $keV/\mu m$. The *mass stopping power* for a given target material, instead, is obtained by dividing the stopping power by the density ρ: $-dE/\rho dx$. The mass stopping power is a useful quantity because it expresses the rate of energy loss of the charged particle per $g \cdot cm^2$ of the traversed medium. In a gas, for example, $-dE/dx$ depends on the pressure, but $-dE/\rho dx$ does not.

The first formulation of the interaction between the projectile and the electrons of the target material atoms was given by Niels Bohr with an approach based on classical physics. Then in the thirties, Bethe and Bloch improved the Bohr model including the quantum mechanical theory, giving the following *Bethe and Bloch formula* [6]:

$$-\frac{dE}{dx} = 2\pi N_a r_e^2 m_e c^2 \rho \frac{Z}{A}\frac{z^2}{\beta^2}\left[\ln\left(\frac{2m_e\gamma^2 v^2 W_{max}}{I^2}\right) - 2\beta^2 - \delta - 2\frac{C}{Z}\right] \tag{1.2}$$

where:

- N_A is the Avogadro constant $= 6.022 \cdot 10^{23}\ mol^{-1}$
- r_e is the classical electron radius $= 2.817 \cdot 10^{-13}\ cm$
- m_e is the electron mass $= 9.109 \cdot 10^{-31}\ Kg$
- ρ is the density of the absorbing material
- Z and A are the atomic number and atomic weight of absorbing material
- z is the charge of incident particle
- $\beta = v/c$ is the velocity relative to the speed of light c, with $\gamma = 1/\sqrt{1-\beta^2}$
- W_{max} is the maximum energy transfer in a single collision for an incident particle with mass M $= \frac{2m_e c^2 \beta^2 \gamma/2}{1+2\gamma m_e/M+(m_e/M)^2}$ [7]
- I is the average excitation potential

$$I = \begin{cases} 12Z + 7 & \text{eV if } Z \leq 13, \\ 9.76Z + 58.8Z^{-0.19} & \text{eV if } Z > 13. \end{cases}$$

- δ is the density correction which takes into account that the particle can polarize the atoms along its path, thus shielding from the full electric field intensity the electrons far from the its path, and an effect that is only relevant for ultra-relativistic charged particles
- C is the shell correction, that considers the effects arising when particle and atomic electrons velocities are comparable.

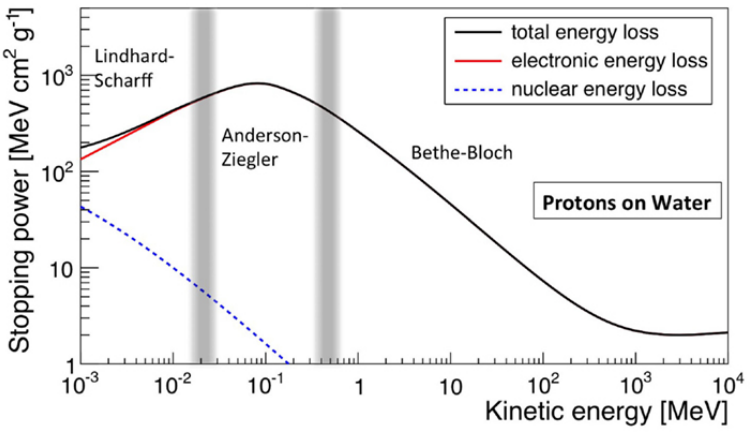

Figure 1.1: Stopping power for protons in water as a function of the kinetic energy [8].

Eq. (1.2) is valid for particles with $0.1 \leq \beta\gamma^2 \leq 1000$ and materials with intermediate charge [7].

CPT aims at reaching deep-seated tumours at a maximum depth of $\sim 30 - 40\ cm$ in the human body and the highest kinetic energies at the CPT beams are about 250 MeV for protons and 450 MeV for carbon ions, corresponding to particle velocities of the order of $\beta \sim 0.6$ and $\beta \sim 0.7$, respectively. Thus, CPT generally deals with "moderately relativistic" particles. An example of the stopping power of protons in water at energies relevant for CPT is shown in Figure 1.1, where the contribution of both the electronic and the nuclear part can be described in terms of the relativistic parameter $\beta\gamma$. At $\beta\gamma \simeq 3$ the curve reaches a minimum of ionization, $dE/dx \simeq 2\ MeV/g \cdot cm^2$, followed at higher energies by a relativistic rise, with a logarithmic dependence on $\beta\gamma$. In this energy region, excluding the constant terms (e.g.: $m_e, N_a, Z/A \sim 0.5$) and the negligible contributions (e.g.: δ), the energy loss in the Bethe-Block formula essentially depends on the absorbing material density and mean excitation potential ($ln(1/I^2)$) and the square of the incident particle charge and velocity (z^2/β^2), without any dependence on the incident particle mass. The main source of energy loss is given by the excitation or ionization of electrons in the target material and the stopping power is commonly defined as *electronic stopping power*. When the particle energy decreases below the ionization minimum, the stopping power increases, according to its $1/\beta^2$ dependence in Eq. (1.2), and the projectile releases most of its energy only close to the end of its path in the medium. Here, the particle velocity is comparable to the orbital velocity of the bounded electrons and the C/Z term becomes important. As the particle further slows down, the rate of energy loss reaches a maximum and then drops again. At even lower velocities the particle captures electrons, and so its effective charge is reduced. Therefore, in Eq. (1.2) the particle charge Z has to be replaced by the effective charge Z_{eff} , which can be described by the following empirical expression [9]:

$$Z_{eff} = Z \cdot (1 - e^{-125\beta Z^{2/3}}) \tag{1.3}$$

Since $Z_{eff} < Z$, the rate of energy loss per unit track length decreases and the dE/dx drops, causing a distal falloff in the depth-dose profile that is sharper for heavier ions than for the lighter ones. The maximum in the depth-dose profile is called *Bragg Peak*

[2]Relativistic parameter calculated as particle momentum normalised by the particle mass: $\beta\gamma = p/Mc$

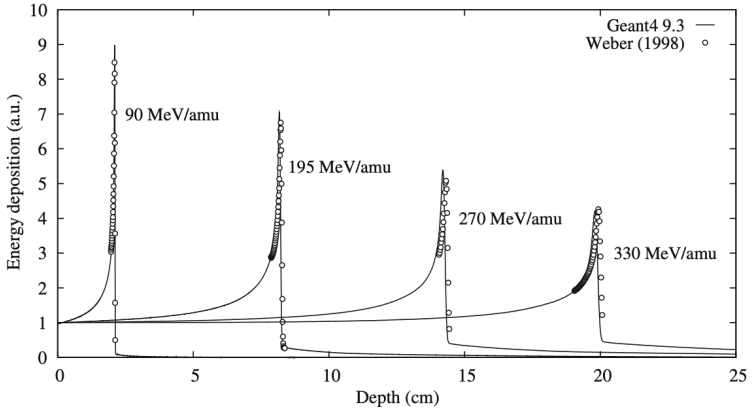

Figure 1.2: Comparison of simulated (with GEANT4) and measured ^{12}C depth-dose profiles in polyethylene ($0.95\ g/cm^3$).

(BP) and it is reached at a projectile velocity of:

$$v \sim Z^{2/3} v_0 \tag{1.4}$$

where $v_0 = e^2/\hbar$ is the Bohr velocity and the corresponding β value is $e^2/\hbar c = 1/137$. For ^{12}C ions this maximum occurs at a specific energy of $\sim 350\ keV/u$. Given an homogeneous material, the depth at which the BP occurs depends on the beam energy. In Figure 1.2, the energy loss as a function of the depth for ^{12}C ions in polyethylene for various energies is compared with GEANT4 [3] simulations.

The *particle range* is defined as the total distance that a particle travels inside a medium before losing all its energy and coming to rest. In a theoretical approach, the range should consider all the small angular deviations given by the elastic Coulomb scatterings that occur between the projectile and the target material nuclei. However, in the CPT clinical regime, the electromagnetic stopping power is the dominant source of energy loss and the angular deviations on the range evaluation are negligible. Assuming a straight line for the projectile path, the mean range (R) can be computed as a function of the particle energy (E_0) in the *Continuous Slowing Down Approximation* (CSDA[4]) with the following expression:

$$R(E_0) = \int_0^{E_0} \left(\frac{dE}{dx}\right)^{-1} dE \tag{1.5}$$

However, the integration of the Bethe-Block formula in Eq.1.2 is complex and different approximations can be adopted. As an example, the *Bragg-Kleeman* formula provides a practical range relationship:

$$R(E_0) \sim \alpha E_0^p \tag{1.6}$$

where $R(E_0)$ is the range in cm, E_0 is the particle kinetic energy expressed in MeV, p and α are constant parameters. For protons at therapeutic energies ($0 - 200\ MeV$), it was found that $p \sim 1.77$ and $\alpha \sim 2.2 \cdot 10^{-3}\ cm/MeV^p$ [10]. Ranges of various ion beams in water are shown in Figure 1.3 According to Eq. 1.5, as the kinetic energy of the primary particle increases the range also increases (Fig. 1.2). Moreover, the

[3] GEANT4 is a toolkit for the simulation of the passage of particles through matter.

[4] The CSDA range is a very close approximation to the average distance traveled by a charged particle as it slows down to rest. In this approximation, the rate of energy loss at every point along the track is assumed to be equal to the same as the total stopping power.

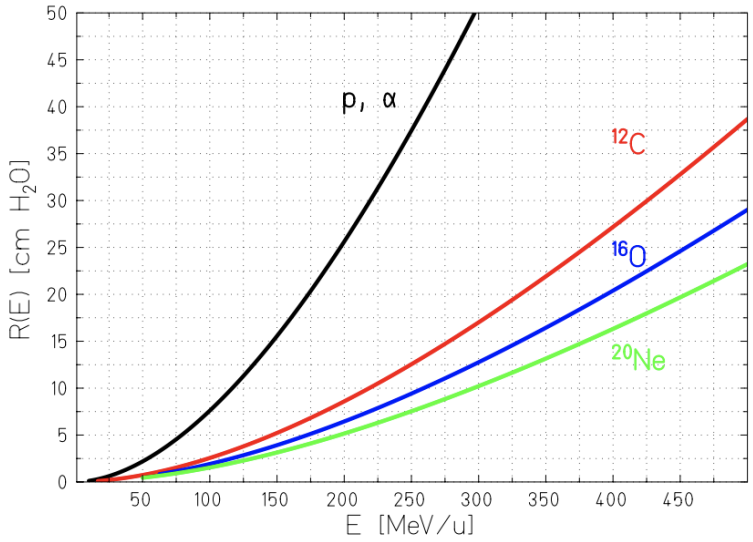

Figure 1.3: Mean range of heavy ions in water [11].

range of different ions with equal initial kinetic energy E per atomic mass unit and crossing the same absorber are related as follows:

$$R_1(E)\frac{Z_1^2}{m_1} = R_2(E)\frac{Z_2^2}{m_2} \tag{1.7}$$

where 1 (2) is for the first (second) ion. This means that, given a certain energy per unit mass, heavier ions show a shorter range than lighter ones (Fig. 1.3). In fact, according to Eq. 1.2 the energy loss is proportional to z^2, so they loose a greater amount of energy per unit path length. For instance, being equal the energy per nucleon, the proton range is approximately three times the range of ^{12}C, while protons and ^{4}He ions have the same range.

Since the stopping power expressed in Eq. 1.2 is a mean value, a large number of collisions in the slowing down process can cause a broadening of the BP, leading to the *energy* and *range straggling* effect. Considering a charged particle passing in a thin material layer, the energy loss distribution is asymmetric with a tail on the high energy region. This is due to the production of high energetic electrons called δ-rays, which are generated by the collisions of the projectile with a large amount of energy transfer. These fluctuations are described by the Vavilov distribution [12] that in the limit of many collisions becomes a Gaussian with a σ_E of:

$$\sigma_E = 4\pi Z_{eff} Z e^4 N_A \Delta x \left(\frac{1-\beta^2/2}{1-\beta^2}\right) \tag{1.8}$$

The variance σ_R^2 of the range straggling is related to the variance σ_E^2 of the energy-loss straggling by:

$$\sigma_R^2 = \int_0^{E_i} \left(\frac{d\sigma_E}{dx}\right)\left(\frac{dE}{dx}\right)^{-3} dE \tag{1.9}$$

The ratio of the straggling width σ_R and mean range R is nearly constant and can be described by:

$$\frac{\sigma_R^2}{R} = \frac{1}{\sqrt{m}} \cdot f\left(\frac{E}{mc^2}\right) \tag{1.10}$$

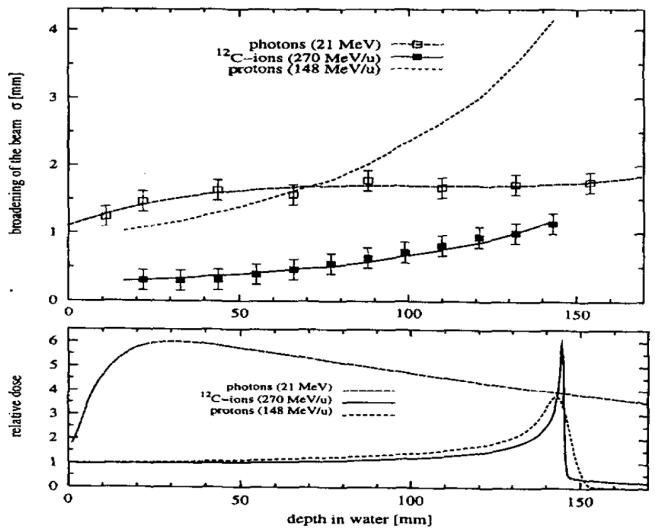

Figure 1.4: Comparison of the lateral scattering of photon, proton and carbon beams as function of the penetration depth (top) and the depth dose correlation (bottom) [15].

where E and m are the energy and the mass of the incident particle and f is a slowly varying function that slightly depends on the absorber.

1.2.2 Multiple Coulomb Scattering

Besides inelastic collisions with the atomic electrons, a charged particle also suffers numerous elastic Coulomb scatterings from the nuclei themselves. Indeed, in addition to the range straggling that occurs along the incident particle direction, the elastic Coulomb scatterings between the projectile and the target material nuclei lead to a lateral deviation of the incident particle direction. Theoretical calculations of the *Multiple Coulomb Scattering* (MCS) are highly complex. One of the most complete models was developed by Molière [13], and various calculations in order to derive more practical formulas were proposed afterwards, for instance by Lewis, Highland, and Gottschalk [14]. Due to the Central Limit Theorem[5], the probability distribution of the net deflection angle of a particle in a thick material is very nearly Gaussian, resulting from the sum of many small random deflections. An approximation for the probability distribution of the net deflection angle by MCS in a material, derived by Highland, is a Gaussian distribution with a σ_θ given by:

$$\sigma_\theta = \frac{14.1\ MeV}{\beta pc} z \sqrt{\frac{L}{L_0}} \left[1 + \frac{1}{9} \log_{10} \left(\frac{L}{L_0} \right) \right] \tag{1.11}$$

where L_0 is the radiation length, L the thickness of the material and z and p are charge and momentum of the projectile, respectively. Eq. 1.11 shows that heavier targets cause a larger angular spread than targets composed of light elements with the same thickness and that the angular distribution shrinks when the particle momentum rises. Hence, heavier charged particle beams exhibit a lower lateral spread and a sharper lateral dose falloff. Figure 1.4 shows that a proton beam at 148 MeV causes a final angular spread almost four times larger than a carbon ion beam at 270 MeV/u having the same range of about 15 cm.

[5] In probability theory, the theorem establishes that when independent random variables are summed up, their properly normalized sum tends toward a Gaussian distribution even if the original variables themselves are not normally distributed.

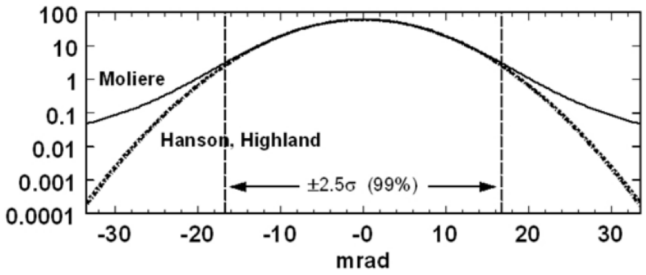

Figure 1.5: Angular distribution for 158 *MeV* protons traversing 1 *cm* of water [17].

However, Eq. 1.11 is only valid for thin targets. Indeed, the particle velocity changes as a function of its depth in the target and the βp term at the denominator is not constant. The extension to thick targets must apply Eq. 1.12 as applying to an infinitesimal slab, then integrate over the target thichkness adding contributions in quadrature [16].

$$\sigma_\theta = 14.1\ MeV \cdot z \left[1 + \frac{1}{9}\log_{10}\left(\frac{L}{L_0}\right)\right] \times \left(\int_0^L \left(\frac{1}{\beta pc}\right)^2 \frac{dx'}{L_0}\right)^{\frac{1}{2}} \tag{1.12}$$

However, besides electromagnetic scattering processes, also nuclear interactions contribute to the final net deflection suffered by the particle. These processes are not taken into account in the Highland approximation, and they create tails in the Gaussian distribution of the scattering angle. An example is shown in Figure 1.5 for 158 *MeV* protons in 1 *cm* of water. At 5σ the Molière distribution is 100 times higher than the Highland approximation.

For clinical applications, the lateral scattering of the beam is as important as the longitudinal. Indeed, the larger the lateral scattering, the higher is the absorbed dose in the surrounding healthy organs. However, for the majority of proton radiotherapy applications Eq. 1.11 is precise enough.

1.2.3 Nuclear Reactions

Ions (hadrons) can undergo nuclear interactions with the material nuclei. Nuclear interactions contributions to energy loss are much smaller compared to electromagnetic interactions. However, while electromagnetic interactions are a well known and analytically understood process a model that allows for a general calculation of nuclear interactions is still missing. Nuclear reactions can be classified in:

- *elastic collisions*: here kinetic energy is conserved, and the nucleus stays intact. This is similar to MCS, but induced by nuclear rather than electromagnetic interactions. Such interactions are not occurring so frequently, but still they cause a certain amount of broadening of the beam, which is taken into account by Monte Carlo models.
- *inelastic collisions*: here, a more violent reaction between projectile and target occurs, where total kinetic energy is not conserved. The projectile may knock out secondary particles (protons, neutrons, deuterons, α, etc.) from the nucleus and break it into fragments if it is an ion.

Since there are some important differences in modeling the nuclear interactions for proton and heavier ions, they will be discussed separately.

Nuclear Interactions of Protons

It is usually assumed that a proton hitting the atomic nucleus starts a series of nucleon-nucleon collisions, which lead to the emission of protons, neutrons, or light fragments. This process can be described as a sequence of three stages [8]:

- *Intra-Nuclear Cascade* (INC) [6] [18]: this model is commonly used to describe nuclear interactions of nucleons with energies from 50 MeV to hundreds of GeV. The basic idea is that the incident particle interacts with quasi-free nucleons in the target nucleus through a series of two-body interactions (since the incident proton is treated as a free nucleon). The target nucleus is modeled as a Fermi gas of cold, free, nucleons. The conditions for the validity of the model are related to the incident particle De Broglie wavelength λ_H. In particular, λ_H must be much smaller than the average distance d between the target nucleons and with respect to the mean free path λ_N inside the nucleus. These conditions are necessary to apply the target nucleons hypothesis and the independent incident nucleons approximation:

$$\lambda_H = \frac{2\pi\hbar}{p} \ll d = \left(\frac{3}{4\pi\rho_N}\right)^{1/3} \tag{1.13a}$$

$$\lambda_N = \frac{1}{\sigma\rho_N} \tag{1.13b}$$

  where σ is the proton-nucleon cross section and ρ_N is the intranuclear density. For the CPT energy range (for example proton beams up to 250 MeV), $\lambda_H \sim 1\ fm$ and d are comparable making Eq. 1.13a invalid. However, the INC model works surprisingly well at much lower energies since quantum effects increase the effective mean free path of nucleons in the nuclear medium.

  For therapeutic proton energies, only elastic scatterings (nucleon-nucleon) are considered because these energies are below the pion production threshold ($\sim$ 290 MeV). The final state particles in the scattering process are called *secondaries*. The time window in which they are produced corresponds to the time-scale of strong interactions: 10^{-22} - 10^{-23} s. Secondaries have high energy and can scatter again in the same nucleus, or escape. Not only protons and neutrons can be emitted, but also light nuclear fragments of high energy formed through the *coalescence mechanism*. All particles are tracked until they are all below a given energy threshold, usually a few tens of MeV. This process is called an *intranuclear cascade*.

- Pre-equilibrium: in this stage, the energy of the particles in the cascade has reached a lower limit, usually a few tens of MeV, but the nucleus is not yet in thermal equilibrium. Protons, neutrons, and light fragments are emitted and the residual nucleus is left in an equilibrium state, with a certain excitation energy shared among the remaining nucleons.

- De-excitation step: depending on the mass of the target nucleus and on the energy, the nucleus can dissipate its remaining energy in several ways:

  – Nuclear evaporation [19]: light fragments (α, H^3, He) with kinetic energies of a few MeV can be successively emitted from the excited nucleus, similar to evaporation from a hot system.

[6] The intra-nuclear cascade refers to the cascade inside the nucleus, as opposed to the inter-nuclear transport of a particle from one nucleus to another.

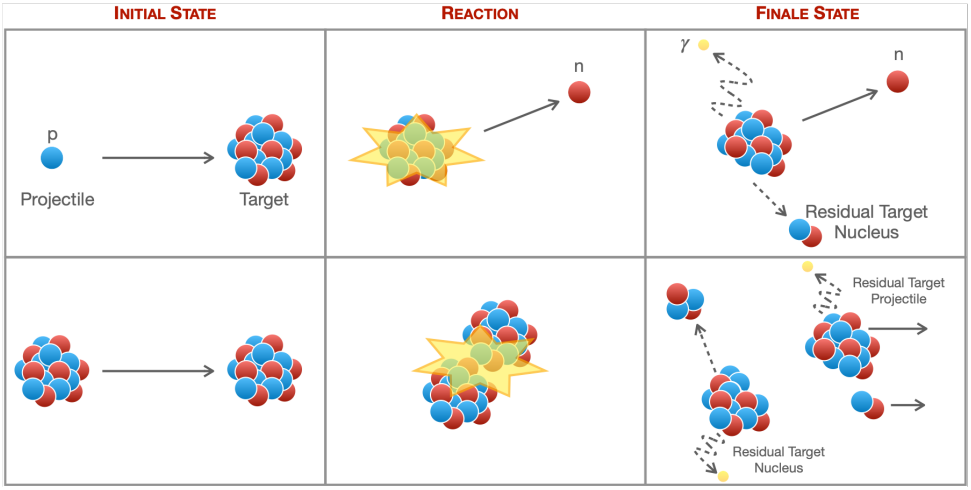

Figure 1.6: Top: sketch of a possible nucleon-nucleus reaction in proton therapy, whereby a neutron is created. Bottom: sketch of nucleus-nucleus reaction in heavy ion therapy, with creation of light fragments.

- Fission: the excited nucleus breaks into two fragments. It applies to high Z nuclei only, roughly $Z \geq 65$. However, high-Z nuclei are not found in the human body and this process is not relevant here.
- Fermi-breakup [20]: this mechanism applies to light nuclei (usually $A \leq 16$), where the excitation energy of the nucleus may be larger than the binding energy of some fragmentation channels. In this case, the excited nucleus disassembles into smaller fragments. This process is relevant for radiotherapy, because the human body is mainly composed of low-Z nuclei.
- Gamma emission: what is left after the previous stages is a residual nucleus, with may be still somewhat excited. The final excitation energy is released through the emission of γ rays.

It must be noted that the emission of secondary particles in proton therapy is entirely due to the target nuclei, as was displayed in Figure 1.6 (top).

Nuclear Interactions of Heavy Ions

The most important difference between nucleon-nucleus reactions and nucleus-nucleus reactions is that the incoming nucleons are not free. This leads to important different phenomenological implications. Most models for nucleus-nucleus interactions are based on the *abrasion-ablation* model [18].

During the fast stage (abrasion, time scale $\sim 10^{-22} - 10^{-23}$ s), the projectile and target nuclei overlap, resulting in a kind of reaction volume. An excited quasi-projectile with much of the initial velocity, a quasi-target fragment at rest, and several excited light fragments are formed. During the slow step (ablation, time scale $\sim 10^{-18} - 10^{-16}$ s), the remaining projectile, target and light fragments de-excite by evaporating light nuclei or fragments. Contrary to proton irradiation, where only the target nuclei can fragment, both target and projectile-nuclei can fragment. This is illustrated in Figure 1.6 (bottom), showing a sketch of a nucleus-nucleus interaction stages. Fragments originated from the primary particles are forward peaked in the laboratory frame due to the high velocity of the projectile, and they have approximately the same velocity and direction of the beam. Fragments originating from the

target nuclei at rest, instead, are emitted almost isotropically and with much lower velocities, so their stopping power is high, according to Eq. 1.2. Therefore, projectile fragmentation leads to an attenuation of the primary particles. Indeed, due to nuclear inelastic processes, a monochromatic incoming beam turns into a mixed beam containing neutrons and lower-Z fragments, which may have a wider energy distribution and greater penetration depth according to Eq. 1.7. These fragments are responsible for the energy depositions which form the tail beyond the BP (see Fig. 1.2). In order to describe this kind of reactions, various models have been developed, differing mainly in the treatment of the nuclear field affecting the propagation of the particles inside the nucleus:

- INC model [18]. The description is similar to what was outlined above for protons. The highly excited nuclei loose energy through a series of two-body reactions and scattering off quasi-free nucleons. More than one nucleon-nucleus interaction can take place in one nucleus-nucleus collision.
- *Quantum Molecular Dynamics* (QMD) model [21, 22]. This model can be seen as a sophisticated form of the INC model. Here, each nucleon is described by a gaussian wave packet, and all nucleons in the projectile and target participate in the collision process. By minimizing the Hamiltonian that describes nucleon-nucleon interactions in the overlapping projectile and target nuclei, it predicts the formation of heavy or light nuclei and secondary protons and neutrons. Because of their complexity, these models are generally much slower in MC codes than the normal INC model.
- *Boltzmann Master Equation* (BME) model [23]. This is a sophisticated model to simulate the pre-equilibrium stage, describing the thermalization of composite nuclei for projectiles with energies below 100 MeV/u down to the evaporation/fission/breakup stage. Based on a set of time-dependent transport equations, BME describes how a statistical state far from equilibrium evolves to an equilibrium state, through a sequence of two body interactions and emission of unbound particles (neutrons/protons) and clusters (heavy/light nuclei).

A fundamental quantity that characterizes nuclear interactions is the *nuclear cross section* which represents the probability of the nuclear reaction between beam and target to occur. The cross section for a general process can be defined as:

$$\sigma = \frac{N}{N_i} \frac{A}{\rho x N_A} \tag{1.14}$$

where N is the number of interactions and N_i the number of incoming particles, while ρ, A, and x are the target density, mass number and thickness respectively. The cross section unit is the barn (b), where $1\ b = 10^{-28}\ m^2 = 100\ fm^2$.

N can be referred to any kind of beam-target interaction (*total cross section* σ) or can be restricted to select only the produced particles that are emitted in a certain solid angle portion $d\Omega$ or in a certain energy range dE (*differential cross section*, $\frac{d\sigma}{d\Omega}$ or $\frac{d\sigma}{dE}$). It is possible to define also the *double-differential cross section* $\frac{\partial^2\sigma}{\partial\Omega\partial E}$.

If N is restricted to a specific kind of process, it is possible to define *partial cross sections*, for example $\sigma_{elastic}$ and $\sigma_{inelastic}$. Moreover, cross sections are very useful to quantify the probability of producing fragments with a given charge (*elemental cross sections*) or the production of a fragment with a given charge and mass (*isotopic*

cross sections). However, despite experimental data about nuclear cross sections being abundant in literature, for light fragments ($A < 20$), the energy range between tens and few hundreds of MeV/u has not been sufficiently covered by experimental measurements (see Section 2.2).

1.3 Biological effects of charged particles

The fact that ionizing radiation produces biological damage has been known for many years [24]. The first case of human injury was reported in the literature just a few months after Roentgen's original paper in 1895 announcing the discovery of *X*-rays. As early as 1902, the first case of *X*-ray induced cancer was reported. Early evidence of harmful effects as a result of exposure to radiation in large amounts existed in the 1920's and 30's, based upon the experience of early radiologists, miners exposed to airborne radioactivity underground, people working in the radium industry, and other occupational groups. The long-term biological significance of smaller, repeated doses of radiation, however, was not widely appreciated until relatively recently, and most of our knowledge of the biological effects of radiation has been accumulated after World War II. An overview on the damages related to hadrons adopted in CPT is presented in the next subsection, followed by a summary of the definitions and the parameters adopted in CPT.

1.3.1 DNA damages

Radiation which is absorbed in a cell can affect a variety of critical targets in the cell, the most important of which is the *DeoxyriboNucleic Acid* (DNA). Evidence indicates that damage to the DNA is the main cause of cell death, mutation, and carcinogenics. The damage occurs via two mechanism:

- the radiation impacts the DNA directly, causing ionization of the atoms in the DNA molecule (*direct damages*). It is a fairly uncommon occurrence due to the small size of the target (the diameter of the DNA helix is only about 2 *nm*).
- the radiation interacts with non-critical target atoms or molecules. This leads to the production of *free radicals*, which are atoms or molecules that have an unpaired electron and thus are highly reactive. These free radicals can then attack critical targets such as the DNA (Fig. 1.7). Since they are able to diffuse in the cell, the initial ionization event does not have to occur so close to the DNA in order to cause damage. Thus, *indirect damage* is much more common than damage from direct action.

Both direct and indirect actions, damage the DNA strands of molecules that make the double-helix structure. Most of this damage consists of breaks in only one of the two strands, *Single Strand Breaks* (SSB), and is easily repaired by the cell, using the opposing strand as a template. If, however, a *Double Strand Break* (DSB) occurs, the cell has much more difficulty repairing the damage and may make mistakes. This can result in mutations, or changes to the DNA code, which can result in consequences such as cancer or cell death. Double-strand breaks occur at a rate of about 1 double-stand break to 25 single-strand breaks. Thus, the radiation damage to DNA is mostly reparable.

The effectiveness of ionizing radiations depends on the different DNA repair systems that contrast the diverse forms of damage caused by different agents. The main goal of CPT is to produce permanent damages in the tumor tissues by means

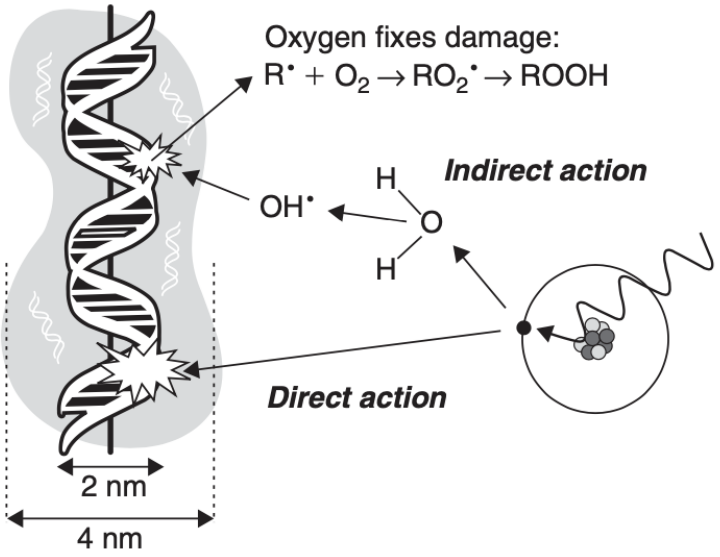

Figure 1.7: Mechanisms of DNA radiation damage [25].

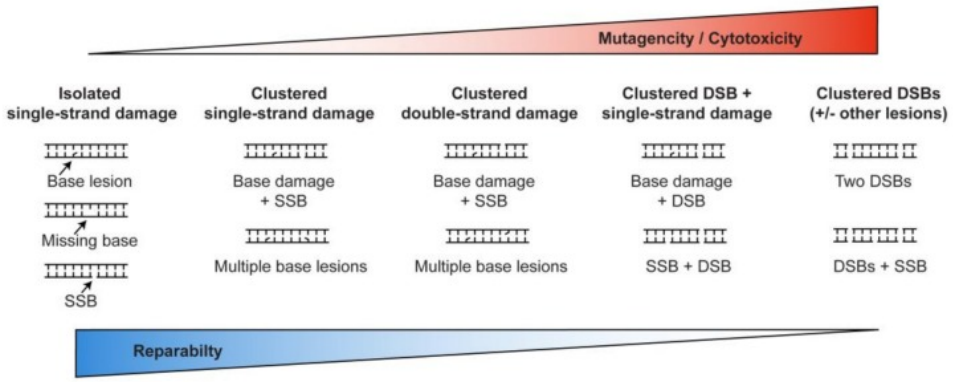

Figure 1.8: Classification of DNA damages. The damage complexity increase from left to right, corresponding to an increase of mutagencity and cytotoxicity and a decrease of the reparability [26].

of clustered DSB lesions. On the contrary, the aim of the space radiation protection is to minimize the lesions induced by radiation. In both cases, the biological effects of ionizing radiation must be estimated precisely. A general trend of the reparability, mutagencity, cytotoxicity and damage complexity is shown in Figure 1.8.

1.3.2 Dose and Linear Energy Transfer

In order to evaluate the radiation effectiveness, the ionizing particle energy release must be quantified. In radiotherapy and space radioprotection it is measured by means of the *Absorbed Dose* (D), defined as the energy deposited in matter (dE) by the ionizing radiation per unit mass (dm) and measured in Gray ($Gy = Joule/Kg$):

$$D = \frac{dE}{dm} \tag{1.15}$$

However, different kinds of radiation that bring at the same amount of absorbed dose can have very different biological effectiveness. A parameter that takes account this diversity is the *Linear Transfer Energy* (LET), defined as the amount of energy

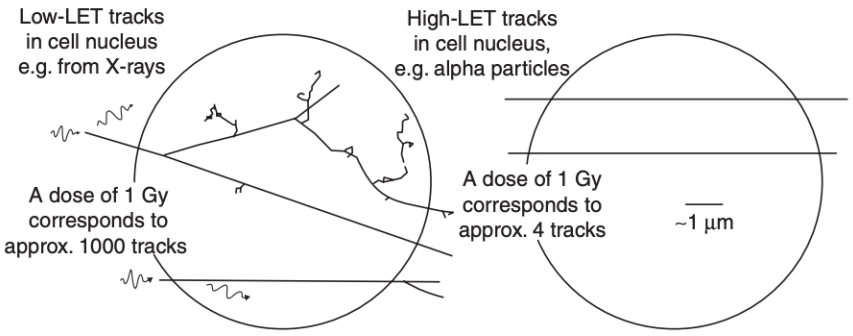

Figure 1.9: The structure of particle tracks for low-LET radiation (left) and α-particles (right). The circles indicate the typical size of mammalian cell nuclei [25].

(dE) locally transferred from an ionizing particle to the material traversed per unit distance (dl). LET is closely related to the stopping power, even if many studies focus upon the energy transferred in the vicinity of the primary particle track and therefore exclude interactions that produce δ-rays with energies larger than a certain value Δ. This energy limit is meant to exclude secondary electrons that carry energy far from the primary particle track, since a larger energy implies a larger range. Thus, this approximation neglects the directional distribution of secondary radiation and the non-linear path of delta rays, leading to a *restricted* version of the stopping power, the so called *restricted LET*:

$$LET_{\Delta} = \frac{dE_{\Delta}}{dl} \tag{1.16}$$

where dE_{Δ} is the energy loss of the charged particle due to electronic collisions while traversing a distance dl, excluding all secondary electrons with kinetic energies larger than Δ. If Δ tends toward "infinity", then there are no electrons with larger energy, and we talk about *unrestricted linear energy transfer* which is identical to the linear electronic stopping power.

X-rays, γ-rays, electrons, and protons are considered low LET radiations as they deposit energy with ionizations occurring at low density along a track. By contrast, heavy charged particles, like carbon ions, are high LET radiation. Indeed, when these charged particles slow down and stop in the BP, the ionization density becomes very high. In Figure 1.9 radiations with low-LET (γ-rays $\sim 0.3\ keV/\mu m$) and high-LET (α-particles $\sim 100\ keV/\mu m$) are compared.

1.3.3 Survival curve and Relative Biological Effectiveness

The different response to ionizing radiations can be represented by cell *survival curves*, such that for human kidney cells (Fig. 1.10) as a function of the dose for eight different radiations, with LET varying from 2 $keV/\mu m$ (250 kVp X-rays) to 165 $keV/\mu m$ (2.5 MeV α-particles). As LET increases, the survival curves become steeper; they also become straighter with less shoulder, which indicates either a higher ratio of lethal to potentially lethal lesions or that high-LET radiation damage is less likely to be repaired correctly. Many biophysical models and theories have been proposed to account for the shape of the cell survival curve. One of the most used is the so called *linear-quadratic model* [25] that assumes that there are two components to cell killing by radiation, one that is proportional to the dose and one that is proportional to the squared dose. According to this model, the expression for

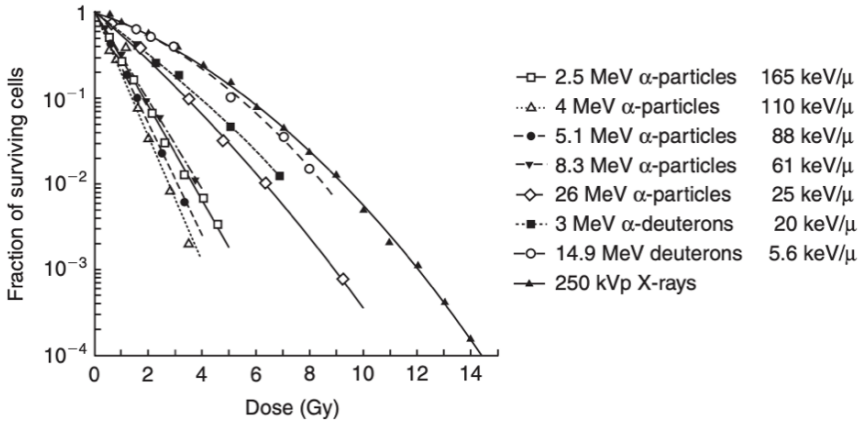

Figure 1.10: Survival of human kidney cells exposed in vitro to radiations of different linear energy transfer [25].

the cell survival curve is therefore:

$$S = e^{-\alpha D - \beta D^2} \tag{1.17}$$

in which S is the fraction of cells surviving a dose D, and α and β are constants. In particular, α is related to the slope of the linear component of the curves and β is related to the non linear part.

The α/β ratio describes the shoulder of the survival curves at low doses and it gives indications related to the reparability of the damages. It depends primarily on the features of the target tissues and secondarily on the incident particle properties. In particular, high α/β ratio is associated to particles with high-LET and it corresponds to radiations that can provide more severe and irreparable damage to the target cells. However, notice that 2.5 MeV α-particles are less efficient than 4.0 MeV α-particles even though they have a higher LET; this is explained with the *overkill* effect shown in Figure 1.11.

In order to fully take into account the different biological effectiveness aspects, a more comprehensive parameter is defined: the *Relative Biological Effectiveness* (RBE). The RBE of a radiation (e.g. a high-LET radiation) is defined as the ratio between the dose of reference radiation to the dose of the test radiation that cause the same damage (i.e. isoeffect):

$$RBE = \left.\frac{\text{dose of reference radiation}}{\text{dose of test radiation}}\right|_{iso} \tag{1.18}$$

The reference radiation is commonly 250 kVp X-rays or ^{60}Co γ-rays since they are low-LET radiation sources regularly available in clinical or experimental facilities.

Figure 1.11 shows the RBE values for the cells featured in Fig. 1.10. In particular the RBE has been calculated at cell survival levels of 0.8, 0.1 and 0.01, showing the fact that it is not constant but rather depends on the level of biological damage and hence on the dose. RBE also depends on LET, and rises to a maximum of about 100 $keV/\mu m$, and then falls for higher values of LET because of the overkill effect. For a cell to be killed, enough energy must be deposited in the DNA to produce a sufficient number of double-strand breaks. Sparsely ionizing, low-LET radiation is inefficient because more than one particle may have to pass through the cell to produce enough DNA double- strand breaks. Densely ionizing, very high-LET radiation is also inefficient because it deposits more energy per cell, and hence produces

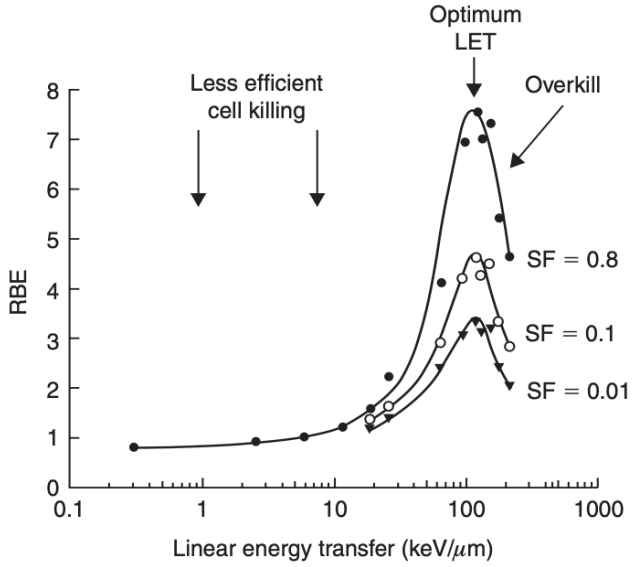

Figure 1.11: Dependence of RBE on LET and the phenomenon of overkill by very high LET radiations [25].

more DNA double-strand breaks than are actually needed to kill the cell. These cells are "overkilled", and then there is a lower probability that other cells will be killed, leading to a reduced biological effect. Radiation of optimal LET deposits the right amount of energy per cell, which produces just enough DNA double-strand breaks to kill the cell.

The RBE depends on different parameters and it is related both with biological and physical aspects. As an example, in the former case it depends on the type of the target cells and on the cell oxygenation level. In the latter case, it depends on the dose and the incident particle species. Typical RBE values for the particles involved in CPT are of the order of $1.5 - 5$ for ^{12}C ions and about 1.1 for protons, depending on the particle energy and LET. The main goal in CPT is to maximize the damage to the tumour sparing the surrounding healthy tissues. To achieve this purpose, the RBE has to be maximized in the BP region and minimized in the entrance channel. As shown in Figure 1.12, heavy ions have similar maximum RBE at the BP, but only for ^{12}C ion the RBE value is about 1 in the entrance channel. This is one of the reasons why carbon ions have been selected as the preferred heavy particle adopted in CPT. Regarding proton therapy, in clinical facilities the proton RBE is assumed to be 1.1 along all the particle path, but some studies indicate a wide range ($0.7 - 3.5$ [2]) of measured proton RBE values close to the BP.

1.3.4 Oxygen Enhancement Ratio

The response of cells to ionizing radiation is also strongly dependent on the Oxygen concentration [27]. This is illustrated in Fig. 1.13 for mammalian cells irradiated in culture. The cell surviving fraction is shown as a function of the administered radiation dose either under normal aerated conditions or under hypoxia, which can generally be achieved by flowing nitrogen gas over the surface of the cell suspensions for a period of 30 min or more. The radiation dose that gives a particular level of cell survival is reduced by approximately the same factor at all levels of survival. Thus, it is possible to define the *Oxygen Enhancement Ratio* (OER) for the same level

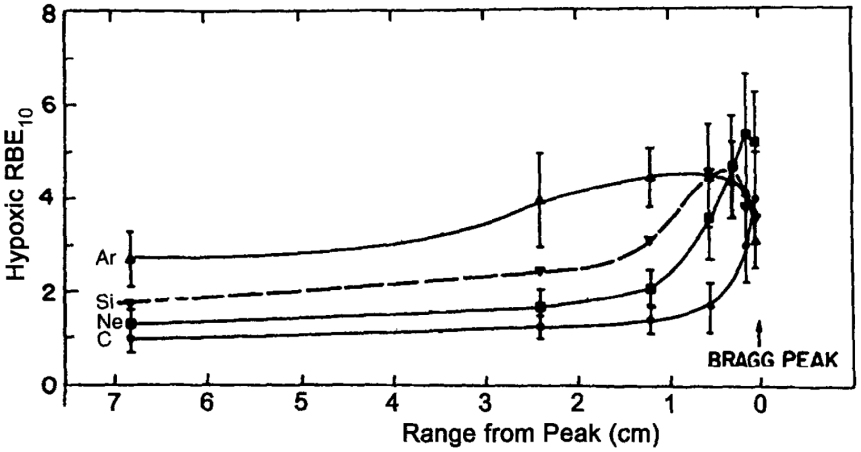

Figure 1.12: RBE for ^{12}C, Ne, Si and Ar ions as function of the penetration depth [15]

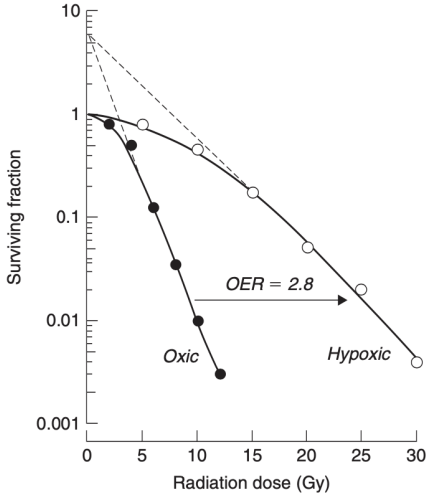

Figure 1.13: Survival curves for cultured mammalian cells exposed to X-rays under oxic or hypoxic conditions, illustrating the radiation dose-modifying effect of oxygen [25].

of biological effect:

$$OER = \left.\frac{\text{Radiation dose in hypoxia}}{\text{Radiation dose in air}}\right|_{iso} \tag{1.19}$$

By definition, the OER under anoxic conditions is 1.0 and, as shown in Figure 1.14, as the oxygen tension increases there is a steep increase in radiosensitivity (and thus in the OER). Indeed, Figure 1.14 demonstrates that cells below 0.15 $mmHg$ (0.02%) are maximally resistant to radiation and the OER starts to rise significantly above 1.0 only when the oxygen tension exceeds this level and then the greatest change occurs from about 0.5 to 20 $mmHg$. The mechanism responsible for the enhancement of radiation damage by oxygen is generally referred to as the *oxygen-fixation hypothesis* and is illustrated in Figure 1.7. As already explained in Section 1.3.1 when radiation is absorbed in a biological material, free radicals are produced, either via direct damage in the target molecule (usually DNA) or indirectly in other cellular molecules, then diffusing far enough to reach and damage critical targets. Most of the indirect effects occur by free radicals produced in water, since it makes about $70 - 80\%$ of mammalian cells. The free radicals produced in the critical target, known as $R^{\bullet}$ (Fig. 1.7), are unstable molecules that react rapidly with oxygen, if present, and produce

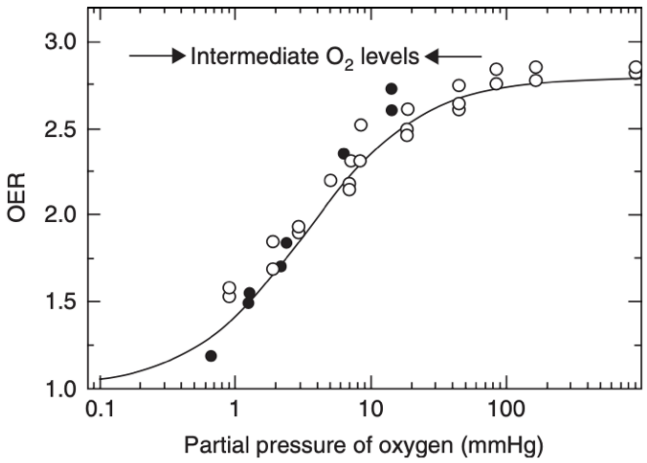

Figure 1.14: Survival curves for cultured mammalian cells exposed to X-rays under oxic or hypoxic conditions, illustrating the radiation dose-modifying effect of oxygen [25].

$RO_2^{\bullet}$. After further reaction, these molecules create the $ROOH$ in the target molecule. In this way, a stable change in the chemical composition of the target molecule is caused and the damage is said to be chemically "fixed". In the absence of oxygen, the unstable $R^{\bullet}$ molecule has a longer half-life and it can react with H^+ chemically restoring its original form, thereby not damaging the target molecule.

1.4 Two important applications: Particle Therapy and Radioprotection

During the last century, physics, and in particular nuclear and particle physics, greatly contributed to the development of instrumentation for medical research, diagnosis and therapy. In particular, the curative capability of ionizing radiation in the treatment of tumors has been exploited since the beginning of the 20th century. Nevertheless, ionizing radiations also represent a potential risk to human health. Radioprotection is a medical physics branch that studies and regulates methods and devices meant to protect people from detrimental effects of radiations in a wide spectrum of situations, from radiology rooms to space travels. Charged particles play a key but opposite role in CPT and space radioprotection: thanks to their favorable dose deposition profile they are extremely suited to treat deep-seated tumors, while in space they can cause severe DNA damage to astronauts and increase secondary cancer risk. In this section, the effects of charged particles induced nuclear fragmentation in these two environments will be discussed and compared.

1.4.1 Particle Therapy: Radiotherapy and Hadrotherapy

Radiotherapy

In 2018, 18.1 million new cancer cases were registered [28] and nowadays, about 60% of oncological patients undergo a radiotherapy treatment, often coupled with surgery and/or chemotherapy.

Radiation therapy uses high-energy radiation ($5 - 10$ MeV γ-rays) produced by *linear accelerators* (LINAC). Generally, the purpose of radiotherapy is to remove all the tumor cells, but this condition is difficult to achieve because it is impossible to deliver a high dose without serious effects on the surrounding normal tissue. There

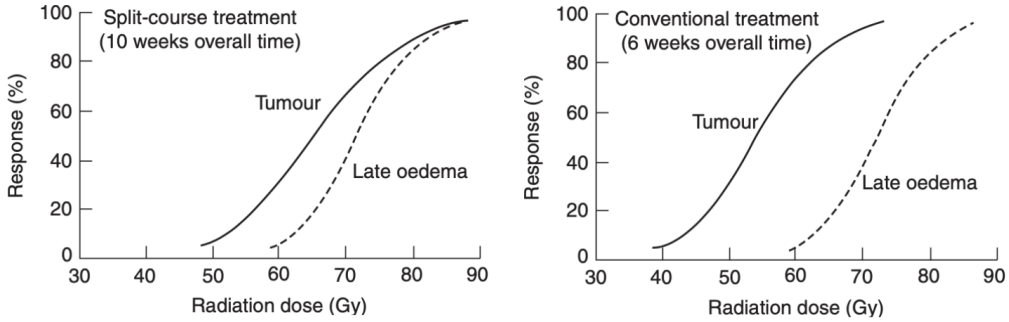

(a) *Therapeutic window for split-course treatment*

(b) *Therapeutic window for conventional treatment*

Figure 1.15: Dose–response curves for local control of laryngeal carcinoma (solid lines) and late laryngeal oedema (dashed lines). Protraction of overall treatment time narrowed the therapeutic window [25].

are two parameters that need to be considered in order to maximize doses in tumor tissue. The first is the probability to obtain tumor control killing the carcinogenic cells, better known as *Tumor Control Probability* (TCP). Another one is the response of normal tissue in the surrounding tumor area which is known as *Normal Tissue Complication Probability* (NTCP). Both TCP and NTCP depend on cell biological effects such as repopulation, repair, redistribution, and re-oxygenation. The relative position-shape of the dose–response curves for tumour control and a given radiotherapy complication determine the possibility of delivering a sufficient dose with acceptable side-effects. Figure 1.15 shows the dose–response curves for tumour control and complications in the same coordinate system for two hypothetical situations: one favourable, where there is a wide therapeutic window between the two curves, and the other one less favourable. For split-course treatment (Fig. 1.15a) the tumour and oedema curves are closer than for conventional treatment (Fig. 1.15b) and the therapeutic window is therefore narrower.

The first attempt at radiotherapy was performed in 1896 using X-rays on a breast cancer [29]. Since then, the technology improvement and the research results to the development of radiotherapy as a well established, successful technique for cancer treatments. Nowadays, many hospitals operate LINAC accelerator to deliver conventional radiotherapy. In particular, radiation therapy is performed with *X*-rays at few MeV and, in order to preserve normal tissues (such as skin or organs which radiation must pass through to treat the tumor) at best, radiation beams are delivered from several angles of exposure to intersect at the tumor, providing a much larger absorbed dose there than in the surrounding healthy tissue. However, inevitably some radiation dose is deposited in healthy tissues. The state of art for the photon radiation therapy is the *Intensity Modulated Radiation Therapy* (IMRT) [30], an advanced form of three-dimensional conventional radiotherapy. Variable radiation intensity is generated across each beam, in contrast to the uniform intensity used in other radiotherapy techniques. Each beam is subdivided into hundreds of beamlets, each with an individual intensity level, enabling a very complex pattern to be constructed. The use of several beams leads to a highly conformal dose distribution, allowing precise shaping to a curved target and thus further sparing of the normal tissues. In Figure 1.16 a conventional radiotherapy (left) and IMRT (right) dose distributions are compared. The former allows a good spatial distribution of the dose, but is still unable to exclude normal tissues surrounded by tumour. In the latter case, instead, the high dose region fits the nodal target volume precisely, protecting the centrally situated

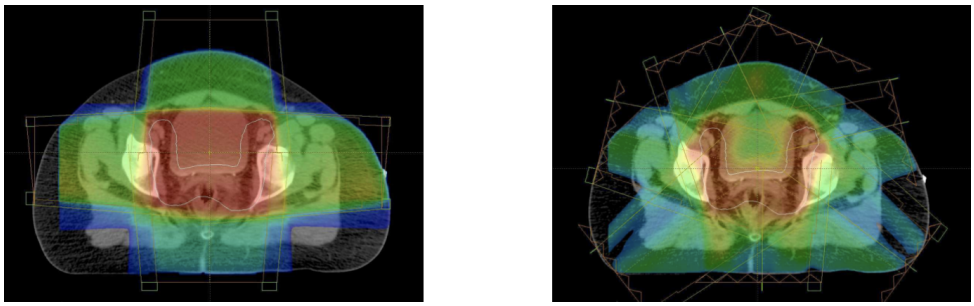

Figure 1.16: Dose colour-wash. (Left) Conventional radiotherapy: the target volume is contoured in white. The high dose region (red) is brick-shaped and includes part of the bladder. (Right) IMRT: the high dose region (red) conforms to the target volume (white) in a concave shape reducing the bladder and bowel dose [30].

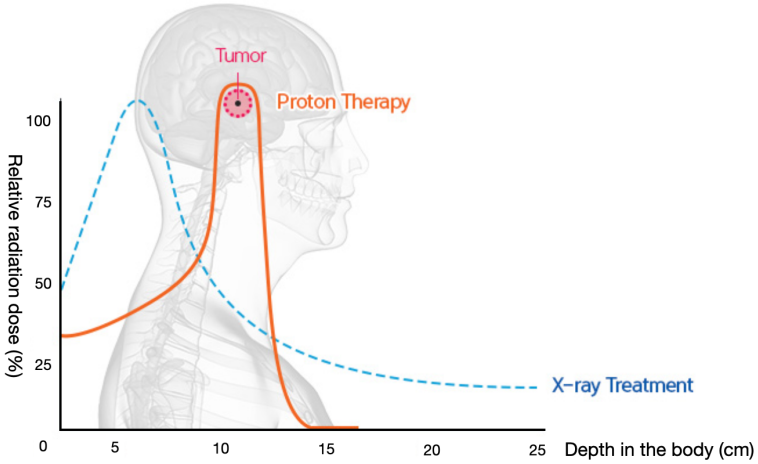

Figure 1.17: Depth-dose profiles of X-rays and protons radiation.

bladder and small bowel.

Hadrontherapy

Some types of cancer are defined as *radioresistant*[7] or surgically inoperable. For this kind of tumour Hadrontherapy is crucial. The advantages of this technique over conventional radiotherapy are related to both biological and physical properties. The former is given by the enhanced biological effectiveness presented in section 1.3. The latter is represented by the different dose deposition profile of charged particles, as illustrated in section 1.2 and shown in Figure 1.17. Indeed, thanks to this characteristic dose deposition profile with the BP at the end of range, charged particles offer the possibility to deposit dose in a much more localized way compared to the photons, so that the dose in healthy tissue is minimized.

The idea of using protons for cancer treatment was first proposed in 1946 by the physicist Robert Wilson, who later became the founder and first director of the *Fermi National Accelerator Laboratory* (FermiLab) near Chicago. The first patients were treated in the 1950s in nuclear physics research facilities by means of non-dedicated accelerators. Initially, clinical applications were limited to few parts of the body, as accelerators were not powerful enough to allow protons to penetrate deep in the

[7]Tumours that, although they have been damaged from radiation, are capable of self-healing after a variable period of time.

tissues. In the late 1970s improvements in accelerator technology, coupled with advances in medical imaging and computing, made proton therapy a viable option. However, it has only been from the beginning of the 1990s that proton facilities have been established in clinical settings, the first one being in Loma Linda, USA. Currently about sixty proton centres are in operation and thirty are under construction worldwide [1]. Although protons are used in several hospitals, the next step in radiation therapy is the use of carbon and other ions. These have some clear advantages even over protons in providing both a local control of very aggressive tumours and a lower acute or late toxicity, thus enhancing the quality of life during and after cancer treatment. Since the birth of hadrontherapy, more than 120000 patients have been treated globally with hadrons, including 20000 with carbon ions. In Europe, the interest in hadrontherapy has been growing rapidly and the first dual ion (carbon and protons) clinical facility in Heidelberg, Germany started treating patients at the end of 2009. Three more such facilities are now in operation: CNAO in Pavia, MIT in Marburg, and MedAustron in Wiener Neustadt [31].

While therapeutic photon beams can be produced by means of a LINAC, charged particles require more sophisticated accelerators:

- *cyclotrons* accelerate charged particles outwards from the center of a flat cylindrical vacuum chamber along a spiral path. The particles are held to a spiral trajectory by a static magnetic field and accelerated by a rapidly varying (radio frequency) electric field. Their final energy depends on the radius, and therefore on the size, of the machines. For this reason a limitation of these accelerators is that they produce fixed energy beams. Cyclotrons are commonly used to accelerate protons, while heavier ions would require a higher magnetic field to maintain the beam trajectory and larger dimensions of the machine to achieve therapeutic energies. This restriction could be at least partly overcome by the use of superconducting cyclotrons.

- *synchrotrons*, a special type of cyclotron which accelerates the beam by means of a radiofrequency, holding it at a constant radius trajectory by means of a variable magnetic field. Both the radiofrequency and the magnetic field are synchronized with the rising energy of the particles. The final energy can therefore be varied according to the needs. Synchrotrons are the preferred solution to accelerate ions like ^{12}C and ^{16}O. The CNAO synchrotron is shown, as an example, in Figure 1.18.

As shown in Figure 1.19, CPT requires a small number of beam entrance positions and it better preserves the healthy tissues with respect to conventional radiotherapy. However, the sharpness of the BP (order of *mm*) for a single ion-beam energy means that only a narrow depth range can be treated to the very high dose, and it is too small to treat tumors that typically have the size of the order of a (few) *cm*. To overcome this problem, a *Spread-Out Bragg Peak* (SOBP) is created by varying the energy of the incident ion beam, using various energies with appropriate weighting to produce a flat SOBP as shown in Figure 1.20. In clinical practice, the SOBP is created by smearing the beam energy with passive or active modulation. In the former case, it is performed by placing passive material layers with grooves called *ridge filters*. The filters are developed to produce a constant biological effect, taking into account the variation of RBE as a function of the depth. In the latter case, the target volume is divided into layers with an equal beam energies and each layer is composed of a grid of points called *voxels*. Then, a pencil beam is delivered by means of a magnetic scanning system to each voxel, modifying the beam energy to switch between layers.

Figure 1.18: CNAO synchrotron [32].

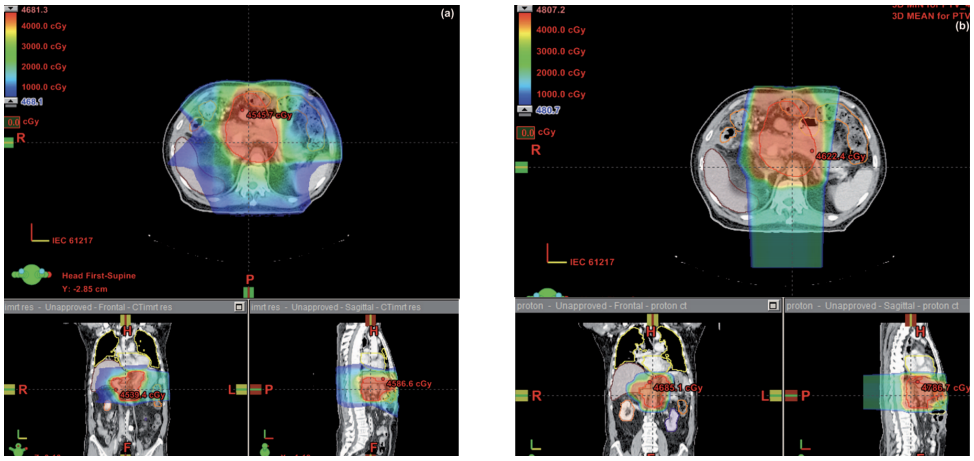

Figure 1.19: Example of a typical dose distribution achievable with X-rays (left) and protons (right) [33].

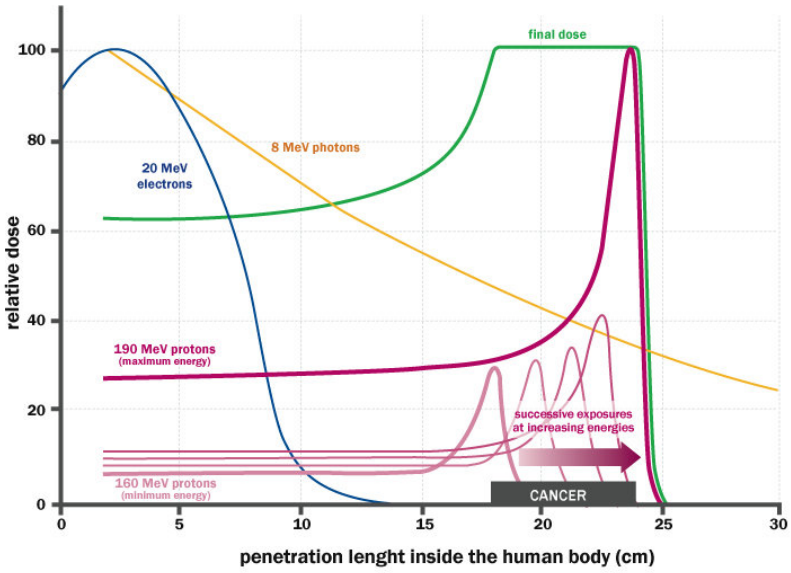

Figure 1.20: SOBP distribution (in green) obtained by the overlapping of many BP corresponding to different energies and intensity.

Moreover, in order to optimize the treatment, different computer algorithms based on MC simulations, defined as *Treatment Planning System* (TPS), are exploited to model the interactions between the beam and the patient's anatomy. Indeed, TPS are at the heart of both radiotherapy and hadrontherapy systems and the key to improved patient outcomes. TPS load image data-sets and once the tumors are identified, the system develops a complex plan for each beam line route for how the therapy system will deliver the beam. These systems compute the expected dose distribution in the patient's tissue and also help navigate beam placement in order to avoid critical structures that are more sensitive to radiation in an effort to reduce unwanted damage from the therapy.

At the moment, all the hadrontherapy centers in the world adopt proton and/or carbon ion beams for the clinical treatments. However, the use of other species of ion beams is under study, focusing the efforts on the possibility to exploit Helium and Oxygen particles [4].

One of the open questions in CPT is related to the effect of nuclear inelastic interactions on the dose deposition and how to include them in current TPS. As described in Section 1.2.3, there are two distinct outcomes from the nuclear inelastic interaction: the projectile fragmentation in case of ion therapy and the target fragmentation both in proton and ion therapy. The two cases and their relative relevance in CPT will be discussed in detail in the next subsections.

1.4.2 Projectile Fragmentation in Particle Therapy

At therapeutic energies, a fragmentation of the incident particle can only occur for projectiles with $A > 1$, thus projectile-fragmentation processes are not considered for protons beams.

The majority of heavy secondary particles have almost the same velocity and direction of the primary, but with a lower mass. On the other hand light fragments are emitted with a wide angular spread, up to 90°. The result is a build up of lower Z

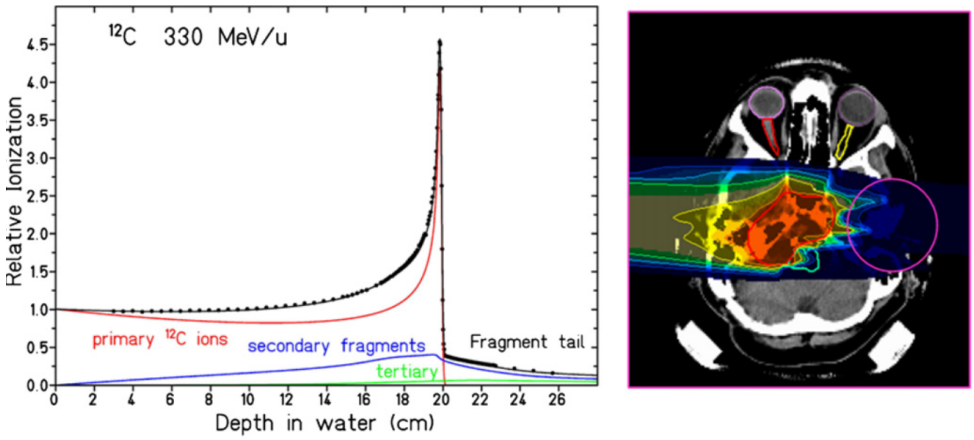

Figure 1.21: Depth-dose characteristics of 330 MeV/u ^{12}C ions stopping in water (left); typical treatment plan for a cancer treatment with ^{12}C ions in the skull base (right). The small dose beyond the target volume is caused by high-energy nuclear fragments [34].

fragments with longer range and larger angular distribution. Indeed, as the range of the particles at same velocity scales with A/Z^2 the depth-dose profile of heavy-ion beams shows a characteristic fragment tail beyond the BP (Fig. 1.21).

Thus, the physical beam models included in TPS for ion ($A \geq 2$) irradiations of cancer patients have to take into account the effects of nuclear fragmentation. An additional complication of the dose evaluation arises from the fact that the RBE depends on the nuclear charge Z and the LET of the particles. Therefore, in order to predict the RBE-weighted dose D_{biol}, the composition of the particle field and the LET-distributions must be known at each point of the treatment volume:

$$D_{biol}(\vec{r}) = \sum_{Z=1}^{Z_P} \int_0^{E_{max}} \Phi(Z,E,\vec{r}) \cdot LET(Z,E) \cdot RBE(Z,E) \frac{1}{\rho(\vec{r})} dE \qquad (1.20)$$

where Φ denotes the particle fluence, ρ the mass density of the target material (tissue) and the sum is taken over the spectrum of charged particles from protons ($Z = 1$) up to the primary ions (Z_p).

For these reasons, several experimental studies of nuclear fragmentation have been performed. For example, the results of the experimental study of nuclear fragmentation of 200 and 400 MeV/u ^{12}C ions in water by E. Haettner are reported in [34]. The angular distributions of secondary fragments produced by a 400 MeV/u ^{12}C ion beam in water at different depths (15.9 cm and 31.2 cm) are reported in Figure 1.22. The first thickness corresponds to the entrance channel and the second to the BP region. These results show that the fragments are strongly focused in the forward direction, and that the width of the angular distribution depends on the nuclear charge Z_f of the fragments. In particular, the *Full Width Half Maximum* (FWHM) ranges from 3° for Boron fragments to 10° for hydrogen. Helium and especially Hydrogen fragments have broad distributions and can still be detected at angles larger than 10°. With increasing Z_f, the distributions become narrower.

Energy spectra of $H-$ and $He-$fragments recorded at different angles near the BP position are shown in Figure 1.23. Noticeable is the detection of fragments with energies up to 700 MeV/u, almost twice the energy per mass unit of primary ^{12}C ions. This phenomenon is explained as an interaction in the collision process, where part of the Fermi momentum is transferred from a nucleon to the fragment [35].

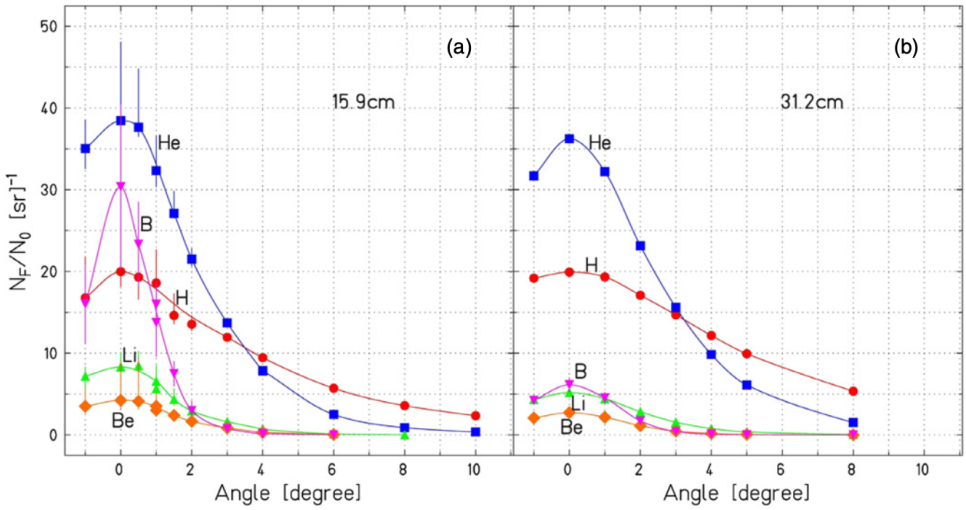

Figure 1.22: Angular distributions of charged fragments produced by 400 MeV/u ^{12}C ions in water targets of 15.9 cm (left) and 31.2 cm (right) thickness [34].

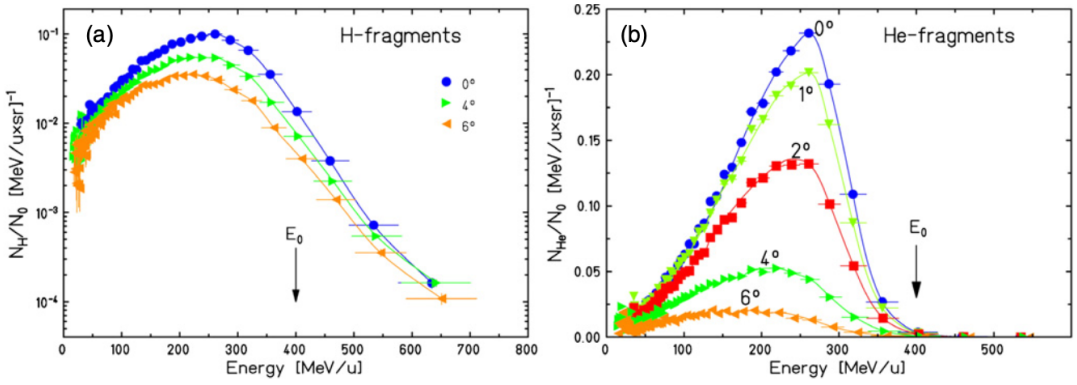

Figure 1.23: Energy spectra of secondary fragments of H (a) and He (b) measured at various forward angles. The target thickness was 27.9 cm of water (corresponding to Bragg peak position). The kinetic energy of the primary ^{12}C ions at target entrance (E_0) is marked by an arrow [34].

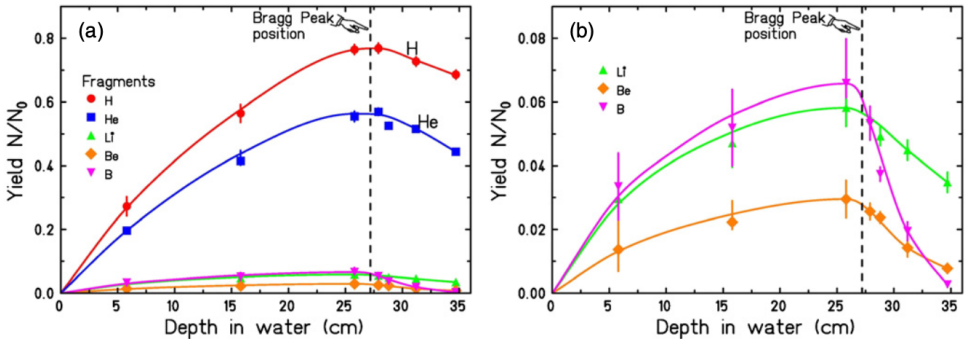

Figure 1.24: Build-up curves of secondary fragments produced by 400 MeV/u ^{12}C ions in water (a) and expanded view of Li-, Be-, B-fragments [34].

The results on the yield of secondary fragments as a function of the target thickness are shown in Figure 1.24. Hydrogen- and Helium-nuclei are produced most frequently while the production yield of heavier fragments (B, Be and Li), is about one order of magnitude smaller. The low yield of Be isotopes can be understood as an effect of the prompt break-up of ^{8}Be into two α particles. The amount of charged fragments increases with increasing depth and a maximum is reached around the BP. At this depth (25.8 cm) the yields (N/N_0) produced by a 400 MeV/u ^{12}C beam are about 0.76 (H), 0.55 (He), 0.06 (Li), 0.03 (Be) and 0.07 (B). Beyond the BP the amount of fragments drops quickly, since all carbon ions have stopped and cannot produce new fragments. The slope of the fall-off depends on the nuclear charge Z_f distribution of the fragments. Light fragments with low charge have longer range and can still be produced from heavier fragments.

As previously remarked, all these effects should be considered in the TPS simulations in order to estimate the dose deposition correctly. A comparison between the measured heavy fragments build-up data and the simulations is shown in Figure 1.25. The MC code is based on *TRiP98* [36], which is the computational kernel for the TPS developed and adopted for the ^{12}C ion therapy at GSI. The mismatch between experimental data and simulation results for the heavy ion fragments build up curves is at most $20-30\%$. There is also a contribution to the dose deposition from secondary neutrons, that has been estimated to be ten times smaller than the dose released by charged fragments [3]. In order to improve the current TPS, more experimental data are necessary to improve the nuclear interaction models and the accuracy of MC simulation codes. In particular, measurements performed on thick targets, as done in [34], are not appropriate to test the nuclear reaction models with sufficient detail. Experiments performed with thin targets, with large acceptance and high resolution spectrometers are needed.

1.4.3 Target Fragmentation in Proton Therapy

Both in proton therapy and in heavy ion therapy, the fragmentation of target nuclei leads to the production of secondary particles, including evaporated neutrons, protons and recoiled heavy target nuclei. The heavy nuclei recoils have a range of the order of micrometers and the angular distribution is roughly isotropic. The short range of these heavy recoil nuclei also means that their LET is high and thus leads to the deposition of relatively large, highly localized doses. Because of their short range, heavy target fragment recoil secondaries typically cannot pass from the target volume into a detector and their effect cannot be measured and considered in the current TPS.

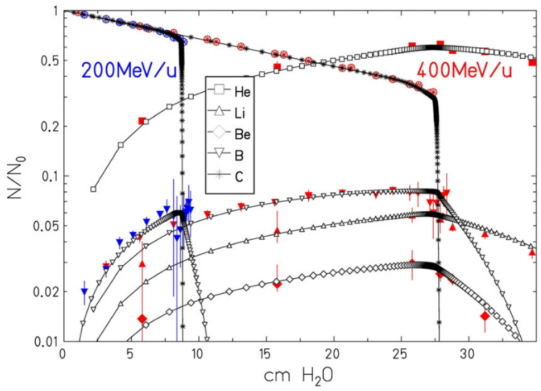

Figure 1.25: Comparison of beam loss and fragment build-up curves obtained from the TPS TRiP98 (open symbols) with experimental data [34].

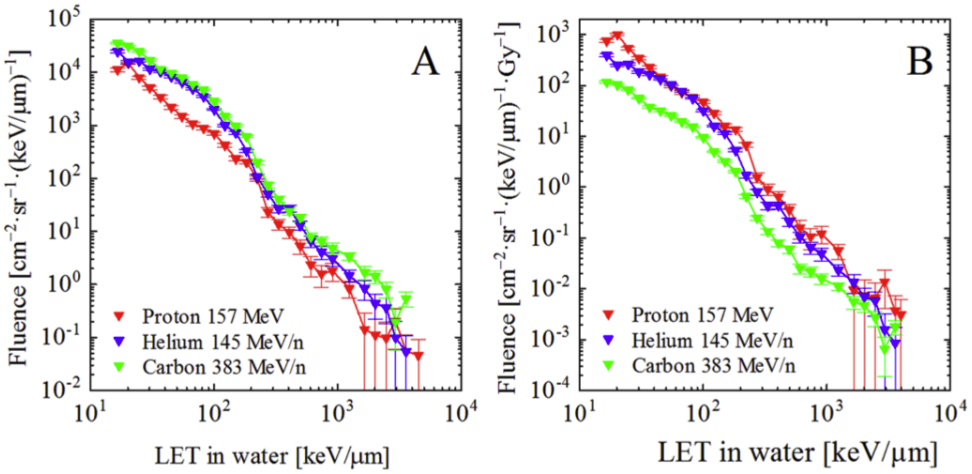

Figure 1.26: (A) LET spectra of secondary target fragments for each primary ion beam and (B) LET spectra in which the fluence is normalized to primary beam dose [37].

A recent study has measured the secondary target fragments fluence and dose contribution generated from CPT projectiles at the Bragg peak plateau using a CR-39 plastic nuclear track detector [37]. Indeed, this detector has the capability to detect short range recoil particles, since the detector itself is also the target volume. The nuclear reaction in CR-39 is similar to the situation in tissues because of the similar composition, consisting mainly of H, C and O. The LET spectra of secondary target fragments are shown in Fig. 1.26 (left). Each spectrum follows a continuous power-law curve with several shoulders due to individual target fragment components. Figure 1.26 (right) shows the LET spectra of secondary target fragments normalized to the absorbed dose of the primary beam (D_p). From the LET spectrum, the absorbed dose (D_s) of secondary particles was determined, as summarized in Table 1.1, for each primary ion beam. The dose ratios of secondary (D_s) to primary (D_p) represent the dose contribution of secondary particles for primary beam in absorbed dose (D_s/D_p). The ratio of fluence of secondary target fragments (F_s) to the fluence of primary beam (F_p) denotes the fragment production rate of secondary particles (F_s/F_p).

In the plateau of the Bragg curve, the production rate and the dose contribution were found to be $1.1 \cdot 10^{-4}$ and 1.2% of the absorbed dose for proton beams, $2.7 \cdot 10^{-4}$ and 0.7% for Helium beams and $4.0 \cdot 10^{-4}$ and 0.2% for Carbon beams. These results illustrate the fact that the absolute fragments fluence from carbon ion beams is four

Primary	Beam energy	D_s [Gy]	F_s (10^6) [cm^{-2}]	D_s/D_p	$F_s/F_p(10^{-4})$
Proton	$157MeV$	0.18 ± 0.01	1.93 ± 0.04	1.2%	1.10
Helium	$145MeV/u$	0.47 ± 0.01	4.75 ± 0.07	0.7%	2.73
Carbon	$383MeV/u$	0.68 ± 0.01	6.62 ± 0.08	0.2%	3.99

Table 1.1: Dose assessment results of secondary target fragments for each primary ion beam [37].

times higher than proton beams due to the higher nuclear cross section. However, the required primary carbon ion fluence is smaller than the primary proton fluence that delivers the same dose. As for the fluence, the target fragments produced by carbon ion beams release a higher dose with respect to proton beams, but the relative dose contribution with respect to the primaries is lower. The results from Helium beam measurements lie between those for proton and carbon ion beams. In all the cases, nuclear interactions make a significant contribution to the dose deposition at the plateau of the Bragg curve that should be therefore considered in the TPS.

As seen from a study performed with MC simulations [2], the target fragments dose deposition ahead of the Bragg peak is even more relevant. Fig.1.27 shows the expected number of cells killed by ionizations and from secondary fragments along the primary beam path, assuming that each cell hit by a secondary particle dies. Both the numbers of ionization and fragmentation events increase when approaching the BP, but the target fragments contribution is about 10% in the entrance channel while it reduces to about 2% at the BP. Previous experimental measurements and MC simulation results are in agreement about the target nuclear inelastic contribution at the Bragg peak. However, further measurements are required to improve the target fragmentation models in MC tools. Furthermore, in the current TPS the proton RBE is assumed to be 1.1 along all the LET range, but several studies show the inaccuracy of this approximation, with RBE values measured up to 3.5 [2], as shown in Fig.1.28. The causes of this fluctuation are still under study, but nuclear interactions are considered one of the possible causes. Even if no clinical data reported severe side effects due to the use of a fixed proton RBE value, a more complete RBE model that includes also the fragmentation effect is necessary to improve current treatment protocols.

In conclusion, nuclear inelastic interactions are not yet properly considered in the current TPS, leading to a possibly relevant underestimation of dose calculation both in heavy ion and in protontherapy. In order to improve the current TPS, to enhance the present nuclear reaction models and to check the MC simulation output, new measurements of fragmentation cross sections at the energies typical of CPT are required.

1.4.4 Radioprotection in space missions

Since the last century, one of the main space endeavors is the exploration of planets and satellites close to the Earth. The *National Aeronautics and Space Administration* (NASA) is gearing up for busy years, looking forward to more exploration firsts. The agency is working toward sending the first woman and next man to the Moon in 2024 and will establish sustainable lunar exploration by the end of the decade as part of the Artemis program, while getting ready for human exploration of Mars [38]. However, one of the most critical aspects of these missions is the health of the crew and the radiation hardness of the involved electronic strumentations. Indeed, once the astronauts leave the Earth with its protective environment provided by the

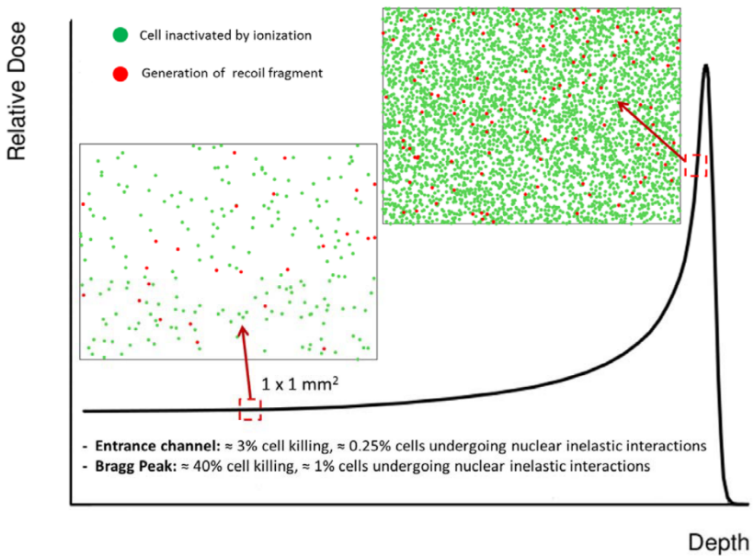

Figure 1.27: Schematic view of cells killed by primary ionization (greed dots) and fragmentation effect (red dots) at the entrance channel and close to the Bragg peak. The depth is of the order of centimeters and the dose is in arbitrary units [2].

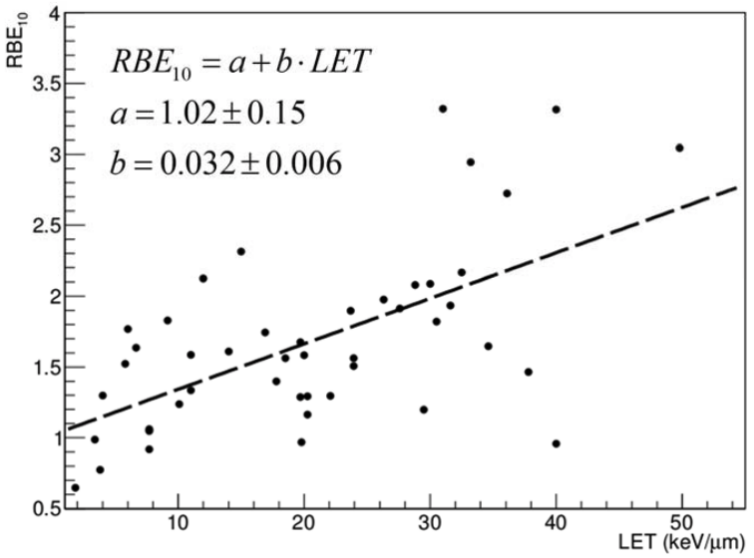

Figure 1.28: Proton RBE values for 10% survival fraction, extracted from database independent of α/β ratio [2].

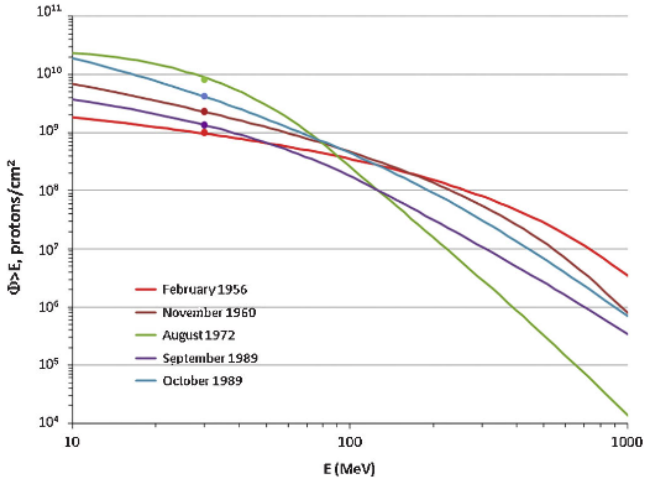

Figure 1.29: Integral energy spectra of intense solar particle events in the 20th century [39].

magnetosphere, they are subject to space radiations composed of different particles over a wide energy spectrum.

There are three main sources of energetic particles in space:

- *Solar Particle Events* (SPE): the Sun continuously emits particle radiation, consisting mainly of protons and electrons, the so-called *solar wind*. The intensities of these low-energy particles vary from 10^{10} to 10^{12} particles $cm^{-2}s^{-1}sr^{-1}$ with velocities between about 300 and 800 $km\ s^{-1}$. The related energies are so low (for a proton between 100 eV and 3.5 keV) that the particles will be stopped within the first few hundred nm of skin. They are therefore not of concern for radiation protection. However, occasionally the surface of the Sun releases large amounts of energy in sudden local outbursts and coronal particles, mostly protons with a small fraction of heavier nuclei, with energies up to several GeV that escape into the interplanetary space.

  In conclusion, SPEs show an enormous variability in particle flux and energy spectra, but the most intense events (Figure 1.29) have the potential to expose unshielded space crews to life threatening doses.

- *Galactic Cosmic Rays* (GCR): they are originated outside the Solar System and impinge isotropically on the Earth. Because of their high energies (up to 10^{20} eV), they most probably originate from supernova explosions, neutron stars, pulsars, or other sources where highly energetic phenomena are involved. Detected particles consist of 98% baryons and 2% electrons. The baryonic component is composed of 85% protons (hydrogen nuclei), with the remainder being helium (14%) and heavier nuclei (about 1%). The GCR make up more than 80% of the effective doses to crews on the *International Space Station* (ISS) because of their higher penetration power to deep seated organs and large quality factors. Figure 1.30 reproduces the differential energy spectra for H, He, O, and other heavier ions. The maximum of the spectrum is around $1GeV/u$ for all ions.

- *Geomagnetically trapped particles* consist of protons and electrons confined by the Earth magnetic field in two regions, called Van Allen belts. Protons reach energies up to a few hundreds MeV in the inner belt, electrons up to 100 keV in the outer belt.

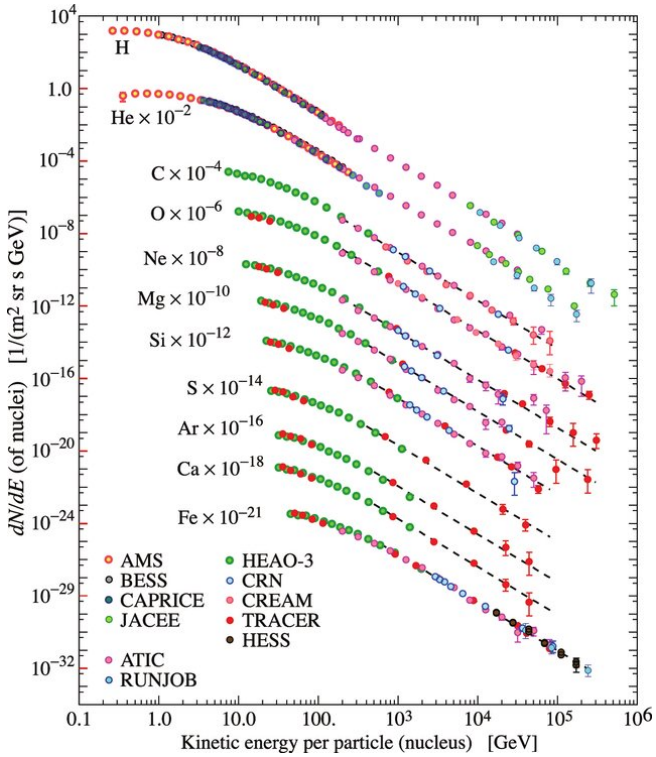

Figure 1.30: Energy spectra of different components of the GCR. Protons as well as helium are the dominating particles. The intensity of the GCR decrease with higher energies [39].

On Earth, radiation protection strategies are normally divided into 3 groups: increasing the distance from the source, minimizing the time of exposure and using radiation shielding

Increasing the distance to the source plays no role in space because the GCRs are omnidirectional, and SPEs permeate along magnetic field lines and become isotropic within a few hours after an event.

Minimizing the time of exposure is problematic for space exploration because it may limit the performance of mission science objectives. Increasing rocket velocity to shorten times to planetary destinations is a long-term goal of space programs.

Radiation protection methods must be developed for future long missions in space, farther destinations, such as the outer planets or interstellar exploration. Thus, developing spacecraft or planetary habitat shielding becomes the major approach for radiation protection with biological countermeasures or genetic selection for radiation resistance. For both GCRs and SPEs, material selection and optimization of topology are major considerations. Spacecraft volumes may be constrained as well as mass when considering shielding augmentation. More importantly, the extra fuel required to launch such shielding compounds the mass available for it. Basic concepts in atomic and nuclear physics can be used to guide material selection augmented with detailed radiation transport code predictions. Engineering considerations on material strength, temperature, UV degradation, flammability, etc. must be considered, alongside radiation protection, and the composite picture must be analyzed. Materials with the smallest mean atomic mass are usually the most efficient shields for both SPEs and GCRs. The energy loss by ionization of a single component of shielding material with atomic number Z is proportional to the number of electrons per atom and thus proportional to Z/A. Materials with small atomic mass have the highest number of electrons per nucleon (e.g., $Z/A = 1$ for hydrogen, 0.5

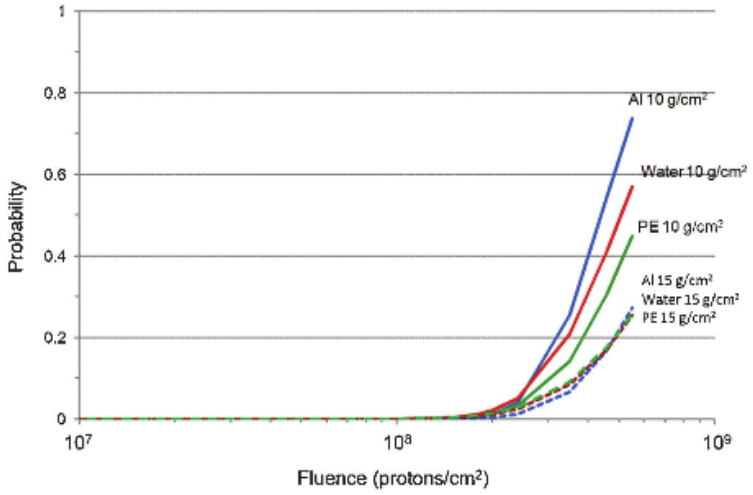

Figure 1.31: Calculations of the probability to exceed the 30- day dose limits for the blood-forming organ of 250 mSv, for different shielding material types and amounts, as a function of the fluence of protons with energy $E > 100$ MeV [40].

for carbon, but 0.48 for aluminum, 0.46 for iron, and 0.40 for lead). Moreover, light mass materials have smaller nuclei and more of them can fit into a given mass, so that there can be more nuclear interactions. Indeed, the ratio of ionization energy loss to nuclear interactions is also dependent on the material density. For liquid hydrogen ($\rho = 0.07\ g/cm^3$), the ratio ~ 14, whereas for aluminum ($\rho = 2.7\ g/cm^3$) the ratio is only 0.5, and for lead ($\rho = 11.3\ g/cm^3$) the ratio is 0.2. From these considerations, an electron plasma would provide the best shield from GCRs. A shield made of liquid hydrogen, which has the highest ratio of electrons to nuclei per atom and produces minimal secondary radiation, is the second best choice. Hence, interest in polyethylene and hydrogen embedded nanofibers. The character of these interactions and the secondary nuclei produced through both projectile and target fragmentation is important. Lighter nuclei have fewer neutrons to release and some nuclei, e.g., carbon, can break into three helium nuclei without releasing any neutrons. In tissue, the release of three helium atoms is much more biological damaging than that of neutrons; however, if produced within spacecraft shielding materials neutrons are a higher concern because of their longer ranges than slow helium particles. At the moment, there are different studies aiming to improve the shielding material and also to develop new protection techniques both for SPEs and GCRs. As an example, polyethylene has been identified to be a valuable shielding material due to its high concentration of hydrogen atoms. For example, Figure 1.31 shows the advantages of polyethylene or water compared to aluminum in protecting against SPEs where the probability of exceeding the 30-day limit has been calculated for increasing 100 MeV proton fluence.

In order to research new shielding materials, to improve the current MC transport codes and to develop new stochastic based risk models for the future long term space missions, new cross section measurements are required. Up to now, many integral cross section data have already been taken, but there is a significant lack of double-differential cross section measurements about light particles production and with new materials of interest [40].

Chapter 2

The FOOT experiment

2.1 Introduction

The *FragmentatiOn Of Target* (FOOT) project is a nuclear physics experiment that aims at measuring differential fragmentation cross sections ($d\sigma/d\Omega \cdot dE$) of particles relevant for both CPT and radioprotection in space [41, 42]. As discussed in depth in Section 1.4, these cross sections are fundamental to improve the quality of CPT treatment plans, to study the shielding material performances and to benchmark nuclear interaction models.

The experiment has been funded in 2017 by the *National Institute for Nuclear Physics* (INFN) and now it is an international collaboration composed of about a hundred physicists from Italy, France, Germany and Japan.

FOOT includes the development of two different experimental setups: an electronic detector setup to measure heavier fragments ($Z \geq 3$) and an emulsion spectrometer for the lighter ones ($Z < 3$). In order to optimize the detector parameters and to perform preliminary studies by means of MC data, the *FLUktuierende KAskade* (FLUKA) code has been adopted for the simulation of both layouts [43–46]. The analysis of MC and experimental data is conducted by means of a dedicated reconstruction software developed within the FOOT experiment.

In this chapter, a comprehensive overview of the FOOT experiment is given. In particular, in Section 2.2 the goals, the strategy of the measurements and the experimental plan are illustrated. The two experimental layouts are discussed in Section 2.3, followed by the description of the experimental requirements in Section 2.4. Finally, a general description of the FLUKA simulation code and the reconstruction software is presented in Section 2.5.

2.2 Goals and measurement strategy

As discussed in Section 1.4 nuclear inelastic interactions play an important role both in CPT and space radiation protection. In particular the current MC simulation codes and the semi-empirical models do not properly take into account all the aspects related to nuclear inelastic interactions. Indeed, the determination of the RBE of fragments by means of radiobiological experiments is difficult and there is a lack of cross section data for the production of fragments after proton irradiation in the energy range of interest (up to 250 MeV for protons and 400 MeV/u for carbon ions). In recent years some experiments have been dedicated to the study of projectile fragmentation for ^{12}C ions, even if this program was carried out only for a few energies [47, 48]. Moreover, also for radioprotection application there is a lack of data. An overview of the nuclear cross section already available can be found in [49], where the gaps in the data and the recommended future measurements with a focus on

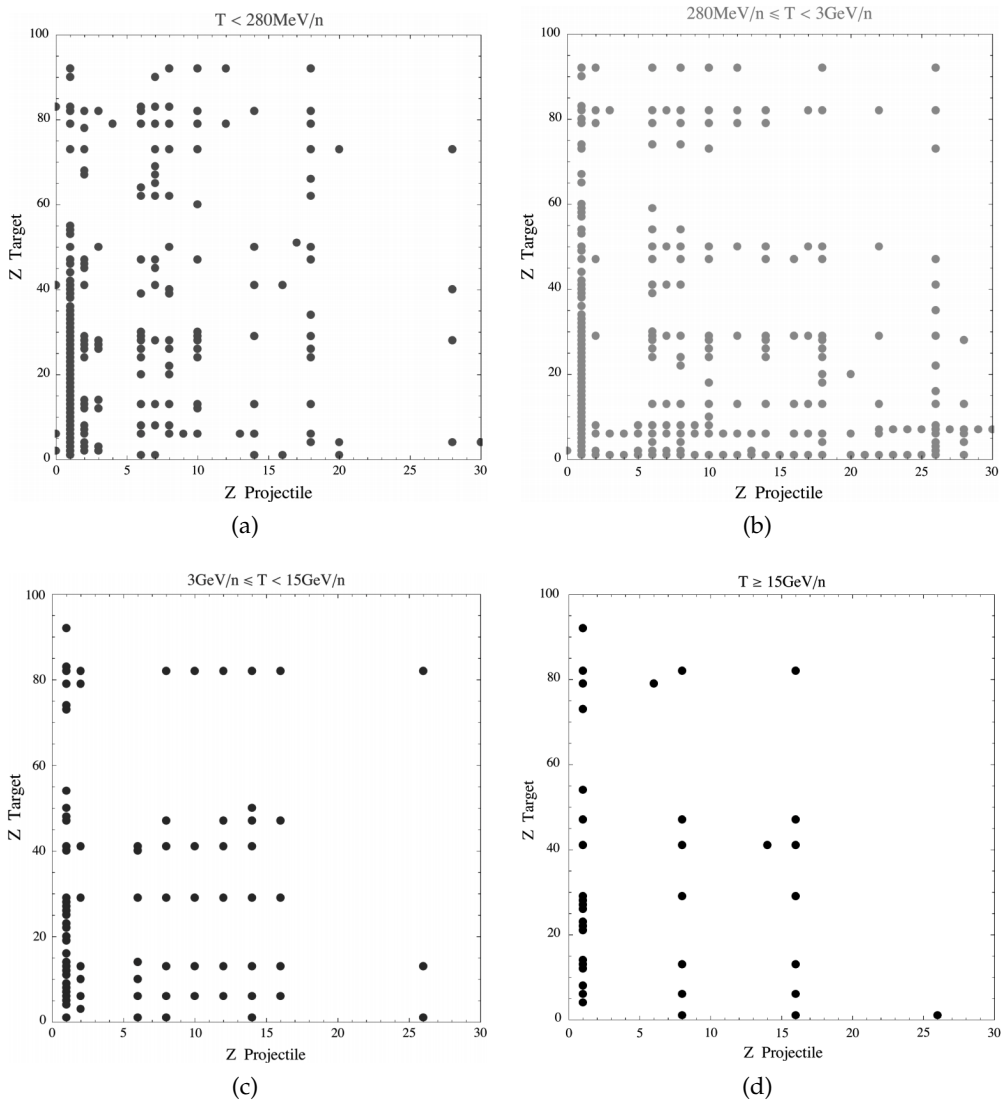

Figure 2.1: Cross section data below the pion threshold (a), between the pion threshold and 3 GeV/u (b), between 3 and 15 GeV/u (b), and greater than 15 GeV/u [49].

space radiation are identified too. The experimental data in terms of well known cross sections are represented in Figure 2.1 in different energy ranges: below the pion threshold ($T < 280\ MeV/u$) in Figure 2.1a, between 280 $MeV/u - 3\ GeV/u$ in Figure 2.1b, between $3 - 15\ GeV$ in Figure 2.1c, and for $T > 15\ GeV/u$ in Figure 2.1d.

The FOOT experiment aims to fill the gap and provide measurements of the double differential cross sections with respect to kinetic energy and angle, for both target and projectile fragmentation effects relevant in CPT and space radiation protection applications.

2.2.1 Inverse kinematic approach and Target

One of the causes for the lack of target fragmentation cross sections data is that due to kinematic reasons target fragments originating from proton-tissue ($p \rightarrow X$) interactions have a very low energy and short range ($\sim \mu m$). Thus, the detection of such particles in a *direct kinematic approach* is not a simple task, since the fragments

can leave the target only if they are produced close to the exit window, in the last few micrometers of material. Moreover, the development and the handling of a target with a thickness of few micrometers is not an easy operation. The nuclear inelastic interaction rate in such a thin target would be strongly reduced and the initial kinetic energy of the fragments cannot be measured with high accuracy due to a non negligible energy loss in the target material.

To overcome this issue, the FOOT collaboration has proposed an alternative solution to study target fragments: the *inverse kinematics approach*. The basic idea is to switch the projectile and target role: instead of shooting a proton beam onto a tissue-like (carbon or oxygen) target, tissue-like nuclei will be accelerated to impinge on a proton target. If the kinetic energy per nucleon is the same, this transformation results only in a reference frame change, from the *patient reference frame* to the *laboratory frame*. In this way, fragments originated from a carbon or oxygen beam, with the same kinetic energy per nucleon that would have a proton beam, are emitted with higher energy. The consequent rise of the mean range ensures an easier detection and reconstruction of the event kinematics, but also the use of a thicker target, with a consequent increase of the interaction rate. Afterwards the *Lorentz transformations* must be applied in order to convert the data collected in the laboratory frame to the patient frame. Indeed, considering that the beam direction is towards the positive part the z-axis, two reference frames can be identified: the laboratory frame S, where the proton target is at rest and the ion beam is moving along z at a constant velocity β towards the target, and the patient frame S', where the ion is at rest while the proton is moving along z with the same velocity β but in the opposite direction. The 4-momentum of the ion in S and the 4-momentum of the proton in S' are $\mathbf{P} = (E/c, \mathbf{p})$ and $\mathbf{P'} = (E'/c, \mathbf{p'})$ respectively, where E and E' are the energies in the two reference frames. In this configuration, the proton 4-momentum components in the S' frame are given by:

$$\frac{E'}{c} = \gamma\left(\frac{E}{c} - \beta p_z\right) \tag{2.1a}$$

$$p'_x = p_x \tag{2.1b}$$

$$p'_y = p_y \tag{2.1c}$$

$$p'_z = \gamma\left(-\beta\frac{E}{c} + p_z\right) \tag{2.1d}$$

This result can be expressed by means of matrix operators. Indeed:

$$\mathbf{P'} = \Lambda\mathbf{P} \tag{2.2}$$

where, making the Eq. 2.2 and the Λ matrix explicit:

$$\begin{pmatrix} E'/c \\ p'_x \\ p'_y \\ p'_z \end{pmatrix} = \begin{pmatrix} \gamma & 0 & 0 & -\beta\gamma \\ 0 & 1 & 1 & 0 \\ 0 & 0 & 1 & 0 \\ -\beta\gamma & 0 & 0 & \gamma \end{pmatrix} \begin{pmatrix} E/c \\ p_x \\ p_y \\ p_z \end{pmatrix} = \begin{pmatrix} \gamma E/c - \beta\gamma p_z \\ p_x \\ p_y \\ -\beta\gamma E/c + p_z \end{pmatrix} \tag{2.3}$$

Thus, the inverse Lorentz transformation is:

$$\mathbf{P} = \Lambda^{-1}\mathbf{P'} \tag{2.4}$$

where Λ^{-1} is:

$$\begin{pmatrix} \gamma & 0 & 0 & \beta\gamma \\ 0 & 1 & 1 & 0 \\ 0 & 0 & 1 & 0 \\ \beta\gamma & 0 & 0 & \gamma \end{pmatrix} \tag{2.5}$$

that means:

$$\Lambda^{-1}(\beta) = \Lambda(-\beta) \tag{2.6}$$

The inverse kinematics strategy requires an emission angle measurement with a resolution of the order of few *mrad* in order to correctly apply the Lorentz boost. Therefore, both the projectile and fragments directions must be measured accurately, and also the MCS of any particle inside the beam must be kept well below the *mrad*. This strongly limits the allowed target thickness and its density, which should be of the order of gcm^2 or less, in order to minimize the probability of secondary fragmentation within the target. A reasonable target thickness is 5 mm, which is a good trade-off between the interaction rate and the required angular resolution.

However, since the FOOT experiment wants to measure the cross sections of fragments created with all the different kind of atoms of the human body (oxygen 61%, carbon 23% and hydrogen 10% [50]), there is the necessity to replicate the human body compounds in different targets and beams. However, only a carbon ion target can be installed in experimental rooms without any complication. Indeed, for the oxygen and hydrogen cases, the handling of a pure gaseous and inflammable material prevents the use of such kind of targets in the accelerator facilities for safety reasons. In addition, the gas low density would deeply drop the interaction rate, making the experiment unsustainable.

In order to overcome these complications, the FOOT experiment adopts carbon targets enriched with hydrogen particles, i.e.: *Poly(methyl methacrylate)* (PMMA) and C_2H_4. The measurements will be combined with the pure carbon target data in order to retrieve the cross sections on oxygen and hydrogen targets. As an example, the calculation of the hydrogen cross section measurement is expressed in Eq. 2.7:

$$\sigma(H) = \frac{1}{4}\Big(\sigma(C_2H_4) - 2\sigma(C)\Big) \tag{2.7}$$

The same procedure is also valid for differential cross sections:

$$\frac{d\sigma}{dE}(H) = \frac{1}{4}\left(\frac{d\sigma}{dE}(C_2H_4) - 2\frac{d\sigma}{dE}(C)\right) \tag{2.8}$$

$$\frac{d\sigma}{d\Omega}(H) = \frac{1}{4}\left(\frac{d\sigma}{d\Omega}(C_2H_4) - 2\frac{d\sigma}{d\Omega}(C)\right) \tag{2.9}$$

The results of this approach from a previous experiment conducted at Ganil [48] are shown in Figure 2.2.

A disadvantage of this strategy, however, is that the resulting cross section uncertainties are the quadratic sum of the uncertainties of the two single targets, therefore the cross sections on hydrogen have a larger error.

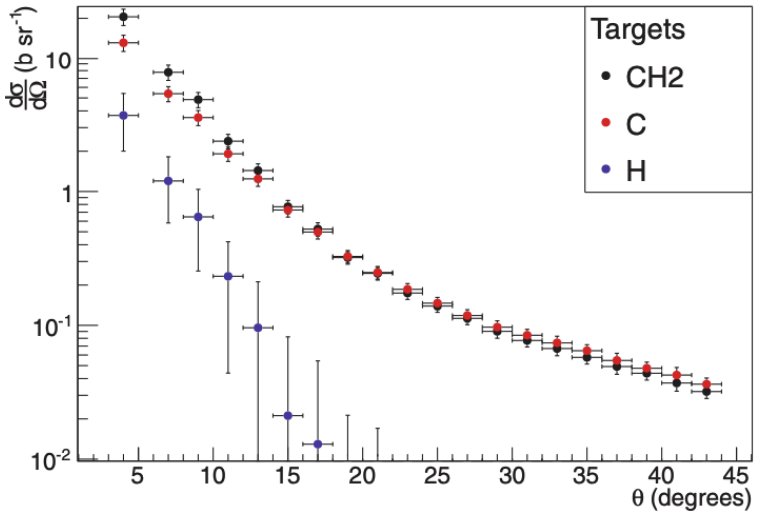

Figure 2.2: Combination of carbon and C_2H_4 targets angular distribution to determine the hydrogen angular distribution for α fragments produced by 95 MeV/u carbon ions [48]

2.2.2 Goals and Research program

Concerning the CPT topic, FOOT will measure the fragmentation cross sections to study both the projectile and target fragmentation, as discussed in the previous sections. For the former case ^{4}He, ^{12}C and ^{16}O beams with kinetic energies in the $200 - 400$ MeV/u range, on targets made of ^{12}C, C_2H_4 and PMMA ($C_5O_2H_8$) will be used. In particular, ^{4}He and ^{16}O beam measurements aim at evaluating the possibility to introduce these ions as new particles for treatments. For the latter case, FOOT will measure the cross sections of ^{12}C and ^{16}O at 200 MeV/u on ^{12}C and C_2H_4 targets, also adopting the *inverse kinematic approach* (see 2.2.1).

The beams selected for hadrontherapy measurements can also be used for the space radiation protection field, since they are present in the galactic cosmic radiation, even though with higher energies. Indeed, as shown in Figure 1.29, the fluxes of different ions included in the galactic cosmic radiations are peaked in a range between 700 MeV/u and some GeV/u. For this reason, FOOT will perform a set of measurements dedicated to the space radiation protection applications, using the same beams (^{4}He, ^{12}C and ^{16}O) but with higher energies (800 MeV/u). These beams will impinge on the same target materials used for the CPT measurements (^{12}C, C_2H_4 and PMMA). A complete overview of the FOOT research program, including beams, targets and energies that will be investigated, is listed in Tab 2.1.

The strategy of the collaboration is to keep the detector as compact as possible[1], making it capable of exploiting particle beams required by the experiment at different therapeutic centers, like: CNAO in Pavia (Italy), GSI in Darmastd (Germany), or *Heidelberg Ion Therapy Center* (HIT) in Heidelberg (Germany).

Two preliminary data takings have been already conducted at GSI with oxygen ions at 200 MeV/u and 400 MeV/u in 04/2019 and 07/2021 and next sessions are already planned for 11/2021 at CNAO and for 2022 at GSI.

The FOOT main goal is to measure the fragment production cross sections with a maximum uncertainty of 5%. To achieve this resolution, FOOT must perform the charge and mass identification with very high accuracy, at the level of $2 - 3\%$ and

[1]The experiment will have to be easily movable and fits the space limitations set by the different experimental and treatment rooms where ion beams of therapeutic energies are available. As consequence FOOT will be a *table top* experiment with an overall detector size within the $1.5 - 2$ m range.

Table 2.1: Overview of the FOOT research program. In the last column, also the facilities providing the beams are reported.

Physics	Beam	Target	Energy (MeV/u)	Kinetic Approach	Facilities
Target fragm. in CPT	^{12}C	C,C_2H_4	200	inverse	CNAO,GSI,HIT
Target fragm. in CPT	^{16}O	C,C_2H_4	200	inverse	GSI,HIT
Beam fragm. in CPT	^{4}He	C,C_2H_4,PMMA	250	direct	GSI,HIT
Beam fragm. in CPT	^{12}C	C,C_2H_4,PMMA	350	direct	CNAO,GSI,HIT
Beam fragm. in CPT	^{16}O	C,C_2H_4,PMMA	400	direct	GSI,HIT
Space Radioprotection	^{4}He	C,C_2H_4,PMMA	800	direct	GSI
Space Radioprotection	^{12}C	C,C_2H_4,PMMA	800	direct	GSI
Space Radioprotection	^{16}O	C,C_2H_4,PMMA	800	direct	GSI

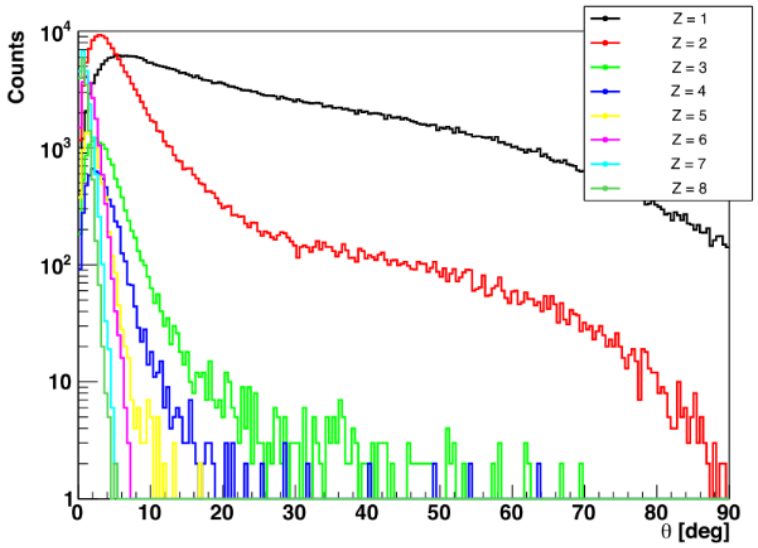

Figure 2.3: Angular distribution of fragments produced by an oxygen beam at 200 MeV/u impinging on a 2 mm thick target made of C_2H_4. Data simulated by means of FLUKA.

5% respectively. For these reasons, the experiment has been designed in order to measure energy loss, kinetic energy, velocity and momentum of the fragments with very high precision. All the details will be discussed in Section 2.4.

2.3 Experimental setup

According to simulations performed by means of the FLUKA MC code the angular distribution of light particles, shown in Figure 2.3, is wide. On the contrary, heavy fragments are mainly emitted inside a cone of 10° with respect to the incoming particle direction. For this reason the FOOT experiment has been designed with two distinct experimental setups: the *Emulsion Cloud Chamber* (ECC) to measure the differential cross section of light fragments ($Z < 3$) and the *Electronic Spectrometer* for the heavier ones ($Z \geq 3$).

2.3.1 Electronic Spectrometer

The FOOT electronic spectrometer has been designed to detect the fragments with $Z \geq 3$ and with an angular acceptance up to about 10°. The total longitudinal length is limited by the space availability of the experimental facilities which can provide

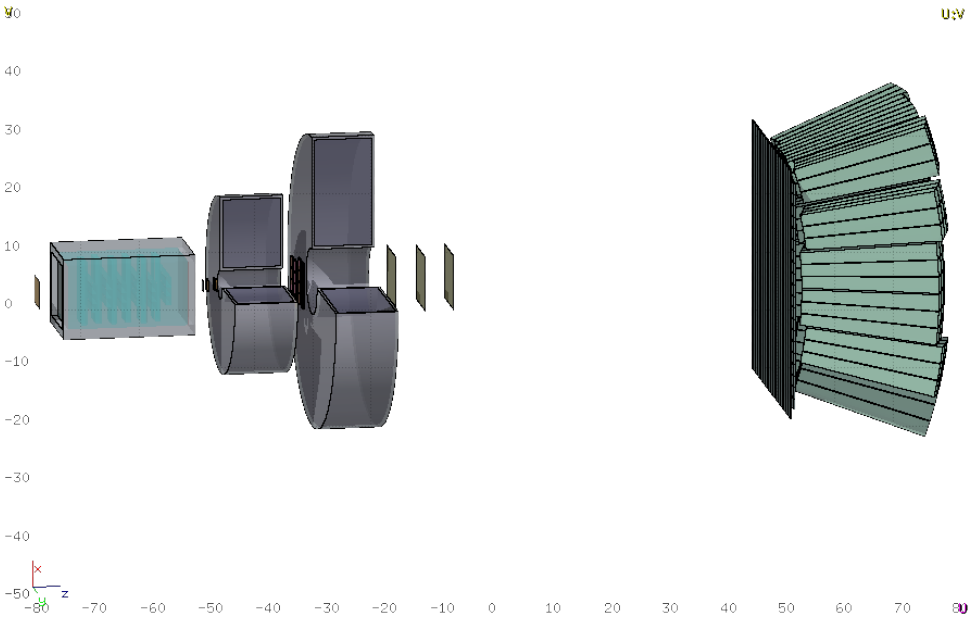

Figure 2.4: Schematic view of the FOOT electronic spectrometer detectors.

the required primary beams. A schematic view of the electronic spectrometer is shown in Figure 2.4.

The layout can be divided in three parts:

- *Upstream region*: it is the region before the target, composed of a plastic scintillator and a drift chamber, also called *Start Counter* (SC) and *Beam Monitor* (BM), respectively. These detectors are used in the event trigger system, in order to provide the "start signal" for the *Time Of Flight* (TOF) measurement, necessary for the measurement of the fragments velocity, and to reconstruct the incoming primary particle trajectory.

- *Magnetic Spectrometer region*: it is composed by two permanent magnets and a set of tracking detectors placed just beyond the target: *Vertex* (VTX) detector, *Inner Tracker* (ITR) and *Micro Strip Detector* (MSD). This region aims to reconstruct the tracks and momenta of the fragments.

- *Downstream region*: it is composed of a plastic scintillator called *Tof-Wall* (TW) and a *Calorimeter* (CAL). The former provides the fragment energy loss $\Delta E/\Delta x$ and the "stop" of the TOF, the latter measures the kinetic energy of charged fragments.

The longitudinal position of the downstream region detectors depends on the incident particle beam energy. For the CPT measurements conducted with primaries with a kinetic energy below or equal to 400 MeV/u, the scintillator and the calorimeter are placed at about 1 meter from the target. For the high energy particle beams with kinetic energies of about $700 - 800$ MeV/u dedicated to the space radiation protection data, the downstream detectors will be placed at about 3 meters from the target position in order to increase the accuracy of the TOF measurement.

A complete description of the different detectors is presented in the next paragraphs.

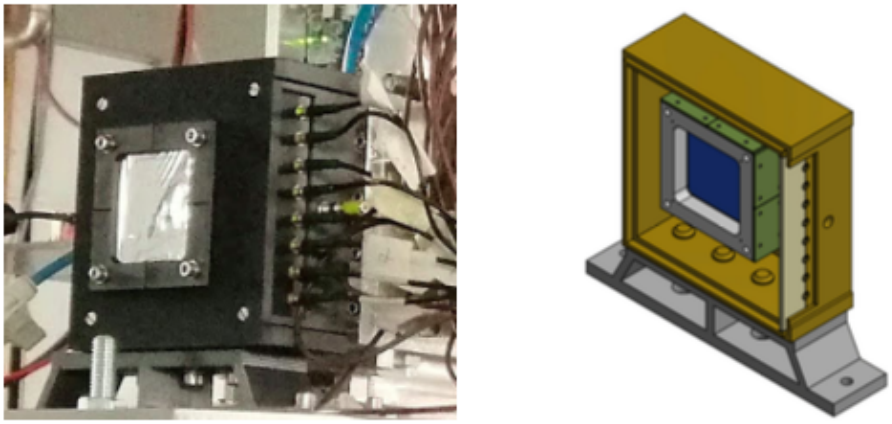

Figure 2.5: A picture (left) and a technical draw (right) of the SC detector. The detector is mounted in an aluminium frame and contained in a black 3D printed box. Two squared windows made of $4\mu m$ of aluminized mylar [53] are placed in the black box corresponding to the beam entrance and exit positions.

Start Counter

The SC detector is a plastic scintillator that measures the beam rate, provides the trigger for the acquisition system and determines the start time of the TOF measurement performed together with the downstream scintillator TW. It is made of a 250 μm thick and 5×5 cm^2 large squared foil of *EJ-228* scintillator [51]. The scintillation light is collected laterally by 48 *Silicon PhotonMultiplier* (SiPM) [52] bundled in 8 channels. A picture of the SC detector is shown in Figure 2.5. The detector has been tested at CNAO and GSI with carbon and oxygen beams at different energies. A time resolution of the order of 60 ps has been achieved for the ^{12}C ion beam with a kinetic energy of 700 MeV/u.

Beam Monitor

The BM is an Ar/CO_2 (80%/20%) drift chamber present in both the electronic and the ECC setups. It is placed between the SC and the target and measures the incoming beam direction and the impinging point position of each primary on the target. In addition, for the electronic spectrometer purpose, the BM multi-track reconstruction capability is exploited to reject the events in which the projectile fragments before reaching the target. It is composed by 12 planes of alternated horizontal and vertical wires, where each of them has 3 rectangular cells (16×10 mm^2) with the long side perpendicular to the beam direction. The total dimensions are $11 \times 11 \times 21$ cm^3. The choice of a drift chamber detector relies on its low density material in order to minimize the MCS and the production of fragments within the detector. The BM is equipped with a front-end electronic which preamplifies the signals that are then digitized by a *Time to Digital Converter* (TDC). While the primary beam energy will be accurately known, each primary particle position is associated with an uncertainty due to the intrinsic beam lateral spread (magnitude of mm). Since the primary $4-$momentum is required to perform the Lorentz boost, the position and the direction of primary particles will be measured by the BM. Dedicated electronics will also be able to detect multi-track events, in order to reject those in which the primary ion

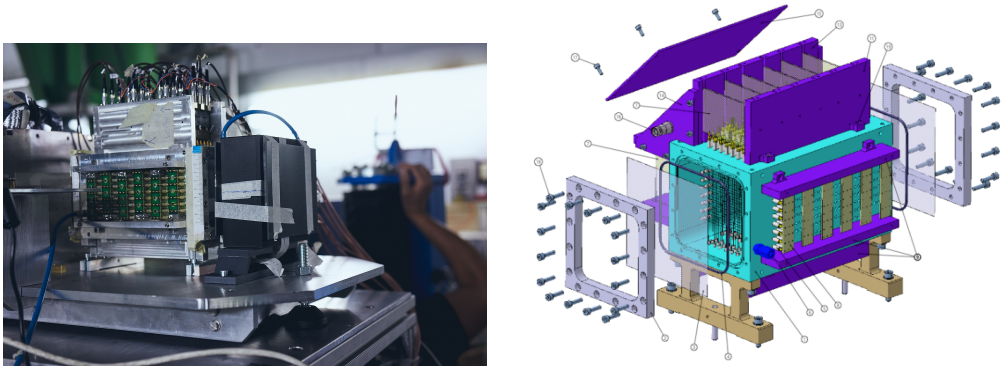

(a) (b)

Figure 2.6: A picture (a) of BM and SC and a technical draw (b) of the BM detector.

has fragmented in the SC. The tracks inside the cells will be reconstructed via a dedicated *Kalman filter algorithm*[2]. The calibration and the performance assessment of the BM has been conducted at the Trento protontherapy facility with protons at 228 MeV and 80 MeV. The spatial resolution is $60 - 100$ μm in the central part of the cell for the two energies, respectively. The angular resolution is 1.62 and 2.1 $mrad$ for higher and lower beam energies, respectively. The hit detection efficiency has been found to be more than 90% [54]. A picture and a technical drawing of the BM is shown in Figure 2.6.

Vertex detector

As shown in Figure 2.7, VTX is composed of four layers of silicon pixel detectors placed at few mm beyond the target, achieving a geometrical acceptance of about 40°. This detector reconstructs the track and the momentum of the particles, together with the other tracking detectors of the magnetic spectrometer (ITR and MSD). In addition, it is exploited to identify the projectile interaction position in the target material matching the BM track. Each layer is composed of 928×960 MIMOSA-28 (M28) belonging to the family of the CMOS *Monolithic Active Pixel Sensors* (MAPS) [55, 56], which are commonly used for experiments in particle and heavy ion physics. The pixels have a pitch of 20.7 μm for a total transverse active area of 2.022×2.271 cm^2. The thickness of the epitaxial layer is 15 μm on a high resistivity substrate of about 400 Ωcm. The total thickness of a single layer is 50 μm and the distance between the layers is $2 - 3$ mm. The overall maximum rate capability of the detector is of the order of $1 - 2$ kHz. This corresponds also to the FOOT electronic spectrometer maximum rate capability, since the VTX is the slowest detector in the acquisition chain. An example of M28 chip is shown in Figure 2.8.

Magnetic system

Beyond the target and the vertex detector, two permanent magnets in a *Halbach configuration*[3] provide the requested magnetic field to bend the fragments making the

[2] In statistics and control theory, the Kalman filter is an algorithm that uses a series of measurements observed over time, including statistical noise and other inaccuracies, and produces estimates of unknown variables that tend to be more accurate than those based on a single measurement alone, by estimating a joint probability distribution over the variables for each timeframe.

[3] A Halbach array is a special arrangement of permanent magnets that augments the magnetic field on one side of the array while cancelling the field to near zero on the other side

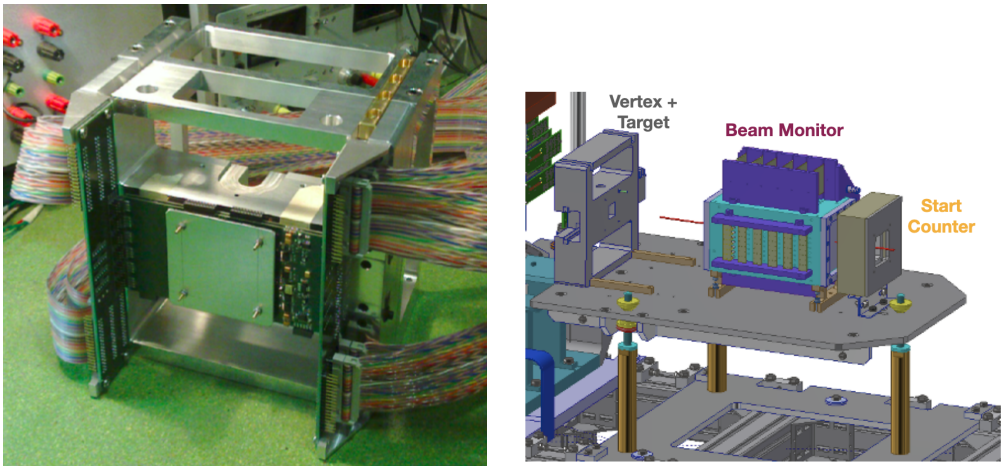

(a) (b)

Figure 2.7: A picture (a) of VTX and a technical draw (b) of SC, BM and VTX detector.

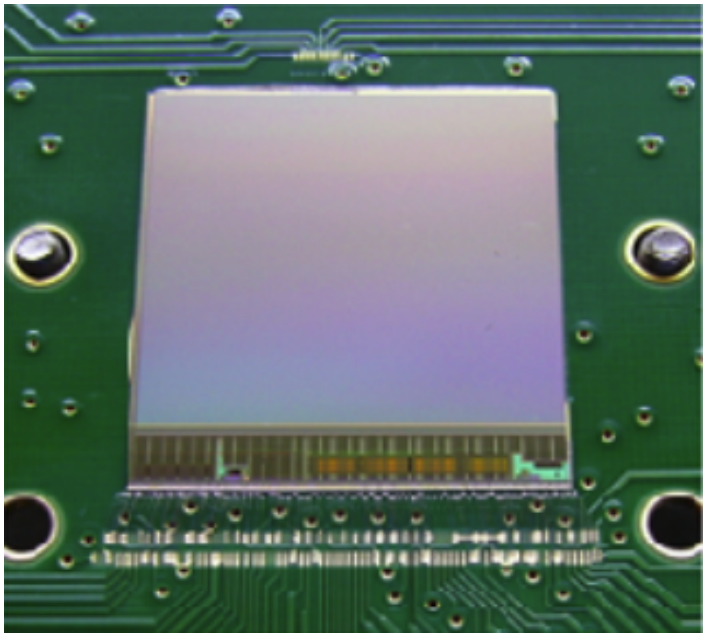

Figure 2.8: Picture of a M28 chip.

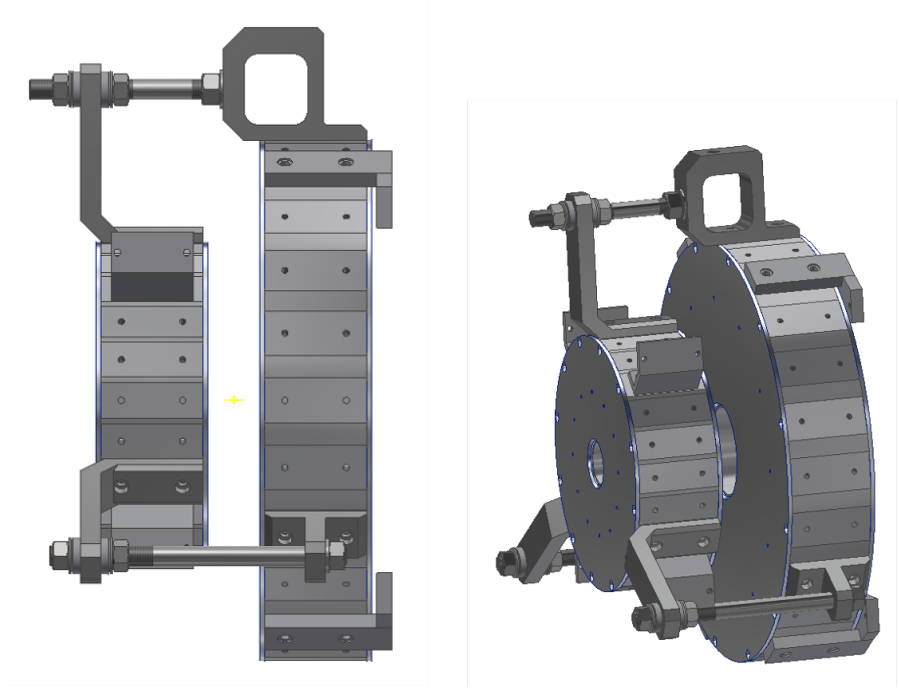

(a) (b)

Figure 2.9: Technical draw of the two Halbach magnets structure.

particles momentum detection possible. The choice of the magnets type and configuration has been driven by the necessity to match the portability of the apparatus with the momentum resolution requirement. Indeed, simulations of different magnet configurations (e.g. one single magnet and two magnets) were performed. The results showed that the magnetic field generated in the region between the two magnets is equal or greater than of one single magnet. Moreover, two magnets have a higher portability and they make the installation of the ITR station in the middle of the magnetic system easier, improving the momentum resolution. Each magnet is composed of 12 blocks arranged in an annular configuration. Since the magnetic field increases with the external radius and decreases with the gap radius, the two magnets have been designed with two different dimensions, in order to provide the required magnetic field maintaining an angular acceptance of 10° for the fragments (Fig. 2.9). The first magnet, close to the vertex detector, has an internal diameter of 5 cm and it provides a maximum magnetic field of 1.4 T. The second one, close to the downstream region, has a gap diameter of 10.6 cm and its maximum magnetic field is 0.9 T. Between the two magnets there is a 50 cm gap where the ITR detector is installed. Both the permanent magnets provide a magnetic field with a Gaussian shape along the Y axis, perpendicular with respect to the beam direction, as shown on the right panel of Figure 2.10.

Several studies have been performed for the choice of the magnets material. Indeed, this choice is driven by considerations about the radiation resistance: in the FOOT setup the magnets will be exposed to various types of radiations, in particular neutrons and light ions (mainly protons and He ions). Radiation exposure can degrade and damage the magnets material altering the produced field. Recent studies [57] about the demagnetization of different magnets materials proved that Sm_2Co_{17} is particularly insensitive to radiation exposure compared to other magnet materials. Therefore, this material has been the choice for the FOOT magnets.

A dedicated mechanical structure has been developed to enclosure and support

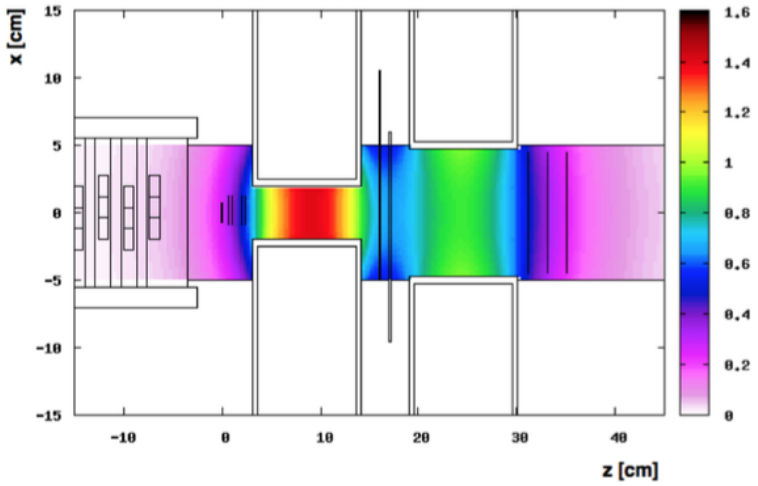

Figure 2.10: Magnetic field map computed by FLUKA Monte Carlo simulation.

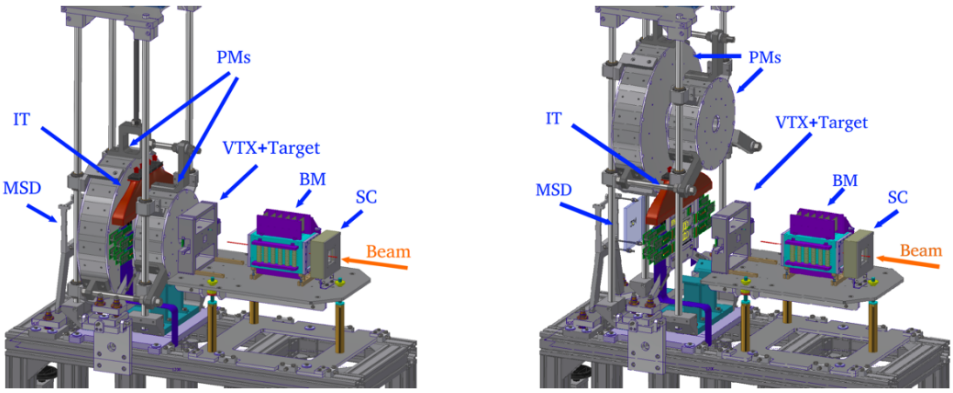

Figure 2.11: The FOOT mechanical structure adopted to contain all the upstream detectors and the magnetic spectrometers during the data taking (left) and during the detectors alignment configuration (right), with the magnets lifted up.

the magnets, managing the total weight of about 250 Kg and the repulsion force of about 2000 N present in the gap between the two magnets. In order to allow the installation and the alignment of the magnetic spectrometer detectors, the mechanical support provides the possibility to lift the magnets, as shown in Figure 2.11.

Inner Tracker detector

The ITR detector is composed of two layers of M28 detectors (the same used for the VTX) placed in the gap of the magnets and used as the second station of the magnetic spectrometer. Studies have shown that the effect of the magnetic field on M28 is negligible [58].

In order to achieve an active area of $8 \times 8\ cm^2$, the M28 sensors are arranged in ladders, as in the *PLUME* project [59]. An example is reported in Figure 2.12.

Each ITR plane is composed of two ladders supported by a mechanical frame as illustrated in Figure 2.13. Each ladder hosts eight M28 sensors, four on each side, glued on a 2 mm thick support structure made of low density silicon carbide (SiC) foam. On each ladder side, the four M28 sensors are glued and bonded on a kapton-metal flex cable that provides the communication with the readout systems. The dead area between two consecutive sensors on the same ladder side is 30 μm.

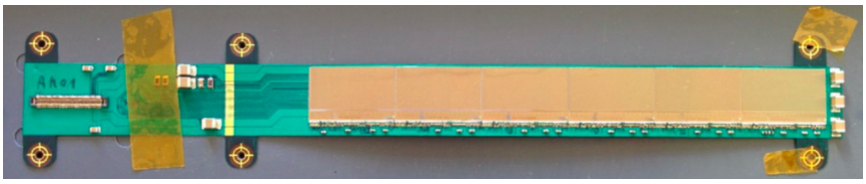

Figure 2.12: Picture of a PLUME ladder.

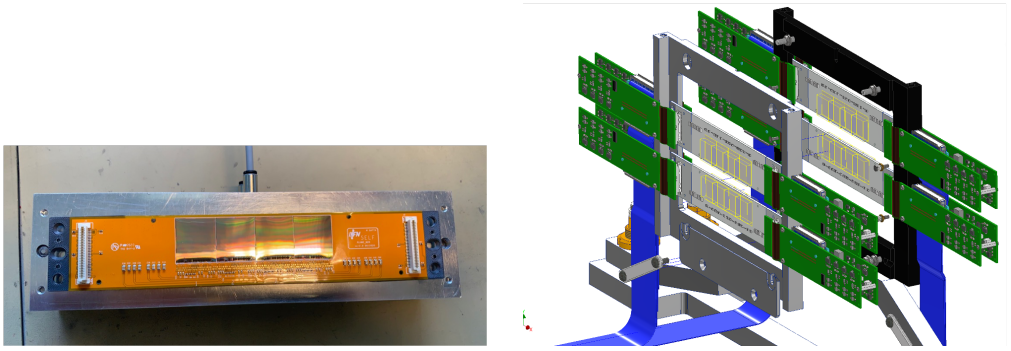

(a) (b)

Figure 2.13: Picture of one ladder (a), and a technical draw of the ITR detector along the beam line (b).

Micro Strip Detector

The MSD is the last station of the FOOT magnetic spectrometer. It is composed of three layers of silicon microstrip detectors placed beyond the two magnets about 35 cm from the target.

The MSD reconstructs the position of the fragments and their energy loss (ΔE) in the silicon. In the former case, in addition to the momentum measurement, the detector is fundamental to match the reconstructed tracks with the downstream scintillator and calorimeter hits. In the latter case, the redundant and independent measurement of ΔE is complementary to the one performed by the TW scintillator, which is necessary for the fragments charge identification. The three MSD layers are separated by a gap of about 2 cm. Each layer has an active area of 9.6×9.6 cm^2 and it is composed of two perpendicular single-sided silicon detector sensors glued on a hybrid *Printed Circuit Board* (PCB) that provides the mechanical support (Fig. 2.14). Each sensor has a thickness of 150 μm and the strip pitch is 50 μm. The expected spatial resolution is about 40 μm.

Tof-Wall scintillator

The TW detector is composed of two layers of plastic scintillator bars ($EJ-200$) that measure the fragments ΔE, position and "stop" the TOF measurement [60, 61]. The two layers are arranged along the vertical and the horizontal coordinate, both perpendicular with respect to the beam line. Each layer is composed of 20 parallel bars wrapped with a reflective aluminum and darkening black tape. The detector active area is 40×40 cm^2 that corresponds to an angular aperture of 10° at ~ 1 m from the target. Each bar has a dimension of $40 \times 2 \times 0.2$ cm^3, ensuring a fragments pile-up frequency smaller than 1%. The bar thickness has been chosen as a compromise between the requirements given by the ΔE resolution on one hand, and the necessity to reduce the secondary fragmentation probability on the other hand. The read out

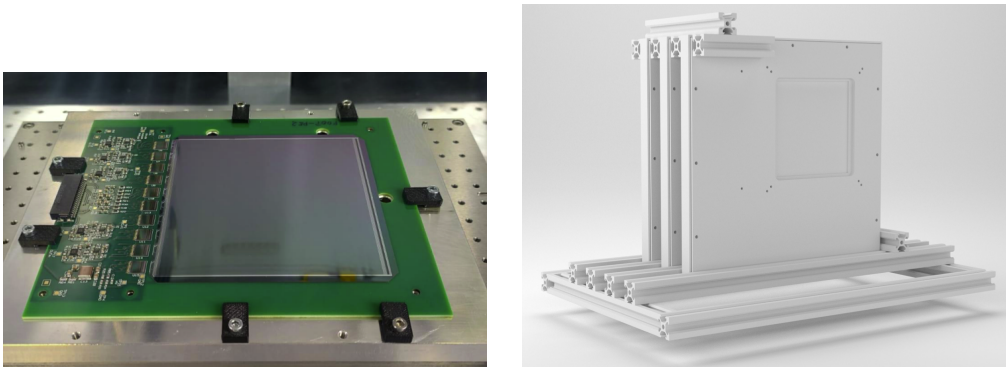

(a) (b)

Figure 2.14: Picture of the silicon strips with the PCB (a), and technical draw of the MSD (b).

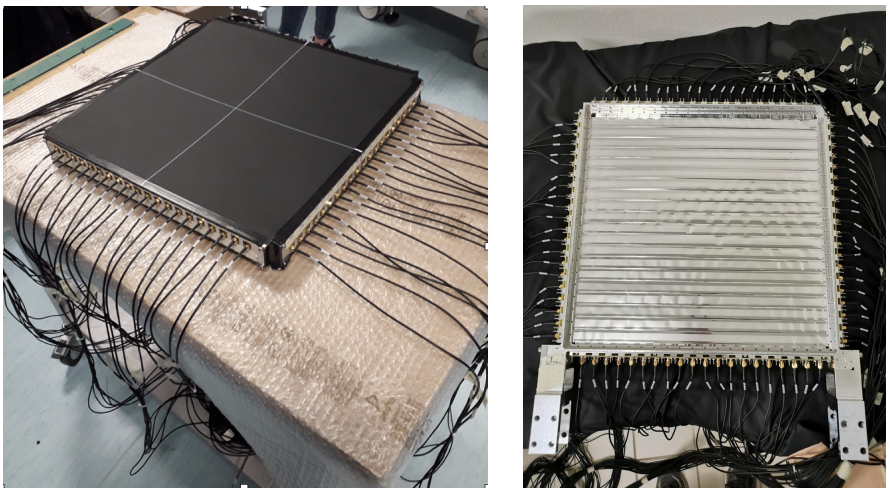

(a) (b)

Figure 2.15: Pictures of TW with (a) and without (b) the darkening black tape.

of each bar is performed by four SiPM placed at both extremities to allow the reconstruction of the hit position along the bar. Each SiPM has an active area of $3 \times 3\ mm^2$ and a microcell pitch of 25 μm, for a total of 57600 pixels coupled at each bar edge. The channels are digitized at $3 - 4\ GS/s$ by a *WaveDAQ* board [62].

The detector has already been tested with different primary beams. As reported in [63] the energy loss resolution $\sigma(\Delta E)/\Delta E$ is $6 - 14\%$ and $5 - 7\%$ and the time resolution is of $120 - 180\ ps$ and $30 - 40\ ps$ for different energies of proton and carbon ion beams, respectively. Finally, the precision on the time measurement allows a hit position reconstruction resolution along the bar with $\sigma_{pos} \leq 8\ mm$. Figure 2.15 shows the TW with and without the darkening black tape. In particular in Figure 2.15b the scintillation bars are visible.

Calorimeter

The last downstream detector in the FOOT electronic spectrometer is a calorimeter placed just beyond the TW, that stops the fragments and measures their kinetic energy [64, 65].

The calorimeter, whose design layout is shown in Figure 2.16, will be composed of 320 *Bismuth Germanate* (BGO) $Bi_4Ge_3O_{12}$ crystals [66], with a truncated pyramid

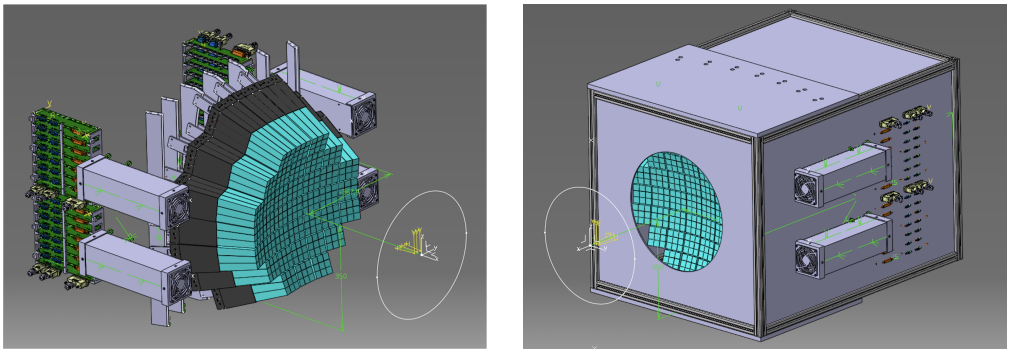

(a) (b)

Figure 2.16: Technical drawings of the calorimeter layout with (a) and without (b) the external cover. The BGO crystals (light blue) will be mounted in 3D-printed 3×3 modules, kept in the nominal position from the back by mechanical holders. On the sides, 4 fans will provide the air flow required to stabilize the temperature and 32 boards will distribute the high and low voltage supply to the front-end boards.

shape. The total dimensions of each crystal are: a front and rear side of $20 \times 20\ mm^2$ and $29 \times 29\ mm^2$, respectively, and a length of $240\ mm$. The BGO high density ($\rho = 7.13\ g/cm^3$) and high atomic number ($Z_{eff} = 74$) guarantee a high stopping power: in the energy range that FOOT will explore, charged fragments are fully contained in the crystal volume, except for the fraction that, through nuclear interactions, generates neutrons that can escape the detector. Crystals are grouped in matrices, the so called *Modules*, 3×3 elements that will be positioned with an approximately circular arrangement (about 22 cm radius). The signal of each crystal is collected by a matrix (*Tile*) of 25 SiPMs with a $22 \times 23\ mm^2$ surface and a $15\ \mu m$ microcell pitch that provides an almost linear response in the energy range up to $\sim 10\ GeV$. Each SiPM Tile signal is readout by a front-end board which sums the light collected by each SiPM and is designed so as to match the Tile size and maximise the compactness. Moreover, the board reads out also the SiPM temperature. Finally, the crystal signals are digitised and sampled at $1 - 2.5\ GS/s$ by the WaveDAQ [62]. Each crystal will be wrapped with a Tyvek reflective foil in order to maximise the light collection.

The performance tests have shown that the energy resolutions in the energy range foreseen by the FOOT experiment are below 2% and 1% for proton and carbon beams, respectively. All the tests performed to make the design decisions for the calorimeter are discussed in depth in Chapter 3.

Data Acquisition System

A dedicated DAQ system has been developed to handle the data stream derived from all the FOOT detectors. The DAQ scheme is shown in Figure 2.17. It is based on the simultaneous use of different computers and specific detector read out systems that communicate through optical fibers and ethernet cables. The DAQ is the controlled by a *Graphical User Interface* (GUI) to start/stop the data acquisition, configure all the DAQ components. During the acquisition phase, different computers perform online monitoring, showing histograms about the general acquisition process and the detectors status (e.g.: detector occupancy, particle energy loss etc.) with a rate of the order of seconds. A storage PC is used during the data taking to collect all the detectors data on a SSD disk at a maximum rate of 400 MB/s. The data

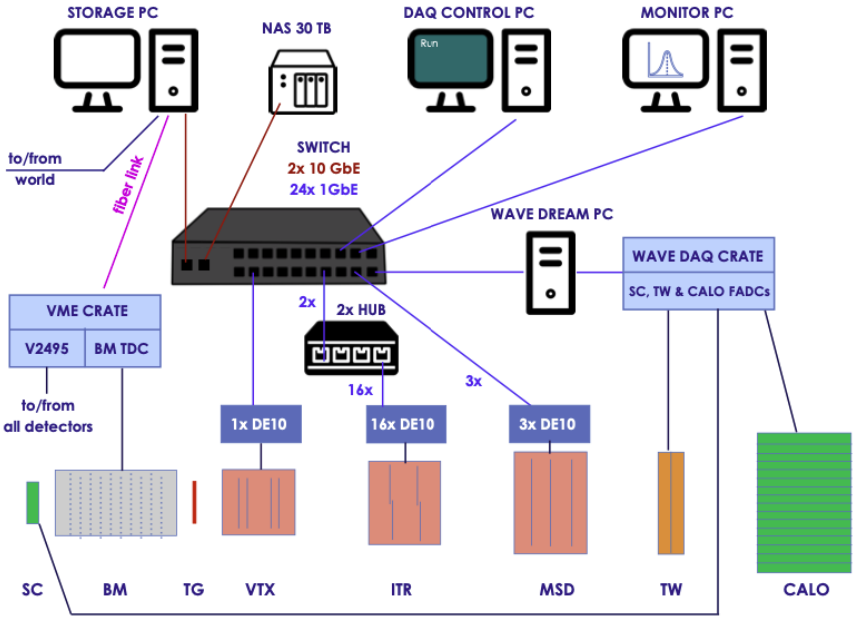

Figure 2.17: The electronic setup DAQ scheme of FOOT.

are then sent to a dedicated *Network Attached Storage* (NAS) system for permanent storage.

The data size is expected to be of the order of 30 kB per event with the main contributions coming from the SC, TW and CAL waveforms ($\geq$ 80%). However, the DAQ can handle a maximum data size of the order of 100 kB per event. The FOOT maximum acquisition rate is set by the slowest detector of the setup represented by the VTX and ITR. The M28 chip has a read out time of 185.6 μs that sets an upper limit on the rate of about 5 kHz. However, in order to reduce the pile-up effects in the M28 chip, the actual acquisition rate must be of the order of 1 kHz.

To process and digitize the data SC, TW and CAL use the WaveDAQ boards, BM uses a TDC VME module and the three tracker stations (VTX, ITR, and MSD) use 1, 16 and 3 *Terasic DE10* boards, respectively.

Trigger

The FOOT experiment foresees two different triggers: a *minimum bias* and a *fragmentation trigger*. The former is adopted to collect unbiased data, avoiding possible sources of systematic uncertainty given by the trigger selection. In particular, it is a majority trigger fired when a minimum number of SC channels signals exceeds a given threshold. However, the expected rate of nuclear inelastic interactions in the target is of the order of 1% and the acquisition rate is of the order of 1 kHz. Thus, the amount of time necessary to acquire a significant sample of fragmentation data ($\sim 10^5$) would be of about $\sim$ 3 hours. Considering that the time availability in the accelerator facilities is limited, a trigger for the fragmentation events is required to increase the amount of interesting data reducing the collection of events without any nuclear inelastic interaction. For this purpose also a fragmentation trigger is foreseen in the experiment. In particular the FOOT electronic spectrometer exploits the TW since it is a scintillator with a fast time response placed in the downstream region after the target. The TW bars placed outside the incident beam direction are discriminated with a low threshold value. In order to fire the trigger, at least two hits of these bars on one or the other view are requested together with the minimum

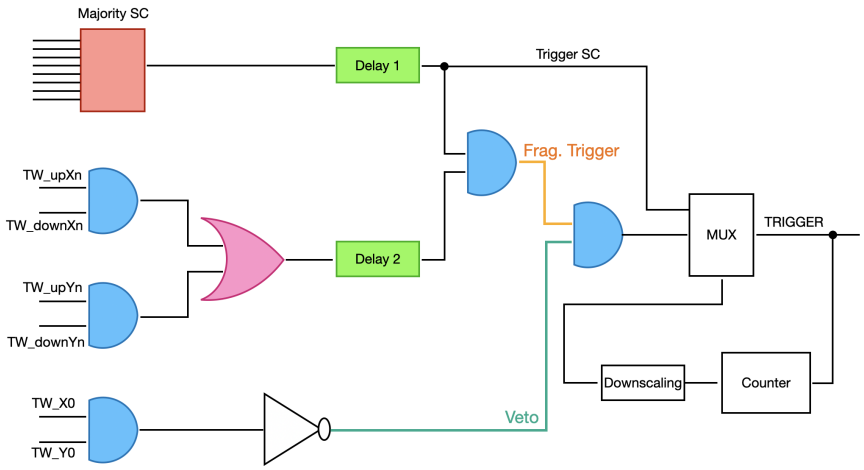

Figure 2.18: The FOOT fragmentation trigger scheme.

bias trigger signal derived from the SC. A veto is set by the AND of the two TW central bars that are hit when no secondary particles are produced. The scheme of the fragmentation trigger adopted during a test performed at GSI is shown in Figure 2.18.

2.3.2 Emulsion Cloud Chamber

To measure the production of light fragments ($Z \leq 3$), an emulsion spectrometer has been included in the FOOT setup.

Among all tracking devices used in particle physics, nuclear emulsion detectors achieve the highest spatial resolution (sub-micrometric) for tracking ionizing particles. Emulsions have a long history and contributed to outstanding achievements and discoveries in particle physics. After a decline with the advent of fast electronic detectors in the sixties, this technique has experienced a vigorous rebirth in the last twenty years thanks to the advances in high-speed automated scanning and the industrial production and handling of emulsions. Nowadays, they are still unsurpassed for the detection of short-lived particles and for specific applications in neutrino physics and other emerging fields [67]. Emulsion chambers integrate target and detector in a very compact setup and provide a very accurate reconstruction of the interactions occurring inside the target. Moreover, no power supply or readout electronics is required and this helps keeping the emulsion setup compact and without angular limitations. The use of emulsions is coupled to the achievements in the automated scanning system technique [68]. Last generation microscopes [69] allow very fast scanning with wide angular acceptances (more than 70°) and real time analysis of huge data sets, about one order of magnitude faster than those used for the *Oscillation Project with Emulsion-tRacking Apparatus* (OPERA) experiment [70].

Emulsion detectors were adopted also in the framework of the *Fragmentation of Ions Relevant for Space and Therapy* (FIRST) experiment [47] to study fragments produced at large angles by 400 MeV/u ^{12}C ions impinging on a composite target. The kinematical properties of protons emitted with angles up to 80° with respect to incident beam axis were investigated with this methodology.

Based on the ECC concept [67], the emulsion spectrometer for the FOOT experiment is designed with passive materials alternated to nuclear emulsions films acting as both high-resolution tracking devices and ionization detectors. The ECC is composed of three sections as shown in Figure 2.19:

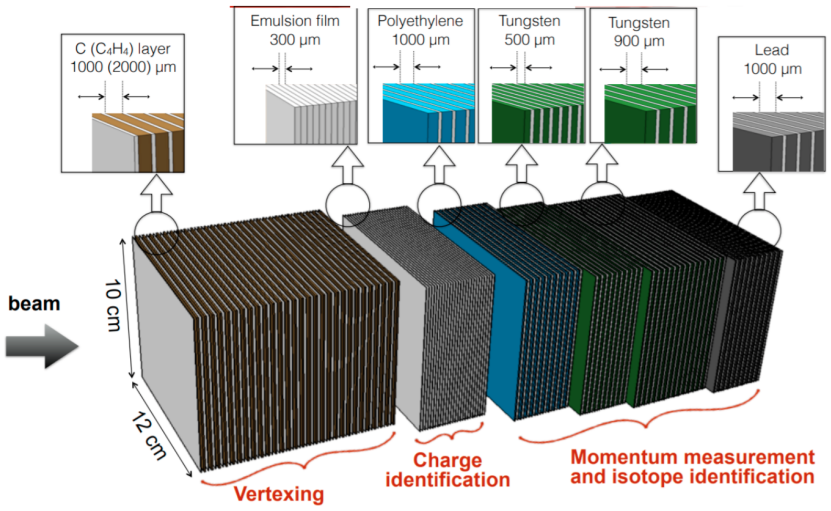

Figure 2.19: Schematic view of the emulsion spectrometer.

- *Target and vertexing section*: the first section is composed of emulsion films alternated with layers of C or C_2H_4 target material with a thickness of 1 or 2 mm, respectively. In this part, the emulsion films operate mainly as vertex detector to reconstruct all the charged fragments tracks. In order to reach a statistically significant number of interaction events, the overall length of this section is defined by the target material and the incident particle charge and energy.
- *Charge identification section*: the central section is completely composed of emulsion films, aiming to measure the fragments charge with the refreshing procedure.
- *Momentum measurement and isotope identification section*: the last section is composed of emulsion films interleaved with absorber layers made of passive high-Z material. The particle momentum and mass can be evaluated by measuring the length of the entire track and the angles between the base-tracks caused by the MCS effect.

The nuclear emulsion films used for FOOT consist of two 70 μm thick sensitive layers deposited on both sides of a 180 μm plastic base, resulting in a total thickness of 320 μm. The sensitive regions are made of $AgBr$ crystals grains of 0.2 μm diameter scattered in a gelatine binder, able to detect *Minimum Ionizing Particles* (MIP). The trajectory of a MIP is recorded by all $AgBr$ crystals along its path, which act as latent image centers. A chemical process, known as *development*, enhances the latent images inducing the growth of silver clusters (*grains*) with a diameter of 0.6 μm, which can be identified with an optical microscope. The grains density is proportional to the ionizations caused by the passage of the charged particle within the dynamical range. After the development, the emulsion is scanned by an automated system. The acquired image is then analyzed by a dedicated software to recognize clusters of aligned dark pixels, which represent the track produced by the penetrating particle. A straight sequence of pixels in one emulsion layer defines a *micro-track*. Two aligned micro-tracks belonging to the top and bottom layers of an emulsion film form a *base-track*, as shown in Figure 2.20a. Base-tracks belonging to a straight line along different films, are connected to form volume-tracks. Through the propagation of track segments from an emulsion layer to the next, the particle track is reconstructed and the segments fitted.

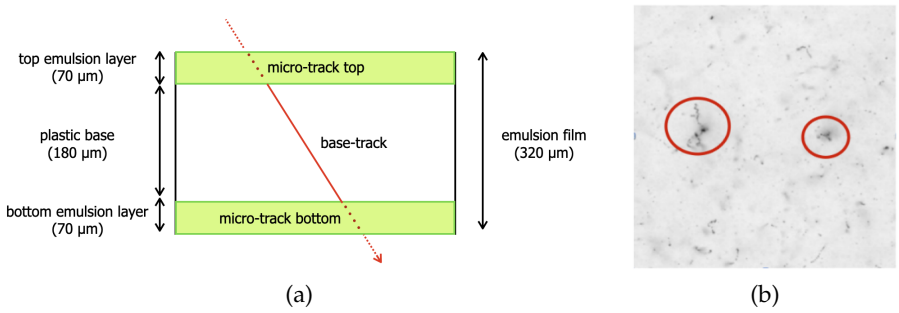

(a) (b)

Figure 2.20: Schematic view of a nuclear emulsion film (a); Picture of the tracks generated by carbons impinging perpendicularly on the emulsion layer. The view size is $300 \times 300\ \mu m$ (b) [71].

2.4 Experimental requirements

In order to fulfill the FOOT experiment goals discussed in Section 2.2.2, different methods are adopted to reconstruct the fragments charge and mass. For heavy fragments ($Z \geq 3$) detected by the electronic spectrometer, the particle energy loss (ΔE), kinetic energy (E_{kin}), velocity (β) and momentum (p) measurements are combined in different ways to identify the charge and mass, perform the inverse kinematic approach and evaluate the double differential cross section.

In order to fulfill the requested mass and charge resolution, the fragments ΔE, E_{kin}, TOF, and p have to be measured with resolutions better than: 5%, 2%, 100 ps, 5%, respectively. The detectors have already been tested and the required performances have been evaluated with the following results:

- *Energy Loss*: ΔE is measured by the MSD and the TW detectors. This measurement is fundamental for the charge identification and the preliminary detector performances show a resolution of the order of $\sigma_{\Delta E}/\Delta E \sim 3 - 10\%$. In particular, the energy resolution of the TW detector can be modelled as:

$$\sigma(\Delta E) \sim a + \frac{b}{\Delta E} \tag{2.10}$$

  where $a = 0.904\ MeV$ and $b = 18.6\ MeV$. Figure 2.21a shows the energy loss resolution of data acquired at CNAO and GSI.

- Kinetic energy: E_{kin} is given by the sum of the energy depositions of the particle in the magnetic spectrometer detectors and in the calorimeter. The latter gives the main contribution to the measurement, setting also the resolution that for an electromagnetic calorimeter can be evaluated as:

$$\frac{\sigma_{E_{kin}}}{E_{kin}} = \frac{a}{\sqrt{E_{kin}}} \oplus \frac{b}{E_{kin}} \oplus c \tag{2.11}$$

  where the first term indicates the stochastic contribution related to the fluctuations in the sampling of the electromagnetic shower development, the second is related to the electronic noise of the readout circuit and the third is the constant contribution related to calibration uncertainties. The tests have shown a resolution below 2% for proton, carbon and oxygen ions in the $70 - 400\ MeV/u$ energy range. A detailed discussion of the calorimeter performance study follows in Section 4.4.

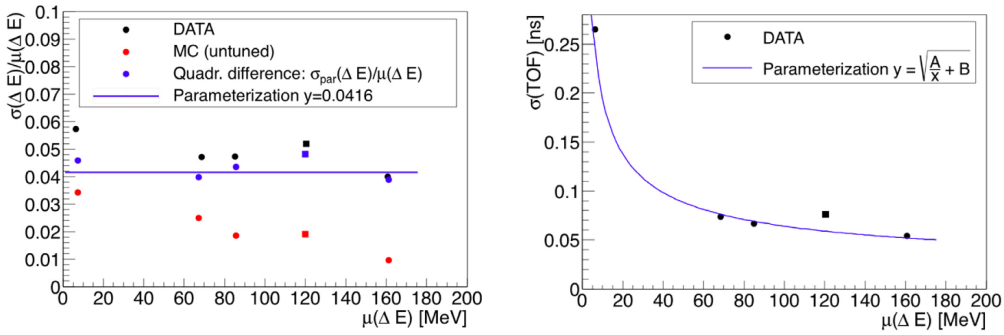

(a) (b)

Figure 2.21: Energy loss resolution results extracted from data in black (a). TOF resolution results (b). The circle and square markers refer to the CNAO and GSI setup, respectively. For both plots is also represented in blue the parameterization used to produce the tuned MC simulations [72].

- *Velocity*: β is evaluated from the particle path length and TOF measurements with the following formula:

$$\beta = \frac{L}{c \cdot \text{TOF}} \tag{2.12}$$

where L is the fragment path length from the production position to the TW detector, that combined together with the SC initial timestamp, provides the TOF measurement. The particle total travelled distance L is given by the global reconstruction algorithm, that includes the bending due to the magnetic field and provides resolution of the order of a few millimeters, considering also the detector positioning uncertainty.

Regarding the TOF resolution, it is evaluated as $\sigma_{\text{TOF}} = \sqrt{\sigma_{\text{SC}}^2 + \sigma_{\text{TW}}^2}$. Different tests have been conducted with the SC and TW detectors at CNAO and GSI facilities with $115 - 400$ MeV/u carbon and 400 MeV/u oxygen ions. The results are shown in Figure 2.21b: for carbon and oxygen ions in the CPT energy range, the overall TOF resolution is of the order of 70 ps. The resolution on the particle velocity is mainly given by the TOF contribution $\sigma_\beta \sim \frac{L}{c \cdot \text{TOF}^2} \cdot \sigma_{\text{TOF}}$ and it is of the order of ~ 0.006.

- *Momentum*: p is evaluated by means of the FOOT magnetic spectrometer. Each detector provides different hits that are elaborated by a global reconstruction algorithm based on a Kalman filter. In the FOOT software, two different Kalman filter codes have been developed and, at the moment, both the algorithms are in a optimization stage. The preliminary results show that the required momentum resolution is of $\sigma_p/p \sim 5\%$ and it is achievable.

2.4.1 Charge and Mass identification

In order to study with limited systematics the produced fragments, the FOOT experiment has been designed with a chain of detectors that can measure fundamental quantities necessary for the evaluation of the cross-sections in multiple ways. Therefore, FOOT will perform redundant measures of the charge and the mass of the fragments. The preliminary results obtained from the tests are shown below, followed by the presentation of the techniques involved for the fragments charge and mass identification.

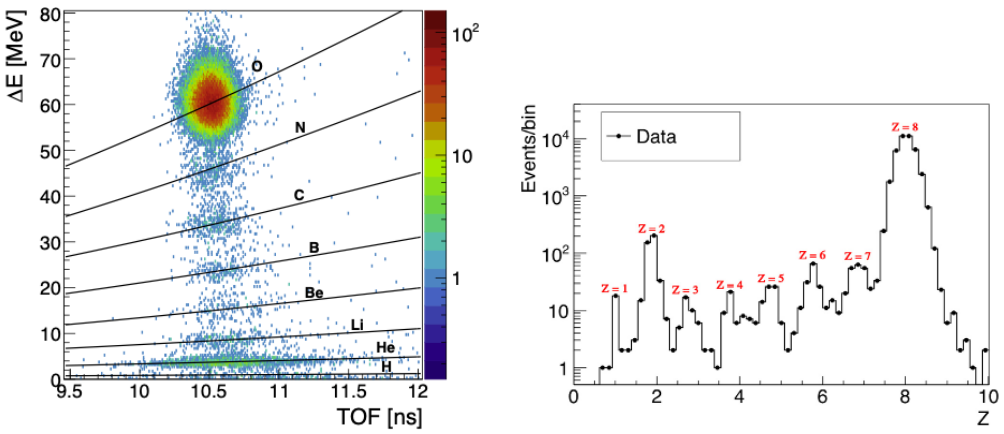

(a) (b)

Figure 2.22: Results of the charge identification performed on the fragments detected by the TW using the energy release ΔE and the TOF measurements. The data has been collected at GSI with an incident oxygen ion beam at 400 MeV/u [72].

Charge identification

The charge of the fragments is measured with two different methods. The first involves the MSD or the TW detectors and consists in the estimate of the Bethe-Bloch energy loss formula shown in Eq. 1.2 and simplified as:

$$\frac{dE}{dx} \sim z^2 \cdot f(\beta) \tag{2.13}$$

where dE/dx is the energy loss, z is the particle charge and $f(\beta)$ is a function of the particle velocity (β), which is expected to be similar to that of the primary particle. In particular, both the detectors measure the particle energy release ΔE, while the path length Δx is considered roughly equal to the detector thickness. The $\Delta E/\Delta x$ ratio is an estimation of the energy loss that combined with the β measurement provides a charge identification. An example is shown in the left panel of Figure 2.22.

The second method is based on the VTX and ITR detectors. When a charged particle crosses a layer of the silicon pixel detector, it fires several adjacent pixels that can be grouped into a *cluster*. The number of fired pixels defines the cluster size and depends on the particle energy loss and, consequently, on the incident particle charge. Considering the results obtained from the data taking conducted in the framework of the FIRST experiment [47] on the $M18$ and $M26$ sensors, which are the previous version of the FOOT VTX $M28$ sensors, an empirical model has been developed to describe the cluster size as a function of the energy loss:

$$n_p = 2\pi r_s \log\left(\frac{\Delta E}{2\pi E_g T_s}\right) \tag{2.14}$$

where n_p is the mean number of pixels, ΔE is the energy loss, E_g is the mean energy for the creation of charge carriers (e.g.: $E_g = 3.6\ eV$ for silicon material), r_s and T_s are two free parameters. Combining Eq. 2.13 and Eq. 2.14, it is possible to extrapolate the particle charge from the cluster size and the TOF measurements. Since the cluster size is related to the energy loss logarithmically, with this method the charge identification capability decreases for the high-energy loss and high charge particles, as shown in the right panel of Figure 2.23.

The best charge identification performances are obtained with the TW detector.

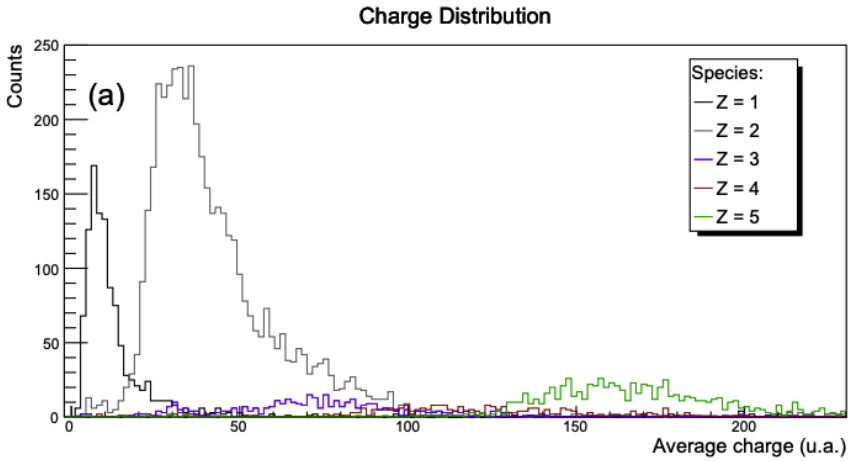

Figure 2.23: Charge distributions of the $M18$ sensors produced by the fragments originated from carbon ion beams at energies between 400 MeV/u and 1000 MeV/u impinging on different materials [73].

Given the ΔE resolution of the order of $3-10\%$. However, the VTX cluster size method can be adopted to cross-check the TW results and it can be employed in the VTX track reconstruction algorithm.

Mass identification

The particle isotopic identification is a more challenging task compared to charge measurement. For this reason, the particle mass is evaluated combining the TOF, momentum and kinetic energy information in three different ways:

1. **TOF and momentum**:

   The mass is derived from:

   $$p = m\gamma\beta = \frac{m\beta}{\sqrt{1-\beta^2}} \rightarrow m = \frac{p\sqrt{1-\beta^2}}{\beta} \tag{2.15}$$

   thus:

   $$A_1 = \frac{m}{u} = \frac{1}{u}\frac{p\sqrt{1-\beta^2}}{\beta} \tag{2.16}$$

   where $u = 931.494\ MeV/c^2$ is the atomic mass unit, p is the particle momentum, γ is the Lorentz factor and β is the particle velocity.

2. **TOF and kinetic energy**:

   The mass is derived from:

   $$p^2 = E_{tot}^2 - m^2 \rightarrow m^2\gamma^2\beta^2 = (E_{kin}^2) - m^2 \tag{2.17}$$

   thus:

   $$A_2 = \frac{m}{u} = \frac{E_{kin}}{u}\frac{1+\sqrt{1+\gamma^2\beta^2}}{\gamma^2\beta^2} \tag{2.18}$$

   where E_{kin} is the kinetic energy.

3. **Momentum and kinetic energy**:

The mass is derived from:

$$E_{tot}^2 = p^2 + m^2 \rightarrow (E_{kin}^2) + m^2) = p^2 + m^2 \tag{2.19}$$

thus:

$$A_3 = \frac{m}{u} = \frac{E_{kin}^2 - p^2}{2E_{kin}} \tag{2.20}$$

Since the calorimeter precision suffers because of neutron production, the best mass identification evaluation is obtained with the combination of TOF and momentum measurements.

However, all the three methods are adopted to reduce the systematic uncertainty and to achieve the best possible results. The redundancy of the mass determination techniques is an important key factor in the FOOT experiment to reach its goal. Indeed, two methods are employed to combine the different mass estimates:

- **Standard χ^2 minimization algorithm**: this method is based on the minimization of the following function:

$$\chi^2 = f(\vec{x}) + \mathbf{A^T}(\mathbf{CC^T})^{-1}\mathbf{A} \tag{2.21}$$

where $f(\vec{x})$:

$$f(\vec{x}) = \frac{(TOF - \overline{TOF})^2}{\sigma_{TOF}^2} + \frac{(p - \overline{p})^2}{\sigma_p^2} + \frac{(E_{kin} - \overline{E_{kin}})^2}{\sigma_{E_{kin}}^2} \tag{2.22}$$

where TOF, p and E_{kin} are the reconstructed values; where σ_{TOF}, σ_p and $\sigma_{E_{kin}}$ are the respective uncertainty; where $\mathbf{A} = (A_1 - \overline{A}, A_2 - \overline{A}, A_3 - \overline{A})$ is the mass estimate vector with A_1, A_2 and A_3 as the mass estimated values and $\overline{A}$ as the output mass from the fit and where the matrix $\mathbf{C}$ is the correlation matrix:

$$\begin{pmatrix} \frac{\partial A_1}{\partial TOF} \cdot \sigma_{TOF} & \frac{\partial A_1}{\partial p} \cdot \sigma_p & 0 \\ \frac{\partial A_2}{\partial TOF} \cdot \sigma_{TOF} & 0 & \frac{\partial A_2}{\partial E_{kin}} \cdot \sigma_{E_{kin}} \\ 0 & \frac{\partial A_3}{\partial p} \cdot \sigma_p & \frac{\partial A_3}{\partial E_{kin}} \cdot \sigma_{E_{kin}} \end{pmatrix} \tag{2.23}$$

- **Augmented Lagrangian Method (ALM)** [47, 74]: this method, based on a iterative procedure of minimization of the Lagrangian function $\mathcal{L}$, performs a constrained minimization in a large parameter space:

$$\mathcal{L}(\vec{x}, \lambda, \mu) = f(\vec{x}) + \sum_{i=1}^{3} \lambda_i c_i(\vec{x}) + \frac{1}{2\mu} \sum_{i=1}^{3} c_i^2(\vec{x}) \tag{2.24}$$

where $f(\vec{x})$ is the function to minimize shown in Eq. 2.22, $c_i(\vec{x}) = (A_i - A)$ are the constraints, A_i are the mass values estimated with the previous methods, A is the mass output parameter from the fit, λ_i are the Lagrange multipliers and μ is a positive penalty parameter that, multiplied by $c_i^2(\vec{x})$, constitutes the augmentation factor. More information about this method can be found in [75].

The results obtained with both methods are similar. As shown in Figure 2.24, considering the expected values of $TOF \sim 70\ ps$, $\sigma_p/p \sim 3.7\%$ and $\sigma_{E_{kin}}/E_{kin} \sim 1.5\%$, the ^{11}C, ^{12}C and ^{13}C peaks are visible and the mass identification can be performed.

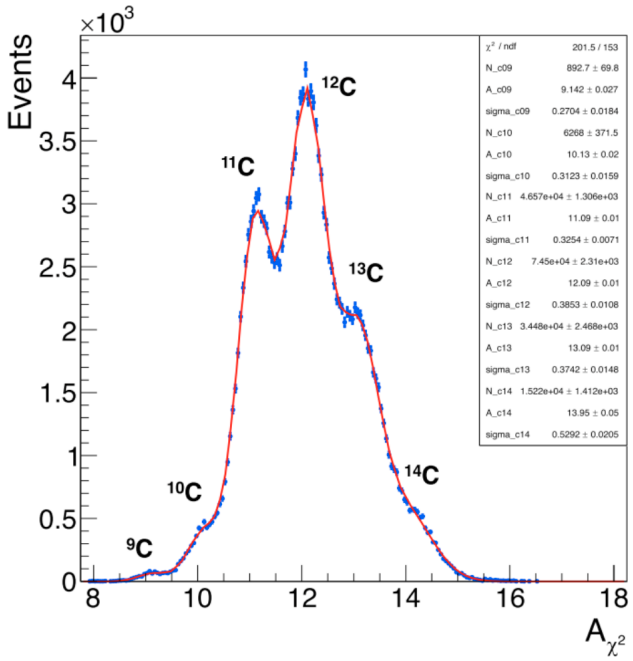

Figure 2.24: Example of mass identification performed with the χ^2 method on MC simulated data. The resolution of the measurements has been set to their expected values: $TOF \sim 70\ ps$, $\sigma_p/p \sim 3.7\%$ and $\sigma_{E_{kin}}/E_{kin} \sim 1.5\%$.

2.5 Simulation and Reconstruction

In order to perform the preliminary studies on the FOOT electronic spectrometer, the FLUKA MC simulation tool has been adopted to generate simulated data. In addition, a custom software has been developed to read and elaborate both real and simulated data. The FOOT analysis software performs the reconstruction of the detector measurements (i.e.: time stamps, energy loss, detector hits and tracks etc.) and the subsequent analysis (i.e.: charge and mass identification, cross section measurement etc.). A brief introduction to the FLUKA simulation tool adopted for the MC data production is presented in this section, followed by the illustration of the FOOT reconstruction software.

2.5.1 Simulation: the FLUKA Monte Carlo code

FLUKA [43, 44] is a MC simulation tool widely employed in different physics branches for the calculations of particle transport and interactions with matter. One of the field in which FLUKA is particularly suitable is CPT since several specific simulation features have been developed for the clinical research. The code is continuously updated with the latest modern physics models, adopting microscopic models whenever possible and checking the latest experimental data as benchmark for the simulation output.

The main models implemented in FLUKA for the description of the principal physics phenomena in hadron-nucloen, hadron-nucleus and nucleus-nuclesus interection are listed below. In addition the presentation of the simulation output scheme specifically developed in the framework of the FOOT experiment is also shown.

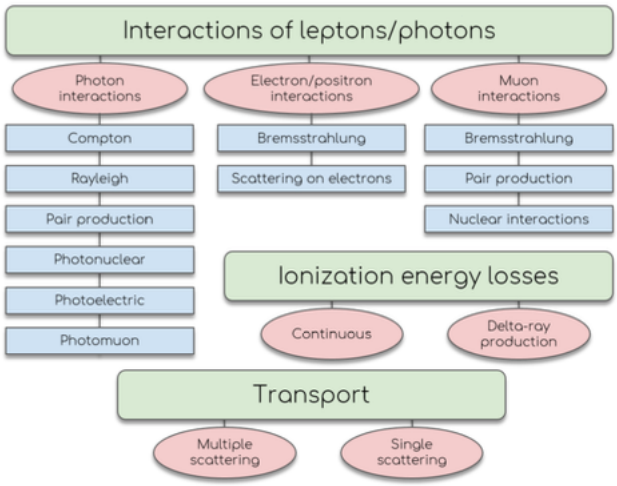

Figure 2.25: Scheme of the electromagnetic interactions models developed in FLUKA [76].

Transport of charged particles

FLUKA can simulate all the interactions summarized in the schematic view of Figure 2.25. Charged particles are propagated into materials by means of an algorithm based on the Moliere theory, that handles some demanding tasks such as the electron back-scattering effect and the energy deposition in thin layers, even in the few keV energy range.

The energy loss mechanism is simulated according to the Bethe-Bloch theory described in Section 1.2.1, considering also the Barkas, Bloch and Ziegler corrections. Optional δ-ray production and transport can be activated taking into account also ionisation fluctuations.

The lepton-photon interactions, listed in Figure 2.25, are simulated in a wide energy range of about 12 energy orders of magnitude, ranging from 1 keV up to 1 PeV. However, for the FOOT experiment purposes, the most interesting processes are nuclear reactions.

Hadron-nucleon interactions

Hadron-nucleon interactions are described by the resonance production and decays for energies below 5 GeV and by a model based on the *Dual Parton Model* (DPM), a phenomenological model of particle production in hadronic and nuclear collisions for energies from 5 GeV up to tens of TeV. The DPM is based on the large-N expansion of non-perturbative *Quantum ChromoDynamics* (QCD)[4] and the Reggeon field theory [77], allowing to describe also the soft collision process for which the QCD perturbation theory cannot be applied.

Hadron-nucleus interactions

The hadron-nucleus interaction initial stage is simulated in FLUKA with two models:

- *PreEquilibrium Approach to NUclear Thermalization* (PEANUT) for particles with momenta below 5 GeV/c. It is based on a detailed *Generalized Intra-Nuclear Cascade* (GINC) model for the initial hadron-nucleus non-elastic interaction

[4] In theoretical physics, the QCD is the theory of the strong interaction between quarks and gluons.

stage. Then, after the emission or absorption of heavy particles, the subsequent pre-equilibrium stage model is adopted to describe the de-excitation of the hot nuclear components, by emission of nucleons and light nuclei ($A < 5$) until thermal equilibrium is reached.

- *Glauber-Gribov cascade*, a field theory formulation of the Glauber model [78] for particles with momentum higher than 5 GeV/c. In this model inelastic interactions are modelled as multiple interactions of the projectile with the target nucleons with the interaction rate obtained from free hadron-nucleon cross sections. As for the PEANUT model, also in this case a subsequent de-excitation phase is described by nuclear evaporation, fission, Fermi break-up and γ de-excitation process, depending on the energy and the target-nucleus mass.

For the FOOT experiment, the PEANUT model is the most relevant since the energy of the particles involved in the measurements is below 5 GeV/c.

Nucleus-nucleus interactions

Depending on the energy, two different models are used in FLUKA to describe nucleus-nucleus interactions:

- For energy below 5 GeV/u, FLUKA adopts a Boltzmann-Master Equation model and *Relativistic Quantum Molecular Dynamics* (rQMD) model respectively [79, 80].
- at higher energies ($\geq$ 5 GeV/u), a DPM and JETs (DPMJET-II or DPMJET-III) model, based on the DPM in connection with the Glauber formalism and it is generally used for the cosmic ray studies, simulates nucleus-nucleus interactions.

2.5.2 FLUKA output for FOOT

For the FOOT electronic spectrometer, a dedicated simulation output of the FLUKA code has been developed by the FOOT team, modifying the FLUKA standard output by means of *user routines* libraries. The customized output includes an event per event data structure necessary to make the reconstruction of each event possible, with all the detectors information particle by particle and event by event. In particular, the custom output is an *American Standard Code for Information Interchange* (ASCII) file that contains all the simulated data and, by means of a specifically developed program, it is converted into a *ROOT*[5] file organized in blocks as follows:

- **Particle block**: it stores the information related to all the particles produced during the simulation: particle mass, charge, barionic number, position and momentum at production and at death, pointer to the parent particle, etc.
- **Detector block**: it stores each FOOT detector output, collecting all the hits information relevant for a given device. For each hit, the energy release, the position and momentum values and all the other quantities of interest for the specific detector are saved. For example, when a particle enters and releases energy in a CAL crystal, in the CAL block a hit is registered with the information about the crystal coordinates, the crystal number, the particle entrance and exit position and momentum, the energy deposition and an index that points to the particle block.

[5]ROOT is a data analysis framework written in C++ developed by CERN.

- **Crossing block**: each time a particle crosses a region defined in the FLUKA geometry, the information about the crossing position, the particle momentum and a pointer to the particle block is saved.

In order to perform MC studies, the FOOT data analysis software is developed to produce the input files adopted by FLUKA to generate the simulated data-set, considering all the geometry parameters of the FOOT detectors. After the event by event simulation, the FLUKA output contains all the detectors simulated hits and measurements and it is used as input to the analysis software to perform the MC study. In this way, all the geometry parameters and the projectile properties for the simulation and the analysis software are consistent.

2.5.3 Data reconstruction code: SHOE

The reconstruction and analysis software developed in the framework of the FOOT experiment is called *Software for Hadrontherapy Optimization Experiment* (SHOE). It has been developed to read both simulated and real data of all the detectors performing firstly a local and then a global reconstruction procedure. In the former case, the simulated hits or the raw measurements are elaborated to reconstruct the physics quantities relevant for each detector. Then, a global reconstruction algorithm processes all the information from the detectors to reconstruct the whole event and extract the fragment tracks and their properties, including charge and mass identification.

In the local reconstruction stage each sub detector has different tasks:

- **SC** and **TW**: on the real data, the waveforms are processed with a virtual constant fraction discriminator algorithm to retrieve the time measurements. In addition, the TW also measures the energy release of each hit by applying a signal amplitude analysis. In case of MC studies, FLUKA directly provides a simulated time stamp and the energy release of each particle in each detector.

- **BM**: on the real data, it combines the time measurements with a given space-time relation to extract the distance measurements. With MC simulations, the distances are directly extracted from the input file. Then, the software performs a track reconstruction procedure to extract the projectile track parameters from the BM hits.

- **VTX**, **IT** and **MSD**: each detector performs a local track reconstruction with the hits positions read from the real data or the MC file. In addition, the energy releases are directly measured by the MSD detector and evaluated by means of the cluster sizes from the pixel detectors.

- **CAL**: in case of real data, the signals from each crystal are read and processed extrapolating an amplitude, charge and shape analysis to retrieve the energy deposition measurements. Otherwise, FLUKA directly provides the information of energy deposition. In both cases, a clustering algorithm is performed to take into account the particles that cross more than one crystal.

In order to take into account the resolution, efficiency, pile-up and the other specific effects of each detector that cannot be directly simulated by FLUKA, SHOE reproduces the detector resolutions, it eliminates the simulated hits according to the efficiencies and it adds the pile-up and the noise hits in order to make the simulation as similar as possible to a real scenario. After the local reconstruction, in the global

reconstruction stage all the information from the detectors is combined to finalize the analysis. At this level, there are no differences in the elaboration of MC or real data.

The following main tasks are completed:

- **Global track reconstruction**: all the tracks and hits reconstructed by the detectors placed beyond the target are collected and processed to reconstruct the particle tracks. To this purpose, two different algorithms based on Kalman filters have been developed. The first one exploits the *GENFIT* code [81], an open source and experiment-independent set of libraries developed for track fitting in nuclear and particle physics. The second algorithm, called *Tracking Of Ejectile* (TOE) is a Kalman filter specifically developed in the framework of the FOOT experiment. It is a lightweight package and it adopts a simplified approach with respect to GENFIT.

  After the track fitting, the particle momentum is provided by the Kalman filter reconstruction algorithm and the TOF, energy release and kinetic energy measurements can be associated to the reconstructed particle.

- **Charge and mass identification**: by combining the particle energy loss, kinetic energy, TOF and momentum measurements, the fragment charge and mass identification can be performed with the aforementioned methods (2.4.1).

- **Cross section analysis**: in the final stage, all the information about the particles measurements and the detectors efficiencies is employed to determine the differential cross section measurements.

At the moment, the local reconstruction code is completed for almost all the detectors. Indeed, it has been successfully adopted during the FOOT electronic spectrometer test beams performed at GSI in 2019 and 2021. The global reconstruction is still in a development and optimization phase: all the particle identification and cross section measurement algorithms have been developed with different independent codes that have to be imported in SHOE. After this task, SHOE will be able to process and analyze all the data that the FOOT experiment will collect.

Chapter 3

Calorimeters in particle physics and in the FOOT experiment

3.1 Introduction

In particle physics a calorimeter is a detector that responds in a proportional way to the energy of the particles that cross through it. Hence, the main goal of a calorimeter is to measure the particles kinetic energy, in particular of electrons, photons and hadrons. Usually, measuring the particle kinetic energy through a calorimeter is a destructive method since particles are often completely absorbed by this detector.

In this chapter, an overview about the calorimeter detectors used in particle physics will be presented in Section 3.2. The FOOT calorimeter is presented in Section 3.3.

3.2 Calorimeters in particle physics

Today, calorimeters are widely used both in high and low energy physics experiments thanks to several advantage:

- The energy resolution improves with the particle kinetic energy ($\sigma_E \propto \sqrt{E}$), as shown in Eq. 2.11.
- Calorimeters are sensitive to all types of particles, charged and neutral (e.g. neutrons). They can even provide indirect detection of neutrinos and their energy through a measurement of the event missing energy.
- They are versatile detectors. Although originally conceived as devices for energy measurement, they can be used to determine the shower position and direction, to identify different particles (for instance to distinguish electrons and photons from pions and muons on the basis of their different interactions with the detector), and to measure the arrival time of the particle. Calorimeters are also commonly used for trigger purposes, since they can provide fast signals that are easy to process and to interpret.
- They are space and therefore cost effective. Because the shower length increases only logarithmically with energy, the detector thickness needs to increase only logarithmically with the energy of the particles.

Calorimeters can be broadly divided into *electromagnetic calorimeters*, used to measure mainly electrons and photons through their electromagnetic interactions

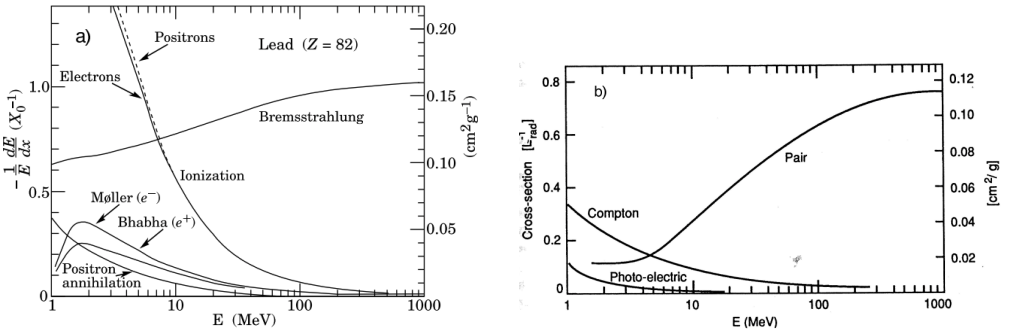

(a) (b)

Figure 3.1: Photon interaction cross-section in lead as a function of energy [82] (a). Fractional energy lost in lead by electrons and positrons as a function of energy [83] (b).

(e.g. *bremsstrahlung*[1], *pair production*[2]), and *hadronic calorimeters*, used to measure mainly hadrons through their strong and electromagnetic interactions. They can be further classified according to their construction technique into *sampling calorimeters* and *homogeneous calorimeters*.

3.2.1 Electromagnetic Calorimeters

Electromagnetic Calorimeters are mainly used to measure the kinetic energy of electrons, photons and muons. The average energy lost by electrons in lead and the photon interaction cross-section are shown in Figure 3.1 as a function of energy. For energies larger than $\sim 10\ MeV$, the main source of electron energy loss is bremsstrahlung, while photon interactions produce mainly electron–positron pairs. At low energies, on the other hand, electrons lose their energy mainly through collisions with the atoms and molecules of the material thus giving rise to ionization and thermal excitation; photons lose their energy through Compton scattering and the photoelectric effect.

As a consequence, electrons and photons of sufficiently high energy ($\geq 1\ GeV$) incident on a block of material produce secondary photons by bremsstrahlung, or secondary electrons and positrons by pair production. These secondary particles in turn produce other particles by the same mechanisms, thus giving rise to a cascade (*electromagnetic shower*) of particles with progressively degraded energies. The number of particles in the shower increases until the energy of the electron component falls below a critical energy ϵ, where energy is mainly dissipated by ionization and excitation and not in the generation of other particles. The main features of electromagnetic showers (e.g. their longitudinal and lateral sizes) can be described in terms of one parameter, the *radiation length* X_0, which depends on the characteristics of the material [83]:

$$X_0(g/cm^2) \simeq \frac{716\ g\ cm^{-2}\ A}{Z(Z+1)\ln(287/\sqrt{Z})} \tag{3.1}$$

where Z and A are the atomic number and weight of the material, respectively. The radiation length governs the rate at which electrons lose energy by bremsstrahlung, since it represents the average distance that an electron needs to travel in a material

[1] It is an electromagnetic radiation (photons) produced by the deceleration of a charged particle when deflected by another charged particle, typically an electron by an atomic nucleus.

[2] It is the creation of a subatomic particle and its antiparticle from a neutral boson. Usually pair production refers specifically to a photon creating an electron–positron pair near a nucleus.

to reduce its energy to $1/e$ of its original energy E_0:

$$\langle E(x) \rangle = E_0 e^{-\frac{x}{X_0}} \tag{3.2}$$

Similarly, a photon beam of initial intensity I_0 traversing a block of material is absorbed mainly through pair production. After traveling a distance $x = 9/7X_0$, its intensity is reduced to $1/e$ of the original intensity:

$$\langle I(x) \rangle = I_0 e^{-\frac{7}{9}\frac{x}{X_0}} \tag{3.3}$$

The critical energy ϵ has been defined as the energy at which the electron ionization and bremsstrahlung losses are equal. For example, Figure 3.1 shows that $\epsilon \sim 7\ MeV$ in lead. Therefore, the mean longitudinal profile can be described by [84]:

$$\frac{dE}{dt} = E_0 b \frac{(bt)^{a-1} e^{-bt}}{\Gamma(a)} \tag{3.4}$$

where $t = x/X_0$ is the depth inside the material in radiation lengths and a and b are parameters related to the nature of the incident particle ($e^{\pm}$ or γ). The shower maximum, i.e. the depth at which the largest number of secondary particles is produced, is approximately located at:

$$t_{max} \simeq \ln \frac{E_0}{\epsilon} + t_0 \tag{3.5}$$

where t_{max} is measured in radiation lengths, E_0 is the incident particle energy, and $t_0 = -0.5(+0.5)$ for electrons (photons). This formula highlights the logarithmic dependence of the shower length, and therefore of the detector thickness needed to absorb a shower, on the incident particle energy.

The transverse size of an electromagnetic shower is mainly due to multiple scattering of electrons and positrons away from the shower axis. Bremsstrahlung photons emitted by these electrons and positrons can also contribute to the shower spread. A measurement of the transverse size, integrated over the full shower depth, is given by the Molière radius, which can be approximated by:

$$R_M(g/cm^2) \simeq 21\ MeV \frac{X_0}{\epsilon(MeV)} \tag{3.6}$$

and represents the average lateral deflection of electrons at the critical energy after traversing one radiation length.

3.2.2 Hadronic Calorimeters

By analogy with electromagnetic showers, the energy degradation of high energy hadrons proceeds through an increasing number of (mostly) strong interactions with the calorimeter material. However, the complexity of the hadronic and nuclear processes produces a multitude of effects that determine the functioning and the performance of practical instruments, and make hadronic calorimeters more complicated instruments to optimize.

The hadronic interaction produces two classes of effects. First, energetic secondary hadrons are produced with a mean free path (*interaction length*) $\lambda = 35\ A^{1/3}\ gcm^{-2}$ between interactions giving rise the so-called *hadronic showers*. Second, in hadronic collisions with the material nuclei, a significant part of the primary energy is consumed in nuclear processes such as excitation, nucleon evaporation, spallation, etc.,

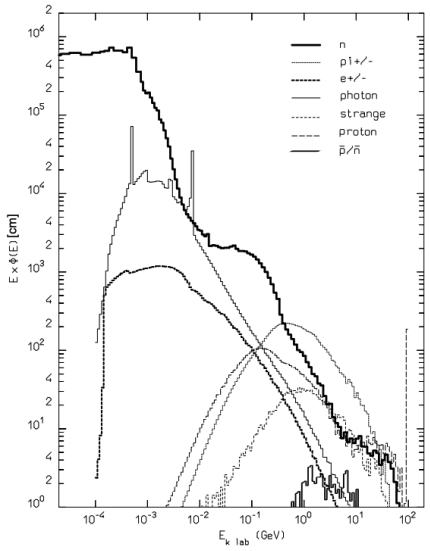

Figure 3.2: Particle spectra produced in the hadronic cascade initiated by 100 *GeV* protons absorbed in lead simulated by FLUKA. The energetic component is dominated by pions, whereas the soft spectrum is composed of photons and neutrons.

resulting in particles with characteristic nuclear energies at the *MeV* scale. The spectra of the major particle components in the shower, averaged over many cascades, induced by 100 *GeV* protons in lead are shown in Figure 3.2. This plot highlights the richness of the physics processes taking place in a hadronic calorimeter.

Because of the charge independence of hadronic interactions, on average one third of the pions produced in a hadronic shower will be π^0. These neutral hadrons will decay to two photons ($\pi^0 \rightarrow \gamma\gamma$) with $\sim$ 99% branching ratio, before having a chance to reinteract hadronically. As shown in 3.2.1 they induce an electromagnetic cascade, proceeding along its own laws of electromagnetic interactions. This physics process transfers energy from the hadronic to the electromagnetic component, which will not contribute further to hadronic processes. As the number of energetic hadronic interactions increases with incident energy, so will the fraction of the electromagnetic cascade. The hadronic fraction F_h can be defined as $F_h = (E/E_0)^k$ with $k = \ln\alpha / \ln m$. The parameter E_0 denotes a cutoff for further hadronic production, m is the multiplicity of fast hadrons produced in a hadronic collision and α gives the fraction of hadrons not decaying electromagnetically (typically $k \approx 0.2$). Values of F_h are of the order of $0.5(0.3)$ for a $100(1000)$ *GeV* shower. The increasing relevance of the electromagnetic component with the incoming particle energy is reflected in the relative hadronic particle fluxes shown in Figure 3.3.

The total energy carried by photons from nuclear reactions ($\pi^0 \rightarrow \gamma\gamma$) is substantial: only a fraction, however, will be recorded in practical instruments, as most of these photons are emitted with a considerable time delay ($< 1\ \mu s$). These delayed photons, soft neutrons, and binding energy all show that nuclear effects produce a form of undetectable energy which cannot be detected at all or only with much reduced efficiency. Thus, for an electromagnetic shower the visible energy E^e_{vis} observed can be defined as: $E^e_{vis} = \eta_e E(em)$ where η_e is the efficiency of the electromagnetic component. Instead for purely hadronic energy that provides visible energy in an instrument can be defined an hadronic efficiency η_h. Therefore, for a pion-induced shower the visible energy E^π_{vis} is:

$$E^\pi_{vis} = \eta_e F_{\pi^0} E + \eta_h F_h E \tag{3.7}$$

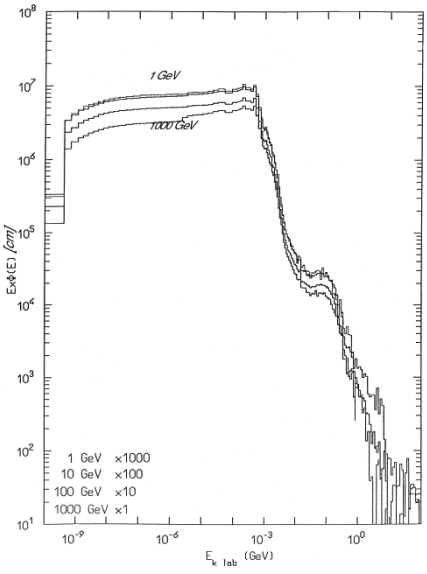

Figure 3.3: Fluxes of the neutron component of hadronic showers for different incident protons on lead.

hence:

$$E^{\pi}_{vis} = \eta_e(F_{\pi^0} + \frac{\eta_h}{\eta_e}F_h)E \tag{3.8}$$

where E is the incident pion energy.

The ratio of observable ("visible"), signals induced by electromagnetic and hadronic showers, usually denoted "e/π", is therefore:

$$\frac{E^{\pi}_{vis}}{E^{e}_{vis}} = \left(\frac{e}{\pi}\right)^{-1} = 1 - \left(1 - \frac{\eta_h}{\eta_e}\right)F_h \tag{3.9}$$

In general $\eta_e \neq \eta_h$, therefore the average response of a hadron calorimeter as a function of energy will not be linear because F_h decreases with incident energy.

For example, Figure 3.4 shows the different shape of hadronic and electromagnetic cascades in the Earth's atmosphere induced by 250 GeV protons and photons.

3.2.3 Homogeneous and Sampling Calorimeters

In this subsection the main techniques used to build homogeneous and sampling electromagnetic calorimeters, and the advantages and drawbacks of the various solutions are discussed.

Homogeneous Calorimeters

The main advantage of homogeneous calorimeters is their excellent energy resolution, which is due to the fact that the whole energy of an incident particle is deposited in the active medium, in contrast with sampling calorimeters. On the other hand, homogeneous calorimeters can be less easily segmented laterally and longitudinally, which is a drawback when position measurements and particle identification are required.

Homogeneous calorimeters can be broadly divided into four classes:

- *Semiconductor calorimeters*: the ionization tracks produce electron-hole pairs in the material valence and conduction bands that give rise to an electric signal.

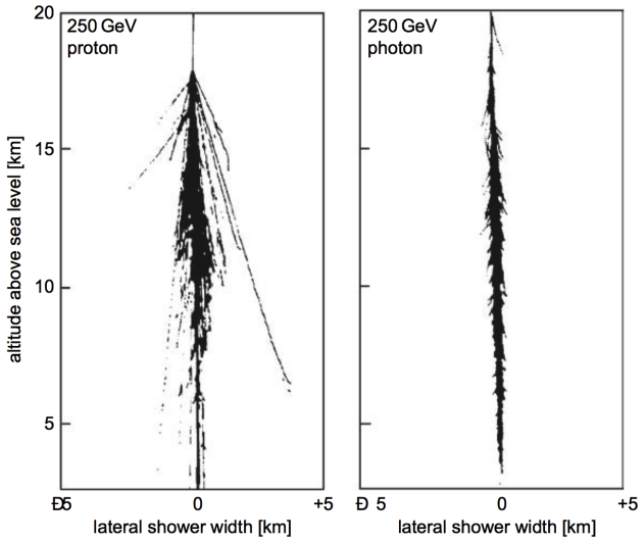

Figure 3.4: Monte Carlo simulations of the different development of hadronic (left) and electromagnetic (right) cascades in the Earth's atmosphere [85].

These detectors provide an excellent energy resolution. Examples are silicon and germanium crystals used in many nuclear physics applications.

- *Cherenkov calorimeters*: the medium is a transparent material in which relativistic $e^{\pm}$ in the shower produce Cherenkov photons. The signal is therefore collected in the form of light. Lead-glass calorimeters are a widely used example.
- *Scintillator calorimeters*: the medium is a material where ionization tracks produce light (fluorescence). Examples are BGO, CsI, and $PbWO_4$ crystals.
- *Noble liquid calorimeters*: the medium is a noble gas (Ar, Kr, Xe) operated at cryogenic temperature. Although in this case both ionization and scintillation signals can in principle be collected, large-scale calorimeters for high-energy physics applications are based on the charge measurement.

In detectors where the signal is collected in the form of light (Cherenkov, scintillators), photons from the active volume are converted into electrons (usually called *photoelectrons*) by a photosensitive device such as a *photomultiplier*. A contribution to the energy resolution comes from statistical fluctuations in the number of photoelectrons. This contribution has the form of $\propto 1/\sqrt{N_{pe}}$, where N_{pe} is the number of photoelectrons, and is important if N_{pe} is small. The number of photoelectrons can be small if the number of photons produced in the active medium is small, as is the case in Cherenkov calorimeters, or if there are losses in the light collection.

Sampling Calorimeters

The energy resolution of sampling calorimeters is in general worse than that of homogenous calorimeters, owing to the sampling fluctuations produced by the absorber layers interleaved with the active layers. On the other hand, sampling calorimeters are relatively easy to segment longitudinally and laterally, and therefore they usually offer better spatial resolution and particle identification than homogeneous detectors. They are almost universally used at accelerators to measure hadronic showers, since they provide enough interaction lengths with a reasonable detector thickness (typically $< 2\ m$). Sampling calorimeters can be classified, according to

the type of active medium, into scintillation calorimeters, gas calorimeters, solid-state calorimeters, and liquid calorimeters. In the first case the signal is collected in the form of light, in the last three cases in the form of electric charge. Commonly used absorber materials are lead, iron, copper and uranium.

3.3 The FOOT Calorimeter: homogeneous scintillation calorimeter

Scintillation calorimeters can be divided into two classes, *organic* and *inorganic*, characterized by two different physical mechanisms for light emission, and by different advantages and drawbacks.

Organic scintillators are fast ($\sim ns$) but suffer from a poor light yield; inorganic scintillators offer a large light yield and good signal linearity, but usually have a slow response ($\sim \mu s$). Calorimeters based on organic scintillators are usually binary or ternary systems consisting of an organic solvent (e.g. a mineral oil) with a small fraction (typically $\leq$ 1%) of a scintillating solute (fluors). The molecules of the solvent are excited by an incident charged particle and transfer the excitation to the solute (for instance through dipole interactions), which produces the detectable signal. Without fluors, the base material would re-absorb a large part of the emitted light. The process of excitation, molecular transfer, and light emission is very fast, of the order of a few nanoseconds. However, the light output is relatively small because the solute concentration is small. The use of organic scintillators for homogeneous calorimeters is very limited, mainly because they are not dense enough, whereas they are commonly chosen as the active medium for sampling calorimeters.

In inorganic scintillators the light emission is related to the crystal structure of the material. Incident charged particles produce electron-hole pairs in the conduction and valence bands of the medium, and photons are emitted when electrons return to the valence band. The frequency of the emitted radiation and the response time depend on the gap between the valence and the conduction bands and on the details of the electron migration in the lattice structure, which vary a lot with the material. Often, in order to increase the light yield (for example by matching the signal wavelength to the photocathode spectral sensitivity) and to obtain a faster response, crystals are doped with tiny amounts of impurities. These dopants, the most commonly used of which is thallium (Tl), create additional activation sites in the gap between the valence band and the conduction band. These sites can be filled by electrons from the conduction band, and can therefore increase the emission probability and change the light wavelength and the material decay time. Table 3.1 summarizes the main properties of the crystals most commonly used for physics applications. $NaI(Tl)$ has been widely employed in the past because of its low cost and large light yield. However, it is hygroscopic and has a relatively long radiation length, not well suited to big experiments where denser materials like BGO and $PbWO_4$, which allow more compact detectors, are preferred.

As explained in 2.3.1, the FOOT calorimeter is the most downstream detector and it is designed to measure the energy of projectile fragments produced in the target. The detector does not measure directly the energy in MeV but a quantity directly proportional to it (electrical signal in mV). Thus, from the evaluation of the detector $mV - MeV$ response curve the energy can be retrieved. The upper bound of the fragments energy range is defined by the beam energy, while the lower bound is set by the intensity of the magnetic field.

Table 3.1: Main properties of crystals commonly used for homogeneous electromagnetic calorimeters.

Properties	$NaI(Tl)$	$CsI(Tl)$	CsI	BGO	$PbWO_4$
Density $[g/cm^3]$	3.67	4.53	4.53	7.13	8.28
X_0 $[cm]$	2.59	1.85	1.85	1.12	0.89
R_M $[cm]$	4.5	3.8	3.8	2.4	2.2
Decay Time $[ns]$	250	1000	10	300	5
Emission Peak $[nm]$	410	565	305	480	440
Light Yield $[\gamma/keV]$	40	50	40	8	0.15
Rad. Hardness $[Gy]$	1	10	10^3	1	10^5

FOOT will operate in an energy range in which fragments are below the energy threshold that triggers a hadronic shower in a calorimeter. Therefore, the mechanisms for energy loss will be driven by the electromagnetic interaction and nuclear interactions: the production of neutrons escaping the calorimeter undetected causes a systematic underestimation of the initial energy. In conclusion the FOOT calorimeter belongs to the scintillator-homogeneous family of calorimeters.

Since FOOT will work at a relatively low beam intensity, the ideal material for this calorimeter is a dense crystal, with good light yield, and without strict requirements on the response speed. BGO is then a natural solution, also because of the opportunity to reuse crystals from past experiments.

All the tests performed to make the design choices (i.e. BGO coating, photodetector, development of the front-end board, design of the DAQ system, design mechanical structure, etc.) and to achieve the performances required by the experiment will be discussed in detail in Chapter 4.

Chapter 4

FOOT calorimeter design tests

4.1 Introduction

The work of my Ph.D. thesis is focused on the CAL detector adopted in the FOOT experiment. I managed both the hardware configurations for the test beams and the software aspects related to the simulation, acquisition, reconstruction and analysis code.

As discussed in Section 2.4 the main requirements of the FOOT calorimeter are energy resolution below 2% and linear response in the full energy range foreseen by the experiment. Thus, in this chapter, all the tests performed to fulfill these performances are presented. In particular, Section 4.2 is an overview of test beams and the data analysis structure. From Section 4.3, instead, all the tests performed, divided for the different design calorimeter components, are discussed in depth. In Section 4.4 the final calorimeter performance are presented.

4.2 Test beam and Data analysis overview

The experimental measurements required to optimize the calorimeter configuration took place at the CNAO facility. Although the CNAO beam monitor is optimised for clinical beam intensities ($> 10^8$ Hz and 10^9 Hz for carbon ions and protons, respectively), the synchrotron was tuned for the delivery of low intensity ($\sim 10^4$ Hz) beams at a set of predefined energies (70, 120, 170 and 227 MeV for protons, 115, 190, 260, 330 and 399 MeV/u for carbon ions), so as to sample the whole accessible energy spectrum and allow the study of the calorimeter response, in different configurations, in terms of linearity and energy resolution.

A typical charged ion signal acquired by the photodetector coupled to the BGO crystal and processed by the front-end board is represented in Figure 4.1.

From each signal two parameters proportional to the initial particle energy can be extrapolated by the fit function (4.1) [86]: the *Maximum Amplitude* (MA) and the *Time Integrated Amplitude* (TIA).

$$f(t) = A \cdot e^{-k_s \cdot (\log \frac{t-t_0}{t_r})^2} \tag{4.1}$$

where k_s embeds the parametrization of the signal shape, t_0 is the starting time, t_r, labelled *rising time*, is the time at which the signal takes its A maximum amplitude.

The TIA is defined as the integral of the fit function in a 200 ns interval, beginning at the signal starting time.

MA and TIA represent the energy deposited in BGO for one signal, but collecting a multitude of them, they can be used to create the energy spectra of the incident

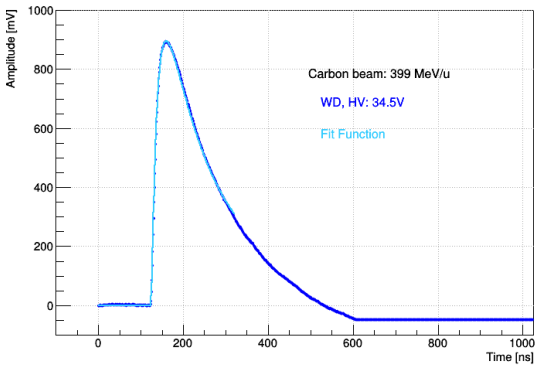

Figure 4.1: Examples of SiPM signals from 399 MeV/u carbon ions sampled by the WaveDAQ at 1 GS/s. The light-blue line is the signal parametrization through Eq. 4.1.

beams. For example, Figure 4.2 shows the energy spectra of proton (bottom) and carbon (top) beams for the above mentioned energies.

The spectra, shown in Figure 1.2, are composed by a peak, representing events in which the particle deposited all its energy in the BGO, and a low tail represents neutron production and γ prompt emission events. Moreover, the ratio between the width and the average value of the peaks represents the calorimeter energy resolution.

The width and average energy can be quantitatively retrieved from the spectra performing a fit with a *Crystal Ball* (CB) function [87]:

$$f(x,\alpha,n,\bar{x},\sigma) = N\begin{cases} e^{-\frac{(x-\bar{x})^2}{2\sigma^2}}, & \frac{x-\bar{x}}{\sigma} > -\alpha \\ A\left(B-\frac{x-\bar{x}}{\sigma}\right)^{-n}, & \frac{x-\bar{x}}{\sigma} \leq -\alpha \end{cases} \tag{4.2}$$

with

$$A = \left(\frac{n}{|\alpha|}\right)^n e^{\frac{-|\alpha|^2}{2}}$$

and

$$B = \frac{n}{|\alpha|} - \alpha$$

and where $\bar{x}$,σ and n,α are the parameters of a Gaussian and a power-law function, respectively.

In all the studies and the plots shown in this thesis the uncertainty on the average energy value $\bar{x}$ is calculated as the σ of the Gaussian peak. Instead, the energy resolution uncertainty is calculated following the *propagation of error formula* as:

$$f(E) = \delta_{\sigma_E/E} = \sqrt{\left(\frac{\partial f(E)}{\partial \sigma_E}\right)^2 \cdot \delta^2_{\sigma_E} + \left(\frac{\partial f(E)}{\partial E}\right)^2 \cdot \delta^2_E} \tag{4.3}$$

Often the error bars are smaller than the markers dimension and thus, not visible.

Following this approach and data analysis procedure several test beams have been performed at CNAO in order to make all the design decisions.

4.3 Calorimeter design

In order to ensure the performance requirements, dedicated test beams were performed to choose each component of the calorimeter: photodector, BGO coating,

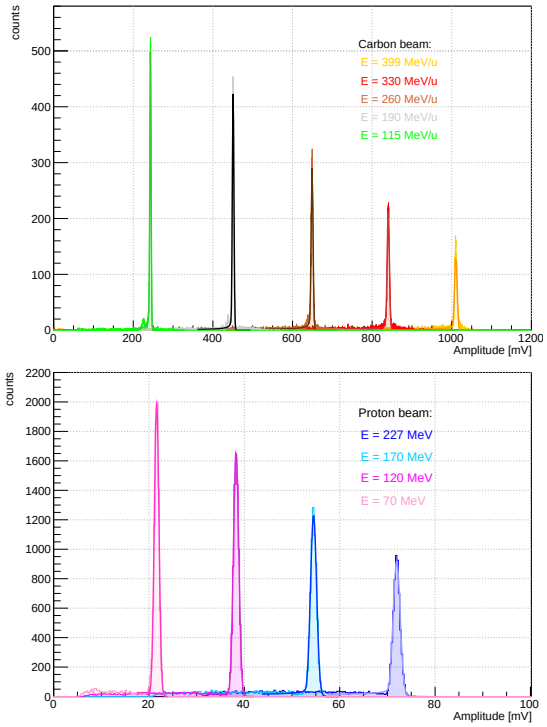

Figure 4.2: Energy spectra for incident carbon (top) and proton (bottom) beams for 115, 190, 260, 330, 399 MeV/u and 70, 120, 170, 220 MeV, respectively. The darker lines are the spectra parametrization with a Crystal Ball function.

front-end board, DAQ system and mechanical structure design.

4.3.1 The Photodetector

To collect the photons emitted in the crystals two options are suitable as photodetectors to be coupled to the BGO crystals:

- **PhotoMultiplier Tube**: it consists of a *photocathode* followed by an electron multiplier (Figure 4.3). A single photon ejects an electron from the photocathode. Electric fields in the *Photo-Multiplier Tubes* (PMT) accelerate the electron onto another surface called a *dinode*. The collision of the electron with the dinode releases several new electrons, which are accelerated into another dinode. This process is repeated several times producing a typical electron gain of $\sim 10^6$ and the current from the PMT can be measured directly.

- **Silicon PhotoMultiplier**: it is a photodetector composed by a matrix of *Avalanche PhotoDiode* (APD) working in *Geiger* mode. A photodiode is a $p-n$ junction that creates a depletion region that is free of mobile charge carriers. When a photon is absorbed in silicon it creates an electron-hole pair. When applying a reverse bias to a photodiode an electric field is set up across the depletion region, that will cause these charge carriers to be accelerated towards the anode (holes), or cathode (electrons). Therefore in a reverse-biased photodiode an absorbed photon will result in a net current flow. When a sufficiently high electric field ($> 5 \cdot 10^5\ V/cm$) is generated within the silicon depletion region, a charge carrier created there will be accelerated to a point where it carries sufficient kinetic energy to create secondary pairs through an ionization process. In this way, a single absorbed photon can trigger a ionization *avalanche*

that spreads throughout the silicon volume subjected to the electric field. The silicon breaks down and becomes conductive, effectively amplifying the original electron-hole pair into a macroscopic current flow. This process is called *Geiger discharge*. A photodiode operated in Geiger mode employs this breakdown mechanism to achieve a high gain and is referred to as a *Single Photon Avalanche Diode* (SPAD). The application of a reverse bias beyond its nominal breakdown voltage creates the necessary high-field gradients across the junction. Thus, the *OverVoltage* (OV) can be defined as the difference between the working and breakdown voltage.

Once a current is flowing it should then be stopped or "quenched". Passive quenching is achieved through the use of a series resistors which limits the current drawn by the diode during breakdown. This lowers the reverse voltage seen by the diode to a value below its breakdown voltage, thus halting the avalanche. The diode then recharges back to the bias voltage, and is available to detect subsequent photons. This cycle of breakdown, avalanche, quench and recharge of the bias to a value above the breakdown voltage, is illustrated in Figure 4.4 (top).

In this way, a single SPAD sensor operated in Geiger-mode functions as a photon-triggered switch, in either an "on" or "off" state. Regardless of the number of photons absorbed within a diode at the same time, it will produce a signal no different from that of a single photon. Indeed, proportional information on the magnitude of an instantaneous photon flux is not available.

To overcome this intrinsic lack of proportionality, SiPM (Figure 4.4, bottom right) integrates a dense array of small, independent SPAD sensors (Figure 4.4 bottom left), each with its own quenching resistor. Each independently operating unit of SPAD and quench resistor is referred to as a *microcell*. When a microcell in the SiPM fires in response to an absorbed photon, a Geiger avalanche is initiated causing a photocurrent to flow through the microcell. This results in a voltage drop across the quench resistor, which in turn reduces the bias across the diode to a value below the breakdown, thus quenching the photocurrent and preventing further Geiger-mode avalanches from occurring. Once the photocurrent has been quenched, the voltage across the diode recharges to the nominal bias value. The time it takes for the microcell to recharge to the full operating voltage is called the *recovery time*. It is important to note that the Geiger avalanche is confined to the single microcell it was initiated in. During the avalanche process, all other microcells remain fully charged and ready to detect photons.

SiPMs would provide two crucial advantages: a compact design and a relatively low voltage power supply. However, they should operate in a range where the effect of optical photons pile-up in a SiPM microcell is negligible, so as to minimize deviations from linearity in the response over the full energy range covered by the fragments to be detected: from tens of MeV for low energy protons to about 10 GeV, corresponding to C or O beam particles up to 800 MeV/u. Since the SiPM response is proportional to the energy of the incoming particle only when the pileup of optical photons in their microcells is negligible, to ensure linearity, the choice of the microcell pitch is crucial. Preliminary calculations suggested that, taking into account the slow BGO response (300 ns decay time constant) and its light yield, the optical pileup should be negligible for a microcell pitch up to 20 μm, as long as the microcell recovery time is smaller than 10 ns. In order to verify the SiPM response

Figure 4.3: Example of PMT.

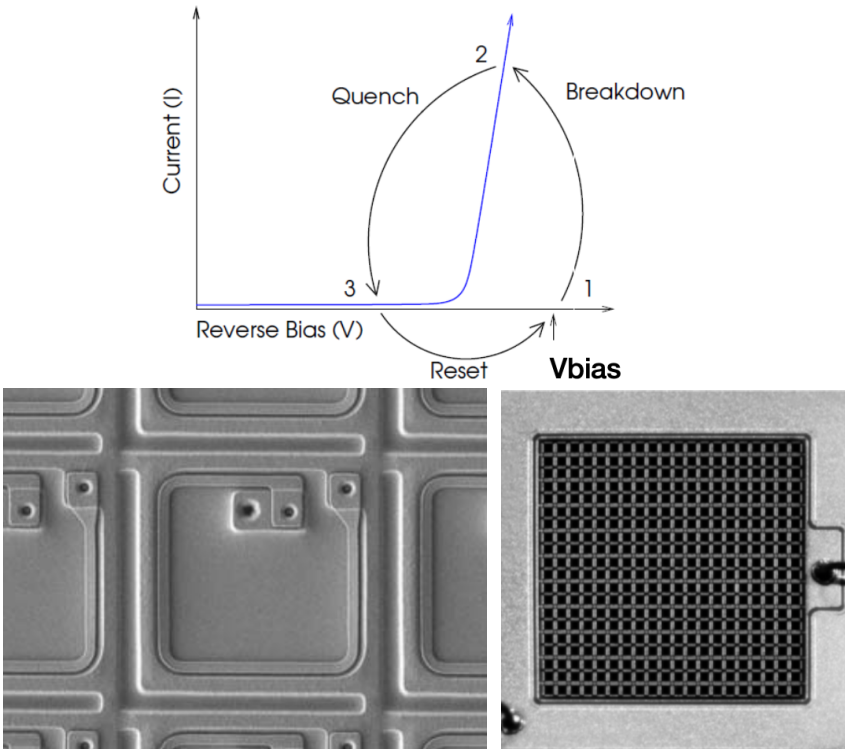

Figure 4.4: Breakdown, quench and reset cycle of a SPAD working in Geiger mode (a); a conceptual illustration of one single SPAD (b) and the whole matrix of SPADs of the SiPM (c).

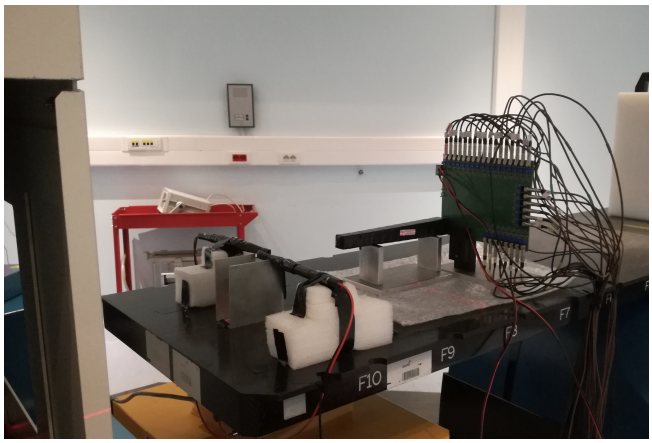

Figure 4.5: Picture of test beam performed at CNAO to define the best SiPM for the FOOT calorimeter.

Table 4.1: Parameters of the 3 SiPM Tiles tested as possible FOOT photodetectors.

Sample	Type	Number of channels	Cell Size [mm^2]	Microcell Pitch [μm]
NUV-HD30	NUV	16	6×6	30
RGB-HD20	RGB	30	4×4	20
RGB-HD15	RGB	30	4×4	15

linearity up to 399 MeV/u carbon beams ($\sim$ 4.8 GeV), three different prototypes provided by *Fondazione Bruno Kessler* (FBK) (see Table 4.1) were tested at CNAO, with monochromatic beams at the 9 energies already mentioned. Moreover, in order to increase the detection area, number of photoelectrons and then energy resolution a matrix of SiPM, the so called *Tile*, are used. Figure 4.5 shows a picture of the test beam performed at CNAO. The crystal is visible on the bed of the CNAO treatment room connected to a readout-board that reads all the SiPM channels independently. The digitizer used for this test beam was the $V1742$ provided by CAEN and the coincidence of two plastic scintillators were used as external trigger.

The FBK provided three different SiPM Tile prototypes: one with a *Photo Detection Efficiency* (PDE) peaked in the *Near UltraViolet* (NUV) spectrum and microcells with a 30 μm pitch, and two SiPM Tiles with a PDE peaked in the *visible light* (RGB) and $15 - 20$ μm microcells pitches, respectively. Figure 4.6 shows the response (i.e. sum of the output signals of each SiPM channel) from the three different prototypes (NUV-HD30, RGB-HD20, RGB-HD15) for carbon ions at 5 different energies. The three responses were parametrized by means a first polynomial function and, while the RGB-HD15 and RGB-HD20 prototypes, with 15 μm and 20 μm microcell pitch respectively, show a linear behaviour, a clear non-linearity is observed for the NUV-HD30 Tile, with 30 μm microcell pitch. This is confirmed also by the χ^2 study of the linear fit: 1.79, 1.22, and 7.61 for RGB-HD15, RGB-HD20 and NUV-HD30, respectively. Therefore, RGB-HD20 and the RGB-HD15 SiPM Tiles can be installed as photodetectors. In order to extend as much as possible the dynamic range of the calorimeter, the RGB-HD15 Tile (Fig. 4.8b) was selected.

Its specifications are shown in Figure 4.7: the PDE is maximum between 500 and 600 nm and increases with the OV; accordingly, the gain linearly increases with the OV.

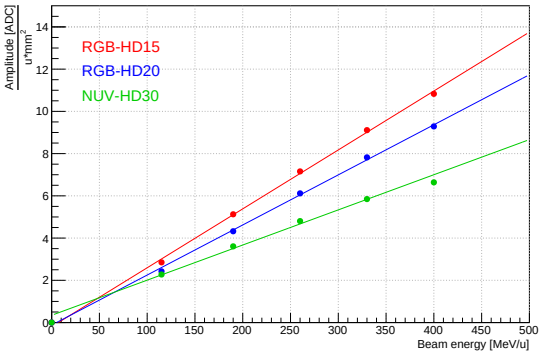

Figure 4.6: Average values of the response of the 3 SiPM Tile prototypes as a function of the beam energy for carbon ion beams and the corresponding linear fits.

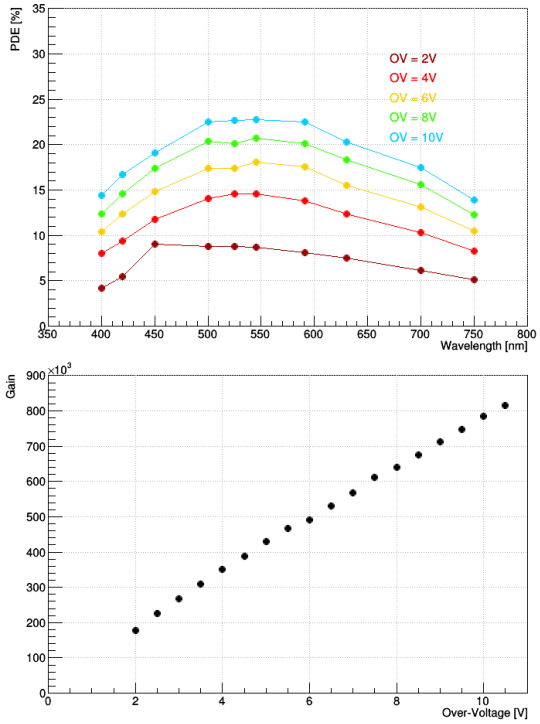

Figure 4.7: RGB-HD15 SiPM Tile specifications: PDE as a function of the wavelength (top) and gain as a function of the OV (bottom).

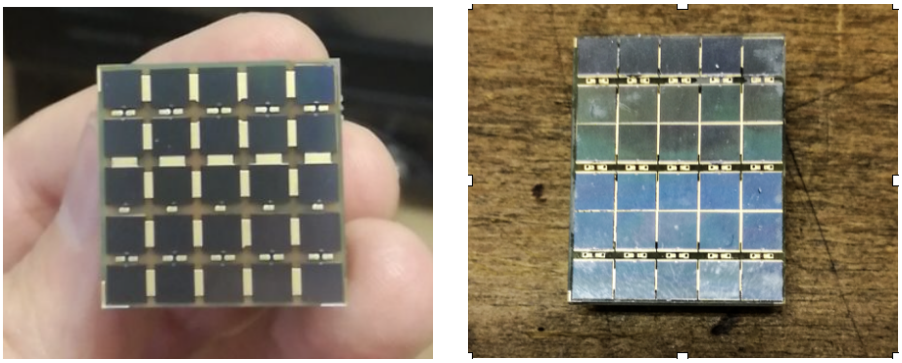

(a) (b)

Figure 4.8: Picture of the RGB-HD15 prototype (a) and the Tile selected for the final calorimeter (b).

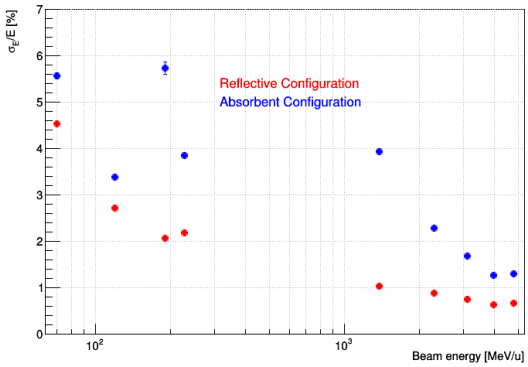

Figure 4.9: Energy resolution as function of beam energy for two different coating configurations: reflective (red) and absorbent (blue). The reflective configuration shows better performances.

The final Tile geometry (Fig. 4.8a) was slightly modified with respect to the prototype: with a rectangular shape ($23 \times 22\ mm^2$) and 25 cells of $4 \times 4\ mm^2$ size, it features a 400 mm^2 active area, corresponding to about 48% of the crystal backend. The SiPM Tile also features a *Negative Temperature Coefficient* (NTC) thermistor that will provide an output proportional to the temperature, that must be monitored throughout the data collection, as its variation causes a variation in the photodetector gain, hence in the system response.

The SiPM Tiles are coupled to the BGO crystals with Dow Corning 3145 RTV glue [88].

4.3.2 Crystal Coating

In order to find the setup that maximises the light yield two different crystal coating configurations have been explored: *absorbent* and *reflective*. Test beams of crystals wrapped with aluminium foils and black tape have shown that the reflective configuration provides better performance as shown in Figure 4.9 where the energy resolution as function of beam energy is provided.

Thus, three different reflective crystal coatings were investigated: *Reflective painting*, *Tyvek* [89] and *Mylar* [90] foils. Figure 4.10 shows an example of three crystals wrapped with the 3 coatings mentioned: Tyvek (right), Mylar (middle) and Reflective painting (left).

Crystals equipped with these wrappings have been tested at CNAO with 5 carbon energies (115, 190, 260, 330, 399 MeV/u) and 4 proton energies (70, 120, 170, 220

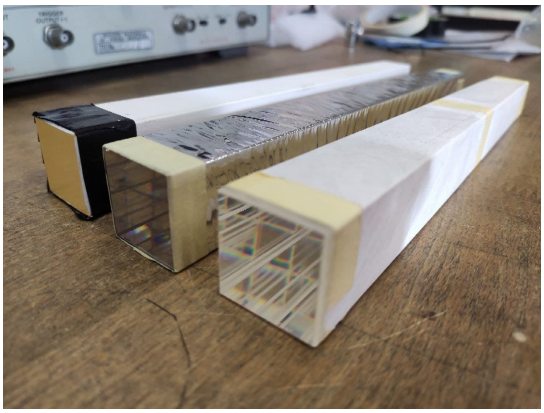

Figure 4.10: An example of three crystals wrapped with Tyvek (right), Mylar (middle) and Reflective painting (left).

MeV). The raw BGO response as a function of the beam energy, reported in Figure 4.11 in terms of MA (top) and TIA (bottom), shows that crystals wrapped in Tyvek provide the highest light yield. Instead, the energy resolution as a function of beam energy for MA and TIA is shown in Figure 4.12 (top) and 4.12 (bottom), respectively. The plots show that Tyvek coating ensures the best performances in particular for lower energies. For this test beam the data were acquired with the *V*1742 CAEN digitizer by means a *software trigger*: i.e. only the signals that crossed a pre-set up threshold were recorded. Indeed this time the trigger scintillators were removed to avoid energy resolution worsening.

Therefore, Tyvek was preferred to Mylar and Reflective White Painting as crystal coating. Besides the advantage of a higher signal to noise ratio, Tyvek is also more resistant than Mylar and Paint, which would be easily scratched during the assembly and multiple transportation procedures.

4.3.3 Front-end board and Readout

The first front-end board prototype was designed in order to read all the SiPM channels independently and to provide the sum in an extra output channel. Moreover the gain of each channel could be tuned by means a potentiometer. However, the board had large dimensions and as soon as the test beam results have shown that the sum channel was good enough to achieve the required performance, a second, more compact, front-end board was designed. Figure 4.13 shows a picture of the first front-end board prototype.

The final version of the front-end board was designed so as to match the SiPM Tile size and maximise the compactness. It provides the power supply to the SiPM Tiles and processes the output signals. Figure 4.14 (right) shows the two sides of the front-end board, which is then mounted on the SiPM Tile as shown in Figure 4.14 (left). Each front-end board sums the signals collected by the 25 SiPM of the Tile, then a digitiser module samples the output signal, so that it can be analysed through both its MA and TIA, as mentioned in 4.2.

Three different digitisers were tested: CAEN V1740, CAEN V1742 and a WaveDAQ [62]. Their main working parameters are reported in table 4.2. Examples of digitised signals for 399 MeV/u carbon ions are shown in Figure 4.15. The signals are parametrized according to the function (4.1).

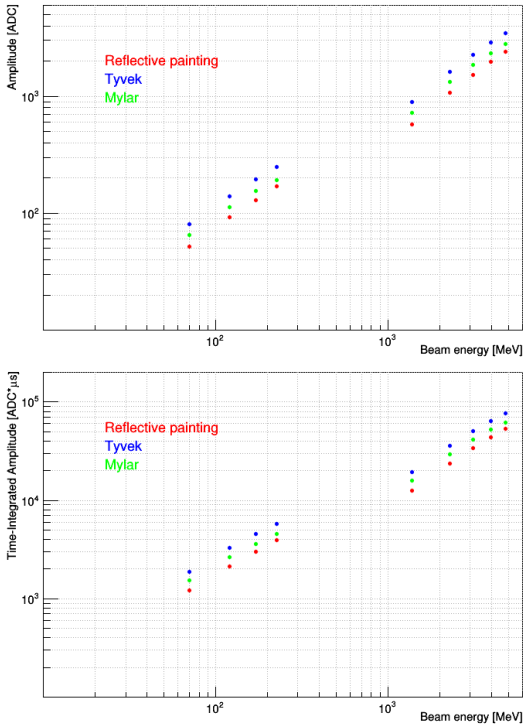

Figure 4.11: Average BGO response as a function of beam energy: MA (top) and TIA (bottom) for crystals wrapped with Reflective painting (red), Tyvek (blue) and Mylar (green).

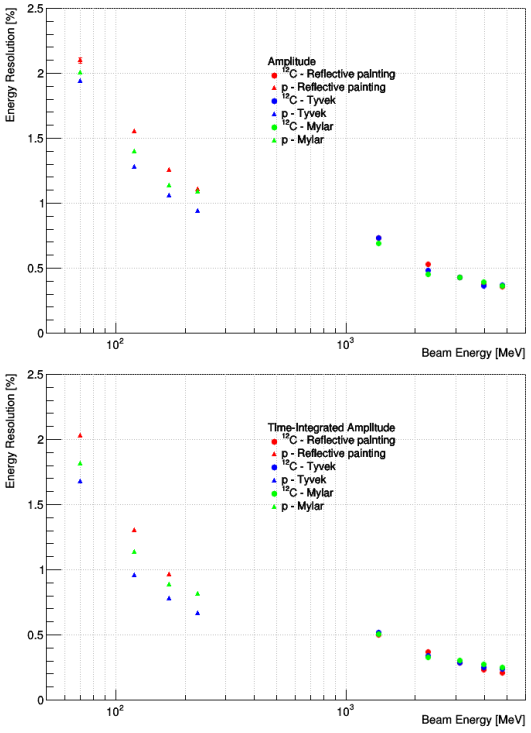

Figure 4.12: Energy resolution as function of beam energy: MA (top) and TIA (bottom) for crystals wrapped with Reflective painting (red), Tyvek (blue) and Mylar (green).

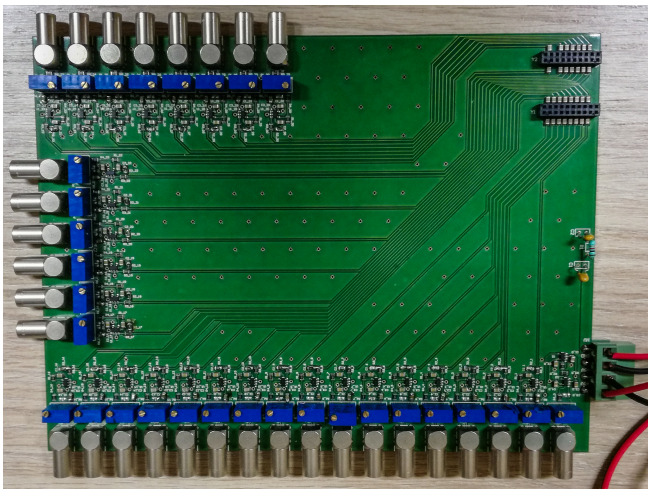

Figure 4.13: Picture of the first front-end board prototype: 31 output channels are visibile (30 are the SiPMs channles, 1 is the sum); in blue the potentiometer.

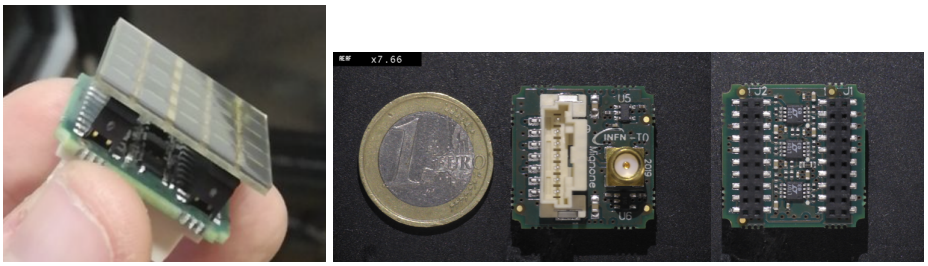

Figure 4.14: Picture of SiPM Tile and Front-end board coupled together (left). Picture of front-end board from the side that connects to the SiPM Tile and from the side that connects to the power supply and DAQ system. (right)

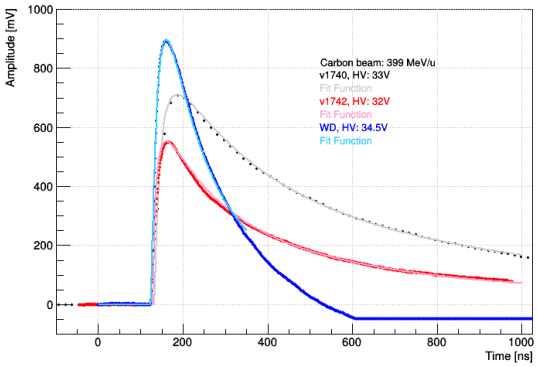

Figure 4.15: Examples of SiPM signals from 399 MeV/u carbon ions sampled by the CAEN v1740 (black), CAEN v1742 (red) and WaveDAQ (blue) digitisers at 62.5 MS/s, 1 GS/s and 1 GS/s, respectively. The SiPM voltage was different for the data taking corresponding to the different digitizers, hence the different gain and peak amplitude.

Table 4.2: Working parameters of the three digitizer tested for the calorimeter

Name	Resolution [bit]	Sampling Frequency	Dynamic Range [V]	Gain
V1740	12	62.5 MS/s	2	1
V1742	12	up to 5 GS/s	1	1
WaveDAQ	16	up to 5 GS/s	1	0.5

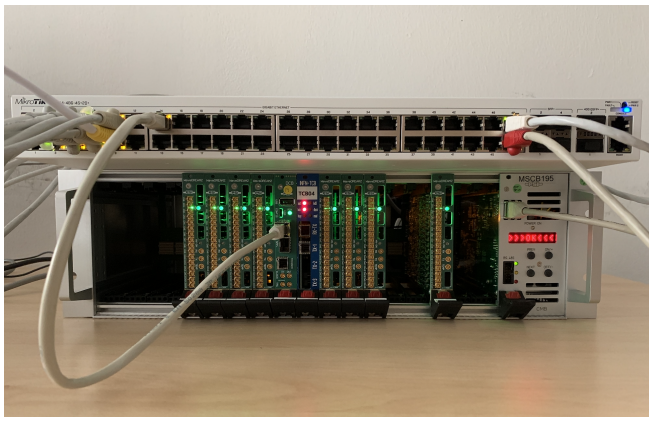

Figure 4.16: WaveDAQ boards in the corresponding crate.

The choice of the digitizer has been driven by a trade off between dynamic range, in order to contain most energetic signals, and sampling frequency, in order to obtain a better measurement of the signal shape. CAEN V1740 has a suitable dynamic range but low frequency rate, by contrast CAEN V1742 digitizer provides a suitable description of the signal shape, thanks to its high sampling frequency, but it has a restricted dynamic range. Accordingly, in order to acquire the most energetic particles with CAEN V1742, the SiPM OV has to be reduced with the consequent deterioration of performance, as shown in Figure 4.7 (top). Thus, the best choice for the FOOT calorimeter is the WaveDAQ because, despite having the same dynamic range of CAEN V1742, it has the possibility to apply an attenuation to the SiPM signals, ensuring high performance and good signal shape description. Each WaveDAQ board can host up to 16 channels so that to cover all the calorimeter channels 20 boards are required. Figure 4.16 shows a crate with some WaveDAQ boards. The crates are then connected to the DAQ Control PC to send data and receive triggers.

4.3.4 Mechanics

The main requirement of the calorimeter mechanical structure is that once fragments coming from the target reach the calorimeter, they should not cross anything but air and the BGO crystals. Since the range in BGO of the most energetic fragments will not exceed 8 cm, the support structure was designed in such a way that it holds the crystals in position from the back. Its 3D-printed modules hold 3×3 crystals each (Figure 4.17) so that the first 12 cm are free of additional material; the whole structure, composed by 37 modules with those on the borders not fully equipped, will be mounted according to the drawing shown in Fig 2.16.

4.4 Final calorimeter performances

4.4.1 Energy resolution and linearity

A test beam at CNAO was performed to assess the calorimeter performances after all the design choices. The signal of one BGO crystal, equipped with a 15 μm SiPM Tile (34.5 V of working voltage) and wrapped with a Tyvek foil, were sampled at 1 Gs/s with a WaveDAQ board. The energy resolution and the crystal response were studied with proton and carbon beams at 70, 120, 170, 227 MeV and 115, 190, 260, 330, 399 MeV/u, respectively. Figure 4.18 shows the results of the FOOT calorimeter

Figure 4.17: The 3D-printed module holder with 9 assembled crystals.

performances: on the energy resolution and on the right the calorimeter response as a function of the energy.

Figure 4.18 (top) shows that the energy resolution values reflect an excellent performance and are consistent with the goal of staying below 2% for fragments above 70 MeV. The function defined in Eq. 2.11 is used to fit the data, with $(a = 10.4 \pm 0.3)\ MeV$, $(b = 0.39 \pm 0.01)$ and $(c = 103 \pm 4.3)\ MeV^2$ as output parameters.

Figure 4.18 (bottom) shows that the raw response is not linear with the incoming particle, with an increasing deviation from linearity when increasing the energy, for both proton and, more visible, for carbon beams. Indeed, two fits with first order polynomial functions for both beams are performed. The resulting parameters are: (0.200 ± 0.001) and $(0.280 \pm 0.001)\ mV/MeV$ for proton and carbon slopes respectively, and (-27.02 ± 2.22) and $(2.32 \pm 0.67)\ MeV$ for proton and carbon y-intercepts, respectively. The fit χ^2 are 4 and 75 for proton and carbon, respectively. Actually, several corrections have to be applied to the raw data in order to improve the linearity of the calorimeter response, i.e. *temperature correction*, *average emission depth correction*, *Birks effect*.

The linear response corrections and the calorimeter calibration protocol will be discussed in detail in chapter 5.

4.4.2 Time resolution

Although BGO crystals are not expected to contribute to the FOOT time of flight measurements, their time resolution was measured in the laboratory, with cosmic rays. The layout is shown in Figure 4.19: two thin plastic scintillators read by PMTs are placed above and below the BGO crystal and their coincidence signal provides a trigger for the BGO readout. An example of registered signals and the fits to their rising edge is shown in Figure 4.20a: the corresponding time tag is taken at 10% of the peak amplitude value.

Figure 4.20b shows the distribution of time difference between the two plastic scintillators used for the trigger, which corresponds, assuming the contributions from the two scintillators are equal and independent, to a time resolution on the single scintillator of about $(410 \pm 25)\ ps$. Figure 4.21 shows the distribution of the difference between the average time in plastic scintillators and the time in the BGO for three different positions along the crystal, at $d = 20, 120$ and $220\ mm$. The standard deviation of the distribution is related to the time resolution, which, after deconvolving the previously estimated contribution from the plastic scintillators, reaches $(640 \pm 30)\ ps$ at the largest distance from the SiPM and degrades to about (675 ± 30)

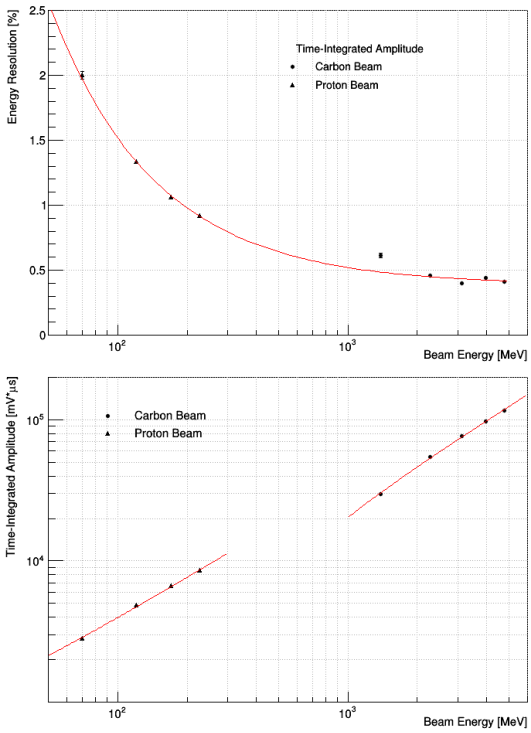

Figure 4.18: Energy resolution (top) and calorimeter response (bottom) calculated with the time-integrated analysis for proton and carbon beams at 70, 120, 170, 220 *MeV* and 115, 190, 260, 330, 399 MeV/u, respectively.

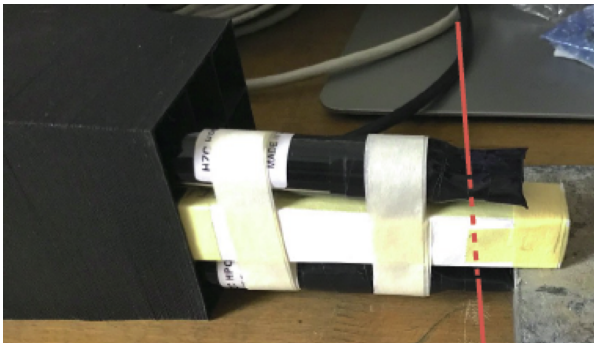

(a)

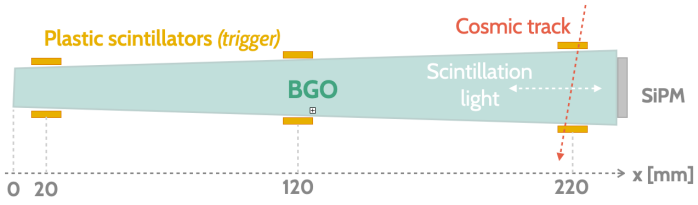

(b)

Figure 4.19: (a) Layout of the laboratory setup for the measurement of the BGO time resolution with cosmic rays. (b) A BGO crystal is sandwiched between two fast plastic scintillators, whose AND signal is taken as a trigger. Measurements were performed triggering at three positions x along the crystal.

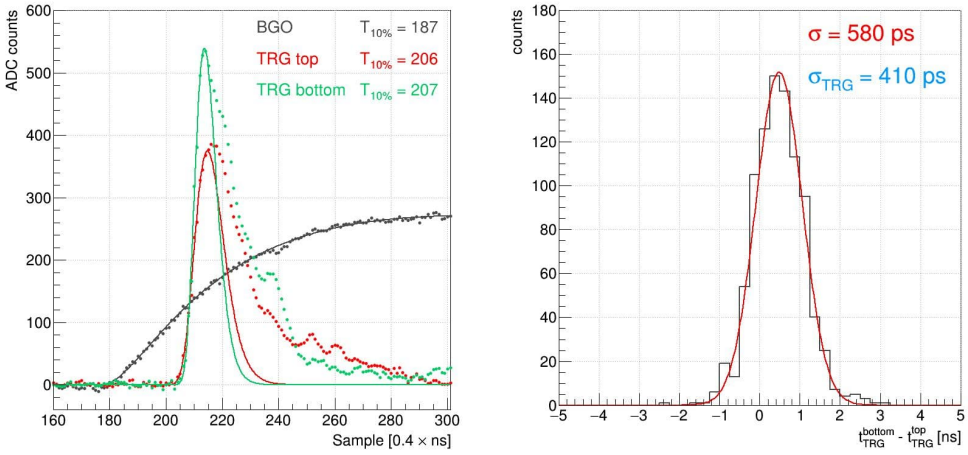

(a) (b)

Figure 4.20: Fragment of registered pulses (dots) and corresponding fits of the rising edge (solid lines) used for extraction of the time in the BGO crystal and in the plastic scintillators (a). Time difference between the timestamps of the two plastic scintillators, as obtained from the fit to the signal shape: assuming the contributions from the two plastic scintillators are equal and independent of each other, their time resolution, according to the error propagation, is evaluated to be about 410 ps (b).

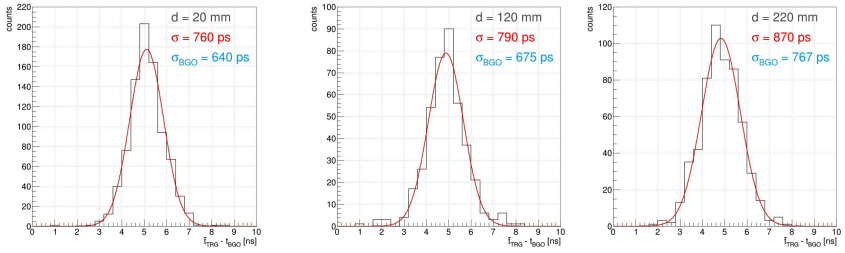

(a) (b) (c)

Figure 4.21: Time difference between the average time from the two plastic scintillators and the BGO, measured at three different positions d along the crystal. The corresponding time resolution for the BGO crystal, obtained by subtracting the previously evaluated time resolution of the trigger system, is about (640 ± 30) ps at $d = 20$ mm, slightly degrading towards the opposite end of the crystal.

and (767 ± 30) ps in the middle point and at the opposite end of the crystal, respectively. The worsening of the time resolution is supposedly caused by the increased difference between the path length of the photons emitted towards the SiPM and those emitted in the opposite direction, effectively making the rising edge of the pulse less steep.

Chapter 5

Crystal response corrections and calibration

5.1 Introduction

The calorimeter measures quantities (i.e. MA or TIA) proportional to the initial fragment energy. Thus, thanks to the detector response function (Fig 4.18 top) the fragment energy can be measured. However, the calorimeter raw response is not linear with the incoming particle energy and corrections have to be implemented. Moreover, the response of each crystal is not perfectly equal: crystals and photodetectors can be slightly different, and thus, crystals calibration is also needed.

The response correction for temperature, particle range and Birks effect are discussed in section 5.2, 5.3 and 5.4, respectively, while in 5.5 the implemented calibration protocol is shown.

5.2 Temperature correction

Both BGO crystal and SiPM are temperature sensitive and a correction has to be taken into account. An example of study of the BGO light yield as a function of the temperature is discussed in [91]. The study shows that the light yield is inversely proportional to the temperature and the coefficient of the percentage variation is $C_{BGO} = -(1.38 \pm 0.11\%)^{\circ}\mathrm{C}$.

On other hand, the SiPM gain G, defined as the number of electrons that contribute to the 1 photo-electron output current $i(t)$:

$$G = \int_0^{\infty} i(t)dt \approx \frac{(V_{bias} - V_{BD})C_j}{e} = \frac{\Delta V C_j}{e} \tag{5.1}$$

where ΔV is the OV, C_j is the junction capacitance of a single SPAD and e is the elementary charge. The plots in Figure 5.1 show as both the breakdown voltage V_{bd} and C_j depend on temperature [92].

Since FOOT will be a portable experiment, and will take data at different facilities (CNAO, GSI, etc.), likely at slightly different temperatures, a study of the stability of the calorimeter response is crucial. As shown, the BGO light yield and the SiPM gain are both sensitive to temperature and require either very stable operational conditions or a method for compensating temperature variations.

Each SiPM tile is therefore equipped with temperature sensors readable through an Analog Digital Converter (ADC) module. For the FOOT calorimeter a system based on an *Arduino UNO* board to monitor the crystal thermal status (Fig 5.2) has been chosen. Indeed, when monitoring the temperature variation during energy scans, i.e. from 70 MeV up to 227 MeV with proton and from 115 MeV/u up to

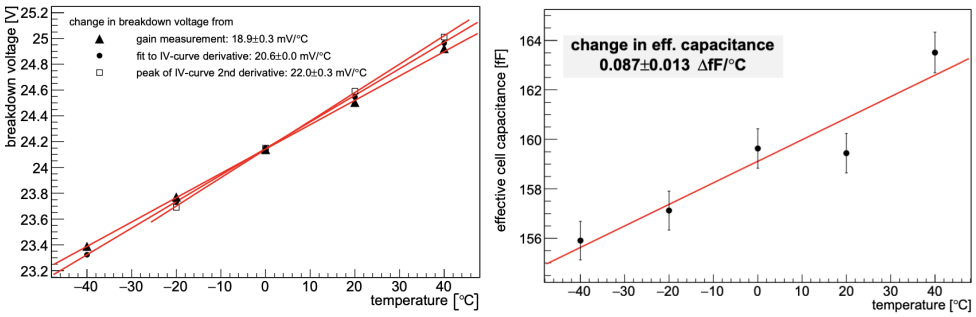

Figure 5.1: Breakdown voltage derived from the derivative of the I-V curves (solid dots), the second derivative of the I-V curves (empty squares), and gain measurements (triangles) for SensL J-series 30035 SiPM (left). Junction capacitance versus temperature for SensL J-series 30035 SiPM (right) [92].

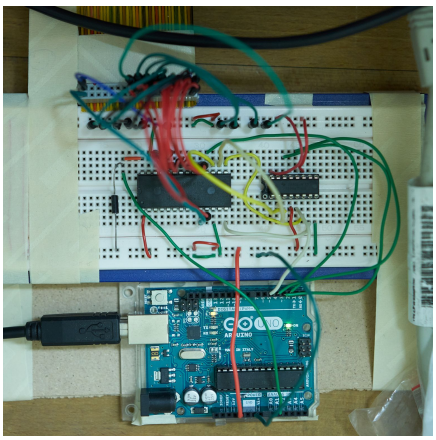

Figure 5.2: System based on Arduino UNO to read the SiPM temperature sensor.

399 MeV/u with carbon beam, at CNAO for a single crystal irradiation, an increase of about 2° was observed, as shown in Figure 5.3 (top). In the plot each run corresponds to a different beam energy.

Moreover, in order to build the correlation curve between the actual temperature (°C) and the sensor response (ADC), measurements in a thermally controlled environment have been performed. The correlation curve is shown in Figure 5.3 (bottom). Figure 5.4, instead, shows a picture of some crystals in the climatic chamber.

In order to assess the relevance of the temperature dependence, a dedicated test beam at CNAO was performed. The energy scan with proton and carbon on one BGO crystal was repeated 4 times: one at room temperature, 3 with a heat gun aimed at the SiPM tile at different distances (Fig. 5.5); the maximum observed temperature variation was about 15°C much larger than expected during data takings.

The results, shown in Figure 5.6 (top), highlight a linear dependency of the SiPM response (scaled by the number of nucleons in the incoming beam) on the temperature, with an angular coefficient that increases with the energy. Each set of points was fitted with a first order polynomial, and the slope parameter of each fit has been evaluated and studied as a function of charge at the selected reference temperatures T_1 (25 °C) and T_2 (34 °C), as shown in Figure 5.6 (bottom). From the measurement of the amplitude (A_{meas}) and temperature (T_{meas}), it is possible, by interpolating the

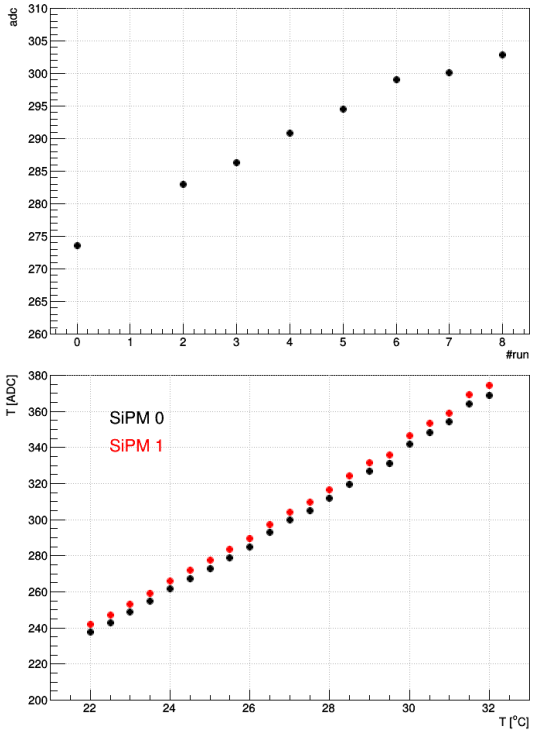

Figure 5.3: Evolution of the temperature during an energy scan. The temperature for run 1 was not recorded (top). NTC temperature sensor output as a function of the room temperature, as measured in a temperature-controlled environment (bottom).

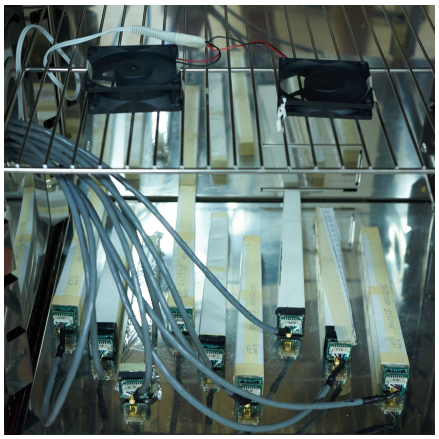

Figure 5.4: Picture of some crystals inside the climatic chamber for the NTC calibration runs.

Figure 5.5: Picture of the test beam at CNAO. One calorimeter module laid on the treatment bed with behind the heat gun to simulate temperature changings.

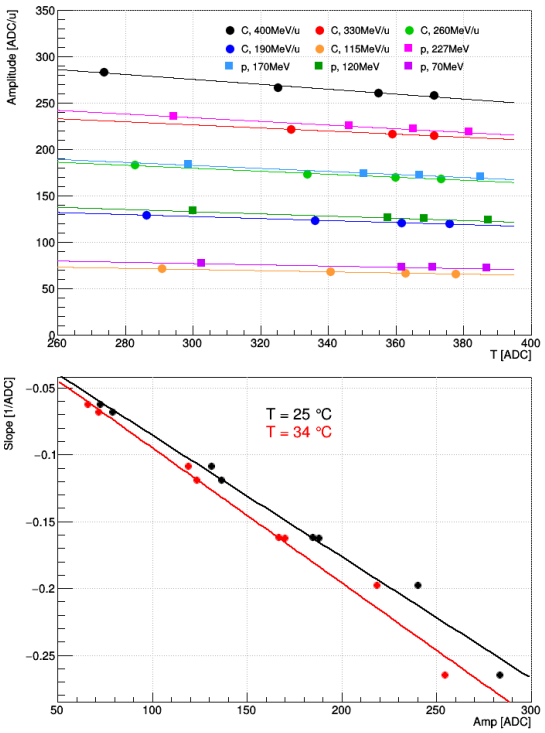

Figure 5.6: Average values of the Maximum Amplitude/nucleon (ADC/u) as a function of the Temperature ($^{\circ}C$): 4 runs, at different temperatures, were recorded at each of the 9 energies of a scan (top). The angular slopes as function of amplitude for two reference temperatures (bottom).

slope values at T_1 and T_2, to compute the actual slope (m_{meas}):

$$m_{meas} = m_1 + \frac{m_1 - m_2}{T_2 - T_1} \cdot (T_{meas} - T_1) \tag{5.2}$$

this angular slope can be used for correcting any energy measurement at T_{meas} to a T_{ref}:

$$A'_{meas} = A_{meas} + m_{meas} \cdot (T_{ref} - T_{meas}) \tag{5.3}$$

Figure 5.7 shows the pulse amplitude distributions obtained at the same beam energy and four different temperatures, before (blue) and after (red) the correction, and which is extremely effective. The comparison between the energy resolution at a fixed temperature and by combining data taken at different temperatures and corrected with the above-discussed method shows that the requirements on the energy resolution are successfully met. For example, the energy distributions for 330 MeV/u carbon ions are shown in Figure 5.7: the energy resolution deteriorates from 0.4% for the data taken at different temperatures separately (blue peaks) to about 0.6% for the total sample after the correction (red peak). Taking into account that the temperature range for which we applied the temperature correction is about $15^{\circ}C$, while the temperature variation during a complete energy scan data taking was measured to be about $2^{\circ}C$, we concluded that the installation of the calorimeter in a temperature-controlled volume is not required, as long as the SiPM temperature sensors response is regularly monitored.

Having validated the temperature compensation method, all the data presented in the following are temperature-corrected, with a reference value of $T = 25^{\circ}C$.

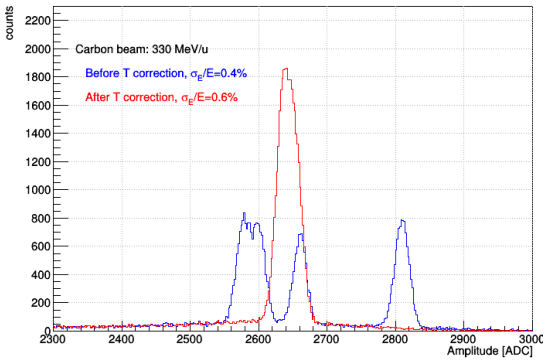

Figure 5.7: Raw measured charge for the 4 runs at 330 MeV/u (blue) and their sum after the temperature correction (red): the energy resolution for a single run is about 0.4%, to be compared to 0.6% for the sum of the runs after the temperature correction.

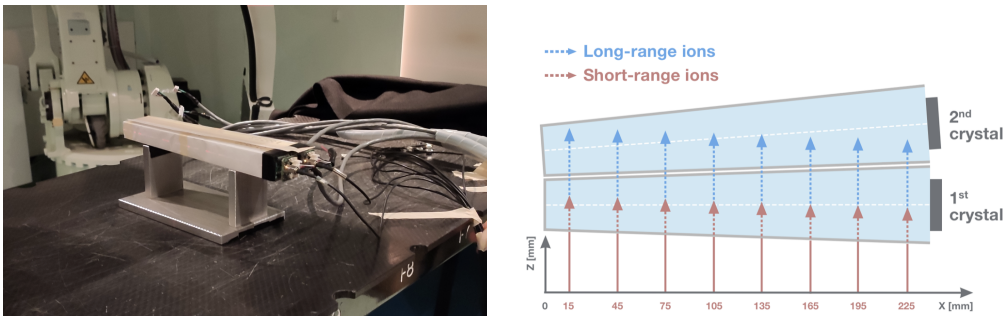

(a) (b)

Figure 5.8: (a) The 2 BGO crystals used for the data taking. (b) The beam was fired on the lateral side of the crystal at different positions, with 30 mm steps. The thickness of two crystals is sufficient to stop 70 MeV protons, 115 and 260 MeV/u carbon ions; for 170 MeV protons the range is shorter than the overall crystal thickness only for $x > 120$ mm.

5.3 Particle range correction

Dedicated test beams, with the goal of improving the understanding of the BGO response and of optimizing the calibration protocol, have shown that the detector response depends on the particle range, causing a non-linearity effect on the detector response.

In order to evaluate the effect of the particle range on the detector response, carbon ion beams at 115 and 260 MeV/u and proton beams at 70 and 170 MeV were aimed at the long side of 2 BGO crystals (Fig. 5.8), at different positions (at a distance $d = 15, 45, 75, 105, 135, 165, 195, 225$ mm from the crystal front face). Carbon ions and protons at the lower energies (115 MeV/u and 70 MeV) stop in the first crystal, while the carbon beam at 260 MeV/u crosses the first crystal, ending its path in the second; the 170 MeV proton beam ends its range in the second crystal only for $d > 120$ mm. Hence, for the first two energies the response in terms of MA and TIA is given by the only energy released in the crystal in front, instead for the higher energy beam the response is the sum of the contribution released in the two crystals.

The beam spot size, which is about 22 mm FWHM (70 MeV protons and 115 MeV/u carbon ions), slightly smaller for the higher energies, impacts on the width of the amplitude distributions, not on the average values reported in the following.

Table 5.1: Results of the exponential fit on CNAO data for amplitude and time-integrated amplitude analysis. The errors on the p170 data-set are larger because only four beam positions are available.

	Maximum Amplitude		Time-Integrated Amplitude	
Beam	$\alpha\ [m^{-1}]$	$R[\%]$	$\alpha\ [m^{-1}]$	$R[\%]$
p70	3.9 ± 0.8	9.9 ± 1.4	3.8 ± 0.8	9.9 ± 1.4
p170	3.8 ± 1.2	10 ± 4	3.3 ± 1.1	9.8 ± 3.0
C115	3.9 ± 0.2	10.2 ± 0.3	3.7 ± 0.2	9.8 ± 0.5
C260	3.5 ± 0.8	10.5 ± 0.3	3.3 ± 0.2	9.9 ± 0.5

A decrease of the MA and the TIA when reducing the distance from the SiPM tile was observed, as shown in Figure 5.9, compatible with the following function:

$$f(x) = A \cdot [R \cdot e^{-\alpha(L-x)} + (1-R)e^{-\alpha(L+x)}] \tag{5.4}$$

where x is the distance from the front side of the crystal, L its length, R the fraction of light that travels directly towards the SiPM tile and α the attenuation constant. The fit results are summarized in table 5.1. The error bars have been evaluated as the convolution of the amplitude peak Root Mean Square (RMS) and the beam position uncertainty. The former has been retrieved by the CB fit on the amplitude distributions; the latter, evaluating Eq. 5.4 in $\pm 1\ mm$ around the data points and taking the maximum uncertainty between $[|\bar{A} - A_-|, |\bar{A} - A_+|]$.

The ratio of the observed light collection at depth $d = x$ to the one at $d = 15\ mm$ as a function of the distance from the front side of the crystal (Fig. 5.10), within the errors, is independent of the particle and the energy: indeed, optical photon losses are expected to be independent of the origin of optical photons. The error bars have been evaluated by means of the propagation of uncertainty formula.

However, having measured a dependence of the response with the emission depth of optical photons, the effect must be corrected for. In order to do so, the range for protons and carbon ions for the CNAO beam energy was simulated with FLUKA, as well as the Average Emission Depth (AED) of optical photons, defined as:

$$AED = \sqrt{\frac{1}{N} \cdot \sum (x_i - x_{mean})^2} \tag{5.5}$$

Figure 5.11 shows both the range, i.e. BP position (circles) and the AED (triangles) for proton (black) and for carbon (red).

The average emission depth provides the correction factor to be applied to raw data: indeed, the scaling factor k_r can be computed by dividing the expected signal at $d = 0$, as if the optical absorption effect was not present, and at $d = AED$ evaluated from Figure 5.9:

$$k_r = \frac{A(d=0)}{A(d=AED)} \tag{5.6}$$

Figure 5.12 shows the comparison between the raw (red) and corrected (green) response both for proton and carbon beams, also corrected for temperature variations. The results of the linear fit after the correction, are reported in Table 5.2 and 5.3 for amplitude and time-integrated amplitude analysis, respectively. The response improvement is confirmed both from χ^2 tests and by the ratio between the data points and the linear fits shown in the bottom pads of Figure 5.12. After the

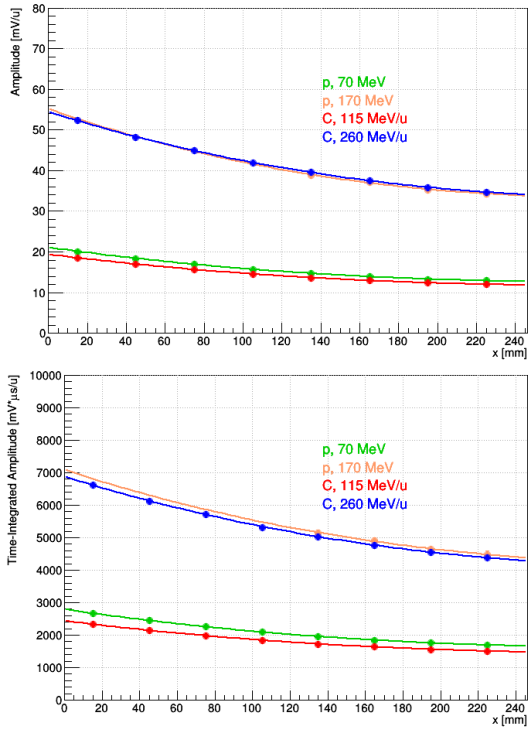

Figure 5.9: Signal Amplitude (top) and Time-Integrated Amplitude (bottom) as a function of the distance from the front side of the BGO crystal, for 70 MeV (green) and 170 MeV (orange) protons, 115 MeV/u (red) and 260 MeV/u (blue) carbon ions.

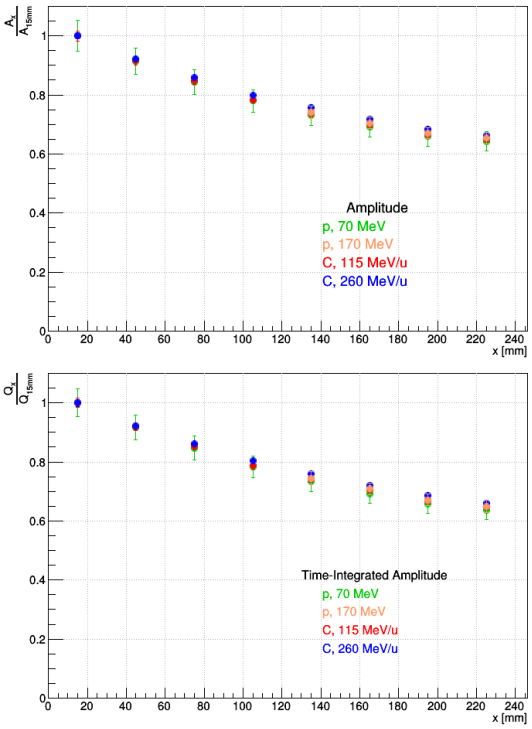

Figure 5.10: Ratio between the signal Amplitude (top) and Time-Integrated Amplitude (bottom) at distances $d = x$ and $d = 15$ mm from the crystal front side for 70 MeV (green) and 170 MeV (orange) protons, 115 MeV/u (red) and 260 MeV/u (blue) carbon ions.

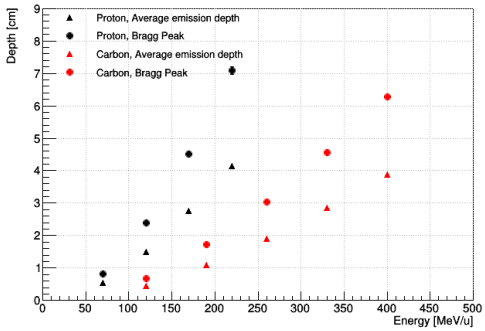

Figure 5.11: Range and AED of protons and carbon at the standard CNAO energy simulated by FLUKA.

Table 5.2: Fit results before and after range corrections for amplitude data.

	Raw Response			Corrected Response		
Beam	$m\ [mV/MeV]$	$q\ [mV]$	χ^2/NDF	$m\ [mV/MeV]$	$q\ [mV]$	χ^2/NDF
C	0.200 ± 0.001	-27.02 ± 2.22	75	0.228 ± 0.001	-68.15 ± 2.22	14
p	0.278 ± 0.005	2.32 ± 0.67	4	0.323 ± 0.005	-0.86 ± 0.67	1

correction the discrepancy between data and fit is $\leq$ 1% both for amplitude and time-integrated amplitude analysis.

The shape of BGO signals was also studied as a function of the beam position along the side of the crystal. Figure 5.13 shows that the rising time increases when the incoming point of the beam gets closer to the SiPM tile, confirming that the signal shape depends on the propagation of optical photons in the crystal. Figure 5.14 shows, for 70 MeV protons and 115 MeV/u carbon ions, the average value of the rising time as a function of the distance of the incoming beam from the front side. The error bars represent the standard deviations of each distribution. The linear fit yields a value related to the propagation speed of optical photons in the BGO. The values for protons, $v_p = (68 \pm 2)\ mm/ns$, and carbon ions, $v_C = (64 \pm 1)\ mm/ns$, when compared to the actual value ($v_{BGO} = c/n_{BGO} = 139\ mm/ns$), provide an estimation of the average optical photon path length, which is about 2.11 ± 0.04 the value expected for photons traveling straight to the photodetector. The comparison of the rising time values obtained for protons and carbon ions also shows that the difference is independent of the beam position: therefore, the shape difference in the signal is, as expected, related to the ionisation pattern, not to a different behaviour of optical photons.

Table 5.3: Fit results before and after range corrections for time-integrated amplitude data.

	Raw Response			Corrected Response		
Beam	$m\ [mV/MeV]$	$q\ [V]$	χ^2/NDF	$m\ [V/MeV]$	$q\ [mV]$	χ^2/NDF
C	26.38 ± 0.12	-5.6 ± 0.3	26	29.44 ± 0.12	-10.0 ± 0.3	1
p	37.4 ± 0.6	0.32 ± 0.09	5.5	43.2 ± 0.6	-0.10 ± 0.09	1.0

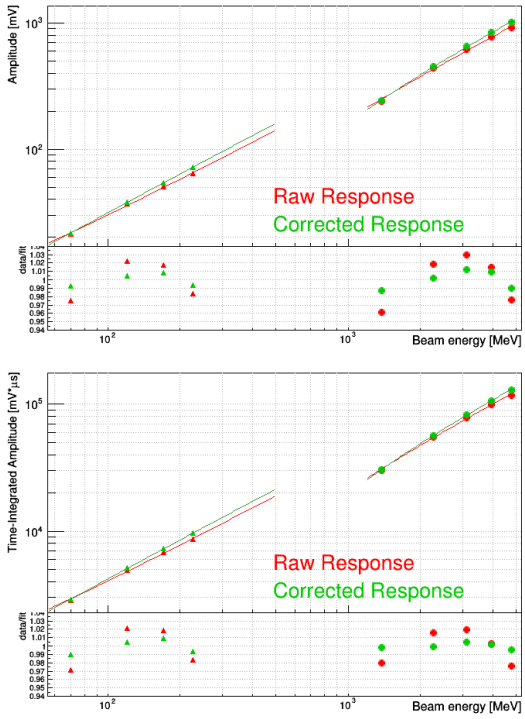

Figure 5.12: Amplitude (top) and Time-Integrated Amplitude (bottom) comparison before and after the particle range correction. The bottom pads show the ratio between the data points and the linear fit before and after the correction.

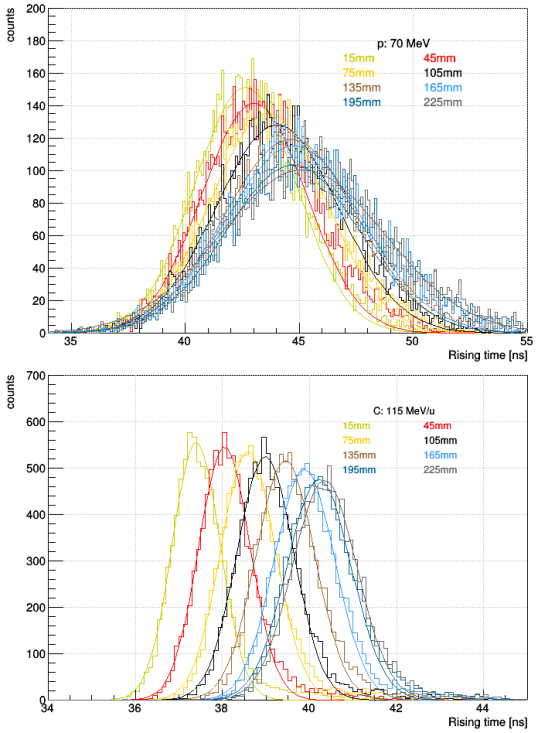

Figure 5.13: Rising time for 70 *MeV* protons (top) and 115 *MeV*/*u* carbon ions (bottom) as a function of the beam incoming position (distance from front face) in the BGO crystal. The rising time increases with the distance from the front face, because of the increasing difference in the travel path for photons traveling directly towards the photodetector, or not.

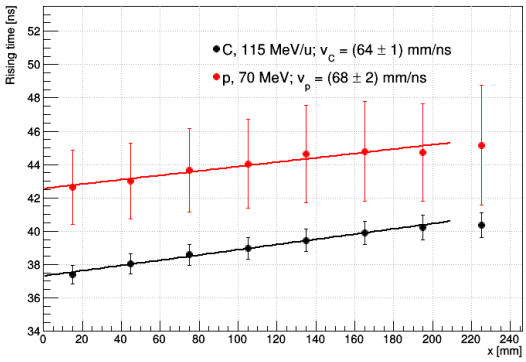

Figure 5.14: Average rising time for 70 MeV protons (red) and 115 MeV/u carbon ions (black) as a function of the beam incoming position (distance from front face) in the BGO crystal. The error bars represent the standard deviations of each distribution.

5.3.1 Monte Carlo simulation

The attenuation of the collected light with the proximity of the beam to the photodetector is counter intuitive, because one would expect the photons produced further away from the photodetector to be more attenuated. This effect was previously presented and investigated also for the Compact Muon Solenoid (CMS) electromagnetic calorimeter, as presented in [93]. However, in order to understand better the impact of this observed behaviour on the FOOT calorimeter, a detailed Monte Carlo simulation of the light propagation in the BGO crystal was implemented. The FLUKA-INFN (version 2020.0) software has been used to model a BGO crystal with $\rho = 7.13\ g/cm^3$ density, $n = 2.15$ refractive index, 10 $photons/keV$ light yield and 300 ns decay time. For each irradiation position (the same of experimental data), 100 primary particles were simulated. The SiPM tile was described as a volume of $30 \times 30 \times 1\ mm^3$, defined as an active area with a refraction index $n = 1.5$. The crystal was wrapped with Tyvek that, since it is made of 100% high density polyethylene fibers, was parameterized as C_2H_4 with 0.96 g/cm^3 density and 100 μm thickness. Since the comparison of the light collected at different beam positions is investigated, the SiPM photodetection efficiency was neglected: the optical photons impinging on the surface were counted and contributed to the definition of the expected output signal. Since the SiPM response was not modeled, the BGO scintillation spectrum and the dispersion of its refractive index were also not considered and all the other optical properties of the simulated volumes were assumed constant for all the wavelengths in the $360 - 650\ nm$ range (roughly corresponding to the $1.90 - 3.30\ eV$ photon energy range).

The simulation output consisted in the number of detected photons per event, their arrival time and coordinates (y,z) on the crystal rear side (i.e., the SiPM tile surface). Although in the experimental configuration the SiPM tile active area only covered the central portion of the BGO rear side, the simulation provided the light distribution on the entire surface, and the sensitive $20 \times 20\ mm^2$ region was selected in the post-processing for the comparison with experimental data. The amount of photons collected along the crystal is expected to depend on its optical properties, mainly on the reflection, absorption and diffusion coefficients. These simulation parameters were tuned by a relative comparison of the simulated number of optical photons as a function of the irradiation position to the trend observed for Time-Integrated Amplitude in the 70 MeV proton data-set, so as to determine the combination that best reproduced the experimental data (*tuning phase*). The validation was obtained by simulating the 115 MeV/u carbon response and by comparing the

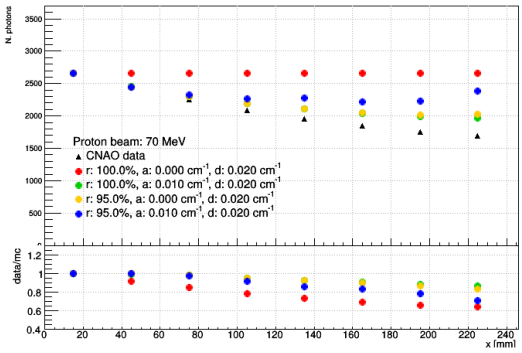

Figure 5.15: Tuning of the FLUKA simulation: choice of the combination of reflection coefficient and absorption coefficient. The bottom section shows the ratio between simulations and experimental data.

results with experimental data in the same manner as for the tuning phase (*validation phase*).

Simulations provide a response in terms of the number of detected optical photons. Therefore, their comparison to experimental data assesses the trend as a function of the irradiation position along the lateral side of the crystal. Unless otherwise specified, the first data point ($x = 15\ mm$) is used to equalize the distributions.

Tuning Phase

The comparison between the data taken at CNAO (black triangles) and the simulations (various coloured circle markers) of the photons collected with the Tyvek reflection coefficient set to $R_T = 100\%$ or 95% combined with the absorption coefficient values $\mu_a = 0.0\ m^{-1}$ and $\mu_a = 1.0\ m^{-1}$ is shown in Figure 5.15. At this stage the Rayleigh scattering coefficient was set to $\mu_s = 2.0\ m^{-1}$. Statistical uncertainties were calculated following the Poisson distribution and they result with dimensions comparable to the markers used in the plots.

Initially, a perfectly transparent crystal ($\mu_a = 0.0\ m^{-1}$) was simulated, while reducing the Tyvek reflectivity by 5%, from 100% (red circles) to $R_T = 95\%$ (yellow circles). The amount of collected light is constant for the case of 100% reflectivity and no absorption. In the remaining cases, the collected light intensity decreases when increasing the beam distance from the front side. For $R_T = 95\%$ and $\mu_a = 1.0\ m^{-1}$ there is a slight increase when the beam is at $x = 200\ mm$.

Since the emitted photons propagate either directly towards the SiPM or in the opposite direction, a higher reflection coefficient corresponds to an increased average path length of the photons inside the crystal, while the introduction of the absorption coefficient increases the probability for photons to be absorbed along their path. The bottom pad shows the ratio between data and Monte Carlo simulations in each beam position and shows that the best agreements ($\leq 20\%$) are achieved with the combinations of 100% and 1.0 m^{-1} or with 95% and 0.0 m^{-1} of Tyvek reflectivity and absorption coefficients, respectively.

Since, according to the literature [89], the reflectivity of Tyvek is about 97%, Figure 5.16 shows the corresponding simulation results compared to those obtained with 100% and with 95%reflectivity. The comparison with 100% is very similar, except for the beam position closest to the SiPM.

The light undergoes multiple scattering within the crystal lattice and non-specular reflections on the Tyvek coating. Therefore, keeping constant the Tyvek reflection

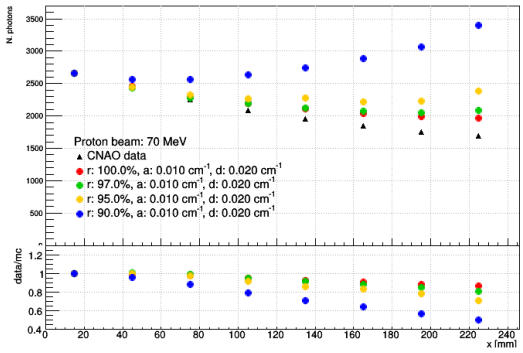

Figure 5.16: Tuning of the FLUKA simulation: fine tuning of the reflection coefficient keeping constant the absorption coefficient (1.0 m^{-1}). The bottom section shows the ratio between simulations and experimental data.

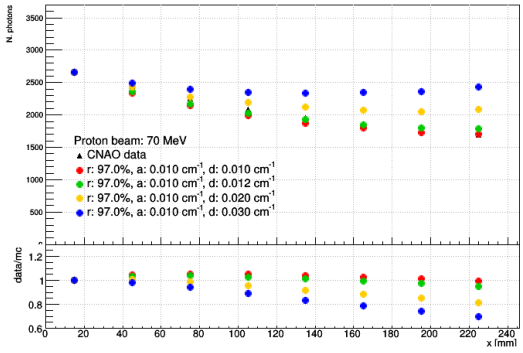

Figure 5.17: Tuning of the FLUKA simulation: fine tuning of the diffusion coefficient keeping constant the reflection coefficient (97%) and the absorption coefficient (1.0 m^{-1}). The bottom section shows the agreement within the 5% between Monte Carlo and experimental data.

coefficient at 97% and the absorption coefficient at $\mu_a = 1.0m^{-1}$, the Rayleigh scattering coefficient, that describes the photon diffusion, was investigated for different values, as shown in Figure 5.17. When increasing the diffusion coefficient the average number of scatterings between optical photons and the crystal lattice decreases and less light is absorbed. The best agreement between the FLUKA simulations and the CNAO experimental data, within a 5% accuracy, is obtained for $R_T = 97\%$, $\mu_a = 1.0\ m^{-1}$ (absorption coefficient) and $\mu_s = 1.0\ m^{-1}$ (diffusion coefficient).

Validation Phase

The parameters values that best fit the 70 MeV proton data sample were then validated on the 115 MeV/u carbon data set. Figure 5.18 shows the comparison between experimental data (black markers) and FLUKA simulations (red markers), for the 70 MeV proton (circles) and 115 MeV/u (triangles) data sets. For both types of particle, an accuracy within 5% is achieved.

5.3.2 Applications of the Monte Carlo simulations

Although the comparison between data and simulations is satisfactory, extra simulations were performed to further investigate some aspects related to the optical photon path.

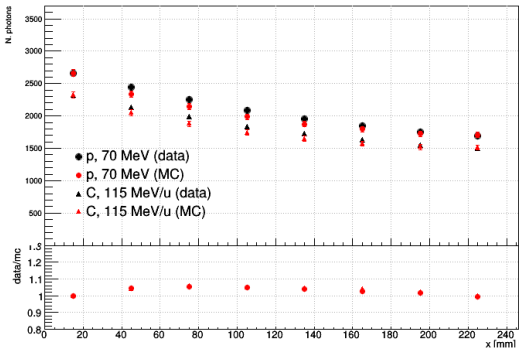

Figure 5.18: Comparison among experimental data (70 MeV protons, black circles, and 115 MeV/u carbon ions, black triangles) and FLUKA simulations (70 MeV protons, red circles, and 115 MeV/u carbon ions, red triangles). The bottom section shows the ratio between simulations and experimental data.

Optical photon tracking

Figure 5.19a and 5.19b shows the path of 5 scintillation photons in the BGO for the two extreme production positions, i.e. $x = 15\ mm$ (a) and $x = 225\ mm$ (b). Optical photons produced closer to the photodetector ($x = 225\ mm$) undergo a significantly larger number of reflections at the crystal surface, and their longer travel path within the crystal increases their probability to be absorbed before reaching the photodetector array. This seems to be one of the main contributing factors in the position-dependence of the amount of light collected in the experimental data.

Figure 5.19c reports the average number of reflections undergone by optical photons as a function of their production position within the BGO. The results, obtained by tracking 1000 primary optical photons at each position, produced by an isotropic optical photon source located in $(x, 0, 0)$, quantitatively confirm that the average number of reflections increases when the scintillation photons are produced closer to the SiPM tile.

Spatial distribution of the detected photons

Figure 5.20 shows the maps of the scintillation photon arrival position on the photodetector surface. Simulations were performed for all the experimental production positions, and also for additional points with $x > 195\ mm$. For clarity, the results are only reported for the most significant production positions, for the 70 MeV proton configuration. The distribution appears homogeneous for all the irradiation positions except for the one closest to the photodetector array (bottom left).

Figure 5.21 shows the percentage of the scintillation photons reaching the SiPM surface that fall within the SiPM tile (red central region in fig. 5.20) and that are thus potentially detectable in the measurements (although the SiPM photo-detection efficiency is not modeled). Results are reported for two extreme cases, considering that the SiPM active area is either concentrated in the central $20 \times 20\ mm^2$ region (blue) or extends to a larger $20 \times 23\ mm^2$ area and the active region is alternated with dead areas (red). In the figure, in addition to the experimental positions (circles), the additional simulated positions close to the SiPM tile (crosses) are reported. For both cases, the percentage is approximately constant for most positions, and equal to about 45%. When approaching the photodetector ($x > 195\ mm$) the percentage increases rapidly, up to 53% and 51%, respectively. This phenomenon can be understood by analysing the maps shown in Figure 5.20: as the beam gets closer

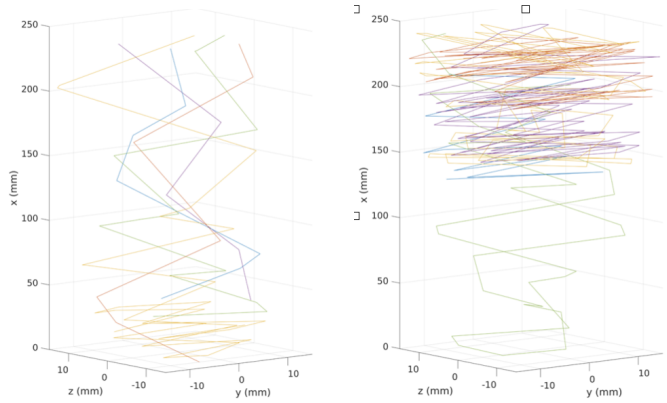

(a) (b)

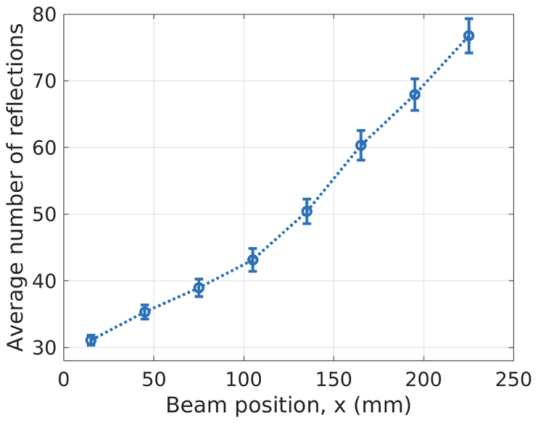

(c)

Figure 5.19: Example paths for 5 scintillation photons in the BGO for the two extreme production positions, $x = 15\ mm$ (a) and $x = 225\ mm$ (b), and (c) average number of reflections undergone by the optical photons as a function of their production position (error bars represent the error on the mean).

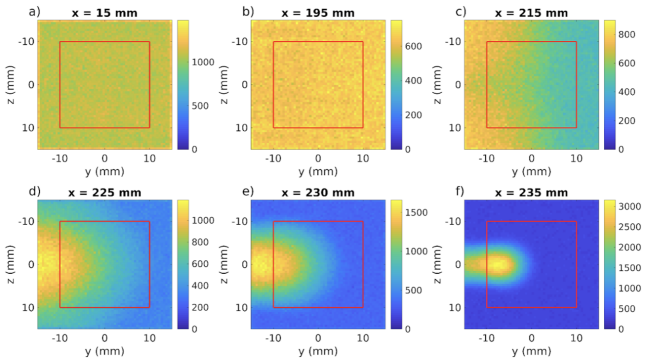

Figure 5.20: Simulated distribution of the arrival position of scintillation photons on the photodetector surface, for the most significant beam positions, for the 70 MeV proton configuration.

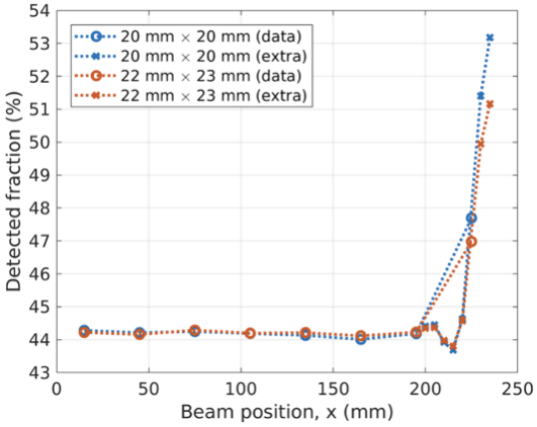

Figure 5.21: Simulation of the fraction of the scintillation photons reaching the SiPM surface that can potentially be detected as a function of the beam position. Circles refer to positions at which experimental data were taken. Statistical uncertainties were smaller than 10% thus error bars are not reported for clarity. The sensitive area is $20 \times 20\ mm^2$; the $20 \times 23\ mm^2$ configuration corresponds to the actual geometry of the SiPM tile, taking into account dead areas between cells.

to the SiPM tile, the direct component of the detected scintillation emission is more concentrated around the Bragg peak, which falls inside the red square. Moreover, since the orange curve corresponds to the counts on a $20 \times 23\ mm^2$ area, then rescaled to an equivalent active area of $20 \times 20\ mm^2$, the detected fraction is smaller than the actual $20 \times 20\ mm^2$ central part of the tile.

Effect of the crystal shape

Besides the effect of physical parameters like the reflection, absorption and diffusion coefficients, we have investigated the impact of the crystal shape on the light collection, using the FLUKA simulation. Figure 5.22 shows the light reaching the SiPM interface for different crystal shapes as a function of the distance from the front side: several configurations were simulated, by keeping the size of the front side ($20 \times 20\ mm^2$) and the length of the crystal ($240\ mm$) fixed and by progressively reducing the dimensions of the rear side, between $30 \times 30\ mm^2$ and $20 \times 20\ mm^2$, with $1\ mm$ side steps. The optical parameters that best reproduce the experimental data were used ($R_T = 97\%$, $\mu_a = 1.0\ m^{-1}$ and $\mu_s = 1.0\ m^{-1}$). As the size of the crystal rear side is reduced, the light loss progressively decreases, until the effect is reversed and the light collection increases when firing closer to the photodetector. In order to best compensate for the light attenuation effect in the crystal, a truncated pyramid with a rear side of $23 \times 23\ mm^2$ would be required.

5.4 Quenching effect in BGO crystal

The calorimeter linearity response is affected by another physical effect called *light quenching* or *Birks effect*.

Indeed, the intensity of the scintillation produced in a crystal depends both on the energy and on the nature of the incident ionizing particle. Called S the amplitude of the voltage pulse from a photodetector, operating under constant conditions, it is proportional to the number of fluorescent quanta produced, and hence S may be used as a measurement of the scintillation intensity. As reported by Birks in [94], for electrons of energy greater than $125\ keV$, the scintillation intensity S from a crystal increases linearly with the energy E [95], so that the fluorescent efficiency dS/dE

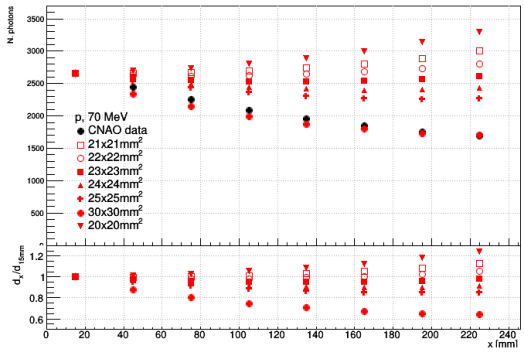

Figure 5.22: Simulated light output collected at the SiPM interface for seven different BGO geometries (same length and front side size of the experimental one, but different shape) as a function of the distance from the front side.

(V/MeV) is constant. For electrons of lower energy, however the efficiency dS/dE is reduced. With heavier particles, which produce more intense ionization, a further reduction in dS/dE occurs, and the scintillation intensity is consequently smaller than that produced by an electron of the same energy.

The response to different ionizing particles can be readily compared by considering the variation of the specific fluorescence dS/dx (V/cm) [96], which is proportional to the number of fluorescent quanta emitted per unit path length, with the specific energy loss dE/dx (MeV/cm), where x (cm) is the range of the particle. At low values of dE/dx (as electrons of $E > 125\,keV$) the specific fluorescence is proportional to the specific energy loss, corresponding to S increasing linearly with E. At high values of dE/dx, dS/dx is practically constant and independent of the specific energy loss. The scintillation intensity S is thus proportional to the residual range x of the particle, rather than to its energy E.

In [94], Birks supports the thesis that the variation of dS/dx with dE/dx may be accounted for by the *exciton* theory introduced by Bowen in [97] to account for the fluorescence of mixed crystals, excited by ultra-violet radiation. In this theory of energy transfer processes in organic crystals, the electronic energy excited by the incident radiation is transferred from molecule to molecule within the crystal, until it is captured by a single molecule, which then either fluoresces or quenches the exciton, depending on the nature of the molecule. This theory has been successfully applied to the energy transfer in mixed crystals of naphthalene and anthracene excited by radiation, where both molecular components fluoresce, but the anthracene molecules have the higher exciton capture probability [98]. It has also been used to explain the deterioration of the fluorescent efficiency of anthracene under prolonged α-particle irradiation [99]. In this case, the molecules damaged by the preceding α-particle irradiation act as quenching agents, having a higher exciton capture probability than the undamaged anthracene molecules.

A similar effect will also occur with individual ionizing particles. The passage of the particle through the crystal produces a local concentration of damaged or ionized molecules along its path. These damaged molecules act as quenching agents for the excitons produced by the ionizing particle. The number of excitons produced per unit path length is proportional to the specific energy loss: $A \cdot dE/dx$. Birks parametrizes the specific fluorescence as:

$$\frac{dS}{dx} = \frac{A \cdot dE/dx}{1 + k \cdot B \cdot dE/dx} \tag{5.7}$$

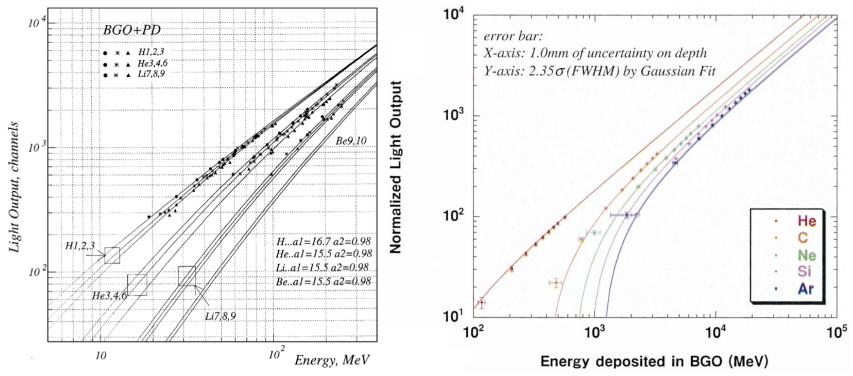

Figure 5.23: BGO crystal response as function of different ion beams [100] left and [101] right.

where A describes the efficiency for converting the energy deposited per unit length into scintillation photons, $B \cdot dE/dx$ represents the density of quenching centers per unit distance and k is the quenching parameter.

In recent years, several experiments have confirmed this effect studying the crystal response for different ions [100–102]. Some examples for BGO crystals are reported in Figure 5.23.

During the performance tests of the FOOT calorimeter, we ran into the Birks effect, which creates non-linearity effect and non-unique calorimeter response, i.e. problems in the energy reconstruction. When normalizing the calorimeter response of Figure 5.16, corrected for temperature and particle range, to the number of nucleons, it is clearly visible that protons and carbon-ions have two different responses (Figure 5.24).

The pulse shape analysis, studied the Eq. 4.1, has shown that is possible discriminate different ions. Figure 5.25 (top) shows the correlation between the rising time and the shape parameter (t_r and k_s, respectively) for protons and carbon ions for all the energies: the two groups are well separated, mostly thanks to the rising time parameter, shown in Figure 5.25 (bottom) for protons and carbon ions at all the different test energies.

However, proton and carbon ions are slightly different particles, the real challenge would be to understand if also oxygen and the other intermediate ions can be discriminated with the pulse shape analysis so far. Unfortunately, there weren't opportunities to deliver other ions on BGO crystals. The HIT facility center (Heidelberg, Germany), one of the Europe's largest and most modern medical center, can provide protons, Helium, Carbon and Oxygen ions and it would be the best option to test the calorimeter response. A proposal to have beam time has been prepared by the Turin group and sent to HIT (we are waiting for an answer).

Anyhow, one of the best ways to reconstruct the fragment energy, is using use the information from other detectors, such as the charge measured by the TW. From this information, it is possible to discriminate among the ion-response curves and reconstruct the correct fragment energies.

5.5 Crystals calibration protocol

One important step in the calorimeter development is its *calibration*. Indeed, in order to reconstruct the fragment energy in the right way the calorimeter response has to be uniform in each BGO crystal. Thus, a calibration protocol must be implemented to equalize the crystal responses.

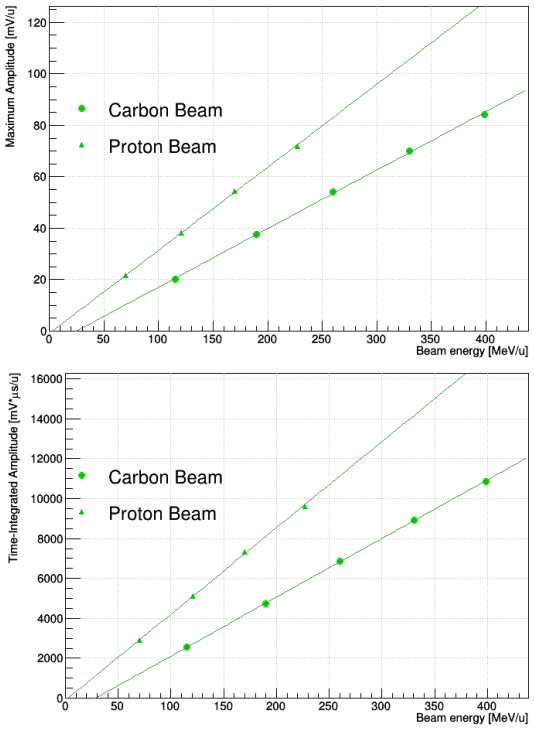

Figure 5.24: Normalized calorimeter response by beam mass number in terms of signal Amplitude (top) and Time-Integrated Amplitude (bottom) as function of beam energy corrected for temperature and particle range.

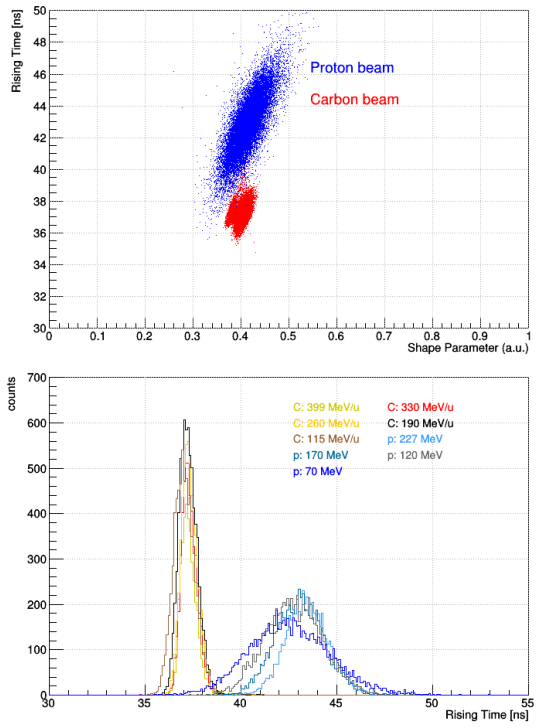

Figure 5.25: Scatter plot of the rising time for proton and carbon signals and the shape parameter (top). Rising time for proton and carbon signal distributions at different energies (bottom).

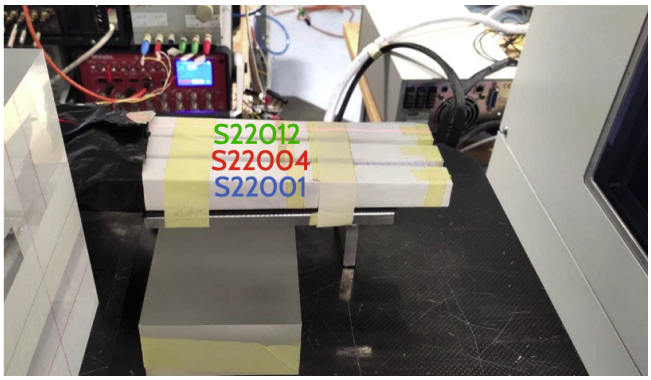

Figure 5.26: Picture of the test beam setup in the treatment room at CNAO. The crystal IDs are reported in the picture.

In the previous sections the response of the SiPM tile for a single BGO crystal irradiated with 9 different energies was discussed. However, when different crystals are irradiated, the average values of the amplitude distributions are slightly different. Even though the BGO crystals should be ideally identical and lead to the same behavior, their responses can be affected by several differences in terms of geometry, crystal lattice structure and mostly SiPM gain fluctuation.

5.5.1 Experimental setup

A dedicated test beam at CNAO was performed to define the calorimeter calibration protocol. Three crystals labeled with *S*22001, *S*22004 and *S*20012 IDs have been irradiated with proton and ion beams. The NTC thermistor monitored the temperature during each run in order to correct the data, as discussed in 5.2. A picture of the experimental setup is shown in Figure 5.26.

Two different calibration methods have been studied (Figure 5.27) in order to understand which provides the best performance:

1. **Lateral scan**: 70 MeV protons and 115 MeV/u carbon ions have been used to perform a lateral scan, where the beam impinged on the long side of the crystal at different positions ($d = 15, 45, 75, 105, 135, 165, 195$, and 225 mm from the front side). The protons and carbon ions at lowest energies available were selected to completely contain the beam in one crystal. The SiPM power supply was set to 34.5 V.

2. **Frontal scan**: the beam at the 9 standard energies (70, 120, 170 and 227 MeV for protons and 115, 190, 260, 330 and 400 MeV/u for carbon ions) was delivered at the front side of the BGO crystals. For this test beam the CAEN digitizer v1742 was used. However, as explained in 4.3.3, this CAEN digitizer doesn't provide the possibility to set an attenuator, and consequently the SiPM power supply was reduced to 32.5 V to contain the signal maximum amplitude of the highest beam energy.

Frontal and lateral scans were used in order to compute the inter-calibration factors associated to each BGO crystal in different configurations. Then, the factors have been applied to equalize the responses of the crystals to the one chosen as reference.

Afterwards, in order to validate the calibration methods, the 3 crystals have been positioned side-by-side and fired with 170 MeV proton and 330 MeV/u carbon ions

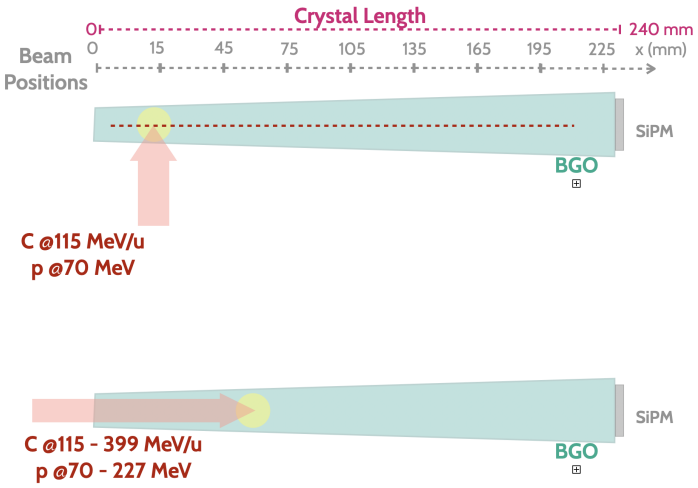

Figure 5.27: Sketch of the lateral (top) and frontal (bottom) scan test.

Table 5.4: Absorption coefficients fit results for 70 MeV proton and 115 MeV/u carbon beam

	$\alpha\ [mm^{-1}]$	
Crystal ID	70 MeV	115 MeV/u
S22001	0.0035 ± 0.0011	0.0027 ± 0.0003
S22004	0.0034 ± 0.0010	0.0032 ± 0.0003
S22012	0.0039 ± 0.0010	0.0037 ± 0.0002

beams at different positions on the long side ($d = 15, 40, 80\ mm$ for 170 MeV proton and $d = 15, 40, 80\ mm$ for 330 MeV/u carbon). The beam first impinged on $S22001$, then $S22004$ and finally $S20012$, releasing three different amounts of energy in each crystal. The three energy contributions were equalized and summed, then compared to amplitude values observed in the frontal scan.

5.5.2 Results

Lateral Scan

In Figure 5.28 the MA values, corrected for temperature, are shown as a function of the beam position for 70 MeV proton and 115 MeV/u carbon ions. In the pad below the average values of temperature associated to each run are presented. As shown in 5.3, the light collected decreases as the beam gets closer to the SiPM tile. A fit with Eq. 5.4 has been performed and by comparing the absorption coefficients α, it can be stated that the trend of the response is compatible within the errors (Tab 5.4).

In order to equalize the crystal response, the inter-calibration factors have been computed using data from the lateral scans. The $S20012$ crystal has been chosen as reference, then the inter-calibratrion factors are evaluated as the ratio of the light extrapolated from the fit to experimental data at $d = 0\ mm$ for the i^{th} crystal to the light observed at $d = 0\ mm$ for the reference one, separately for protons (k_{p_i}) and carbon ions (k_{C_i}):

$$k_{(p/C)_i} = \frac{A_i(d = 0\ mm)}{A_{ref}(d = 0\ mm)} \tag{5.8}$$

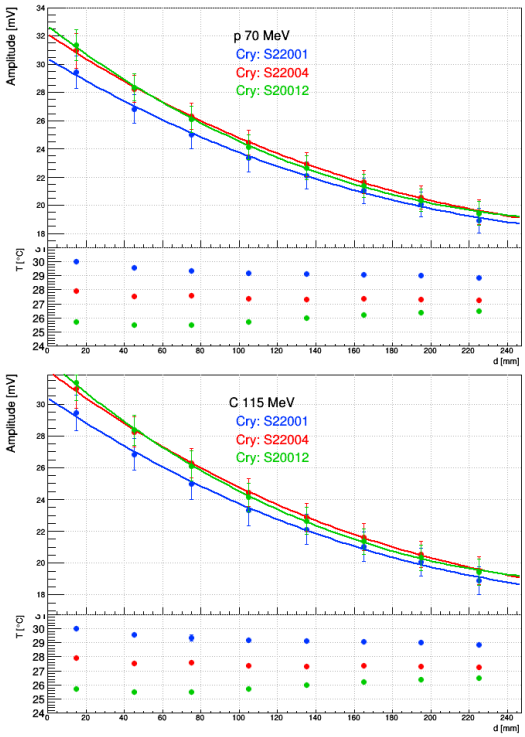

Figure 5.28: Amplitude values, corrected for temperature, as a function of the beam position for 70 MeV proton (top) and 115 MeV/u carbon beam (bottom). The bottom pads shows the temperature values recorded during the scan.

Table 5.5: Inter-calibration factors evaluated from the lateral scan

Crystal ID	k_p	k_C	$\bar{k}_{eq}$
S22001	0.929 ± 0.013	0.927 ± 0.004	0.928 ± 0.007
S22004	0.982 ± 0.013	0.982 ± 0.003	0.982 ± 0.007
S22012	ref	ref	ref

where $i = S22001, S22004, S20012$. The inter-calibration factor (k_i) associated to the i^{th} crystal, is then computed as the mean of the factors evaluated from the protons lateral scan and the carbon ions one according to:

$$\bar{k}_{eq_i} = \frac{k_{p_i} + k_{C_i}}{2} \tag{5.9}$$

The resulting inter-calibration factors are summarized in Table 5.5.

As shown in section 5.3, from the lateral scan also the range correction factors can be evaluated. A set of range correction factors have been evaluated by using the AED associated to the 9 energies of the frontal scan, previously mentioned. In principle, the range correction factor has no dependence on the particle type but since the absorption coefficients α retrieved by the fit function are similar but not equal from crystal to crystal, the k_{range} factors could be different. Therefore, range correction factors have been evaluated for each energy and for each crystal separately. The correction k_{range} values for each energy and for each crystal are summarized in Table 5.6.

Table 5.6: Range correction factors for the three crystals tested and for the 9 predefined energies.

Beam Energy [MeV/u]	k_{range} S22001	S22004	S22012
70	1.0129	1.0142	1.0162
120	1.0373	1.0410	1.0468
170	1.0694	1.0762	1.0871
220	1.1047	1.1150	1.1315
115	1.0107	1.0117	1.0134
190	1.0272	1.0299	1.0342
260	1.0477	1.0524	1.0599
330	1.0717	1.0787	1.0900
399	1.0985	1.1082	1.1237

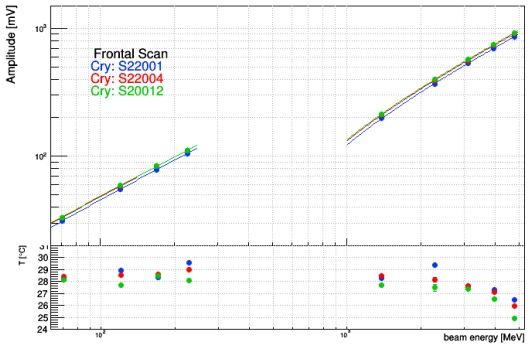

Figure 5.29: Average values of the MA distribution, temperature and range-corrected data, recorded during the frontal scan as a function of the total beam energy. The bottom pads shows the temperature values recorded during the scan.

Frontal Scan

The plot in Figure 5.29 shows the average values of the MA, temperature and range corrected, as a function of the total beam energy and their linear fits. In the pad below the average values of temperature associated to the run are presented. By choosing a reference crystal (S20012), a set of inter-calibration factors are evaluated as the ratio of the average amplitude values of the i^{th} crystal to the average amplitude values of the reference one: therefore, each factor k_{E_j} are evaluated at energy j^{th}.

$$k_{i_{E_j}} = \frac{A_{i_{E_j}}}{A_{ref_{E_j}}} \tag{5.10}$$

where $i = (S22001, S22004, S20012)$ and $E_j = (70, 127, 170, 227)\ MeV$ for proton and $Ej = (115, 190, 260, 330, 400)\ \mathrm{MeV}/u$ for carbon ions.

Then the mean of the set for the i^{th} crystal is evaluated:

$$\bar{k}_{eq_i} = \frac{1}{N}\sum_{E_j} k_{i_{E_j}} \tag{5.11}$$

where $N = 9$, the number of energies under study. The inter-calibration factors are summarized in Table 5.7.

Table 5.7: Inter-calibration factors evaluated from the frontal scan

Crystal ID	k_{70}	k_{120}	k_{170}	k_{227}	k_{115}	k_{190}	k_{260}	k_{330}	k_{399}	$\bar{k}_{eq}$
S22001	0.937	0.931	0.929	0.920	0.927	0.945	0.933	0.931	0.934	0.932 ± 0.006
S22004	0.985	0.981	0.979	0.978	0.986	0.986	0.995	0.987	0.985	0.985 ± 0.005
S22012	ref	ref	ref	ref	ref	ref	ref	ref	ref	ref

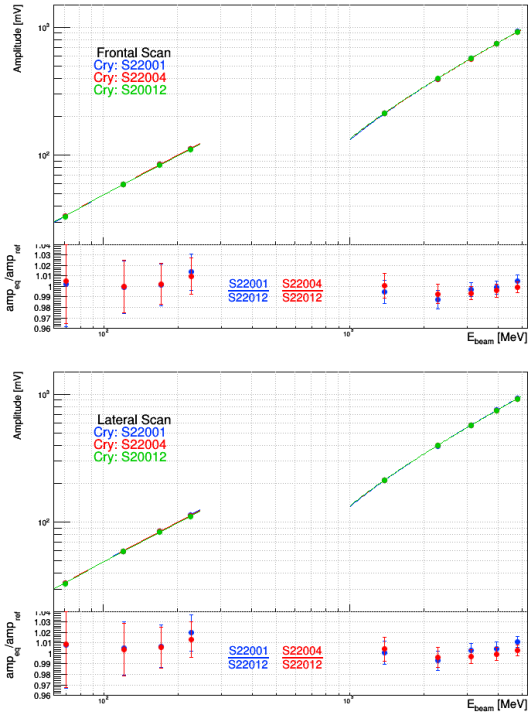

Figure 5.30: Calibrated average amplitude values as a function of the beam energy, using frontal scan method (top) and using lateral scan method (bottom). The plots below show the ratio of the calibrated amplitude value to the reference one.

5.5.3 Calibration protocol validation

In order to have a first validation of the procedure, the inter-calibration factors evaluated by both the frontal and the lateral scan, presented in Table 5.5 and 5.7, have been applied to equalize the crystal response. Figure 5.30 (top) and 5.30 (bottom) show the response calibrated with the factors computed from the frontal and lateral scan, respectively. In the bottom pads the ratios of the MA values of the i^{th} crystal to the reference ones have been evaluated. In principle, since there are similar condition among the crystals, the expected ratios after the calibration are ~ 1. Indeed the ratios are close to 1, in both configurations, and it can be stated that both the inter-calibration methods are reliable.

During the test beam dedicated runs have been carried out in order to validate the inter-calibration methods. The three crystals have been positioned side-by-side and 170 MeV proton and 330 MeV/u carbon ions beam have been fired at the long side of the $S22001$ crystal, in three different positions ($d = 15, 45, 80\ mm$ for 170 MeV proton and $d = 15, 45, 65\ mm$ for 330 MeV/u carbon, from the front side of the BGO crystal). The previous energies have been selected in order to allow the beam to cross the three crystals, thus obtaining different amounts of energy in all of them. The three energy loss contributions must be calibrated by using the proper inter-calibration factor associated to each crystal. The setup is sketched in Figure 5.31.

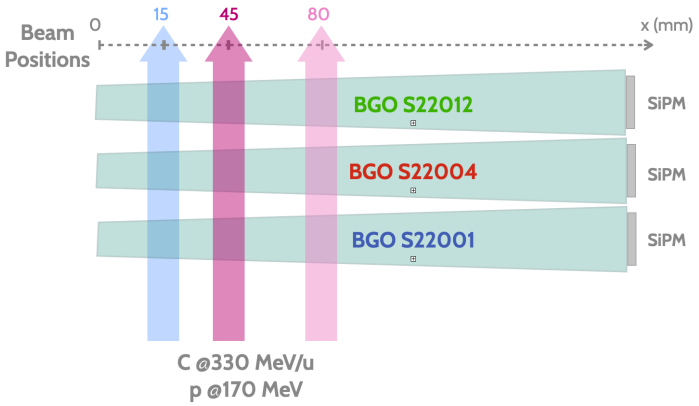

Figure 5.31: Sketch of the test performed in order to validate the calibration method.

The raw amplitude distributions of the three energy depositions for the 170 MeV proton beam impinging at 15 mm are shown in Figure 5.32 (top). The sum of the raw amplitude distributions for the 170 MeV proton beam impinging at the 3 beam positions and compared with the amplitude distribution for the 170 MeV proton beam fired at the front side of the crystal (yellow filled) are shown in 5.32 (bottom).

Then, the inter-calibration was applied: the three amplitude contributions have been calibrated with the factors evaluated from the frontal scan, as shown in Figure 5.33 (top), and the ones from the lateral scan, as shown in Figure 5.33 (bottom), then they have been summed together and, in the end, compared with the amplitude distribution observed for the 170 MeV proton beam of the frontal scan (yellow filled).

Even though both the inter-calibration factors were applied, there is no agreement between the amplitude sum of the three contributions and the amplitude value observed from the frontal scan. Indeed, the range correction must be applied. Range correction factors have been computed by taking into account the three different beam positions ($d = 15, 40, 80$ mm) at which the beam was fired and the different responses of each crystal shown in Figure 5.28. By applying the range correction, the amplitude distributions peak all at the same value with a discrepancy below 1% for both the inter-calibration methods, as shown in Figure 5.34.

The same validation has been applied to the 330 MeV/u carbon ions beam. The inter-calibrated and range-corrected amplitude distributions of the sum are shown in Figure 5.35. In this test, no amplitude distribution from the frontal scan can be compared, since the carbon ions beam at 330 MeV/u leads to a saturation of the dynamic range of the digitizer if the power supply of the SiPM is set to 34.5 V . Therefore, for this run the SiPM HV was lowered to 32.5 V and hence the comparison is not meaningful. Taken as reference the amplitude distribution at the 65 mm beam position, there is a discrepancy of 12% and 11% for the amplitude distribution measured at 40 mm and 15 mm beam positions, respecitvely.

5.5.4 Protocol optimization for 320 BGO crystals

Since about 30 min are required to perform a lateral (8 runs) or frontal scan (9 runs) and that beam time at CNAO is available only in the night ($22pm - 5am$), about $30 - 40$ nights would be needed to calibrate all the 320 calorimeter crystals. Therefore, in order to speed up the calibration procedure, it was investigated whether lowering the number of points in a scan worsens the quality of the calibration.

The study aims at investigating the factor variations when they are evaluated using less than 9 points of the frontal scan or less than 8 points of the lateral scan.

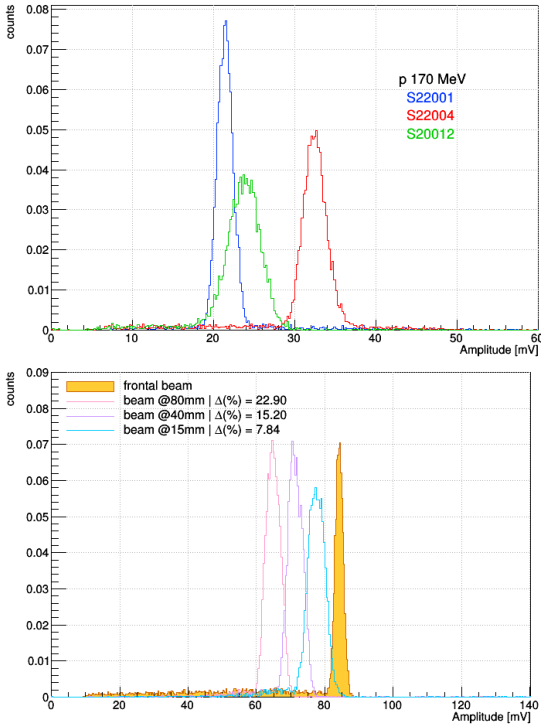

Figure 5.32: Temperature-corrected amplitude distributions of the three energy loss contribution in the three crystals tested for 170 *MeV* proton beam impinging at 15 *mm* (top). Amplitude distributions of the sum of the three contributions, with no calibration, for the 170 MeV proton beam fired at the 3 beam positions (15 *mm*, 45 *mm* and 80 *mm*). The amplitude distribution at the same energy beam fired at the front of the BGO crystal is filled in yellow. (bottom)

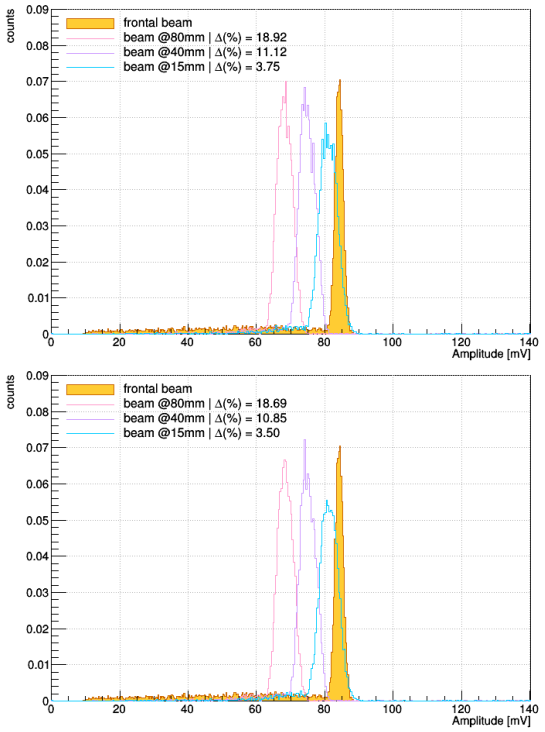

Figure 5.33: Calibrated amplitude distributions of the sum of the three contributions for the 170 *MeV* proton beam fired for the 3 beam positions, equalized using the frontal scan method (top) and the lateral scan method (bottom). The amplitude distribution for the same beam fired at the front of the BGO crystal is filled in yellow.

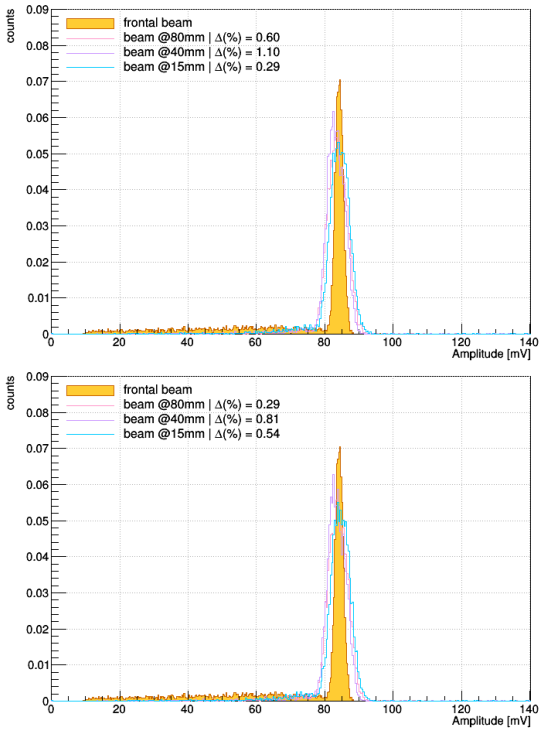

Figure 5.34: Calibrated and range-corrected amplitude distributions of the sum of the three contributions for 170 MeV proton beam fired for the three beam positions equalized using the frontal scan method (top) and the lateral scan method (bottom). The amplitude distribution for the same beam fired at the front of the BGO crystal is filled in yellow.

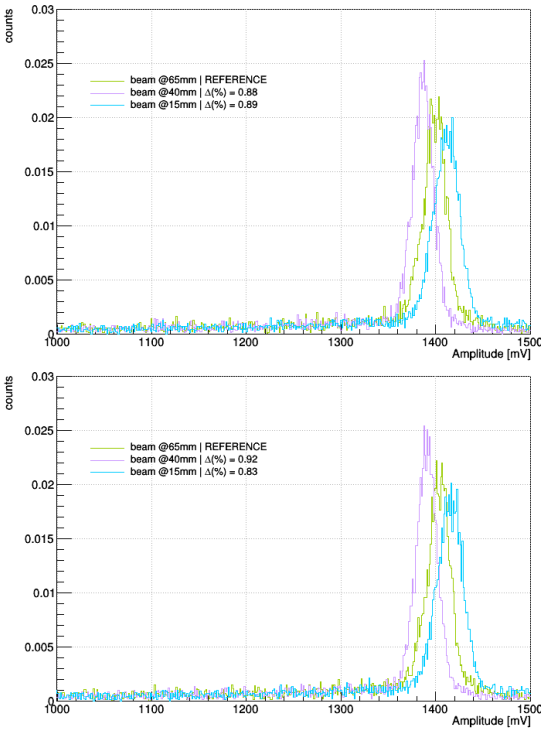

Figure 5.35: Calibrated and range-corrected amplitude distributions of the sum of the three contributions for 330 MeV/u proton beam fired at 3 beam positions ($d = 15, 40, 65$ mm), equalized using the frontal scan method (top) and the lateral scan method (bottom). The distributions are normalized by the number of events.

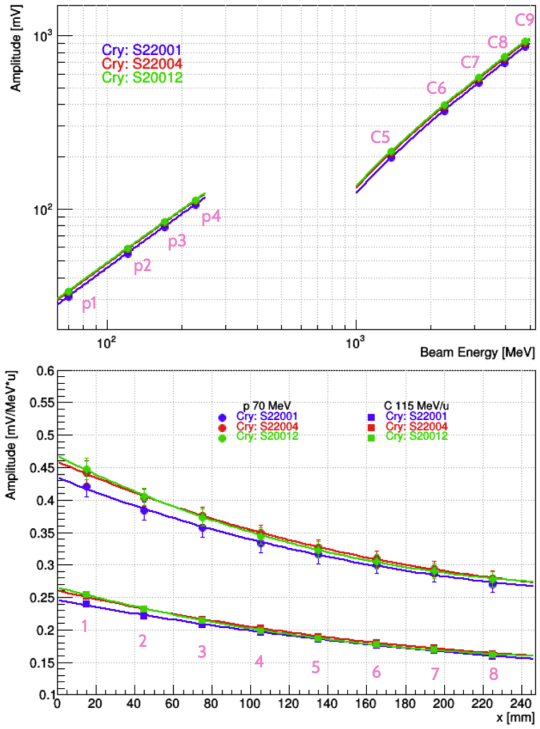

Figure 5.36: Frontal (top) and lateral (bottom) scan for *S*22001, *S*22004 and *S*20012 crystals with the labeled runs.

Table 5.8: Inter-calibration factors evaluated from different combination of points of the frontal scan.

Combinations	k_{eq} *S*22001	*S*22004
all 9 points	0.9318 ± 0.0064	0.9851 ± 0.0051
p1, p3, C5, C7, C9	0.9320 ± 0.0034	0.9853 ± 0.0038
p2, p4, C6, C8	0.9316 ± 0.0088	0.9848 ± 0.0063
p1, p4, C5, C8, C9	0.9347 ± 0.0059	0.9873 ± 0.0047
p2, p3, p4, C5, C7, C9	0.9336 ± 0.0058	0.9860 ± 0.0048
p1, p4, C5, C9	0.9356 ± 0.0063	0.9888 ± 0.0040

Different combinations of the points have been considered: points from frontal scan have been labeled from 1 to 9 and those from the lateral from 1 to 8, as shown in Figure 5.36.

The different combinations and factors used in the frontal scan are summarized in Table 5.8.

Figure 5.37 (top) shows the inter-calibration factors as a function of the different combinations of the frontal scan selected points. The first combination is related to the calibration factor computation with all the 9 energies. In the pad below, the ratio of the inter-calibration factors of the combination under exam to the ones of the combination that considers all the points of the scan is shown.

The same study has been made for the lateral scan points and the results are presented in Figure 5.37 (bottom) and summarized in Table 5.9. The evaluation of the inter-calibration factors both from frontal and lateral scan, using different combinations of points, leads to a maximum variations of the k_{eq_i} values of less than 0.4% and 0.8% for the lateral and frontal scan, respectively. Since the variation of the k_{eq_i} can be considered negligible in all the combinations of points, the calibration procedure

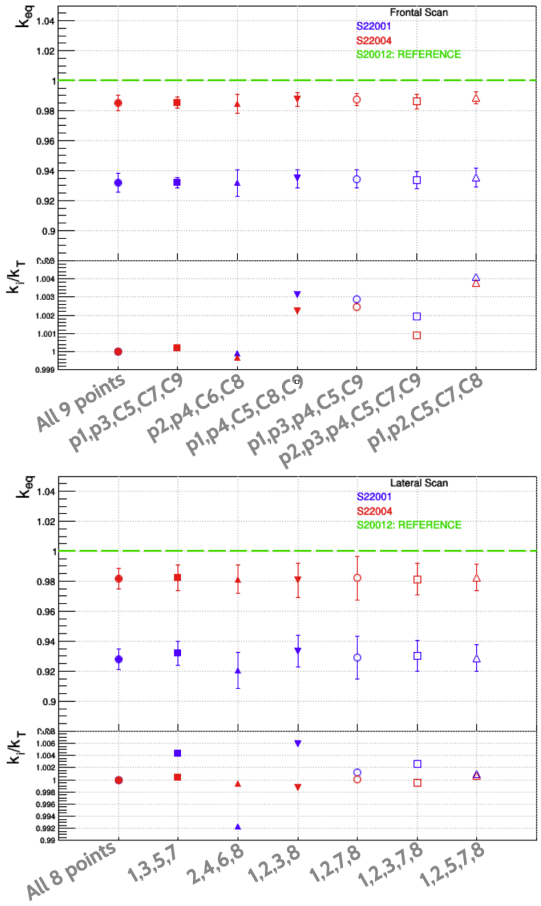

Figure 5.37: Inter-calibration factors as a function of the different combination of points of the frontal scan (top) and lateral scan (bottom). The pad below shows the ratio of the inter-calibration factor evaluated with a specific combination to the factor evaluated using all the points.

can be pursued using less points, reducing time consumption.

In conclusions, frontal and lateral calibrations lead to similar results. The advantage of the lateral calibration is due to the additional information on the range correction. Indeed, from the lateral scan, the range correction factors for each crystal can be also evaluated, a crucial step in order to have a proper energy reconstruction, as shown in Figure 5.34.

	k_{eq}	
Combinations	*S*22001	*S*22004
all 8 points	0.9278 ± 0.0068	0.9819 ± 0.0069
1, 3, 5, 7	0.9206 ± 0.0079	0.9812 ± 0.0088
2, 4, 6, 8	0.9320 ± 0.0118	0.9823 ± 0.0094
1, 2, 3, 8	0.9334 ± 0.0107	0.9806 ± 0.0112
1, 2, 7, 8	0.9289 ± 0.0143	0.9820 ± 0.0144
1, 2, 3, 7, 8	0.9318 ± 0.0102	0.9819 ± 0.0105
1, 2, 5, 7, 8	0.9288 ± 0.0089	0.9825 ± 0.0087

Table 5.9: Inter-calibration factors evaluated from different combination of points of the lateral scan.

Chapter 6

GSI 2021 test beam

6.1 Introduction

The GSI is an international accelerators facility that can deliver beams of different ions, including unstable nuclei produced by fragmentation or fission of heavy projectiles. The field of research at GSI includes plasma physics, nuclear physics, biophysics and medical physics.

In the last few years, different data takings and test beams have been conducted by the FOOT experiment at GSI using Oxygen beams accelerated by the $SIS - 18$ Synchrotron with both with the emulsion and the electronic spectrometer.

The first test beam was performed in April 2019 with an electronic setup, which included only a sub-set of the FOOT detectors: SC, BM, VTX, and TW. In addition, one single BGO crystal was tested in standalone acquisition mode. Some months later, in October 2019, a test beam dedicated only to the emulsion setup was performed. Then, a third GSI test beam was performed in July 2021 where all the detectors except for the ITR and for the magnets were used in the data takings. The setup used and a front view scheme of the calorimeter with the BGO IDs are shown in Figure 6.1a and Figure 6.1b, respectively.

After almost two years of stop due to the pandemic situation, the Collaboration has decided to exploit at best the beam time and test different configurations. Thus, runs with 200 and 400 MeV/u ^{16}O beam were performed and data with ^{12}C and C_2H_4 target of 5 and 10 mm thickness were acquired. Finally, also different trigger systems (*minimum bias* or *fragmentation*, shown in 2.3.1) were tested.

Since the calorimeter is still under construction, the goals of the calorimeter group were to integrate for the first time one Module in the global FOOT DAQ and to calibrate the central crystal with Oxygen beams.

6.2 Experimental Setup

Due to delays in the SiPM Tile production, the calorimeter Module used at GSI was not the final one. Indeed, only 9 crystals with glued SiPM were available, but only four of them ($S22001$, $S22004$, $S20012$, $S04121$) had the final design (i.e. Tyvek coating). In particular, three of them were the BGOs used for the protocol calibration presented in Section 5.4 ($S22001$, $S22004$, $S20012$). Four of the remaining crystals ($S13044$, $S13249$, $S13242$, $S13246$) had been previously modified coupling very thin (~ 1 mm) fast scintillators on the their front faces, because they had to be tested for a different application not discussed in this Thesis. The last crystal ($S00000$), had been coated with a white reflective painting, because it was used during the test beam focused on the coating choice.

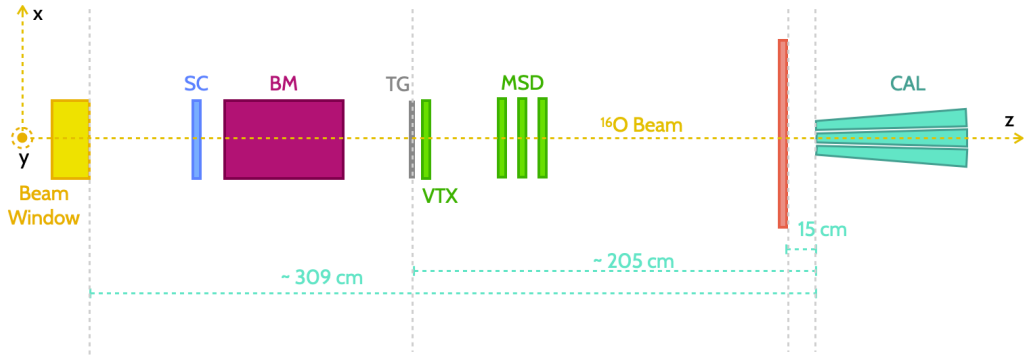

(a)

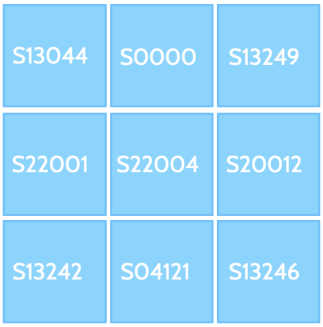

(b)

Figure 6.1: (a) Scheme of the experimental setup adopted by the FOOT electronic spectrometer during the GSI 2021 test beam. (b) Front view scheme of the calorimeter module used in the test beam with the BGO IDs.

The GSI beam line is delivered at $\sim$ 2 m height, thus two IKEA® shelves were arranged to raise the Module on y axis. Moreover, some thicknesses in aluminium were used for the height fine tuning in order to have the beam perfectly centered on the central crystal. On the beam axis (z) the Module was placed as last detector, 15 cm far from the TW and aligned on its central bars so that the crystal front faces matched the area created by the crossed bars.

The whole Module was powered by a power supply which provided both the HV for the SiPMs and the LV for the front-end readout boards ($\pm 5V$). The crystals were connected to one WaveDAQ board which was set to sample at $1GS/s$ and to apply an attuenuation of 0.5 to signals. Then, the WaveDAQs were integrated in the global DAQ, as shown in 2.3.1.

Moreover, to avoid that the ambient light increase the optical noise in the SiPMs, the calorimeter was covered with a black blanket, leaving open only the front face, and all the lights in the Cave were turned off during the data acquisitions.

Some pictures of the calorimeter setup are reported in Figure 6.2.

6.3 Calibration runs

The first two runs were dedicated to the calorimeter calibration. Thus, all the detector in front of the calorimeter were removed and $200 - 400$ MeV/u ^{16}O beams were delivered directly to the Module. For these runs, the data were acquired using the WaveDAQs in standalone mode. The trigger was provided by the WaveDAQ, based on a threshold set so that only signals above threshold were acquired.

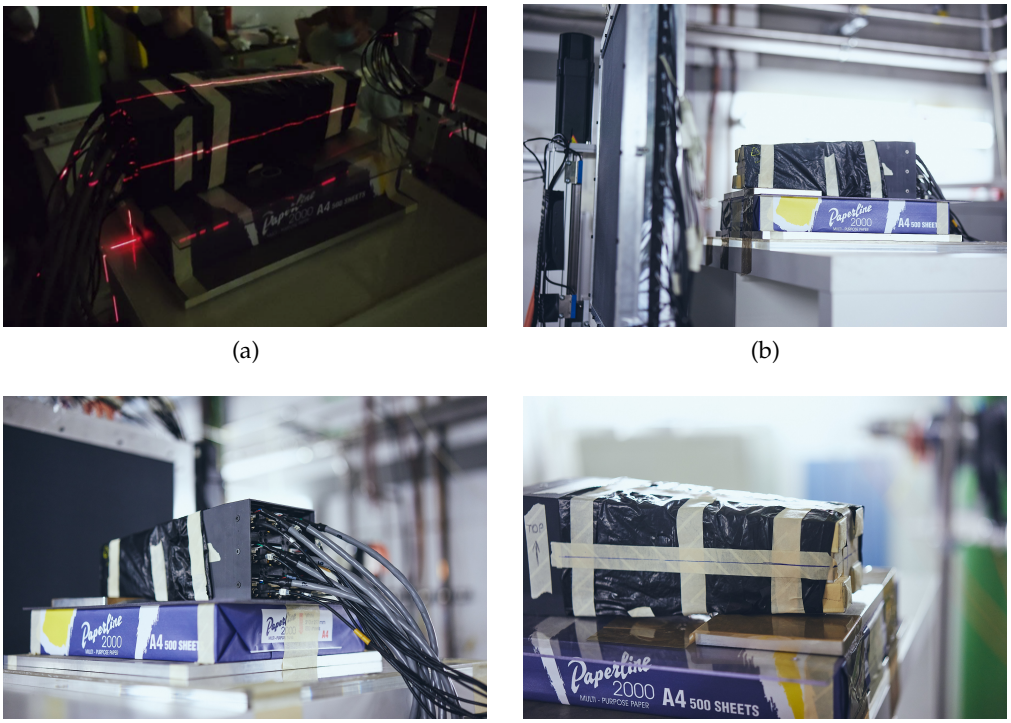

Figure 6.2: Pictures of the calorimeter setup during the GSI test beam.

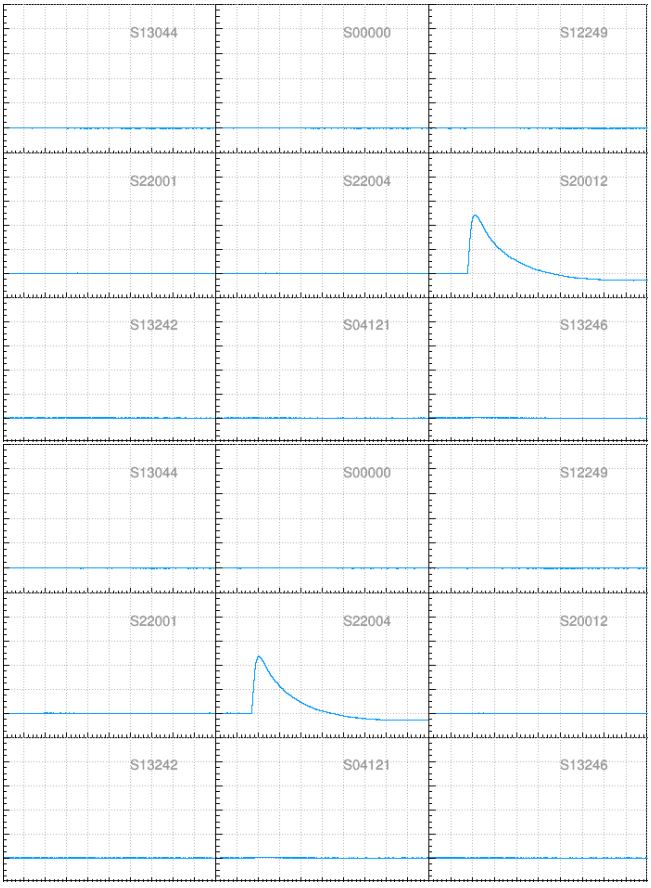

Figure 6.3: Two example events of signals in the Module with 200 MeV/u ^{16}O beam with a SiPM HV of 34.5 V.

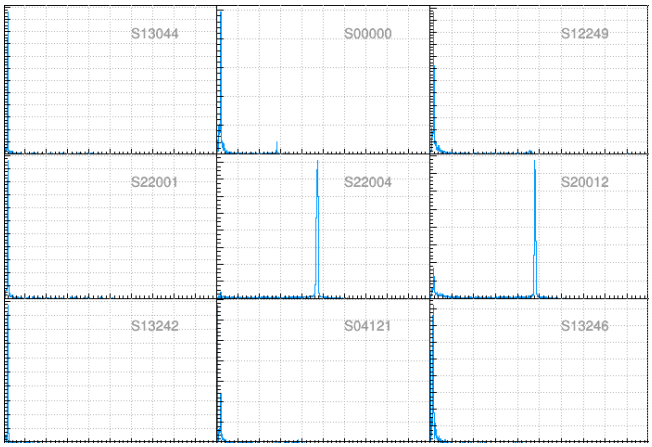

Figure 6.4: MA distributions for all the 9 crystals for 200 MeV/u ^{16}O beam with a SiPM HV of 34.5 V.

6.3.1 200 MeV/u (34.5 V SiPM HV)

Two example events for all the 9 crystals in the Module for 200 MeV/u are shown in Figure 6.3. Each pad has on the x axis the time-window of the WaveDAQ, from 0 to 1 μs, and on the y axis the WaveDAQ dynamic range, from 0 to 1 V. In the first event the beam was delivered in crystal $S20012$, while in the second one in crystal $S22004$. This shows that the beam was not perfectly stable but oscillated between crystal $S22004$ and $S20012$, probably because the accelerator calibration was still not finished. The same SiPM HV (34.5 V) used at CNAO was provided for this test beam in order to perform reasonable comparisons. However, the two events show that the signals cover about half of the WaveDAQ dynamic range and probably range saturation could occur with the higher Oxygen energy.

Figure 6.4 shows the MA distributions in the $0-1$ V range for all the crystals for 270000 events. The MA distributions on $S22004$ and $S20012$ confirmed that the beam was not stable but was split in the two crystals. In the surrounding crystals almost nothing was acquired.

The MA distributions of $S22004$ and $S20012$ were fitted with a crystal ball function (Eq. 4.2) in order to retrieve the energy resolution and the calorimeter response. In Figure 6.5, the results show an energy resolution about 0.8% and 0.65% for $S22004$ and $S20012$, respectively.

As shown in the previous chapter temperature monitoring is important to properly correct the raw amplitude. For this reason, the temperature was monitored for all the crystals for the whole beam time. In particular, the temperature as a function of the time for this first run is shown in Figure 6.6. The graph shows that the temperature in the GSI Cave ($\sim 40°$) was about $10°$ higher than the usual temperature measured at CNAO ($\sim 30°$) and that the higher temperature was in the central crystal, probably due to the electronic components heating the 8 surrounding crystals.

In order to compare the GSI data with the CNAO data, temperature and range corrections are performed, as explained in 5.2 and 5.3. The comparison between the raw and the corrected MA distribution for $S22004$ and $S20012$ crystals are shown in in Figure 6.7. The plots shows that the temperature and particle range contributions are not negligible but correct the raw response by about $15-20\%$. Moreover, the comparison of the calorimeter response, normalised to the number of nucleons and the energy resolution between GSI and CNAO data are shown in Figure 6.8a, 6.8b and 6.8c, respectively.

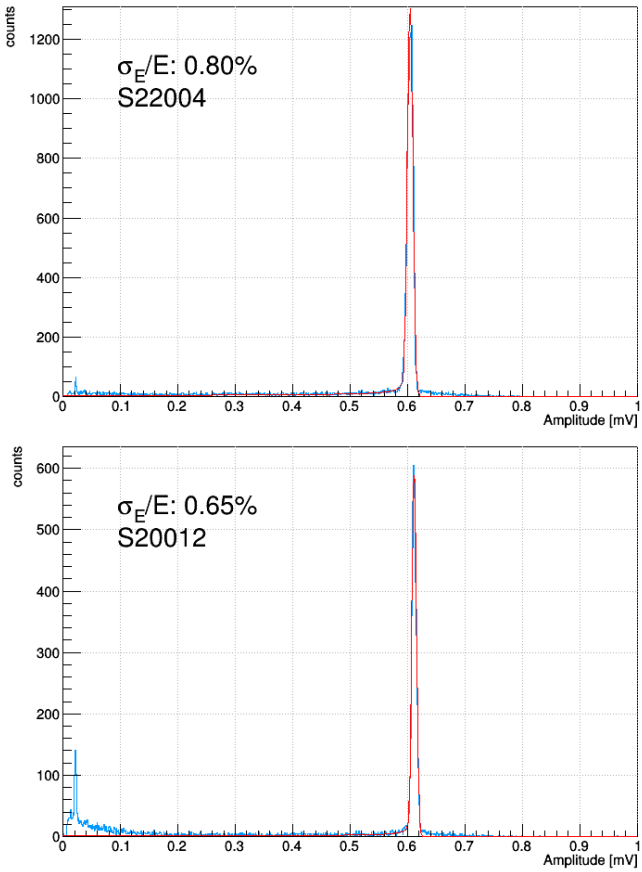

Figure 6.5: MA distributions fitted by means the crystal ball function for *S*22004 (top) and *S*20012 (bottom) crystals for 200 MeV/u ^{16}O beam with a SiPM HV of 34.5 V.

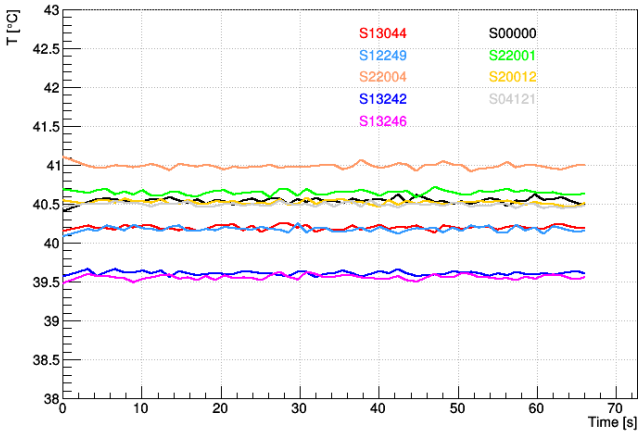

Figure 6.6: Temperature as function of time during the first run with 200 MeV/u ^{16}O beam

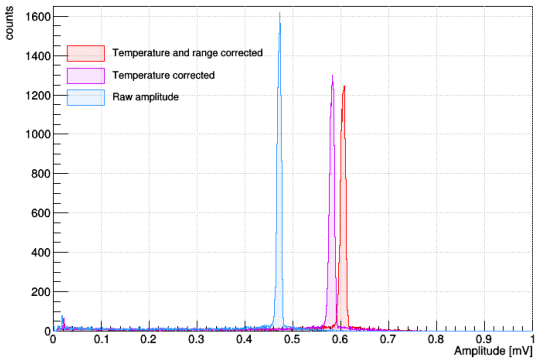

(a) *S*22004

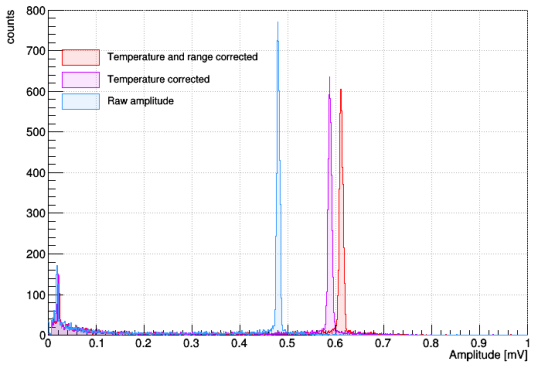

(b) *S*20012

Figure 6.7: Comparison among raw, temperature and temperature-range corrected amplitude distributions for *S*22004 (top) and *S*20012 (bottom) crystals.

The Oxygen beam data added in the linearity plot are consistent with the Carbon data taken at CNAO. However, few conclusions can be drawn with only one energy point. Indeed, more Oxygen energy points would have given more information about the Birks quenching effect in BGO crystals. The energy resolution is degraded with respect to CNAO data by 0.15% and 0.3% for the *S*20012 and *S*22004 crystals, respectively. This could be a combination of two effects: the high SiPM HV combined with a higher temperature than the CNAO treatment rooms could increase the noise and the cross-talk between the microcells, in addition to the longer path of the ^{16}O ion in the air before hitting the crystals. This could also explain the better resolution achieved for crystal *S*20012 which had a lower temperature (Fig. 6.6). However, the temperature correction has to be revised because of the calorimeter response was not calibrated up to such high temperature.

6.3.2 200-400 MeV/u (33 V SiPM HV)

The second run was performed with 400 MeV/u ^{16}O beam. However, since the previous run at 200 MeV/u already covered the half of the WaveDAQ dynamic range, in order to avoid the digitizer range saturation, the SiPM HV was lowered to 33 V. For this reason the 200 MeV/u ^{16}O beam was repeated with the lower HV. Unfortunately, the GSI and CNAO calorimeter linearity can not be compared, due to the different SiPM high voltages used.

Figure 6.9 shows the amplitude distributions matrix for the two energies. In this run the beam position was more stable and centered on the *S*22004 crystal.

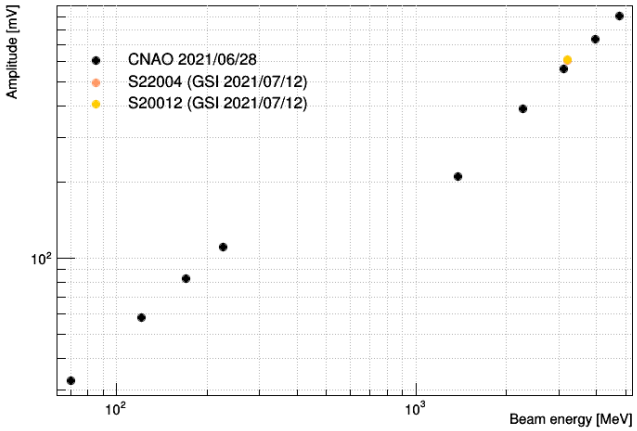

(a)

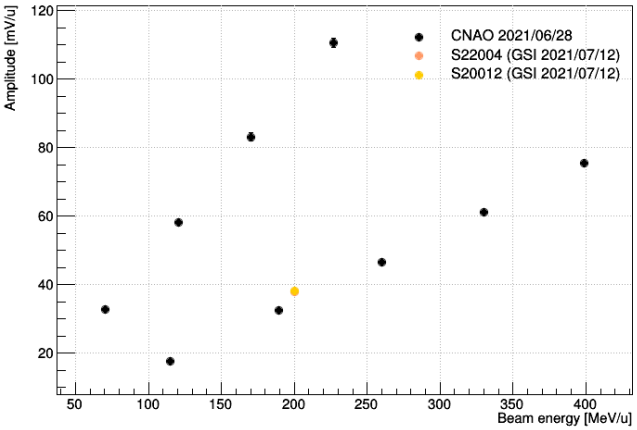

(b)

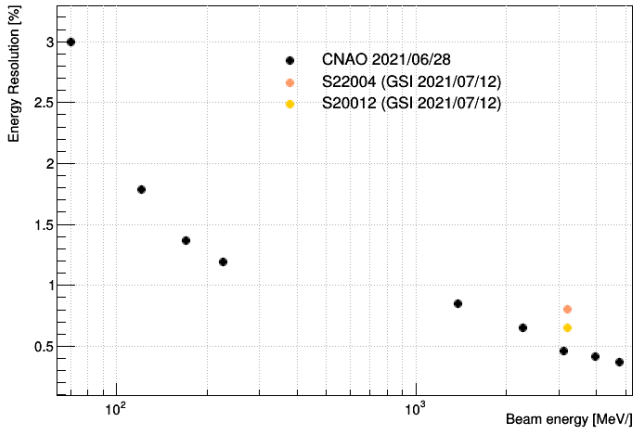

(c)

Figure 6.8: Comparison of the calorimeter response (a), the calorimeter response normalised by the number of nucleons (b) and energy resolution (c) between the GSI and CNAO.

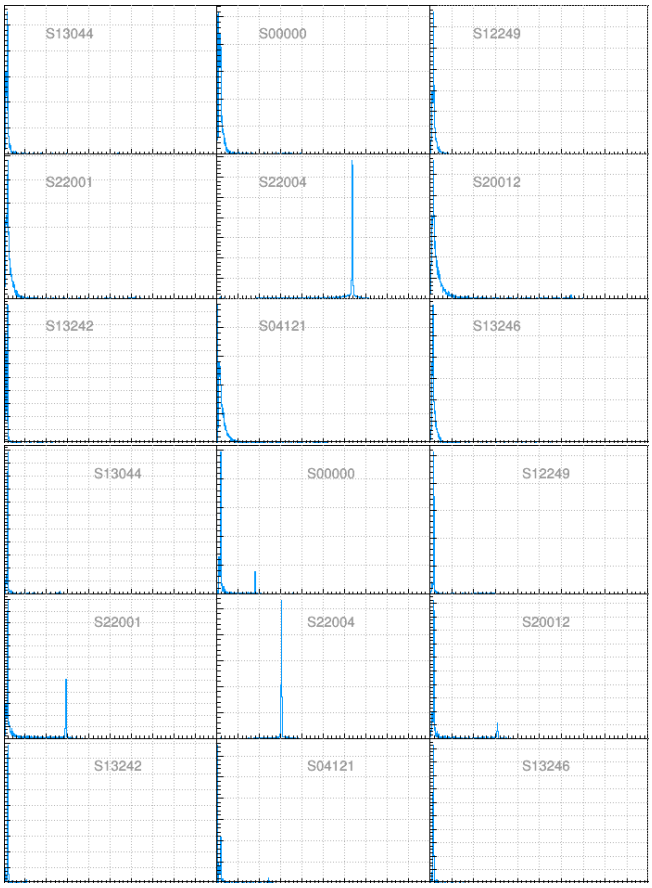

Figure 6.9: MA distributions for all the 9 crystals for 400 MeV/u (a) and 200 MeV/u ^{16}O beam with a SiPM HV of 33 V. On x axis is plotted the WaveDAQ dynamic range $(0 - 1\ V)$ while on y axis the counts.

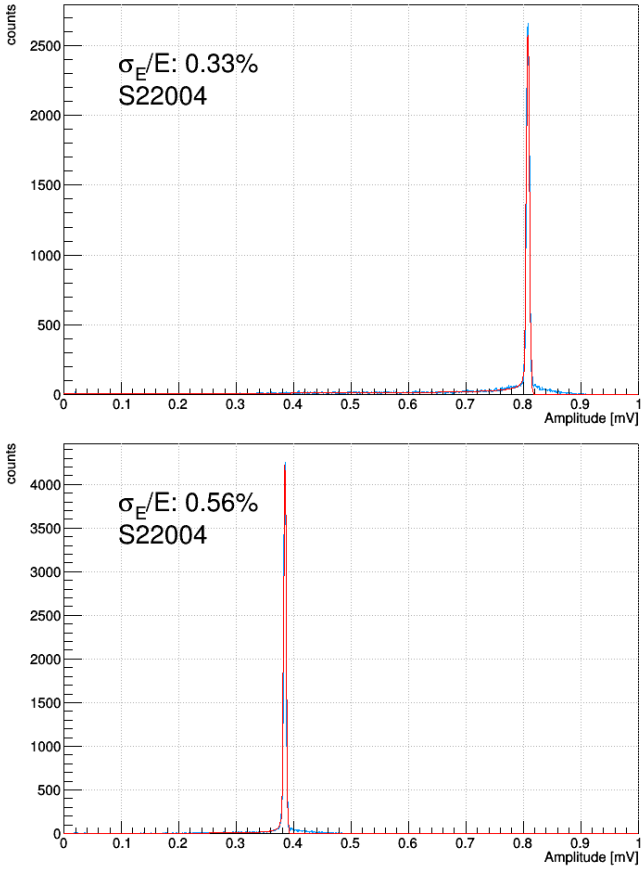

Figure 6.10: *S*22004 MA distributions fitted with a crystal ball function for 400 MeV/u (a) and 200 MeV/u ^{16}O (b) beams with a SiPM HV of 33 V.

The amplitude distributions for the *S*22004 crystal, corrected in temperature and particle range, have been fitted with a crystal ball function. The fit results show an improvement on the energy resolution: 0.33% and 0.56% for 400 and 200 MeV/u beam, respectively. This improvement with respect to the previous run can be explained by the lower noise cross-talk in the SiPM microcells thanks to the lower SiPM HV.

The energy resolution values have been compared with the CNAO data in Figure 6.11.

6.4 Full FOOT Experiment runs

After the calibration runs, all the other detectors were placed in front of the calorimeter and data takings in different configurations were performed:

- no targets and minimum bias trigger
- 5 mm thick carbon target with minimum bias and fragmentation trigger
- 5 mm and 10 mm thick polyethylene target with minimum bias and fragmentation trigger
- calorimeter module shifted and rotated by $2 - 4^{\circ}$ respect to the beam line with fragmentation trigger (Fig. 6.12).

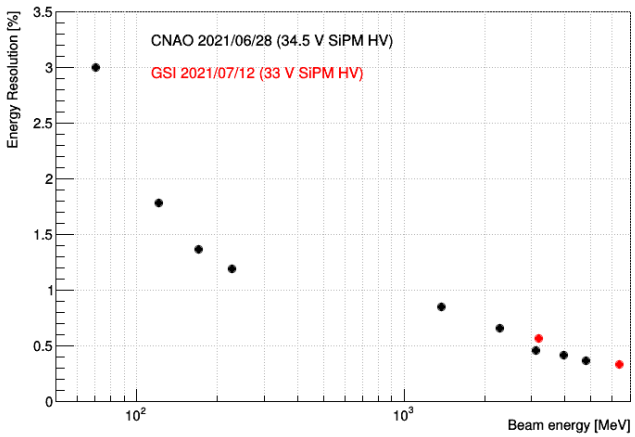

Figure 6.11: Energy resolution comparison between GSI and CNAO data.

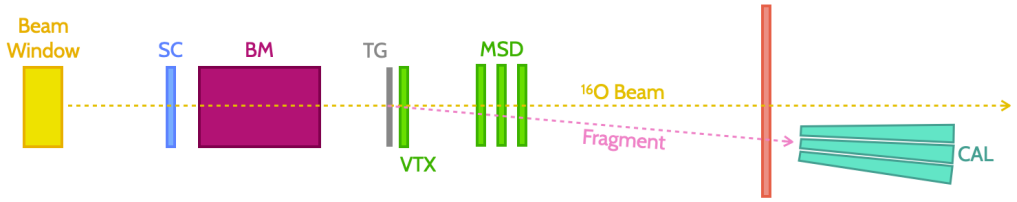

Figure 6.12: Scheme of the experimental setup.

Figure 6.13 shows the MA distributions of the nine crystals for several runs in different configurations. 6.13a shows the 4242 run, where 200 MeV/u ^{16}O beam has been delivered on 5 mm thick carbon target and events were selected with the minimum bias trigger. In Figure 6.13b and 6.13c are reported the results of run 4245 and 4272 where the same trigger but a 5 mm thick C_2H_4 target with 200 and 400 MeV ^{16}O, respectively, were used. Finally, run 4341 with the fragmentation trigger of 400 MeV ^{16}O beam on the 10 mm thick C_2H_4 target is shown. All the information about the run configurations are summarized in Table 6.1.

As contrary to the calibration runs, signals were acquired for all the crystals, and not only by the central one. In the central crystal the amplitude distribution of Oxygen beam is visible, while in the others the amplitude distributions of fragments created in the target or inside the calorimeter itself.

In run 4349 the calorimeter was shifted off the beam line and rotated by 4° in order that the beam has not impinged the Module. Due to the small area covered by the Module, very few fragment events have been collected in this run and some examples are shown in Figure 6.14. Figure 6.14 (top) shows the fragment amplitude distributions and Figure 6.14 (bottom) one fragment event.

The GSI test beam analysis has been performed using the calorimeter stand-alone

Table 6.1: Run information summary

Run	Target	Target thick $[mm]$	Beam Energy $[MeV/u]$	Trigger	Rotation angle
4242	C	5	200	minimum bias	
4245	C_2H_4	5	200	minimum bias	
4272	C_2H_4	5	400	minimum bias	
4311	C_2H_4	10	400	fragmentation	
4349	C_2H_4	10	400	fragmentation	4°

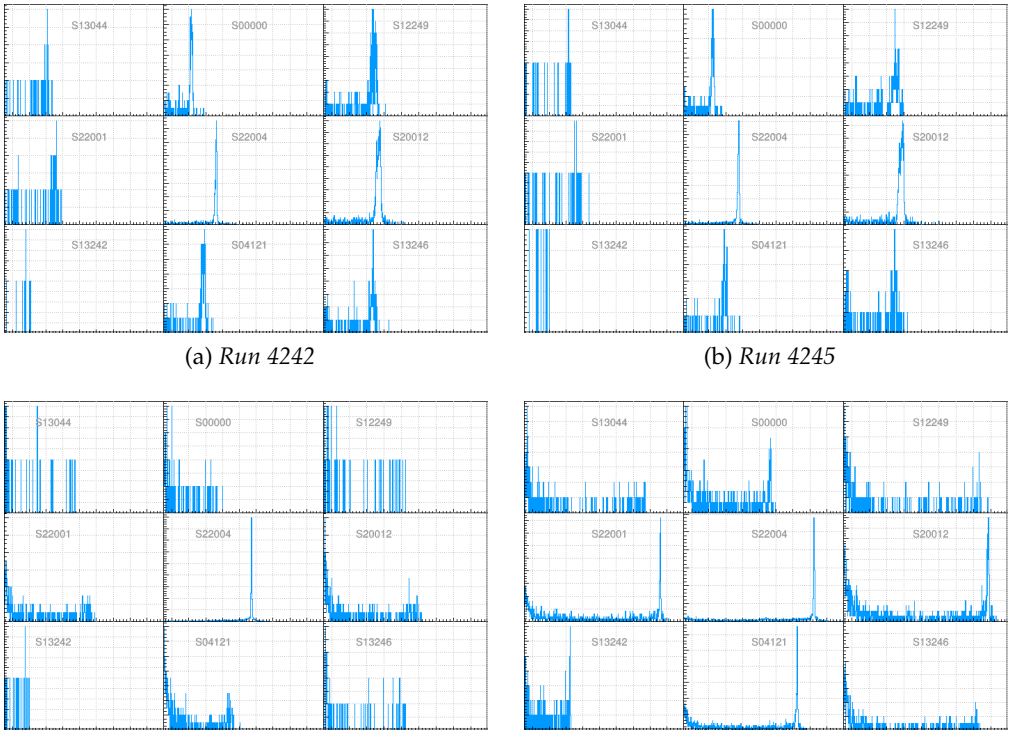

(a) *Run 4242* (b) *Run 4245*

(c) *Run 4272* (d) *Run 4311*

Figure 6.13: Amplitude distributions for different runs where on x axis there is the WaveDAQ range dynamic $(0 - 1\ V)$ and on y axis the counts. All the run information are summarized in Table 6.1.

code and using only the calorimeter data. Unfortunately, few results can be retrieved with calorimeter-only data and fragment mass reconstruction is not possible. In the next future a cross-analysis with the other FOOT detectors, in particular with the TW, will be performed with the SHOE software.

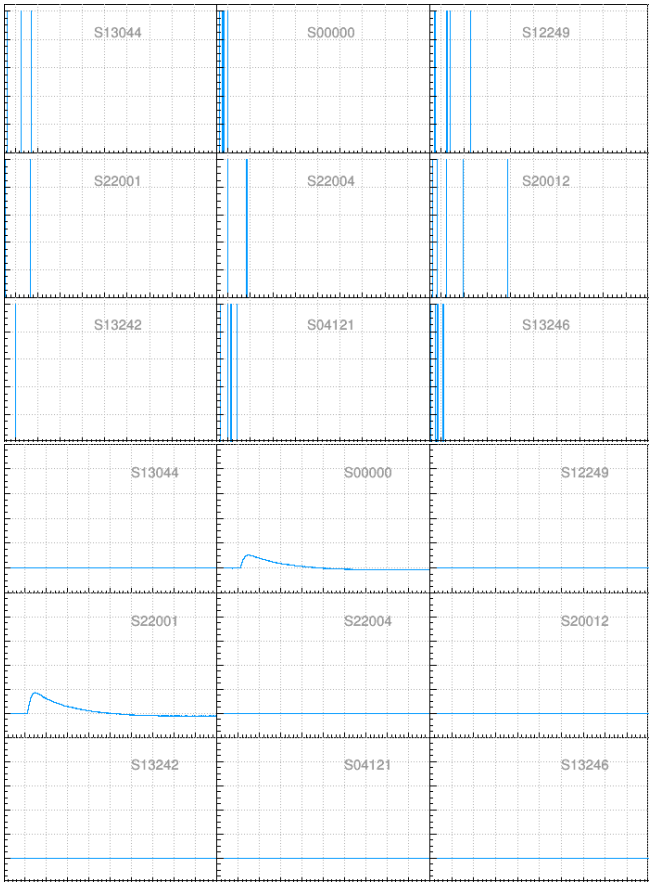

Figure 6.14: Fragment amplitude distributions where on x axis there is the WaveDAQ dynamic range ($0 - 1\ V$) and on y axis the counts (a). Example of one event with two fragment pulses in two different crystals (b).

Chapter 7

Calorimeter in the FOOT software framework

7.1 Introduction

The FLUKA Monte Carlo code was adopted to perform the simulations of the FOOT experimental setup. FLUKA was thoroughly tested through the comparison with many experimental data-sets and nowadays it is extensively adopted in many physics fields of study, such as particle, nuclear and medical physics. FLUKA has been preferred to other simulation frameworks (i.e., GEANT4) because both the physics models and the user interface, have been optimized for its application in the context of CPT. Indeed, FLUKA is used at CNAO and HIT for clinical and research purposes.

This chapter describes the development of the calorimeter geometry with FLUKA for the FOOT simulations in section 7.2. Moreover, the calorimeter chain reconstruction software developed for SHOE is described in section section 7.3.

7.2 Calorimeter geometry in FLUKA

To run a simulation in the FOOT software framework, the user must prepare an input file, which can be written with an ordinary text editor or by means of the Flair graphic interface. FLUKA inputs are ASCII files with extension *.inp* and are composed of a variable number of commands, each one consisting of one or more lines, which are called *cards* for historical reasons. Each card is composed of one keyword, six floating point values called WHATs, and one character string called SDUM. A card example is shown in Figure 7.1.

A fundamental part of the FOOT simulations are the detector geometry definitions. In FLUKA the combinatorial geometry is based on the concept of *bodies* and *regions*. *Bodies* are either closed solid figures such as spheres (*SPH*), cylinders (*RCC*), parallelepipeds (*RPP*), etc., or semi-infinite portions of space such as half-spaces, infinite cylinders, etc., whereas *regions* are created by combining *bodies* through Boolean operations, i.e. addition, intersection and subtraction (Fig. 7.2). The syntax of the body cards is not unique, indeed the *WHATs*, which in the body definition cards correspond to dimensions and global positions, are body-type depending. Regions are the core elements of FLUKA geometry since, differently from

```
*...+....1....+....2....+....3....+....4....+....5....+....6....+....7....+...
BEAM          1.E+04   0.0D+00       0.0       0.0       0.0       0.0PROTON
*keyword    momentum mom.spread  diverg.   X-width   Y-width  ignored particle
*            WHAT(1)   WHAT(2)   WHAT(3)   WHAT(4)   WHAT(5)   WHAT(6)  SDUM
```

Figure 7.1: Example of FLUKA card [76].

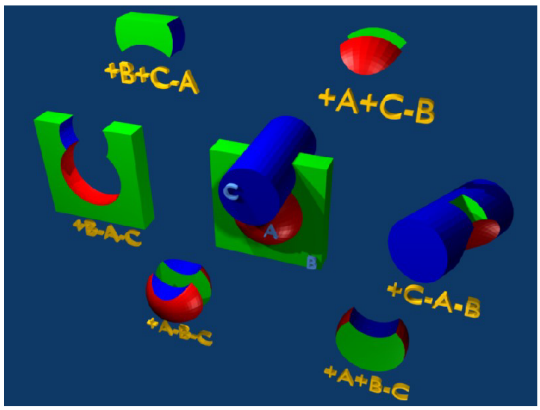

Figure 7.2: Illustrative examples of FLUKA combinatorial geometry [76].

Figure 7.3: Cards of the FLUKA input file containing the six parameters of the *PLA* bodies (red box) and the region cards (green box) in the Flair interface (left).

bodies, which are merely shapes in the space, they represent physical objects, each one composed of one single material. In the FOOT software framework the geometry part is stored in a *.geo* configuration file which is then recalled by the standard *.inp* file.

The BGO crystal geometry (truncated pyramid shape) was not among the FLUKA standard bodies and the only way to implement it, was to intercept six different planes, using the so-called *PLA* bodies. A *PLA* body is defined in FLUKA by six parameters: three coordinates of a point (x, y and z) and three components of a vector (N_x, N_y and N_z), as shown in the example in Figure 7.3 in the red box. In principle, the region of each crystal is defined by joining the six planes, but since the calorimeter is surrounded by air, the geometry region must be defined as the air minus the sum of the six planes that compose the crystal, as shown in the green box in Figure 7.3. In Figure 7.4 (left) the sketch of this geometry concept for a truncated pyramid BGO crystal is presented.

However, since a single crystal is defined by six planes and each plane has six parameters, the developments of the whole calorimeter geometry, and thus the definition of the related regions of the 320 BGO crystals, results very tricky: an example is shown in Figure 7.5. Moreover, due to the very large number of bodies and to FLUKA code limitations, the air has been divided in sub-air boxes.

For this reason, the FLUKA developers team, on request by the FOOT Collaboration, has implemented three new additional truncated pyramid bodies: *PYX*, *PYY* and *PYZ* oriented respectively along the x, y and z axes. However, the new bodies were implemented only for FLUKA and they could not be visualized on Flair. For this reason, I contributed to the development of the Flair source code in order to implement a new and user-friendly geometry for the BGO crystals.

The new truncated pyramid bodies are defined by seven parameters: the three

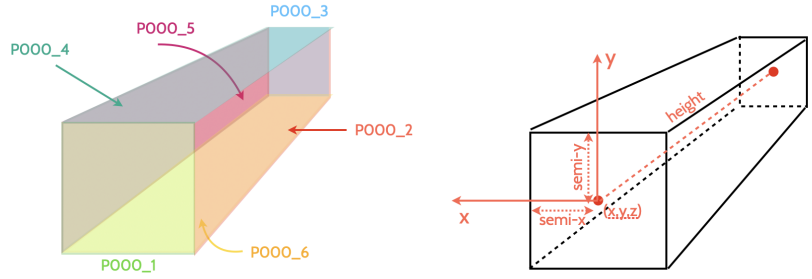

Figure 7.4: Sketch of the BGO implementation intercepting six different *PLA* bodies of FLUKA (left) and using the new FLUKA truncated pyramid body (right).

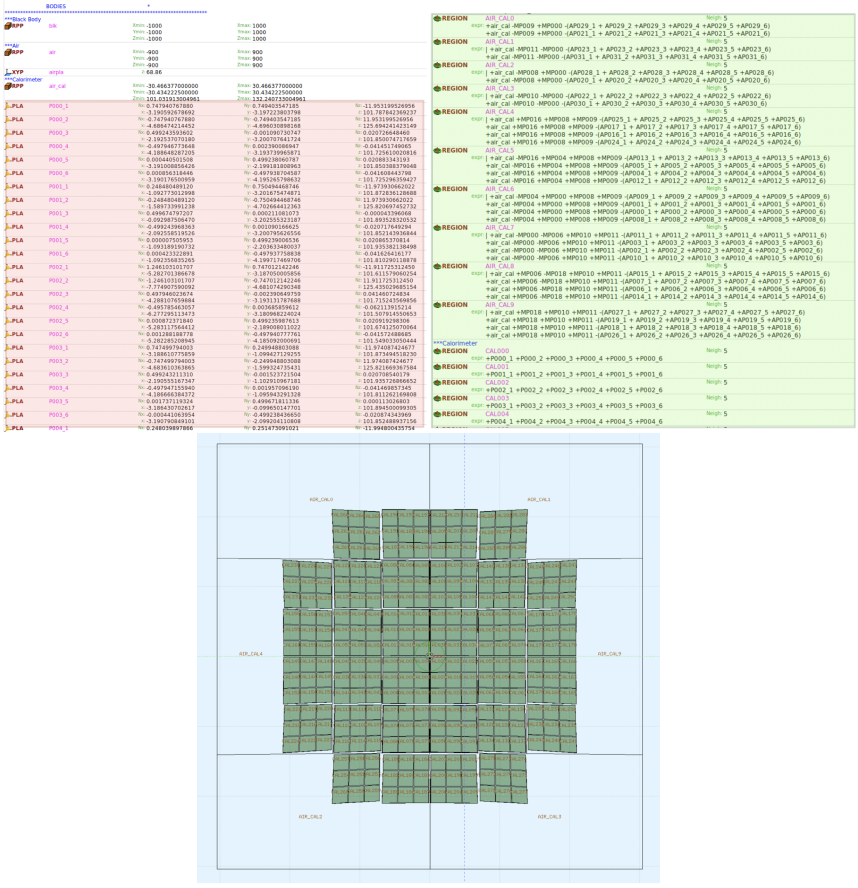

Figure 7.5: Cards of the FLUKA input file containing the *PLA* bodies (red box) and region (green box) definitions for the full calorimeter geometry (top). Picture of the whole calorimeter with Flair (bottom).

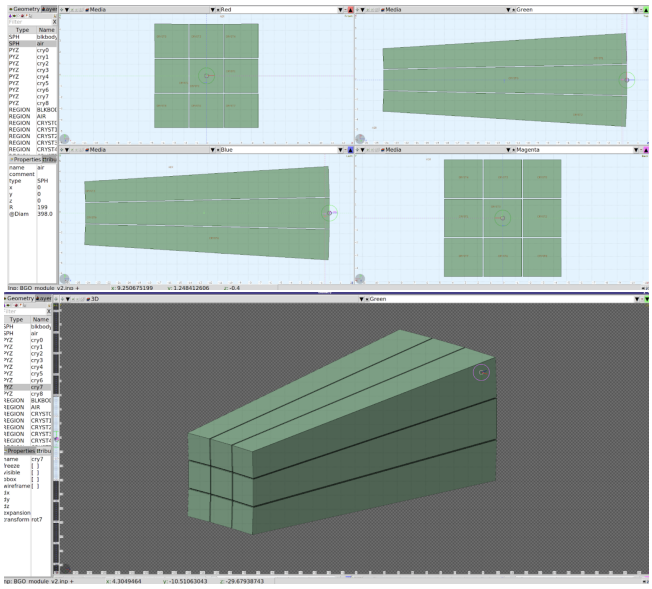

Figure 7.6: 2D (top) and 3D (bottom) visualization in Flair of one Calorimeter Module. This geometry has been used in the simulations for the GSI 2021 test beams.

coordinates of the center of the minor base (x, y and z) that also define the reference frame of the body, the half-side dimensions of the minor base (e.g. semi-x and semi-y for the PYX body), the height of the truncated pyramid and the ratio of smaller base area to greater base one (in other word the ratio between edge of the greater and smaller base). An example is shown in Figure 7.4 (right).

This new concept simplifies the definition of the geometry in Flair and it results easier and more user-friendly than the previous one. The 3×3 module geometry has been already tested in simulations and it has been used for the GSI test beam of July 2021 (Fig. 7.6).

Finally, the whole calorimeter geometry has been implemented (Fig. 7.7) and integrated in the SHOE software.

7.3 Calorimeter in SHOE

As discussed in 2.5.3, the FOOT reconstruction and analysis software (SHOE) has been developed to read both simulated and real data of all the detectors performing firstly a local and then a global reconstruction procedure. In SHOE each detector has a set of C++ classes which allow the creation of its geometry and provide the physical quantities either from real data or simulation. Concerning the geometry, the *parGeo* classes, one for each detector (Fig. 7.8, green boxes), generate the geometry both in the FLUKA and in the ROOT format. These classes create the *TGeometry* volumes required to configure each detector. The volumes represent elements of the geometry described in a local coordinate frame, and they can be nested one inside the other to produce the desired detector configuration.

A specific macro, *MakeGeo.cxx* (Fig. 7.8, purple boxes), calls in each detector geometry class the *PrintBodies* and *PrintRegions* (Fig. 7.8, blue boxes) methods, which implement the logic to write the FLUKA geometry. Then starting from a basic-almost empty FLUKA input file and a parameter header file (Fig. 7.8, magenta box), the macro produces an executable code which is able to modify the *.inp* file and to create *ex novo* the correct *.geo* file containing the geometrical description of the entire FOOT setup in the FLUKA readable format.

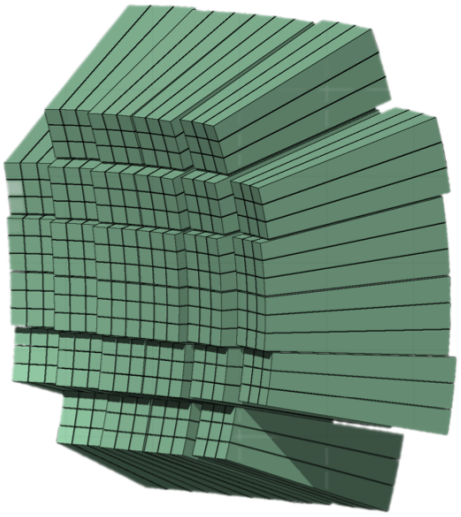

Figure 7.7: 3D picture in Flair of the whole FOOT Calorimeter.

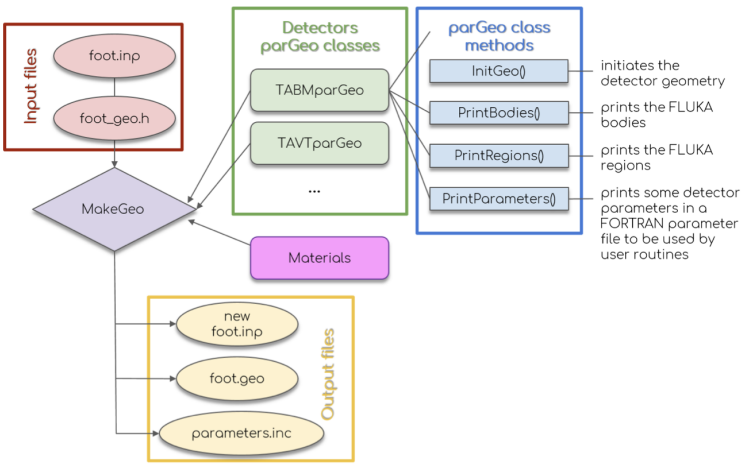

Figure 7.8: Block diagram of the *MakeGeo* software.

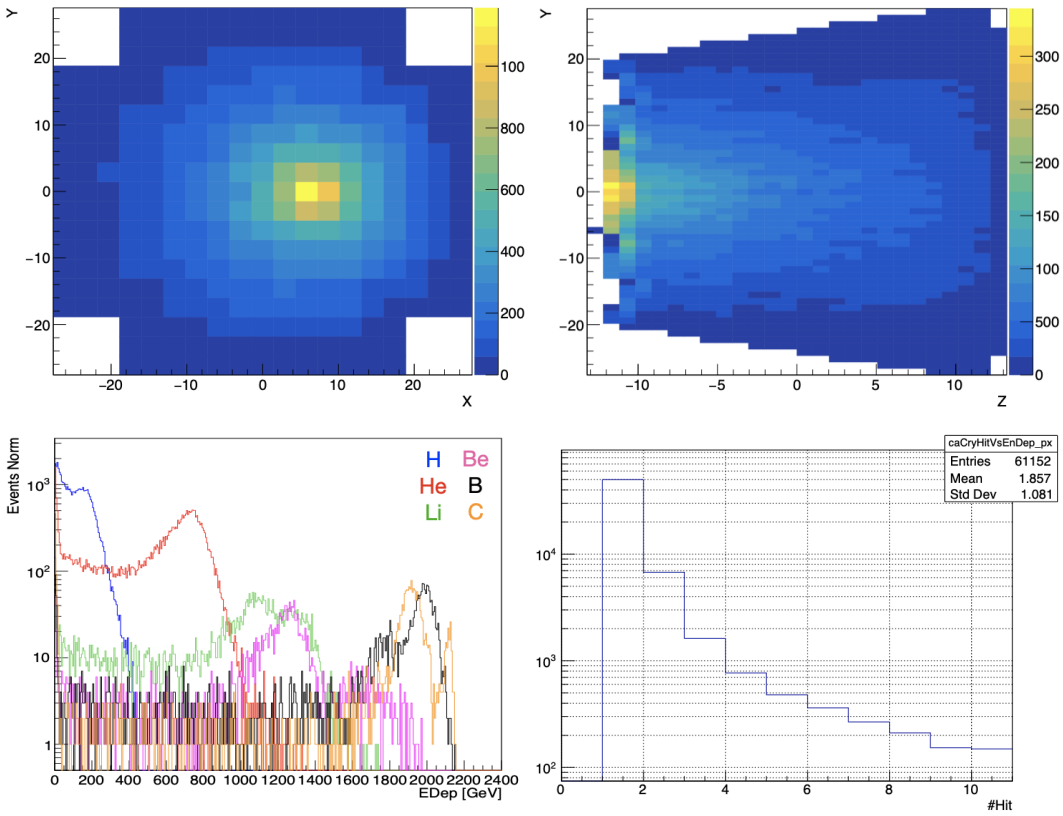

Figure 7.9: simulation output example of local reconstruction of 10^7 200 MeV/u ^{12}C delivered on C target.

Once the geometry is created, SHOE processes and stores the raw simulation outputs (particle ID, particle energy, particle first and last energy release position, time, etc.). Then the calorimeter classes perform the energy digitization evaluating the detector energy resolution function, measured at CNAO (Fig. 4.18 top), and applying to the FLUKA raw energy a gaussian smearing. The energy reconstruction steps follow with the creation of the so called *hit*[1] object. Finally, a clustering algorithm has been implemented to collect and group different hits generated by the same particle in neighbouring crystals. The final energy information is provided as input for the global reconstruction code in order to correlate it with the TOF or momentum and retrieve the fragment mass.

The calorimeter geometry and the calorimeter reconstruction chain has been tested by simulating 10^7 200 MeV/u ^{12}C primaries on a C target. In Figure 7.9 top left and top right the results of the hit maps on front ($x-y$) and top ($y-z$) view in the calorimeter are presented ; the ion energy distribution and the hit multiplicity in the calorimeter are shown in Figure 7.9 bottom left and bottom right, respectively.

Concerning the simulation, the calorimeter SHOE classes are completed and they are currently used for the local reconstruction.

Concerning the real data, the calorimeter reconstruction chain is different. Indeed, the code is designed to skip the geometry construction and the data digitization classes, but it performs the globalDAQ data decoding instead. Then, by reading the configuration and calibration files, the temperature and range correction and the

[1] A hit in SHOE is a ROOT object containing particle ID, energy, time, and position of every particle detected by the calorimeter.

crystal calibration factors are applied. Then, as for the simulation, the hit objects are created and the cluster algorithm is performed.

Since the studies of the calorimeter response are not finalized yet (as discussed in 4.4), both for simulation and real data a dummy function to perform the energy calibration is implemented. The next months will be useful to investigate in depth the Birks effect and implement a method to compensate them in retrieving the fragment energy information.

Chapter 8

Conclusions

FOOT is a nuclear physics experiment that aims at measuring the differential cross sections $(d^2\sigma/d\Omega \cdot dE)$ of particles relevant for both CPT and radioprotection in space. The final experimental data will be adopted as benchmark for MC simulation tools, to improve the current TPS for particle therapy and to develop a new shielding design suitable for future space missions. FOOT consists of two different experimental setups: an emulsion spectrometer based on the nuclear emulsion technology developed to measure the light fragments ($Z \leq 3$), and an electronic setup composed of different sub-detectors optimized for the detection of heavy fragments ($Z \geq 3$).

This Ph.D. project has contributed to the FOOT calorimeter design, construction, and data analysis. In particular, all the performance tests, that took place at CNAO, to make the calorimeter design choices (crystal size and wrapping, photodetector type and configuration, readout parameters), the linearity corrections (i.e. temperature and range), the optical simulations, the crystal calibration protocol, and the data analysis of the GSI test beam have been presented and discussed.

According to the test beam results, the final calorimeter setup foresees BGO crystals wrapped with Tyvek reflective foils and glued to SiPM matrix of 15 μm microcells pitch. A custom front-end board was designed to match the SiPM Tiles size and maximise the compactness. WaveDAQ boards have been chosen to digitise and sample the crystal signals with frequencies from 1 GS/s (used for all the tests) to 5 GS/s.

Thus, the final setup allowed to achieve the required performance: energy resolution below 2% in the full energy range foreseen by the FOOT experiment (up to at least 5 GeV); time resolution, evaluated with cosmic rays, ranging from (640 ± 30) ps to (767 ± 30) ps with a slight dependence on the distance from the front side of the crystal. However, the raw response is not perfectly linear with the incoming particle, and it shows an increasing deviation from linearity with increasing the energy, for both proton and carbon beams. Temperature and particle range corrections have been developed and applied to raw data in order to improve the calorimeter response linearity. Indeed, a method, based on raw data, for compensating temperature variations, that cause changes in the SiPM and in the crystal response with a rate of about 0.5 $\%/^{\circ}C$, was successfully developed. As observed in irradiating the long side of the crystals at different positions, the response decreases with the distance from the front-face: in order to compensate for this effect a method based on the knowledge of the fragments range at a given energy was developed, and linearity was recovered with a non-linearity effect $\leq 1\%$.

Several FLUKA MC simulations have been performed to understand the observed behaviour. The results have shown that the effect is a convolution of several

physical effects, related to the Tyvek reflectivity, the photon absorption and diffusion, the crystal shape, and the geometrical acceptance and position of the photodetector.

Test beams have shown that another contribution that affects the detector linearity is the Birks effect which is related to the crystal response dependency on the ion mass and charge. The signal shape analysis allows the identification of protons and carbon ions, but it is not yet clear whether it will provide information precise enough to disentangle fragments with a similar charge to mass ratio. Thus, no corrections for this effect have been implemented yet. A combination with measurements from other detectors, as the charge measured by the TW, can be exploited to reconstruct the fragment kinetic energy.

The performance test results and the optical absorption simulations in BGO crystals have been presented as talk to the *IEEE Nuclear Science Symposium and Medical Imaging* conference on October 2021 and they will be published in two different papers: *"Performance of the Calorimeter Module for the FOOT experiment"* and *"Simulation of the optical photon propagation in the FOOT calorimeter module"*, respectively, in 2022.

One important step in the calorimeter development was the calibration. Indeed, in order to reconstruct the fragment energy in the right way the calorimeter response must be uniform in each BGO crystal. Thus, a calibration protocol has been defined to equalize the crystal responses. The inter-calibration factors have been evaluated from the data of the frontal and the lateral scan. In order to validate the calibration methods the energy loss contribution of three crystals positioned side-by-side, has been equalized, summed and corrected, showing a discrepancy from the frontal scan amplitude distribution smaller than 1%. The two calibration methods have provided similar results and have shown that both are reliable. Moreover, the advantage of the lateral calibration is linked to the additional information that can be extrapolated. Indeed, from the lateral scan, the range correction factors for each crystal can be also evaluated, a crucial step in order to obtain a proper energy reconstruction.

The calibration procedure must be performed on all the 320 BGO crystals. Since frontal or lateral scans must be carried out on each crystal, the calibration procedures have been repeated reducing the point numbers: different combinations of data from the lateral and frontal scans have been considered. The evaluation of the inter-calibration factors from both methods, using different combinations of points, leads to a maximum variations of the calibration factors smaller than 0.4% and 0.8% for the lateral and the frontal scan, respectively. Hence, a calibration performed with $3-4$ points, instead of $8-9$, is possible, making the procedure faster.

Moreover, in July 2021, one calorimeter module has been successfully integrated for the first time in the FOOT global DAQ during the GSI test beam. Calorimeter-standalone runs with Oxygen beam have been performed in order to compare ^{16}O data with the carbon data taken at CNAO. Then, the calorimeter was included in the whole FOOT electronic setup and runs with different targets and triggers were performed. Energy resolutions of 0.33% and 0.56% were achieved for 200 and 400 MeV/u O^{16} beam, respectively, and they are compatible with what achieved with carbon beams.

The *R&D* stage for the FOOT calorimeter is now completed; it provided all the information required to complete the design for the calorimeter construction and the performance measurements were fulfilled successfully. The construction stage is presently ongoing. In early 2022 a crucial test beam at CNAO with the whole electronic setup will be performed and an almost final calorimeter arrangement ($5-10$ Modules) will be used.

Acronyms

ADC Analog Digital Converter. 87, 88

AED Average Emission Depth. 92, 94, 107, 158

ALM Augmented Lagrangian Method. 57

APD *Avalanche PhotoDiode*. 73

ASCII *American Standard Code for Information Interchange*. 60, 129

BGO *Bismuth Germanate*. 48, 49, 69–74, 78–80, 82–85, 87, 88, 91, 93–96, 99, 100, 102, 103, 105, 109, 111, 112, 117, 118, 122, 130, 131, 137, 138, 155–161

BM *Beam Monitor*. 41–44, 50, 61, 117, 155

BME *Boltzmann Master Equation*. 12

BP *Bragg Peak*. 5–7, 12, 15, 17, 21, 22, 24, 25, 27, 29, 92, 154

CAL *Calorimeter*. 41, 50, 60, 71

CB *Crystal Ball*. 72, 92

CMS Compact Muon Solenoid. 96

CNAO *Centro Nazionale Adroterapia Oncologica*. 2, 22, 39, 40, 42, 53, 54, 71, 72, 76, 78, 82, 87–89, 92, 94, 97, 98, 105, 110, 120, 122, 123, 125, 126, 129, 134, 137, 138, 155–160, 163

CPT *Charged Particle Therapy*. 1–3, 5, 6, 10, 13, 17, 19, 22, 24, 28, 29, 35, 36, 39–41, 54, 58, 129, 137

DAQ *data acquisition system*. 2, 49, 50, 70, 73, 81, 82, 117, 118, 138, 155, 156

DNA *DeoxyriboNucleic Acid*. 13, 14, 16–19, 153

DPM *Dual Parton Model*. 59, 60

DSB *Double Strand Break*. 13, 14

ECC *Emulsion Cloud Chamber*. 40, 42, 51

FBK *Fondazione Bruno Kessler*. 76

FermiLab *Fermi National Accelerator Laboratory*. 21

FIRST *Fragmentation of Ions Relevant for Space and Therapy*. 51, 55

FLUKA *FLUktuierende KAskade*. 35, 40, 46, 58–61, 66, 92, 94, 97–99, 101, 129–132, 134, 137, 155, 156, 158, 161

FOOT *FragmentatiOn Of Target*. 2, 35–41, 43, 45–55, 57–63, 69–71, 76, 82, 83, 87, 96, 103, 117, 127, 129, 130, 132, 133, 137, 138, 154–156, 161, 163

FWHM *Full Width Half Maximum*. 25, 91

GCR *Galactic Cosmic Rays*. 1, 31–33, 154

GINC *Generalized Intra-Nuclear Cascade*. 59

GSI *Gesellschaft fur Schwerionenforschung*. 2, 27, 39, 40, 42, 51, 53–55, 62, 87, 117–120, 122, 123, 126, 132, 137, 138, 155, 160, 161

GUI *Graphical User Interface*. 49

HIT *Heidelberg Ion Therapy Center*. 39, 40, 103, 129

IMRT *Intensity Modulated Radiation Therapy*. 20, 21, 153

INC *Intra-Nuclear Cascade*. 10, 12

INFN *National Institute for Nuclear Physics*. 35

ISS *International Space Station*. 31

ITR *Inner Tracker*. 41, 43, 45–47, 50, 55, 117, 155

LET *Linear Transfer Energy*. 14–17, 25, 27–29, 153, 154

LINAC *linear accelerators*. 19, 20, 22

MA *Maximum Amplitude*. 71, 79, 80, 87, 91, 92, 106, 108, 109, 120, 121, 124–126, 156, 159, 160

MAPS *Monolithic Active Pixel Sensors*. 43

MC *Monte Carlo*. 1, 12, 24, 27, 29, 33, 35, 40, 54, 58, 61, 62, 137, 155

MCS *Multiple Coulomb Scattering*. 8, 9, 38, 42, 52

MIP *Minimum Ionizing Particles*. 52

MSD *Micro Strip Detector*. 41, 43, 47, 48, 50, 53, 55, 61, 155

NAS *Network Attached Storage*. 50

NASA *National Aeronautics and Space Administration*. 29

NTC *Negative Temperature Coefficient*. 78, 89, 105, 157

NTCP *Normal Tissue Complication Probability*. 20

OER *Oxygen Enhancement Ratio*. 17, 18

OPERA *Oscillation Project with Emulsion-tRacking Apparatus*. 51

OV *OverVoltage*. 74, 76, 77, 82, 87, 156

PCB *Printed Circuit Board*. 47, 48, 155

PDE *Photo Detection Efficiency*. 76, 77, 156

PEANUT *PreEquilibrium Approach to NUclear Thermalization*. 59, 60

PMMA *Poly(methyl methacrylate)*. 38–40

PMT *Photo-Multiplier Tubes*. 73, 75, 83, 156

QCD *Quantum ChromoDynamics*. 59

QMD *Quantum Molecular Dynamics*. 12

RBE *Relative Biological Effectiveness*. 16–18, 22, 25, 29, 30, 35, 153, 154

RMS Root Mean Square. 92

rQMD *Relativistic Quantum Molecular Dynamics*. 60

SC *Start Counter*. 41–44, 50, 51, 54, 117, 155

SHOE *Software for Hadrontherapy Optimization Experiment*. 61, 62, 127, 129, 132, 134

SiPM *Silicon PhotonMultiplier*. 42, 48, 49, 72, 74–79, 81–83, 85, 87, 88, 90, 92, 94, 96, 97, 99, 101, 102, 105, 106, 110, 117–122, 124, 125, 137, 156, 157, 159, 160, 163

SOBP *Spread-Out Bragg Peak*. 22, 24, 154

SPAD *Single Photon Avalanche Diode*. 74, 75, 87, 156

SPE *Solar Particle Events*. 1, 31–33

SSB *Single Strand Breaks*. 13

TCP *Tumor Control Probability*. 20

TDC *Time to Digital Converter*. 42, 50

TIA *Time Integrated Amplitude*. 71, 79, 80, 87, 91, 92, 156

TOE *Tracking Of Ejectile*. 62

TOF *Time Of Flight*. 41, 42, 47, 53–57, 62, 134, 155

TPS *Treatment Planning System*. 1, 24, 25, 27–29, 137, 154

TW *Tof-Wall*. 41, 42, 47, 48, 50, 51, 53–56, 61, 103, 117, 118, 127, 138, 155

VTX *Vertex*. 41, 43, 44, 46, 50, 55, 56, 117, 155

Bibliography

[1] PTCOG. *Statistics about patients treated with particles*. URL: https://www.ptcog.ch/.

[2] Marco Durante and Francesco Tommasino. "Proton radiobiology". In: *Cancers (Basel)* 7.02 (2015), pp. 353–381. DOI: https://doi.org/10.3390/cancers7010353.

[3] K Gunzert-Marx. "Secondary beam fragments produced by 200 MeV u-112c ions in water and their dose contributions in carbon ion radiotherapy". In: *New Journal of Physics* 10.7 (2008). DOI: 10.1088/1367-2630/10/7/075003.

[4] Francesco Tommasino and Marco Durante. "New ions for therapy". In: *International Journal of Particle Therapy* 2.3 (2015), pp. 428–438. DOI: 10.14338/IJPT-15-00027.1.

[5] Luca Arrabito. "Track reconstruction in the emulsion-lead target of the OPERA experiment using the ESS microscope". In: *Journal of Instrumentation* 2 (2007). DOI: 10.3322/caac.21492.

[6] Emilio Segrè. *Experimental nuclear physics Vol.2*. John Wiley and Sons, 1953.

[7] M. Tanabashi (Particle Data Group). "Review of Particle Physics D". In: *Reviews of modern physics* 98 (2018). DOI: https://doi.org/10.1103/PhysRevD.98.030001.

[8] Aafke Christine Kraan. "Range verification methods in particle therapy: underlying physics and Monte Carlo modeling". In: *Frontiers in Oncology* (2015). DOI: https://doi.org/10.3389/fonc.2015.00150.

[9] W.H. Barkas. *Nuclear research emulsions Vol.1*. Academic Press, 1963.

[10] T. Bortfeld. "An analytical approximation of the Bragg curve for therapeutic proton beams". In: *Medical Physics* 24.12 (1997), pp. 2024–2033. DOI: 10.1118/1.598116.

[11] Dieter Schardt. "Heavy-ion tumor therapy: Physical and radiobiological benefits". In: *Reviews of modern physics* 82.383 (2010). DOI: https://doi.org/10.1103/RevModPhys.82.383.

[12] P.V. Vavilov. "Ionization losses of high energy heavy particles". In: *Soviet Phisics JEPT* 5.4 (Nov. 1957).

[13] G. Moliere. "Theorie der Streuung schneller geladener Teilchen II. Mehrfach- und Vielfachstreuung". In: *Zeitschrift fur Naturforschung A* 3.2 (1948), pp. 78–97. DOI: 10.1515/zna-1948-0203.

[14] V. L. Highland. "Some practical remarks on multiple scattering". In: *Nuclear Instruments and Methods* 192.2 (1975), pp. 497–499. DOI: https://doi.org/10.1016/0029-554X(75)90743-0.

[15] G. Kraft. "Tumor therapy with heavy charged particles". In: *Progress in Particle and Nuclear Physic* 45 (2000), pp. 473–544. DOI: 10.1016/S0146-6410(00)00112-5.

[16] Bernard Gottschalk. "Multiple coulomb scattering of 160 MeV protons". In: *Nuclear Instruments and Methods in Physics Research Section B: Beam Interactions with Materials and Atoms* 74.4 (1993), pp. 467–490. DOI: https://doi.org/10.1016/0168-583X(93)95944-Z.

[17] Bernard Gottschalk. "Radiotherapy Proton Interactions in Matter". In: (2018).

[18] R. Serber. "Nuclear reactions at high energies". In: *Physical Review Journals Archive* 72 (1947), pp. 1114–1115. DOI: https://doi.org/10.1103/PhysRev.72.1114.

[19] V. Weisskopf. "Statistics and Nuclear Reactions". In: *Physical Review Journals Archive* 52 (1937), pp. 295–303. DOI: https://doi.org/10.1103/PhysRev.52.295.

[20] E. Fermi. "High energy nuclear events". In: *Progress of theretical physics* 5 (1950), pp. 570–583. DOI: 10.1143/ptp/5.4.570.

[21] J. Aichelin. "'Quantum' molecular dynamics: A Dynamical microscopic n body approach to investigate fragment formation and the nuclear equation of state in heavy ion collisions". In: *Physics Reports* 202.5 (1991), pp. 233–260. DOI: 10.1016/0370-1573(91)90094-3.

[22] G.F.Bertsch and S. Das Gupta. "A guide to microscopic models for intermediate energy heavy ion collisions". In: *Physics Reports* 160.4 (1988), pp. 189–233. DOI: https://doi.org/10.1016/0370-1573(88)90170-6.

[23] M. Cavinato et al. "Boltzmann Master Equation Theory of Nuclear Reactions: From Nucleons to Heavy Ions". In: *Topics in Atomic and Nuclear Collisions* (1994), pp. 25–41. DOI: 10.1007/978-1-4615-2431-1_2.

[24] R. L. Warters and K. G. Hofer. "Radionuclide Toxicity in Cultured Mammalian Cells: Elucidation of the Primary Site for Radiation-Induced Division Delay". In: *Radiation Research* 69.2 (1977), pp. 348–358. DOI: https://doi.org/10.2307/3574442.

[25] Michael Joiner and Albert Van der Kogel. *Basic Clinical Radiobiology*. 2009. ISBN: 978 0 340 929 667.

[26] N. Sharma Jac A. Nickoloff and L. Taylor. "Clustered DNA Double-Strand Breaks: Biological Effects and Relevance to Cancer Radiotherapy". In: *Genes (Basel)* 11.1 (2020), p. 99. DOI: 10.3390/genes11010099.

[27] P. H. Flanders and A. Pirie. "The Effect of Breathing Oxygen on the Radiosensitivity of the Rabbit Lens and the Use of Oxygen in X-Ray Therapy". In: *Radiation Research* 7.4 (1957), pp. 357–364. DOI: https://doi.org/10.2307/3570563.

[28] Freddie Bray. "Global cancer statistics 2018: GLOBOCAN estimates of incidence and mortality worldwide for 36 cancers in 185 countries". In: *CA Cancer J Clin.* 68.6 (2018), pp. 394–424. DOI: 10.3322/caac.21492.

[29] James Slater. *From x-rays to ion beams: A short history of radiation therapy. Ion Beam Therapy: Fundamentals, Technology, Clinical Applications, Biological and Medical Physics, Biomedical Engineering*. 2012.

[30] A. Taylor and M.E.B. Powell. "Intensity-modulated radiotherapy-what is it?" In: *Cancer imaging* 4 (2004), pp. 68–73. DOI: 10.1102/1470-7330.2004.0003.

[31] *What is Hadron Therapy?* URL: https://enlight.web.cern.ch/what-is-hadron-therapy.

[32] Fondazione CNAO. *The CNAO's Synchrotron*. URL: https://fondazionecnao.it/en/.

[33] Francesco Dionisi. "Proton therapy in adjuvant treatment of gastric cancer: Planning comparison with advanced x-ray therapy and feasibility report". In: *Acta Oncologica* 53 (2014), pp. 1312–1320. DOI: 10.3109/0284186X.2014.912351.

[34] Francesco Dionisi. "Experimental study of nuclear fragmentation of 200 and 400 MeV/u 12C ions in water for applications in particle therapy". In: *Physics in Medicine and Biology* 58.23 (2013), pp. 8265–8279. DOI: 10.1088/0031-9155/58/23/8265.

[35] R.T. Santoro H.W. Bertini and O.W. Hermann. "Calculated nucleon spectra at several angles from 192-, 500-, 700-, and 900-MeV 12C on 56Fe". In: *Phys. Rev.* C.14 (1976), p. 590.

[36] M Krämer and M Schol. "Treatment planning for heavy-ion radiotherapy: calculation and optimization of biologically effective dose". In: *Physics in Medicine and Biology* 45.11 (2000), pp. 3319–3330. DOI: 10.1088/0031-9155/45/11/314.

[37] et al. Satoshi Kodaira Hisashi Kitamura. "Contribution to dose in healthy tissue from secondary target fragments in therapeutic proton, he and c beams measured with CR-39 plastic nuclear track detectors". In: *Scientific Reports* 9.12 (2019). DOI: 10.1038/s41598-019-39598-0.

[38] NASA. *NASA Perseveres Through Pandemic, Looks Ahead in 2021*. URL: https://www.nasa.gov/feature/nasa-perseveres-through-pandemic-looks-ahead-in-2021.

[39] J. Beringer et al. (Particle Data Group). "Review of Particle Physics". In: *Phys. Rev. D* 86 (2012). DOI: 10.1103/PhysRevD.86.010001.

[40] M. Durante and A. Cucinotta. "Physical basis of radiation protection in space travel". In: *Reviews of modern physics* 83.4 (2011), pp. 1245–1281. DOI: 10.1103/revmodphys.83.1245.

[41] S.M.Valle et al. "FOOT: a new experiment to measure nuclear fragmentation at intermediate energies". In: *Perspectives in Science* 12 (2019). DOI: https://doi.org/10.1016/j.pisc.2019.100415.

[42] G. Battistoni et al. "Measuring the Impact of Nuclear Interaction in Particle Therapy and in Radio Protection in Space: the FOOT Experiment". In: *Frontiers in Physics* 8 (2021). DOI: https://doi.org/10.3389/fphy.2020.568242.

[43] P. Sala et al. A. Ferrari. "FLUKA: A multi-particle transport code". In: *Technical Report* CERN-2005-10, INFN/TC 05/11,SLAC-R-773, CERN, INFN, SLAC (2005).

[44] G. Battistoni et al. "The FLUKA Code: An Accurate Simulation Tool for Particle Therapy". In: *Frontiers in Oncology* 6.116 (2016). DOI: https://doi.org/10.3389/fonc.2016.00116.

[45] F. Cerutti et al. T.T. Boehlen. "The FLUKA Code: Developments and Challenges for High Energy and Medical Applications". In: *Nuclear Data Sheets* 120 (2014), pp. 211–214. DOI: https://doi.org/10.1016/j.nds.2014.07.049.

[46] T. Boehlen et al. G. Battistoni. "Overview of the FLUKA code". In: *Annals of Nuclear Energy* 82 (2015), pp. 10–18. DOI: https://doi.org/10.1016/j.anucene.2014.11.007.

[47] M. Toppi et al. "Measurement of fragmentation cross sections of 12C ions on a thin gold target with the FIRST apparatus". In: *Physical Review C* 93.6 (2016), p. 064601. DOI: 10.1103/PhysRevC.93.064601.

[48] J. Dudouet et al. "Double-differential fragmentation cross-section measurements of 95 MeV/u 12C beams on thin targets for hadron therapy". In: *Physical Review C* 88.2 (2013), p. 024606. DOI: https://doi.org/10.1103/PhysRevC.88.024606.

[49] J. W. Norbury and J. Miller. "Review of Nuclear Physics Experimental Data for Space Radiation". In: *Health Physics* 103.5 (2012), pp. 640–642. DOI: 10.1097/hp.0b013e318261fb7.

[50] Duda Krzysztof and Zoladz Jerzy A. *Muscle and Exercise Physiology*. Academic Press, 2019. ISBN: 978-0-12-814593-7.

[51] R.A. Weldon Jr. "Measurement of EJ-228 plastic scintillator proton light output using a coincident neutron scatter technique". In: *Nuclear Instruments and Methods in Physics Research Section A: Accelerators, Spectrometers, Detectors and Associated Equipment* 953 (2020). DOI: https://doi.org/10.1016/j.nima.2019.163192.

[52] A. Ghassemi. "MPPC". In: *Hamamatsu - Photon is our Business* (2020). DOI: https://doi.org/10.1016/j.nima.2019.163192.

[53] Azo Materials. *Polyethylene Terephthalate Polyester (PET, PETP) - Properties and Applications*. URL: https://www.azom.com/article.aspx?ArticleID=2047.

[54] Y. Dong et al. "The Drift Chamber detector of the FOOT experiment: Performance analysis and external calibration". In: *Nuclear Instruments and Methods in Physics Research. Section A, Accelerators, Spectrometers, Detectors and Associated Equipment* 986 (2020). DOI: https://doi.org/10.1016/j.nima.2020.164756.

[55] L. Greiner et al. "A MAPS based vertex detector for the STAR experiment at RHIC". In: *Nuclear Instruments and Methods in Physics Research A* 650.1 (2011), pp. 68–72. DOI: https://doi.org/10.1016/j.nima.2010.12.006.

[56] I. Valin et al. "A reticle size CMOS pixel sensor dedicated to the STAR HFT". In: *Journal of Instrumentation* 7 (2012). DOI: https://doi.org/10.1088/1748-0221/7/01/C01102.

[57] N. Simos et al. "Demagnetization of $Nd_2Fe_{14}B$, $Pr_2Fe_{14}B$, and Sm_2Co_{17} Permanent Magnets in Spallation Irradiation Fields". In: *IEEE Transactions on Magnetics* 54.5 (2018). DOI: https://doi.org/10.1109/TMAG.2017.2769040.

[58] W. de Boer et al. "Measurements with a CMOS pixel sensor in magnetic fields". In: *Nuclear Instruments and Methods in Physics Research. Section A, Accelerators, Spectrometers, Detectors and Associated Equipment* 487.1 (2002), pp. 163–169. DOI: 10.1016/S0168-9002(02)00960-9.

[59] PLUME. *Plume Project*. URL: http://www.iphc.cnrs.fr/PLUME.html.

[60] E. Ciarrocchi et al. "The ΔE-TOF detector of the FOOT experiment: Experimental tests and Monte Carlo simulations". In: *Nuclear Instruments and Methods in Physics Research A* 936 (2019), pp. 78–79. DOI: https://doi.org/10.1016/j.nima.2018.08.117.

[61] M. Morrocchi et al. "Performance Evaluation of the TOF-Wall Detector of the FOOT Experiment". In: *IEEE Transactions on Nuclear Science* 68.5 (2021), pp. 1161–1168. DOI: 10.1109/TNS.2020.3041433.

[62] L. Galli et al. "WaveDAQ: An highly integrated trigger and data acquisition system". In: *Nuclear Instruments and Methods in Physics Research. Section A, Accelerators, Spectrometers, Detectors and Associated Equipment* 936 (2019), pp. 399–400. DOI: 10.1016/j.nima.2018.07.067.

[63] M. Morrocchi et al. "Development and characterization of a ΔE-TOF detector prototype for the FOOT experiment". In: *Nuclear Instruments and Methods in Physics Research. Section A, Accelerators, Spectrometers, Detectors and Associated Equipment* 916 (2018), pp. 116–124. DOI: 10.1016/j.nima.2018.09.086.

[64] L. Scavarda. "Design and performance of the Calorimeter for the FOOT experiment". In: *Nuovo Cimento* 43 C (2020). DOI: 10.1393/ncc/i2020-20123-3.

[65] L. Scavarda. "The Foot Experiment: Measuring Proton and Light Nuclei Fragmentation Cross Sections up to 700 MeV/A". In: *Bulletin of the Russian Academy of Sciences: Physics* 84 (2020), pp. 480–484. DOI: https://doi.org/10.3103/S1062873820040267.

[66] Saint-Gobain. *BGO Bismuth Germanate Scintillation Material*. URL: https://www.crystals.saint-gobain.com/sites/imdf.crystals.com/files/documents/bgo-material-data-sheet.pdf.

[67] G. de Lellis et al. *Nuclear Emulsions*. Springer, 2011.

[68] M. de Serio et al. "High precision measurements with nuclear emulsions using fast automated microscopes". In: *Nuclear Instruments and Methods in Physics Research. Section A, Accelerators, Spectrometers, Detectors and Associated Equipment* 554.1 (2005), pp. 247–254. DOI: 10.1016/j.nima.2005.08.017.

[69] V. Tioukov A. Alexandrov and M. Vladymyrov. "Further progress for a fast scanning of nuclear emulsions with Large Angle Scanning System". In: *Journal of Instrumentation* 9.2 (2014), p. C02034. DOI: 10.1088/1748-0221/9/02/C02034.

[70] Taku Nakamura et al. "The OPERA film: New nuclear emulsion for large-scale, high-precision experiments". In: *Nuclear Instruments and Methods in Physics Research. Section A, Accelerators, Spectrometers, Detectors and Associated Equipment* 1.556 (2006), pp. 80–86. DOI: 10.1016/j.nima.2005.08.109.

[71] M.C. Montesi et al. "Ion charge separation with new generation of nuclear emulsion films". In: *Open Physics* 17.1 (2019), pp. 233–240. DOI: https://doi.org/10.1515/phys-2019-0024.

[72] A.C. Kraan et al. "Charge identification of nuclear fragments with the FOOT Time-Of-Flight system". In: *Nuclear Instruments and Methods in Physics Research. Section A, Accelerators, Spectrometers, Detectors and Associated Equipment* 1001 (2021). DOI: https://doi.org/10.1016/j.nima.2021.165206.

[73] E. Spiriti et al. "CMOS active pixel sensors response to low energy light ions". In: *Nuclear Instruments and Methods in Physics Research. Section A, Accelerators, Spectrometers, Detectors and Associated Equipment* 875 (2017). DOI: 10.1016/j.nima.2017.08.058.

[74] M. J. D. Powell. *A method for nonlinear constraints in minimization problems*. New York: Academic Press., 1969. ISBN: 0-12-260650-7.

[75] W. S. Cho et al. "OPTIMASS: A Package for the Minimization of Kinematic Mass Functions with Constraints". In: *J. High Energy Phys.* 2016.1 (2016), p. 26. DOI: 10.1007/jhep01(2016)026.

[76] FLUKA. *FLUKA manuals*. URL: http://www.fluka.org/fluka.php.

[77] A. Capella et al. "Dual parton model". In: *Physics Reports* 236.4 (1994), pp. 225–329. DOI: 10.1016/0370-1573(94)90064-7.

[78] R.J. Glauber et al. "High-energy scattering of protons by nuclei". In: *Nuclear Physics B* 21.2 (1970), pp. 135–157. DOI: 10.1016/0550-3213(70)90511-0.

[79] V. Andersen et al. "The FLUKA code for space applications: recent developments". In: *Advances in Space Research* 34.6 (2004), pp. 1302–1310. DOI: 10.1016/j.asr.2003.03.045.

[80] W. Greiner H. Sorge H. Stoecker. "Poincaré invariant Hamiltonian dynamics: Modelling multi-hadronic interactions in a phase space approach". In: *Annals of Physics* 192.2 (1989), pp. 266–306. DOI: https://doi.org/10.1016/0003-4916(89)90136-X.

[81] C. Hoppner et al. "A Novel Generic Framework for Track Fitting in Complex Detector Systems". In: *Nuclear Instruments and Methods in Physics Research Section A: Accelerators, Spectrometers, Detectors and Associated Equipment* 620.2 (2010), pp. 518–525. DOI: 10.1016/j.nima.2010.03.136.

[82] C. W. Fabjan et al. "Energy measurement of elementary particles". In: *Reports on Progress in Physics* 52.12 (1989). DOI: https://doi.org/10.1088/0034-4885/52/12/002.

[83] K. Hagiwara et al. "Review of Particle Physics". In: *Physical Review D* 66 (2002), p. 010001. URL: http://pdg.lbl.gov.

[84] E. Longo and I. Sestili. "Monte Carlo calculation of photon-initiated electromagnetic showers in lead glass". In: *Nuclear Instruments and Methods* 128.2 (1975), pp. 283–307. DOI: https://doi.org/10.1016/0029-554X(75)90679-5.

[85] T. C. Weekes. "Very high energy gamma-ray astronomy". In: *Physics Reports* 160.1-2 (1980), pp. 1–121. DOI: https://doi.org/10.1016/0370-1573(88)90177-9.

[86] L. F. Miller et al. "Digital pulse shape discrimination". In: *Radiation Protection Dosimetry* 126.1-4 (2007), pp. 253–255. DOI: 10.1093/rpd/ncm052.

[87] Mark Joseph Oreglia. "A study of the reactions $\psi' \to \gamma\gamma\psi$". PhD thesis. 1980. URL: https://www.slac.stanford.edu/cgi-bin/getdoc/slac-r-236.pdf.

[88] DOW website. *DOWSIL™ 3145 RTV Mil-A-46146 Adhesive / Sealant*. URL: https://www.dow.com/en-us/pdp.dowsil-3145-rtv-mil-a-46146-adhesive-sealant.01059548z.html.

[89] Dupont website. *what is Tyvek*. URL: https://www.dupont.com/tyvekdesign/design-with-tyvek/why-tyvek.html.

[90] Dupont website. *Mylar polyster film*. URL: http://usa.dupontteijinfilms.com/wp-content/uploads/2017/01/Mylar_Electrical_Properties.pdf.

[91] P. L. Wang et al. "Study on the temperature dependence of BGO light yield". In: *Science China. Physics, Mechanics and Astronomy* 57.10 (2014), pp. 1898–1901. DOI: 10.1007/s11433-014-5548-4.

[92] A. N. et al. "Characterization of Three High Efficiency and Blue Sensitive Silicon Photomultipliers". In: *Nuclear Instruments and Methods in Physics Research Section A: Accelerators, Spectrometers, Detectors and Associated Equipment* 846 (2017), pp. 106–125. DOI: https://doi.org/10.1016/j.nima.2016.09.053.

[93] E. Auffray et al. "Beam tests of lead tungstate crystal matrices and a silicon strip preshower detector for the CMS electromagnetic calorimeter". In: *Nuclear Instruments and Methods in Physics Research A* 412.2-3 (1998), pp. 223–237. DOI: 10.1016/S0168-9002(98)00464-1).

[94] J. B. Birks. "Scintillations from Organic Crystals: Specific Fluorescence and Relative Response to Different Radiations". In: *Proceedings of the Physical Society A* 64.874 (1954). DOI: https://dx.doi.org/10.1088/0370-1298/64/10/303.

[95] J. I. Hopkins. "Electron Energy Studies with the Anthracene Scintillation Counter". In: *Review of Scientific Instruments* 22.29 (1951). DOI: https://doi.org/10.1063/1.1745734.

[96] J. B. Birks. "Scintillation Efficiency of Anthracene Crystals". In: *Proceedings of the Physical Society A* 63.11 (1950), p. 1294.

[97] E. J. Bowen. "Resonance Transfer of Electronic Energy in Organic Crystals". In: *Proceedings of the Physical Society A* 62.1 (1949), p. 26.

[98] J. B. Birks. "Scintillations from Naphthalene-Anthracene Crystals". In: *Proceedings of the Physical Society A* 63.9 (1950), p. 1044.

[99] J. B. Birks and F. A. Black. "Deterioration of Anthracene under α-Particle Irradiation". In: *Proceedings of the Physical Society A* 64.5 (1951), p. 511.

[100] N. Matsufuji et al. "The response of a BGO scintillator to relativistic heavy ions". In: *Nuclear Instruments and Methods in Physics Research A* 430 (1999), pp. 60–68. DOI: https://doi.org/10.1016/S0168-9002(99)00180-1.

[101] V. Avdeichikov et al. "Range-energy relation, range straggling and response function of CsI(Tl), BGO and GSO(Ce) scintillators for light ions". In: *Nuclear Instruments and Methods in Physics Research A* 439 (2000), pp. 158–166. DOI: https://doi.org/10.1016/S0168-9002(99)00944-4.

[102] J. Tammen et al. "Quenching comparison of BGO and BSO for heavy ions". In: *Nuclear Instruments and Methods in Physics Research B* 360 (2015), pp. 129–138. DOI: https://doi.org/10.1016/j.nimb.2015.07.127.

List of Figures

List of Tables

Acknowledgements

Purtroppo non sono bravo con i ringraziamenti (non parliamone a scriverli); avevo infatti pensato di schivarli agilmente ma mi sono reso conto che era DOVEROSO lasciare una dedica ed un ringraziamento ad alcune persone che dal 2017, conclusa la laurea Magistrale, mi hanno accompagnato, seguito, consigliato, insegnato per tutti questi anni.

Vorrei partire dal gruppo di Torino ed in particolare dalle due persone con cui ho condiviso maggiormente questi anni: Piergiorgio e Nazar. Ogni test beam, ogni notte al CNAO o al GSI sono state delle vere e proprie avventure che non dimenticherò mai. Grazie per tutto quello che mi avete trasmesso lavorativamente e non solo.

Un ringraziamento speciale anche per tutti gli altri del gruppo torinese: Stefano, Francesca, Luciano, Michele, Elisa, Veronica, Francesco. Ognuno di voi è riuscito a trasmettermi e ad insegnarmi qualcosa che ha contribuito al mio percorso.

Un grandissimo ringraziamento a tutta la collaborazione FOOT che, fin dal primissimo giorno, mi ha fatto sentire "parte della famiglia". Ricorderò sempre quel "Software Tutorial" a Bologna: prima trasferta solitaria con un nuovo gruppo di lavoro e, sopratutto, primissimo faccia-faccia con SHOE (lascio a voi i commenti). Ma nonostante tutto mi sono sentito subito uno di voi. L'elenco è lunghissimo ma vorrei lasciare un carissimo saluto a: Alessio, Vincenzo, Ilaria, Giacomo, Giuseppe, Riccardo, Serena, Esther, Aafke, Matteo, Roberto S., Roberto Z., Francesco, Mauro, Sofia, Giusy, Marco P., Yun, Marco T., Chris. La miglior Collaborazione che potessi trovare.

Non potevo non fare un ringraziamento a parte per Michela che mi ha sopportato in tutti questi anni accollandosi un inesperto ed imbranato neo-laureato. Grazie per la pazienza e per tutto.

Poi tocca alle due persone che c'erano prima dell'inizio di questo percorso e che ci saranno sempre: Riccardo e Luca. Con voi posso condividere tutto e nonostante il lavoro ci abbia geograficamente allontanato è come se fossimo sempre vicini. Amici di sempre.

Penso che non ci siano abbastanza parole per te, Vichi. Grazie per tutto quello che fai. Grazie per l'immensa pazienza che hai avuto e scusami per tutti gli sbalzi di umore che hai dovuto sopportare. Grazie per essermi stata vicino in ogni situazione, per continuare ad incoraggiarmi e per essere sempre orgogliosa di me. Il futuro che ci aspetta non può che essere meraviglioso.

Infine un gigantesco GRAZIE a Mamma e Papà per esserci, le due persone più importanti fra tutte.